Hall probe microscopy and magnetometry of flux penetration in high temperature superconductors

Gregory, James Kevin

Award date:
2003

Awarding institution:
University of Bath

Hall Probe Microscopy and Magnetometry of Flux penetration in High Temperature Superconductors

Submitted by James Kevin Gregory

for the degree of

Doctor of Philosophy

of the University of Bath

2003

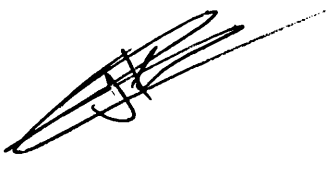

ProQuest LLC
789 East Eisenhower Parkway
P.O. Box 1346
Ann Arbor, MI 48106-1346

Acknowledgements

As is so often said "there are more people to thank than can be mentioned here", none the less I'm going to give it a good go, so if you're not one of the people that needs thanking I suggest you skip to the contents page.

I would like to start by thanking my supervisor, Professor Simon Bending, for his guidance and supervision throughout the project. Without his support and enthusiasm, I would not have been able to complete the work presented here.

I would also like to take this opportunity to express my sincere gratitude to the following people, from the department of physics, who have helped me on numerous occasions over the course of the last three years. Mr. Bob Draper for his technical assistance, practical help and for always knowing where everything was. Ms. Wendy Lambson for keeping the clean room facilities in working order. Mr. Eddie Lambson for keeping the level 5 workshop in a useable state despite everyone's best efforts. Mr. Mike Harriman for his advice with all things electrical and many interesting discussions. The now ex-staff of the central scientific workshop, which unfortunately is no longer in existence. Dr. Peter Ford for explaining the black art that is ordering from the University whilst still receiving the item within a reasonable amount of time. Ms. Eva Ashford for helping me with all the various forms and paper work over the years, and for seemingly knowing everybody and everything. Mr. Adrian Hooper for his IT support and all the departmental office staff, past and present, for their always cheery greetings even when I was just coming in to pinch some staples.

I am also very grateful to my colleagues and friends Dr. Arturo Ortigosa, Dr. David Lawton, and William Reeves for proving that not all scientists fit the stereotype, well, not all at the same time anyway. Dejan Uzur, David Cole, Paul Bennett, and Richard Martin for providing if not at times stimulating, but always amusing lunch time

conversation. Dr. Sasha Grigorenko, Dr. Sivapathasundaram Sivaraya, Dr. Matt James, Dr. Alex Pross, Alex Brook and all the other members of the group past and present for their support and encouragement. Also, I would like to thank the members of the optics group who have allowed me to accompany them on numerous coffee breaks and social gatherings, in particular John Pottage, Greg Antonopoulos and William Wadsworth deserve a mention here as does Dr. Brian Mangan who's kind offer of accommodation in times of need saved the author the pleasure of experiencing the practicalities of homelessness.

Then there are the many people who have helped me keep a healthy perspective on life outside of science. I would like to thank Rob, Tsumi, Richard and Rachel for accompanying me on various mountain biking expeditions into the wilds of the British Isles, and for always being there to talk to when it was all getting a bit too much. I would also like to thank Andy, Owen, Jason, Matt, Dan, and Barry for their unflinching dedication to my attending many refined social gatherings organized by their good selves, long may it continue.

Special thanks go to all the members of my family, in particular my son Ruben, whose arrival was an unexpected one but very welcomed, and who is a source of great joy to all of us.

Finally, I would like to thank Jude for being the best mother a child could wish for and a father could imagine.

Abstract

The main goal of this project was the development of a scanning Hall probe microscope (SHPM) for large area magnetic imaging down to cryogenic temperatures. This has been achieved by building a SHPM around a closed-cycle refrigerator capable of cooling samples down to 35 K. The performance of the system is assessed and its potential illustrated with images of the local magnetic induction at the surface of various magnetic recording media at room temperature as well as images of various superconducting samples at temperatures down to 35K.

The large area SHPM has been used in two main studies; Scanning Hall probe microscopy of flux penetration into a superconducting $Bi_2Sr_2CaCu_2O_{8+\delta}$ platelet-like single crystal sample, and preliminary local magnetic induction imaging in ferromagnetic GaMnAs films. The results of the former compare favourably with existing theories at low fields. Near the second magnetisation peak a new regime is indicated, which is interpreted in terms of the reversal of the direction of screening currents at the interface between low and high pinning material.

In conjunction with the development of the large area SHPM micron-sized linear Hall probe arrays have been used to investigate the effects of irradiation on surface barriers for flux penetration in individual superconducting $Bi_2Sr_2CaCu_2O_{8+\delta}$ whiskers. Samples were irradiated with 2.5 MeV electrons or 9 GeV heavy (Pb) ions. At all temperatures, irradiation by high-energy electrons or swift heavy ions is found to substantially reduce the penetration field. In addition a high-resolution SHPM has also been used to measure flux profiles across one "wire" of a long $YBa_2Cu_3O_{7-\delta}$ thin film meander line, and a correlation between the surface topography of the meander line edges and the regions of penetration established.

Contents

Chapter 1

1. Introduction

1.1. Motivation

Various techniques exist to investigate the local magnetic induction of magnetic materials. A technique that has been shown to be a very sensitive, non-invasive technique for obtaining quantitative measurements of surface magnetic field profiles is scanning Hall probe microscopy (SHPM). The existing range of Hall probe magnetic imaging techniques developed in Bath, prior to the work presented in this thesis spanned the length scales 0.1-100μm allowing detailed comparisons between theory and experiments, including the observation of magnetic domains in ferromagnetic materials, quantized flux vortices in type II superconductors, and the non-destructive evaluation (NDE) of various electronic materials. In particular the magnetic properties of the highly anisotropic high temperature superconductors (HTS) have attracted considerable attention. Flux lines in high temperature superconductors are known to exhibit a wide range of novel phenomena due, in part, to the strong crystalline anisotropy of this class of materials, which allows flux lines to behave as weakly coupled flux pancakes under some circumstances. In addition, the high possible measurement temperatures lead to much higher thermal fluctuations and the clear observation of effects such as first order vortex solid melting. Bulk pinning can also be extremely weak over much of the H-T phase diagram, and surface barriers frequently dominate irreversible magnetisation and transport properties. Previous work in Bath has established that many of the properties of real superconducting samples (e.g. the critical current) are limited by sample inhomogeneties; an aspect that is missing from all current theoretical models. The

physical mechanism controlling the penetration field (H_p) at which flux first enters the bulk of the zero-field-cooled superconductor also remains controversial.

The purpose of the work presented in this thesis was to extend the range of Hall probe magnetic imaging techniques available from 0.1-100μm to 0.1μm-25mm allowing larger areas of real superconducting samples to be investigated. Once the system was operational information from a range of complementary measurements on HTS thin films and single crystals was to be brought together to provide a better understanding of flux structures and vortex dynamics in these materials. Possible material improvements obtained by the controlled introduction of artificial pinning sites were also to be explored.

1.2. Overview of Thesis

Initially the project was to design and construct a large area SHPM to increase the range of Hall probe magnetic imaging techniques to 25mm, thus allowing the local magnetic induction of physically larger samples to be investigated. However, due to complications with the installation and subsequent recall of the closed-cycle refrigerator, which the SHPM was to be built around, completion of the SHPM was severely delayed. In the meantime the investigations; "Suppression of surface barriers for flux penetration in $Bi_2Sr_2CaCu_2O_{8+\delta}$ whiskers by electron and heavy ion irradiation", and "Scanning Hall probe microscopy of flux penetration into a superconducting $YBa_2Cu_3O_{7-\delta}$ thin film strip", were carried out. On completion of the large area SHPM various magnetic samples were investigated to test its performance and the system used to investigate flux penetration into a superconducting $Bi_2Sr_2CaCu_2O_{8+\delta}$ platelet-like single crystal sample and the domain structure in two different ferromagnetic GaMnAs films. Below is a brief description of the content of each individual chapter contained in this thesis which it is hoped will give the reader a general overview of the thesis and better understanding of the work therein.

Chapter 2 presents the basic principles that underlie the subject of superconductivity. The chapter sets out to introduce the magnetic aspects of superconductivity and

emphasizes the macroscopic aspects of the subject. High temperature superconductors (HTS) are not covered in this chapter but the concepts needed to understand their behaviour introduced.

Chapter 3 covers the subject of HTS concentrating on the topics that will help the reader better understand the work presented in this thesis. A number of topics, such as flux creep and flux lattice melting are discussed. The subjects of Bean-Livingston barriers and geometrical barriers to flux line motion are also covered as these are both relevant to work presented later in this thesis.

Chapter 4 gives a brief description of the important material properties of Yttrium Barium Copper Oxide (YBCO) and Bismuth Strontium Calcium Copper Oxide (BSCCO), both studied in various sample forms in this thesis. A comparison of the two material structures is given and the differences in their magnetic behaviour discussed.

Chapter 5 gives a brief description of the Hall effect utilized by the sensors employed in this thesis. Details of the Hall probes used in the project are presented and the design and fabrication of the different sensors, and the materials used described.

Chapter 6 details the design and construction of the large area SHPM used to collect the majority of the results presented in this thesis, along with brief descriptions of any existing techniques and equipment used.

Chapter 7 presents the results of two separate investigations. The first investigation looks at the suppression of surface barriers for flux penetration in BSCCO whiskers by electron and heavy ion irradiation, and the second investigation looks at flux penetration in a superconducting YBCO thin film strip using scanning Hall probe microscopy.

Chapter 8 presents the results of flux penetration studies into a superconducting $Bi_2Sr_2CaCu_2O_{8+\delta}$ platelet-like single crystal using the large area SHPM. All the work

was carried out on the same $Bi_2Sr_2CaCu_2O_{8+\delta}$ platelet-like single crystal sample placed in a perpendicular magnetic field and the local magnetic induction investigated at various field and temperature values.

Preliminary local magnetic induction scans at the surface of two different GaMnAs films with in-plane magnetisation are presented in chapter 9, revealing information about the domain structures within these materials. The results were recorded using the large area SHPM developed as part of this thesis and another custom built high-resolution SHPM previously developed at the University of Bath.

Chapter 10 presents the conclusions from each of the investigations carried out in this thesis and contains an evaluation of the large area SHPM performance. Extensions to the work presented in this thesis are given along with suggestions of future applications of the large area SHPM.

Chapter 2

2. Introduction to Supconductivity

This chapter presents the basic principles that underlie the subject of superconductivity. The chapter sets out to introduce the magnetic aspects of superconductivity and emphasizes the macroscopic aspects of the subject. High temperature superconductors are not covered in this chapter but the concepts needed to understand their behaviour introduced. The difference between type I and type II superconductors is explained. Flux quantisation and the notion of vortex lines are discussed and the prevention of vortex-line motion, known as flux pinning introduced. The role of bulk pinning and surface pinning in type II superconductors current carrying properties are also introduced here.

2.1. History and Discovery

One of the principal characteristics of a metal is its electrical resistivity, and physicists have long been interested in the dependency of this quantity on temperature. In 1908, H Kamerlingh-Onnes succeeded in liquefying Helium at his laboratory in Leiden, and he undertook a systematic study of the properties of matter at low temperatures. He chose mercury as his sample, because it could be obtained in a sufficiently pure form.

In 1911, Karmerlingh-Onnes discovered the phenomenon of superconductivity. This phenomenon is actively studied from then to the present day and is one of the major branches of condensed matter physics. Kamerlingh-Onnes discovered that at a temperature close to 4K the electrical resistance of mercury abruptly vanishes.

The phenomenon of superconductivity is manifested by the electrical resistance vanishing at a finite temperature (called the critical temperature and denoted T_c). Interestingly, adding impurities to mercury did not destroy superconductivity, so that the original reasons for which Karmerlingh-Onnes chose mercury turned out to be unimportant.

The absence of any resistance is a fundamental characteristic of superconductors but not the only one. They possess anomalous magnetic, thermal, and other properties, some of which will be described later.

2.2. Basic Properties of Superconductors

In 1933, Meissner and Ochsenfeld discovered one of the most fundamental properties of superconductors. They found that magnetic fields were expelled from a superconducting sample below T_c. At temperatures above T_c, as in any normal metal in an external field, there was a finite magnetic field inside the sample. Meissner and Ochsenfeld found that at the moment the superconducting transition occurs, the magnetic field was expelled from the sample such that $\mathbf{B} = 0$ (where $\mathbf{B}$ is the magnetic induction). This phenomenon of superconductors is known as the Meissner effect.

All metals except ferromagnetic ones have zero magnetic induction in the absence of an external field, since their magnetisation $\mathbf{M}$ is zero. When an external field $\mathbf{H}$ is applied, there appears a finite induction $\mathbf{B}$ given by $\mathbf{B} = \mu_r\mu_0\mathbf{H}$. The coefficient μ_r is the relative magnetic permeability and μ_0 is the permeability of free space. When $\mu_r > 1$ (paramagnetic), the applied field is enhanced. In diamagnetic materials ($\mu_r < 1$), the applied field is weakened and $\mathbf{B} < \mu_0\mathbf{H}$. In superconductors, $\mathbf{B} = 0$, corresponding to zero permeability. This effect is called *perfect diamagnetism* and arises in superconductors due to the external field inducing a supercurrent on the surface of the sample in such a way that its magnetic field opposes the applied field. As a result there is zero magnetic induction deep inside the sample.

At any given temperature below T_c there is a magnetic field of sufficient strength that will overcome the Meissner effect and destroy superconductivity. This value is known as the *critical magnetic field, $H_c(T)$.* At T=0, the upper limit of the critical magnetic field is

$H_c(0)$. At T_c, the critical magnetic field goes to zero i.e. $H_c(T_c) = 0$. The dependence of H_c on T is approximately given by the formula

$$H_c(T) = H_c(0)\left[1-\left(\frac{T}{T_c}\right)^2\right], \tag{2.1}$$

A typical type I superconductor excludes all magnetic fields below H_c and admits magnetic fields without hindrance when H exceeds H_c i.e. *perfect diamagnetism.* Since in any material the applied magnetic field **H** is related to the magnetisation **M** and the magnetic induction **B** by the relation [1] $\mathbf{B} = \mu_0(\mathbf{H} + \mathbf{M})$. Therefore, $\mathbf{M} = -\mathbf{H}$, so that $\mathbf{B} = 0$. This exact cancellation gives type I superconductors the magnetisation curve of a perfect diamagnet, as shown in figure 2.1. For any value of **H**, there is exactly one corresponding value of **M,** and **B** is either zero or $\mu_r\mu_0\mathbf{H}$. This is true regardless of the path by which the magnetic field is introduced.

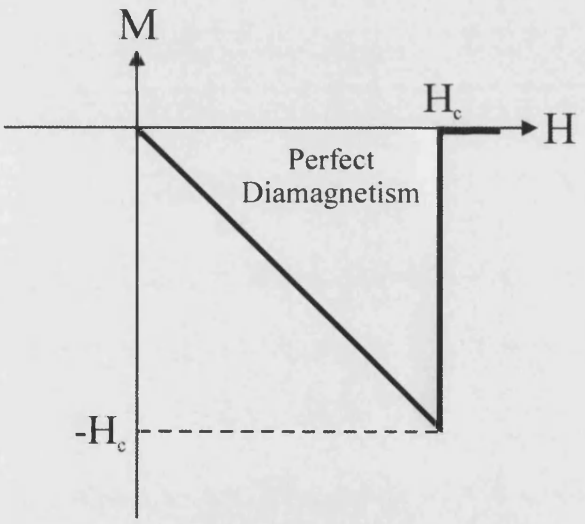

Fig. 2.1 Variation of magnetisation, M, with applied magnetic field, H, for a type I superconductor. The material shows perfect diamagnetism below H_c.

The Meissner effect cannot be explained using conventional models of electromagnetism in solids, instead F. and H. London applied the laws of

electromagnetism to a material with infinite conductivity and then applied certain restrictions to describe the expulsion of flux in the Meissner state. They hypothesized that, since current flows unimpeded within a superconductor, there should be circulating currents inside the superconductor which set up a magnetic field that exactly cancels the magnetic field being applied externally. The form required for such circulating currents is shown below; following Kittel's presentation [2].

Magnetic field **B** is related to the vector potential **A** by $\mathbf{B} = \nabla \times \mathbf{A}$, the London hypothesis assumes that the current density **j** is linearly proportional to **A**:

$$\underline{j} = \frac{-1}{\mu_0 \lambda_L^2} \underline{A} \tag{2.2}$$

This London equation is very different from the normal Ohm's law, $\mathbf{j} = \sigma\mathbf{E}$. Using Maxwell's equations the vector potential can be exchanged for the magnetic field by taking the curl of both sides obtaining

$$\nabla \times \underline{j} = \frac{-1}{\mu_0 \lambda_L^2} \underline{B} \tag{2.3}$$

From Maxwell's equations, in the absence of a time-varying electric field

$$\nabla \times \underline{B} = \mu_0 \underline{j} \tag{2.4}$$

taking the curl of this equation

$$\nabla \times \nabla \times \underline{B} = \mu_0 \nabla \times \underline{j} \tag{2.5}$$

Using the Maxwell equation that states $\nabla.\mathbf{B} = 0$ equation (2.5) reduces to

$$-\nabla^2 \underline{B} = \mu_0 \nabla \times \underline{j} \tag{2.6}$$

and invoking equation (2.3) yields

$$\nabla^2 \underline{B} = \frac{1}{\lambda_L^2} \underline{B} \tag{2.7}$$

The only constant solution inside the superconductor must be $\mathbf{B} = 0$ i.e. magnetic fields excluded from within the sample. In the pure superconducting state the only field allowed is exponentially damped moving into the superconductor from an external surface. Assuming a semi-infinite superconductor occupies the space on the positive side of the x axis, if B_0 is the field at the plane boundary, the field inside is given by

$$B(x) = B_0 \exp\left(-\frac{x}{\lambda_L}\right) \tag{2.8}$$

The distance λ_L is known as the London penetration depth and is the distance at which the flux density has fallen to 1/e of its full value outside the superconductor.

Although the London model predicts the Meissner effect and describes the electromagnetic properties of a type I superconductor very well, it is purely phenomenological and does not fully describe the later discovered type II superconductors. The two classes of superconductors are distinguished as type I and type II superconductors, sometimes known as *soft* and *hard* superconductors, because of the dramatic difference in their magnetic and current-carrying properties. Just as superconductors have a critical temperature T_c and a critical magnetic field H_c, they also have a critical current density J_c. That there must be some upper limit to the current density in a superconductor is required by the relationship between current and magnetic field; consider a wire of radius a carrying current I, the magnetic field at the surface is $\mu_0 I/2a$. The current cannot exceed an amount that produces a critical magnetic field H_c at the superconductor otherwise it will become normal, which implies a critical current $I_c = 2aH_c/\mu_0$, and $J_c = 2H_c/\pi a\mu_0$. For real superconductors and superconducting samples, the actual critical current density is different to this upper limit and the critical current is determined by other physical mechanisms, some of which are investigated in this thesis.

For a type I superconductor, critical current is simply a consequence of the critical magnetic field H_c. However, in a type II superconductor the relationship is much more complicated. Unlike the type I superconductor where there is an exact cancellation of an applied field by an equal and opposite magnetisation resulting in zero magnetic induction inside the superconductor up to the critical field where superconductivity vanishes. In a type II superconductor the Meissner effect only exists up to the very small field H_{c1}. The magnetic field starts penetrating into the material at this lower critical field H_{c1} along discrete lines, where the superconductor is normal. Penetration increases until at the upper critical field H_{c2} the material is fully penetrated and the normal state is restored. The lines of magnetic flux are surrounded by circulating supercurrents and are

known as vortices (or fluxons), and the phase where they exist is known as the mixed state. The phase diagrams for type I and type II superconductors are shown in figure 2.2(a) and (b) respectively.

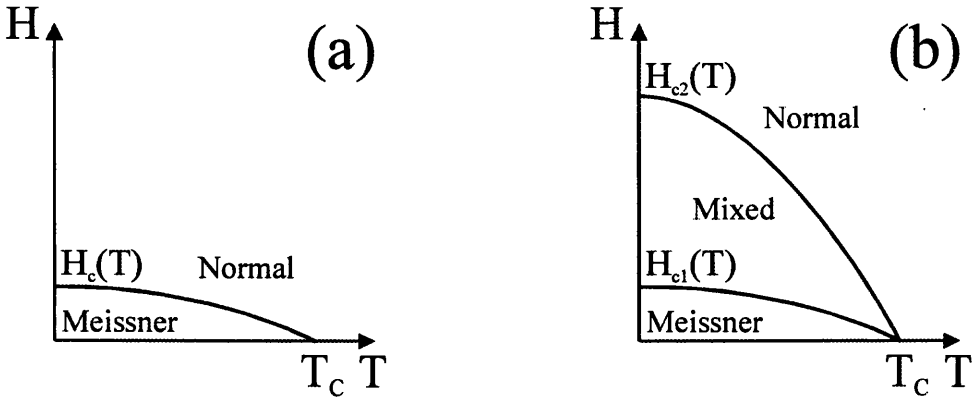

Fig. 2.2 Generic phase diagrams for (a) type I superconductors, and (b) type II superconductors.

The magnetisation curve of Figure 2.3 shows the behaviour of type II superconductors, in which **M** rises to a negative maximum at H_{c1}, at which point **M** falls again as flux lines begin to penetrate. The cancellation of **H** by **M** is no longer perfect, and **B** becomes finite within the superconductor. To fully understand this an alternate theory was suggested by Ginzburg and Landau [3] who introduced the concept of a coherence length, which is a characteristic length scale over which the electron pair density can vary.

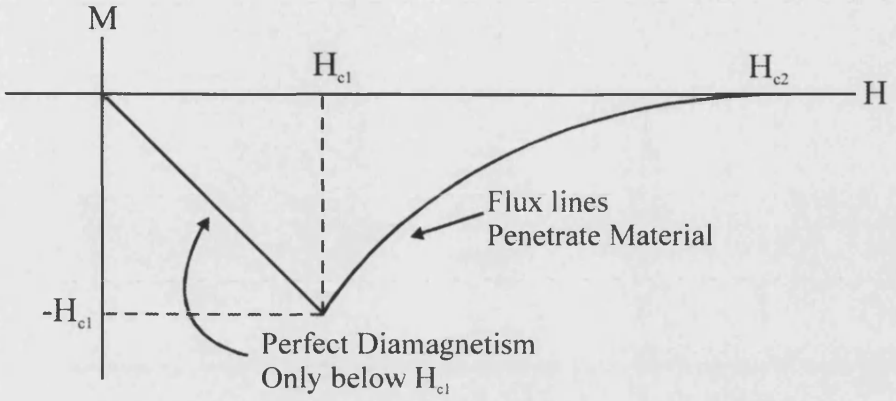

Fig. 2.3 Magnetisation as a function of applied magnetic field for an ideal type II superconductor. Above H_{c1} magnetic flux begins to penetrate the material until at H_{c2} there is no magnetisation, and the material returns to the normal state.

Although this thesis is interested primarily in the phenomenological rather than the microscopic theory of superconductivity, it seems appropriate to mention the mechanism of superconductivity in conventional superconductors. A microscopic theory of superconductivity, which explains the nature of this phenomenon in conventional superconductors, was proposed in 1957 by Bardeen, Cooper and Schrieffer (BCS theory) [4].

The discovery of the isotope effect, the reduction of the critical temperature in isotopes of an element with increasing atomic mass, clearly indicated that in an explanation of superconductivity the interaction between electrons and the crystal lattice must be taken into account. This lead to the discovery of the central feature of BCS theory in which two electrons in the superconductor are able to form a bound pair known as a Copper pair [5], due to the interaction of the electrons with the crystal lattice. The nature of this interaction is as follows. An electron moving in a metal deforms, or polarizes, the crystal lattice by means of electric forces. The passage of the electron causes nearby ions to move inward towards the electron, resulting in a slight increase in the concentration of positive charge in this region. The second electron of the Cooper pair, approaching before the ions have had a chance to return to their equilibrium positions, is attracted to

the distorted (positively charged) region. The net effect is a weak delayed attractive force between the two electrons resulting from the motion of the positive ions. The attractive force between two Cooper electrons is an *electron-lattice-electron interaction*, where the crystal lattice serves as the mediator of the attractive force. This is also sometimes referred to as a *phonon-mediated mechanism* since quantised lattice vibrations are called *phonons*.

A Cooper pair in a superconductor consists of two electrons having equal and opposite momenta and spin. Hence, in the superconducting state and in the absence of any supercurrents, the Cooper pair forms a system having zero total momentum and zero spin. Because Cooper pairs have zero spin, they have a Bosonic character and can all be in the same state. In the BCS theory, a ground state is constructed in which all electrons form bound pairs. In effect, all Cooper pairs are "locked" into the same quantum state of zero momentum. This can be viewed as a condensation of all electrons into the same state.

The BCS theory has been very successful in explaining the characteristic superconducting properties of zero resistance and flux expulsion. Lattice imperfections and lattice vibrations, which effectively scatter electrons in normal metals, have no effect on Cooper pairs. In the absence of scattering, the resistivity is zero and the current persists indefinitely.

As mentioned earlier, the superconducting state is one in which the Cooper pairs act collectively rather than independently. The condensation of all pairs into the same quantum state makes the system behave like a giant quantum mechanical system that is quantised on the macroscopic level. The condensed state of the Cooper pairs is represented by a single coherent wave function that extends over the entire volume of the superconductor.

The stability of the superconducting state is critically dependent on strong correlation between Cooper pairs. At high temperatures, sufficiently intense thermal motion pushes the positive ions far enough away from the electrons in the Cooper pairs and destroys the positively charged region attracting the second electron forming the Cooper pair. Hence, the Cooper pairs are no longer formed and superconductivity is lost. Cooper pairs are

also eventually destroyed by the orbital motion induced by an applied magnetic field; the Lorentz force acts in opposite directions for the two electrons of the pair. In addition, because the two electrons of a Cooper pair have opposite spin angular momenta, an external magnetic field raises the energy of one electron and lowers the energy of the other. If the magnetic field is large enough, it becomes energetically favourable for the pair to break up into a lower energy state where both spins are pointing in the same direction. The value of the external field which causes the break up of the Cooper pairs corresponds to the critical field.

2.3. Ginzburg Landau Theory

A central contribution to the theory of superconductivity was made by Ginsburg and Landau, [3] who proposed an alternative theory using an order parameter to describe superconductivity, which introduced the notion of a coherence length, generally denoted by ξ. This was an improvement over the London theory because it could allow for situations where the field has penetrated the sample and locally suppresses superconductivity, such as in the mixed state of type II superconductors.

Their hypothesis assumed that if superconductivity were an interaction among electrons, then this interaction would occur within some limited distance. Basically, ξ is a measure of how likely it is that a pair of electrons will interact with each other and is derived from representing the behaviour of the superelectrons (those electrons which carry current without resistance) by a pseudo wave function or order parameter. The coherence length is temperature dependent, and varies in a similar way to the London penetration depth, diverging at T_c and approaching a saturation value at lower temperatures.

To categorize superconductors the Ginsburg-Landau ratio is often used, defined as $\kappa = \lambda/\xi$. In type I superconductors $\kappa < 1/\sqrt{2}$ i.e. the coherence length is larger than the penetration depth. The fundamental difference in type II superconductors is that this relationship is reversed, i.e. $\kappa > 1/\sqrt{2}$.

A comparison of λ and ξ in type I and II superconductors is shown in figure 2.4. In a type I superconductor ($\kappa < 1/\sqrt{2}$), the magnetic field does not penetrate far enough to

affect the electrons within a coherence length. For type II superconductors ($\kappa > 1/\sqrt{2}$), superconductivity is confined to within such a small coherence length that it can still exist with a nearby magnetic field that has penetrated the material.

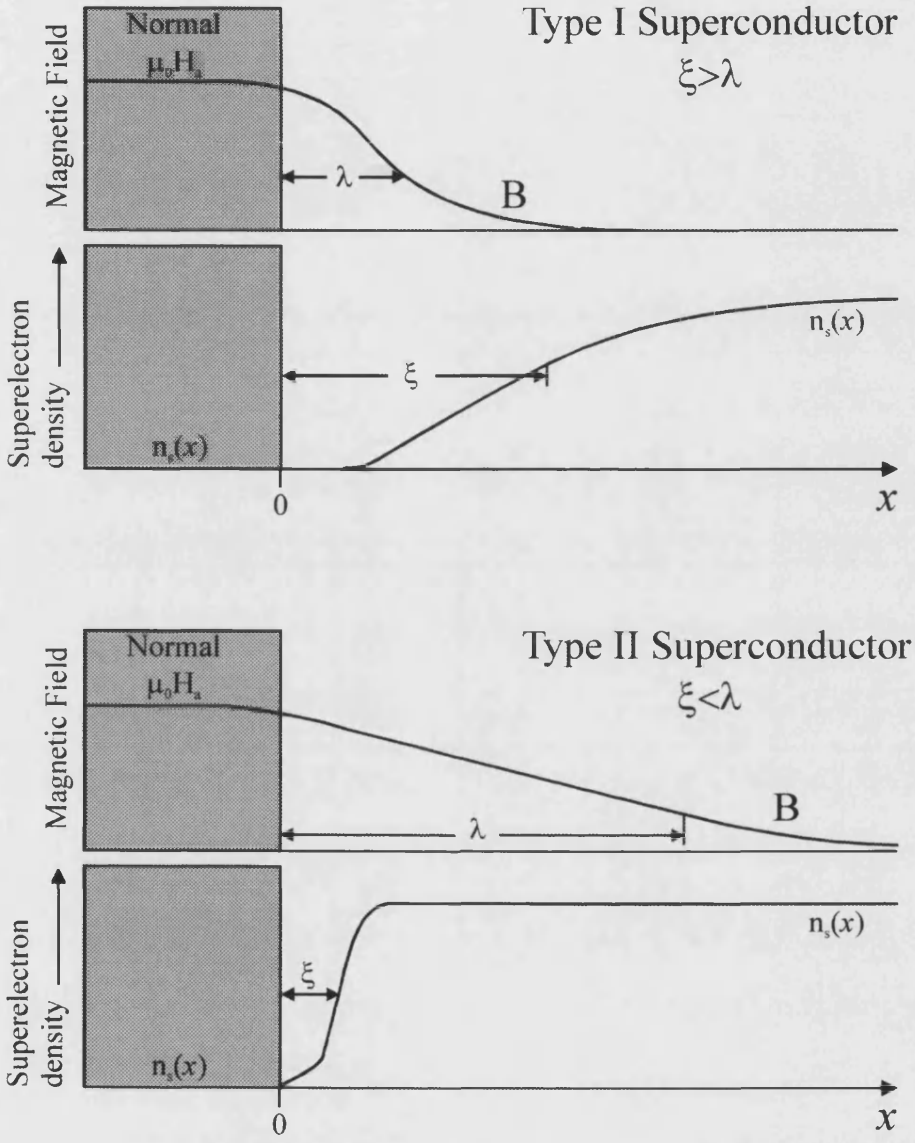

Fig. 2.4 The magnetic field and the superelectron density, $n_s(x)$, at the boundary between superconducting and normal regions, for both type I and type II superconductors.

2.4. Flux Quantisation

As with electric charge (the electron) magnetic flux lines also have quantised values. Flux quantisation has been observed in many type II superconductors and for high temperature superconductors (discussed in the following chapter) but is not seen in type I superconductors. This is a very clear difference between type I and type II superconductors. The explanation is quantum mechanical, involving the single valued ness of the "wave function" used to represent the behaviour of the superelectrons around a loop. The derivation yields the flux quantum, or fluxoid

$$\Phi_0 = \frac{h}{2e} = 2.0678 \times 10^{-15} Webers$$

where h is Plank's constant and e is the charge on the electron. The important consequence of this quantisation of flux is that any magnetic field penetrating a superconductor is quantised.

Magnetic field actually penetrates one flux-quantum at a time, each one being a single normal vortex core with a superconducting circulating current around it, surrounded by superconducting material. Moreover, the flux lines arrange themselves into a regular array, known as the Abrikosov lattice [6]. This configuration is very important for flux pinning, which determines how much current a superconductor can ultimately carry without dissipating energy. In section 2.6 this is discussed in more detail and the role of flux pinning in high-temperature superconductors discussed in the following chapter.

2.5. The Vortex/Mixed State

The mixture of normal and superconducting regions co-existing in the bulk of a superconductor is known as the mixed state, predicted to exist theoretically by Abrikosov [7], using the G-L theory. The state of mixed normal and superconducting regions arises because of the thermodynamic condition to minimize the free energy of the system. Consider a surface between two phases of a material where there will be an associated surface energy. If the surface energy is positive, the material will minimize the surface area/volume ratio by having only one borderline. If the surface energy is

negative, it will be energetically advantageous to have many borders between regions, and the equilibrium configuration will be one with as many as possible normal and superconducting zones; the limit of size being set by fluxoid quantisation.

For all superconductors, when a magnetic field is first applied, the Meissner effect will screen the field. As the field is increased, it costs more energy to screen it, and the free energy difference between the normal and superconducting states diminishes. In a type I superconductor the surface energy is always positive, hence it expels field until the normal and superconducting free energies are equal, beyond which point superconductivity vanishes.

In a type II superconductor field is expelled up to H_{c1}, as the applied magnetic field increases further the surface energy associated with the border [8] becomes negative, and hence it is energetically favourable for some of the material to switch to the normal state in order to accommodate lines of flux. Small cylindrical regions form, which are normal inside but have supercurrents circulating outside to shield the magnetic field.

The structure of a normal core surrounded by a circulating supercurrent is known as a magnetic flux vortex, or fluxon, and the dimensions of these are intimately related to the superconducting parameters. The core is approximately circular and has a radius of ξ, the coherence length, and the field decays over a distance λ outside the core, leading to the vortex structure shown in figure 2.5. The flux density decays to 1/e of the value at the core centre over a distance of λ, and the superelectron density falls to zero at the centre of the core over a distance ξ. The sign change of the supercurrent density is a result of the circular motion of the supercurrents as they circulate around the core.

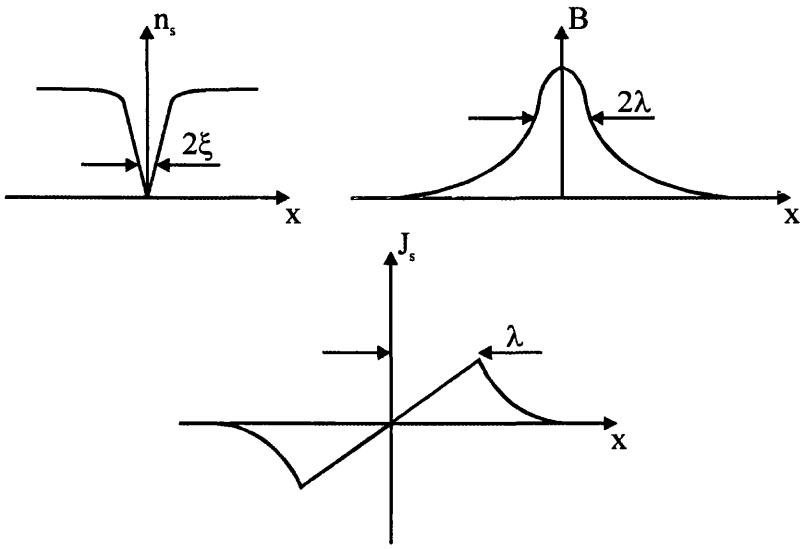

Fig. 2.5 Variation in superelectron density, n_s, flux density, B, and supercurrent density, J_s, for a flux vortex.

At the lower critical field H_{c1} flux lines start to penetrate, each flux quantum Φ_0 occupies a core of approximate radius equal to the coherence length ξ. However, the spacing between them approximately equals the penetration depth λ. Thus the measured value of H_{c1} offers a way to estimate λ

$$H_{c1} \sim \frac{\Phi_0}{\pi\lambda^2}, \tag{2.9}$$

If the applied field is further increased to the upper critical field H_{c2}, the maximum numbers of flux lines penetrate, separated by ξ. The coherence length can be estimated by

$$H_{c2} \sim \frac{\Phi_0}{\pi\xi^2}, \tag{2.10}$$

(Although not done rigorously here, the only difference when done so is a minor numerical factor) From equations (2.9) and (2.10) the ratio of H_{c2} to H_{c1} is $\lambda^2/\xi^2 = \kappa^2$. In extreme type II superconductors (of which high-temperature superconductors are examples), κ is very large and H_{c2} can be many Tesla, even though field penetration

begins at H_{c1}, typically a small fraction of a tesla. It is this property that makes type II superconductors useful for real world applications.

Because of the interaction between the supercurrent of one vortex with the fields of a neighbouring vortex, there will be an inter-vortex interaction. Since the single quantum vortex is the most energetically favourable the interaction between two parallel vortices must be repulsive. This inter-vortex repulsion leads to the formation of a stable lattice structure of vortices in the mixed state of type II superconductors. The stable lattice configuration in a perfect superconductor is a hexagonal lattice with a vortex on each vertex of an equilateral triangle, as seen experimentally by Bending *et al* [9]. The breakdown of this ordering shall be discussed in the next chapter in relation to high-temperature superconductivity.

2.6. Flux pinning, Current Flow and the Bean Critical State Model

In the mixed state of a perfect type II superconductor, the vortex lattice is stabilized by the inter-vortex repulsion and the vortex-surface repulsion. However, if a transport current, **J**, is applied, there will be a Lorentz force, $\mathbf{F_L}$, which acts on the vortices, causing them to move. The Lorentz force per unit length is given by

$$\underline{F}_L = \underline{J} \times \Phi_0 \qquad (2.11)$$

where Φ_0 is a vector along the vortex axis. The resulting eddy currents, induced by the vortex motion, cause the dissipation of energy and hence a potential difference in the superconductor i.e. resistance.

If the flux lines always moved, type II superconductors would never carry current without resistance. Fortunately, most superconductors have the ability to counter this. A Flux line can be stopped from moving and is said to be pinned. A nearby flux line, approximately one penetration length away, feels the influence of the pinned line. Thus, when another moving flux line bumps into that one, it too stops moving, and soon the collection of flux lines form a lattice, none of which can move unless they all move at once. The word "frozen" is used to denote the idea that the lattice of flux lines behaves very much like a solid, with mutual repulsion holding the lines a fixed distance apart.

Flux pinning is a result of a local depression in the Gibbs free energy for the vortices, and can be caused by material impurities, grain boundaries, local inhomogeneities or geometrical effects such as grooves or indentations. These pinning mechanisms are generally active throughout the material and are known as bulk pinning effects, whereas surface pinning forces (such as geometrical barriers or Bean-Livingston barriers described later) are only important near the edges, generally only in samples which have very little bulk pinning.

The pinning force per unit length, $\mathbf{F_p}$, opposes flux motion and the Lorentz force must not locally exceed this for a vortex to be stable, leading to the critical state. In the critical state, the Lorentz force exactly matches the pinning force locally and the vortices are on the verge of moving. In this case, the critical condition is given by

$$\underline{J} \times \Phi_0 = \underline{F}_p \tag{2.12}$$

where $\mathbf{J}$ is the total current density (transport current + Meissner current) and Φ_0 is the flux quantum. The Bean critical state model [10] is the best known model used to describe bulk superconductors in the critical state and is sketched here.

In the Bean critical state model two assumptions are made. First, the Meissner state is ignored and secondly, for low applied fields the outer part of the superconductor is assumed to be in the critical state whilst the inner part is shielded from the currents and fields. In the critical region, the critical current (which is the maximum current that can be sustained without dissipation) is dependent on the magnetic flux density.

From Maxwell's equation $\nabla \times \mathbf{B} = \mu_0 \mathbf{J}$, the critical condition can be expressed as

$$(\nabla \times \underline{B}) \times \frac{\underline{B}}{\mu_0} = \underline{F}_p \tag{2.13}$$

This is a very difficult problem to solve, since in general the pinning force will have a complicated dependence on $\mathbf{B}$, and may have components in either two, or all three dimensions. The situation can be simplified if an infinite slab geometry is used, with a field applied parallel to the plane. In this case, (2.13) reduces to

$$\frac{\partial B_z}{\partial y} B_z = \mu_0 \left| F_p(B_z) \right| \tag{2.14}$$

In order to find the flux profile $B_z(y)$, only the dependence of the pinning force on **B** is required. In the Bean model, a dependence of $F_p = J_c B_z$ and a field-independent critical current is involved and, applying this to (2.14), gives a linear dependence of B_z on y

$$B_z(y) = \mu_0 J_c |y| + c \tag{2.15}$$

where the constant c is determined by the boundary condition that at the sample edges, $\mathbf{B} = \mu_r \mu_0 \mathbf{H_a}$.The shape of B_z predicted by this model is sketched in figure 2.6, where it is shown that as the applied field is increased from zero, the flux density begins to penetrate from the edges towards the centre, with a constant slope equal to $\mu_0 J_c$. Full field penetration occurs when there is no longer any vortex free region in the centre, which occurs at a field $\mathbf{H_p} = J_c W$, where 2W is the thickness of the slab.

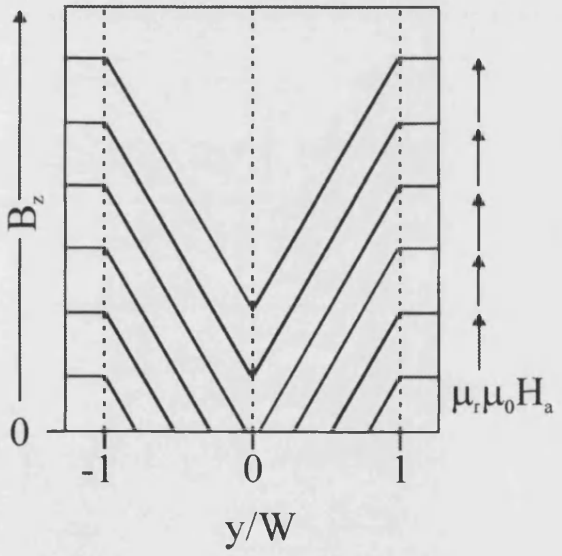

Fig. 2.6 Flux profiles across an infinite slab, predicted by the Bean model, for increasing values of applied field from an initially unmagnetised state.

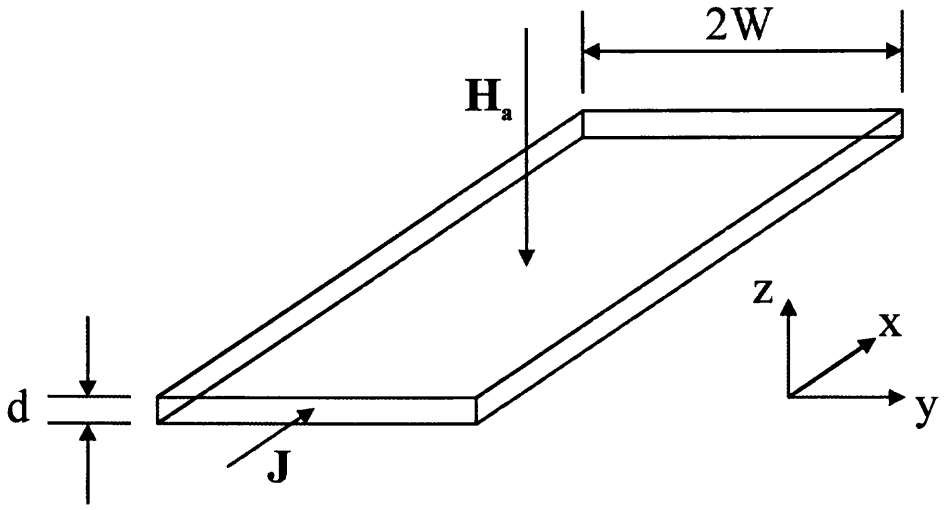

Fig. 2.7 Geometry used in Brandt's thin film model.

To model a more realistic experimental geometry, Brandt and Zeldov independently considered the case of a field applied normal to a thin film, and calculated the resulting flux profiles in the critical state both with, and without an applied transport current [11],[12],[13]. The geometry used is shown in figure 2.7. In this geometry demagnetization effects are crucial. The field at the edges of the superconductor, $\mathbf{H_{edge}}$, is given by

$$H_{edge} = \frac{1}{1-N_D} H_a, \tag{2.16}$$

where N_D is the demagnetising factor. For long ellipsoidal geometries with the field applied along the long length, $N_D = 0$, and for spheres $N_D = 1/3$, but for a field normal to the platelet geometry described above, $N_D \approx 1$. This means that flux enters the superconductor almost as soon as a field is applied (neglecting surface barriers and flux pinning). Brandt showed that the flux profile is given by

$$B_z = 0 \qquad |y| < b \tag{2.17}$$

$$B_z = \mu_0 |H_a| \tanh^{-1}\left(\frac{\sqrt{y^2 - b^2}}{c|y|}\right) \qquad b < |y| < W, \tag{2.18}$$

$$B_z = \mu_0 |H_a| \tanh^{-1}\left(\frac{c|y|}{\sqrt{y^2 - b^2}}\right) \qquad |y| > W, \tag{2.19}$$

where (W-b) is the distance into the superconductor that vortices have penetrated for a given applied field, and is described by

$$b = \frac{W}{\cosh\left(\frac{|H_a|}{|H_c|}\right)}, \tag{2.20}$$

and c is a constant given by

$$c = \tanh\left(\frac{|H_a|}{|H_c|}\right), \tag{2.21}$$

Figure 2.8 shows the profiles obtained from Brandt's model for a field applied normal to an initially unmagnetised semi-infinite film.

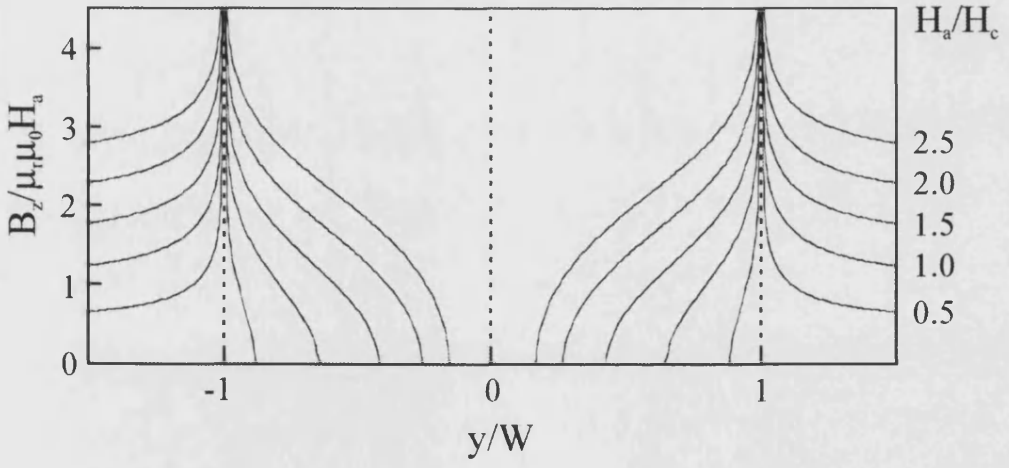

Fig. 2.8 Flux profiles calculated from Brandt's model of the critical state in a thin film.

Pinning centres prevent vortices from reaching the equilibrium arrangement for the flux lattice and effectively create a "vortex glass" structure, and the only way of overcoming this is to go beyond the critical state. However, Anderson showed that at finite temperatures, and over a long enough time scale, vortices may jump from their pinning sites via thermal activation [14]. This relaxation process is known as thermally activated flux or vortex creep and is particularly relevant in HTS because of the relatively large thermal energies available, discussed further in the next chapter. According to the theory of Anderson, and subsequent experiments by Kim [15] and others, the magnetisation should decay logarithmically towards an equilibrium value, with vortices entering the superconductor on the increasing leg of the hysteresis loop and exiting the superconductor on the decreasing leg. This relaxation process is symmetric with respect to vortex entry or exit, although effects such as surface barriers have been shown to modify this symmetry (see chapter 3).

2.7. Hysteresis in Superconductors

The magnetic behaviour of materials is generally represented by plotting the magnetisation **M** versus the applied field **H**. When **M** depends only upon the instantaneous value of **H** and nothing else the material returns to its initial magnetic state when the applied field returns to its initial state and no energy is dissipated. This is known as a reversible process. However, when **M** is not a single-valued function of **H**, the material will dissipate magnetic energy when **H** is cycled and **M** does not return to its initial value. This is known as an irreversible process.

In superconductors, hysteresis arises from flux pinning. When there is no flux pinning, there is no irreversibility i.e. the magnetic behaviour of the superconductor is perfectly reversible. This is the case for type I superconductors. In an ideal (no pinning) type II superconductor the behaviour is also reversible, with **B, H** and **M** uniquely related to one another. If the **M-H** curve were plotted the line for increasing **H** would be exactly retraced as **H** decreases. However, no real material gives the exact retracing of the idealized curve. Bulk pinning effects such as material impurities, grain boundaries, local inhomogeneities and geometrical effects such as grooves or indentations prevent flux

lines from moving freely through the crystal. Even in samples that have relatively weak bulk pinning hysteresis can occur as a result of geometrical or Bean-Livingston barriers. A more realistic type II superconductor undergoes a more complicated magnetic history, which is sketched in figure 2.9.

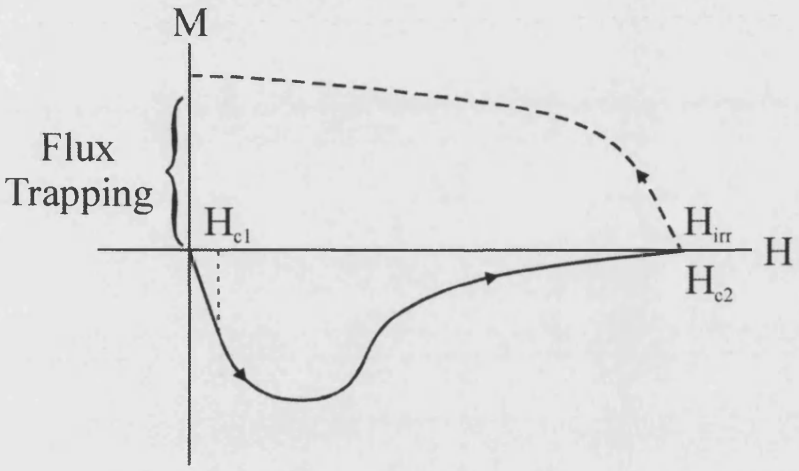

Fig. 2.9 A realistic type II superconductor hysteresis curve showing the effects of pinning. Flux pinning causes remnant magnetisation which remains until the temperature is raised above the transition temperature. The field at which irreversibility begins, H_{irr}, is virtually the same as H_{c2}.

Unlike in the ideal case there is no sudden change in magnetisation **M** as **H** passes through H_{c1}, instead the deviation from linearity of the **M** versus **H** curve shows that the diamagnetism is no longer perfect and that some flux is penetrating the material. Eventually, increasing H leads to extensive flux penetration, **M** decreases, and at H_{c2} penetration is complete, $\mathbf{B} = \mu_r\mu_0\mathbf{H}$ and the material goes normal. In the superconducting state, much of the flux is pinned inside the superconductor. As **H** is decreased, **B** remains elevated, and since $\mathbf{B} = \mu_0(\mathbf{H} + \mathbf{M})$, this means that **M** rises to a positive value. As **H** declines further **M** changes and leaves **B** finite even when $\mathbf{H} = 0$, which is due to flux trapped in the material. This permanent or remnant magnetisation remains until the temperature is raised.

This topic is further discussed in the next chapter, which is concerned with flux motion in HTS and in particular the effects of surface pinning forces on flux motion in HTS.

Chapter 3

3. High-Temperature Superconductivity (HTS)

In this chapter the subject of HTS is discussed concentrating on the topics that the author feels will help the reader better understand the work presented in this thesis. A number of new topics, such as flux creep and flux lattice melting are discussed. The subject of Bean-Livingston barriers and geometrical barriers to flux line motion is also covered as these are both relevant to work presented later in this thesis.

3.1. History

In 1986, Bednorz and Müller discovered superconductivity in a compound of Lanthanum, Barium, and Copper Oxide, which had a critical temperatue of 35K [16]. This was higher than the limit of 23K, which had been reached 13 years earlier by Gavalar in Nb_3Ge [17], and it earned them a Nobel Prize in the following year. This discovery was soon followed up with other ceramic superconducting materials which had critical temperatures of 90K ($Y_1Ba_2Cu_3O_7$) [18] 110K ($Bi_2Sr_2CaCu_2O_3$) [19] and 130K (TlBaCaCuO) [20] being discovered in a remarkably short space of time. The fact that many of these new materials had transition temperatures greater than the boiling point of liquid nitrogen (77K) made practical applications of superconductivity a real possibility. However, the initial excitement surrounding HTS has been tempered with the realization that the ceramic nature of the high temperature superconductors presents significant materials science problems. Despite this, HTS has found applications in areas

such as feed throughs for high-field magnets, very sensitive magnetic sensors known as SQUIDs (Superconducting Quantum Interference Devices), and electronic components such as mixers, filters and antennas [21].

Although of practical importance high temperature superconductors are also of great scientific interest as the mechanism of superconductivity within them is not well understood. The magnetic properties appear to be very complex (see chapter 4.3 for a discussion of YBCO and BSCCO), and many of their parameters are extremely large, with values of H_{c2} exceeding 100T for some HTS at low temperatures. Measurement of the fundamental superconducting length scales λ and ξ for these materials is not trivial (see chapter 4.2 for the case of YBCO and BSCCO), but is nevertheless important, since they can yield information about the underlying mechanism of superconductivity, and define properties such as H_{c1} and H_{c2}. As mentioned in the previous chapter HTS have large Ginzburg-Landau parameters, and are extreme type II superconductors, with the mixed state taking up a large proportion of the magnetic phase diagram. However, as mentioned previously in section 2.6, the elevated temperatures possible in HTS make thermal fluctuations more important in these materials and lead to effects such as giant vortex creep, and a smearing of the transition at H_{c2}, as described later in this chapter.

The crystal structure of HTS also has a profound effect on their superconducting properties. All these materials are based on a perovskite structure, with varying numbers of copper-oxide (CuO) planes per unit cell. The basic perovskite structure is shown in figure 3.1, and consists of two metallic cations (A and B), with 12 anions lying on the cube edges. The A cation is larger, and lies in the centre of the cube.

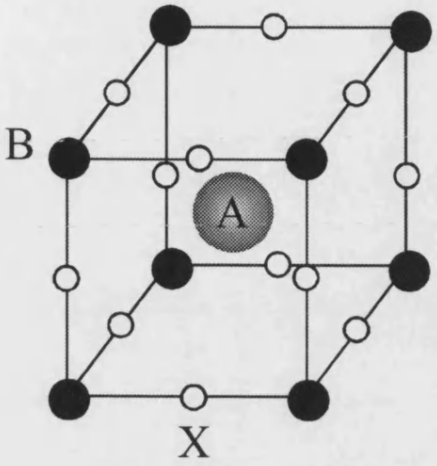

Fig. 3.1 Basic perovskite structure.

This perovskite structure provides the basic building block for all HTS with the X anion frequently, but not always, being oxygen. In the case of YBCO, the A sites are occupied by barium and yttrium ions, and the smaller copper ions occupy the B sites. Stacking of these structures leads to a very anisotropic crystal structure, with the copper and oxygen ions creating CuO_2 planes, which are separated by the larger ions in the structure. Diagrams of the crystal structures of YBCO and BSCCO are given in chapter 4, along with a comparison of the two materials and their respective magnetic phase diagrams.

The effect of this layered structure on the superconductivity is dramatic; since the CuO_2 planes are weakly coupled, the superconductivity is mainly confined to these planes, leading to highly anisotropic transport properties. Also, in the mixed state with a magnetic field applied perpendicular to the planes, a vortex is formally viewed as a stack of two-dimensional "pancake" vortices, which are only weakly coupled together along the c-axis (via the Josephson interaction and electromagnetic coupling). In certain regimes these pancakes can become completely decoupled, leading to a two-dimensional behaviour, which has implications for effects such as thermal activation and vortex creep.

This topic is further discussed later in this chapter and in the following chapter, which is concerned with the comparison between the YBCO and BSCCO superconductors and the effects of anisotropy on their magnetic properties.

3.2. The Irreversibility Line

In chapter 2, the behaviour of a realistic type II superconductor was discussed and its magnetisation curve illustrated in figure 2. 9. It was shown how flux is pinned and trapped inside the superconductor, leaving a remnant magnetisation. The result of this is that the magnetic induction **B** is finite even when the applied magnetic field **H** is zero, a condition that mimics a permanent magnet until the sample is warmed up and superconductivity is lost.

Non-moving flux lines are not harmful to superconductivity, since they dissipate no energy. The microscopic origin of the dissipation of energy is usually attributed to eddy currents in the core. In hard superconductors, hysteresis dissipates energy and a voltage is needed to sustain the current. The hystersis loop in the **M-H** plane determines the energy loss per cycle for low-frequency applications. For DC applications, $\partial \mathbf{B}/\partial t$ is zero, flux is pinned, and there is no loss.

In a superconductor, the field above which the **M** vs **H** curve is no longer hysteretic is known as the irreversibility field H_{irr}. In conventional type II superconductors, this field is extremely close to H_{c2}, and there is no important distinction between them. However, in HTS thermal activation is much greater, which leads to easier flux line motion near H_{c2}. Hence, a new phenomenon takes place, as shown in figure 3.2. After reaching H_{c2}, when H is reduced, flux lines are initially free to move, and so the trajectory of M retraces its path. The superconductor is "soft". As flux pinning becomes stronger there comes a point where **B** declines slower than **H**, and **M** deviates from the increasing-H curve. The superconductor changes to "hard". The value of H_{irr} in HTS is appreciably lower than H_{c2}, whilst still reasonably far above H_{c1}.

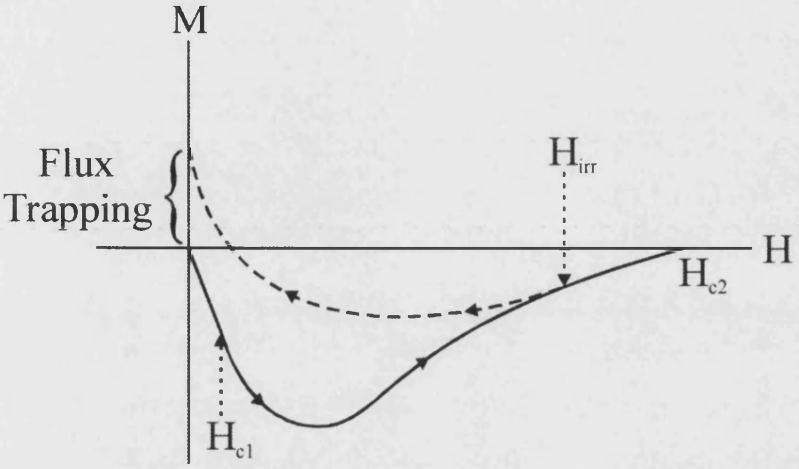

Fig. 3.2 Typical high temperature superconductor magnetisation curve. Initially the return curve retraces the forward curve as the applied field is reduced below H_{c2}. The magnetisation is reversible above H_{irr}. As the applied field is further reduced flux pinning occurs and the magnetisation becomes irreversible at lower fields.

For any given choice of temperature, there is a corresponding **M** vs **H** diagram, and with it a value of H_{irr}. These values can be assembled into an irreversibility line as a function of T. Figure 7.4 of chapter 7 shows the irreversibility line of the BSCCO Whiskers used to study the suppression of surface barriers for flux penetration by electron and heavy ion irradiation.

3.3. Basic Concepts of Flux Pinning

As mentioned in the previous chapter, when a certain number of flux lines penetrate a type II superconductor, they begin to feel one another's presence when separated by approximately one penetration depth λ. In the absence of disorder their mutual repulsion forms the flux lines into a regular geometric array called the Abrikosov Lattice [22]. In a conventional type II superconductor this takes the form of a hexagonal lattice with a vortex on each vertex of an equilateral triangle. In HTS, the anisotropy of the crystal lattice results in certain changes in the flux lattice: the vortices for an applied field

parallel to the *c* direction in orthorhombic structures are elliptical, not circular, due to the differences between penetration depths in the *a,b* directions and the vortices are spaced farther apart along one lattice direction than another [23].

Pinning is characterized by an energy well of depth U_0 and interwell distance *d*. Both U_0 and *d* have less than perfect definitions [8]: U_0 is related to the thermodynamic critical field H_c and the coherence length ξ, whereas *d* is the hopping distance through which a flux line moves when a jump occurs. For HTS, not every pinning well has exactly the same depth. Therefore, the constant value U_0 should be replaced [24] by a probability function $f(U_0)$.

Often the resistivity of a superconductor is plotted as a function of current. This is misleading because the resistivity is only the slope of the curve of electric field *E* vs. current density *J*. It is more informative to work with *E* vs. *J* plots, recognising that when the relationship is nonlinear the resistivity is no longer constant.

The use of a linear resistance axis in the presentation of the transition to superconductivity is also misleading, as it creates the illusion that the resistance is truly zero below T_c. In reality, the resistance never reaches zero in these materials, except in the limit $T \rightarrow 0$ or $T = 0$.

At zero temperature, the variation of *E* with *J* is simple. The solid line in figure 3.3 shows that below J_c, $E = 0$, because the material is fully superconducting and the flux vortices are pinned and immobile. Above J_c, flux flow begins, and *E* rises proportional to $(J - J_c)$; the proportionality constant is termed the flux flow resistivity ρ_f. As the applied magnetic field increases, J_c decreases and the slope of the *E* vs. *J* plot in the flux flow regime increases. Ultimately, at very high fields, the material becomes normal J_c is driven to zero, and the slope is the normal resistivity ρ_n.

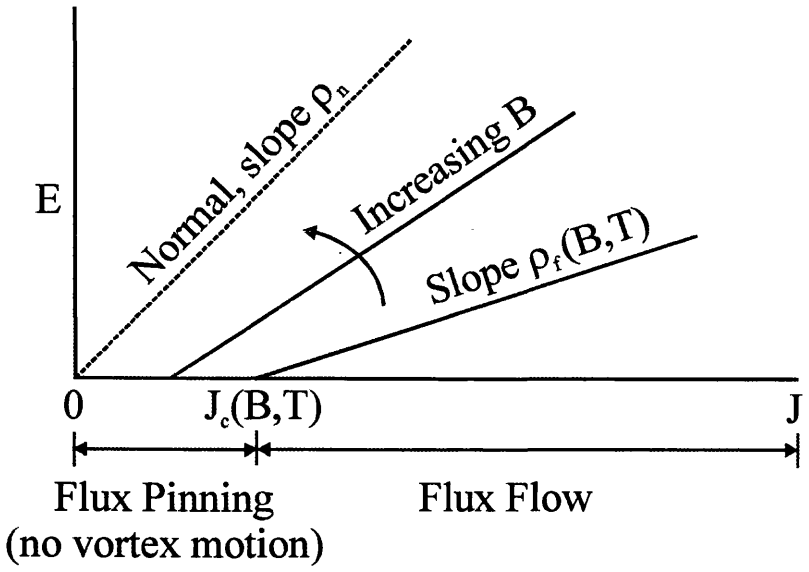

Fig. 3.3 Plot of electric field as a function of current at absolute zero. Below J_c all flux vortices are pinned; above J_c flux begins to flow and energy is dissipated.

3.4. Thermal Activation

The importance of thermal activation in the evolution of the understanding of flux pinning is the main reason for its appearance here. In later sections of this chapter and in the next chapter, it will be explained why very little of this is applicable to the HTS, whose anisotropy and other unique properties cause their flux motion to differ from this conventional model. However, because almost all workers active in the development of better flux pinning models began from this starting point, it is presented here.

At low temperatures (< 4K), the zero-temperature picture of E vs. J almost holds, except for minor curvature (instead of a sharp break) very close to J_c. This small effect is due to thermally activated motion of flux vortices, known as flux creep. As temperature increases, the effect of thermal activation becomes much more pronounced and at high temperature (> 77K) it is mandatory to take thermal activation into account. By defining a current parameter J_{th} (proportional to k_BT), it is convenient to identify regions in the E vs. J plot corresponding to thermally activated resistance, flux creep, and flux flow. This is shown in figure 3.4. The electric field varies as

$$E = E_0(T)\sinh(J/J_{th}), \tag{3.1}$$

for currents below J_c. Above J_c full-scale flux flow sets in and the E vs. J relationship changes to a different form. Again, E is linear in $(J - J_c)$ with a proportionality constant that depends on the applied magnetic field and the normal state resistance

$$\rho_f = \rho_n(H/H_{c2}), \tag{3.2}$$

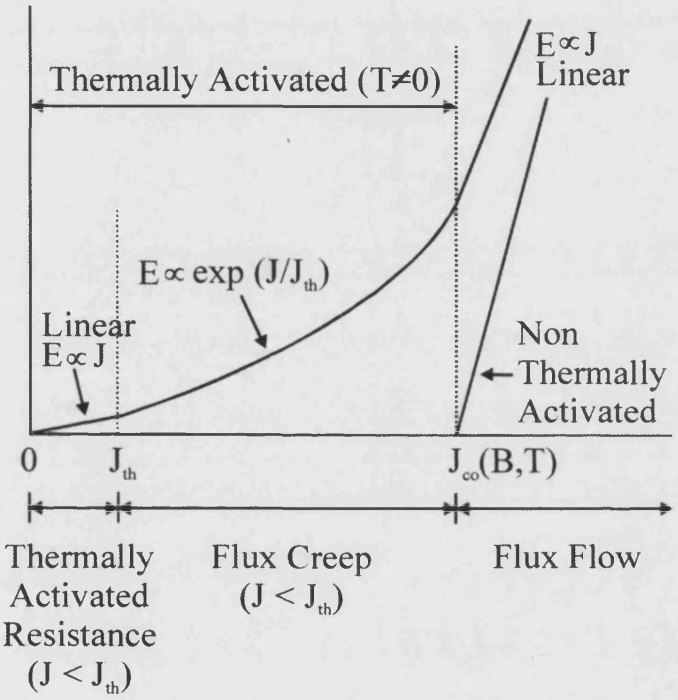

Fig. 3.4 E vs. J plot at finite temperature, showing the effect of thermally activated flux motion. This giant flux creep causes dissipation of energy at currents well below J_c.

Referring to figure 3.4, J_{c0} is defined as the J_c value that would have been obtained in the absence of flux creep. The large excursion away from the weak low temperature curvature of E vs. J justifies the term giant flux creep to describe the behaviour of HTS at high temperature. The linear region at very low currents has no more significance than that $\sinh(x) \approx x$ for small x.

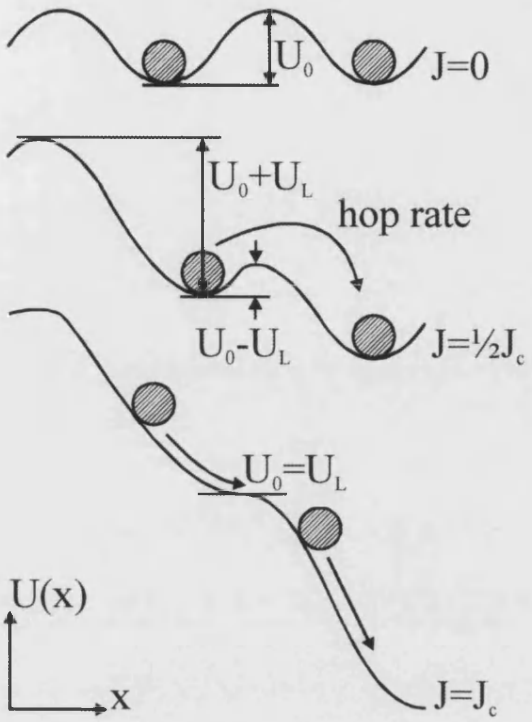

Fig. 3.5 Mechanism of flux flow. The presence of current in a magnetic field generates a Lorentz force which tilts the washboard, allowing flux lines to hop out of their pinning wells more easily.

These concepts can be brought together within a model known as thermally activated flux flow (TAFF). In either flux creep or flux flow, a flux line or a flux bundle is imagined to hop over a pinning energy barrier. Figure 3.5 illustrates [25] how, under the influence of a Lorentz force (proportional to J), a series of wells evolves into a tilted washboard potential with progressively less opposition to flux motion. Within this model, the energy dissipated (the resistance) is given by

$$\rho(T) = \rho_0 \exp\left(\frac{-U_0}{k_B T}\right), \tag{3.3}$$

However, U_0 itself is a function of temperature and magnetic field, and $U_0 \rightarrow 0$ as $T \rightarrow T_c$; so a simple exponential relationship on 1/T is not expected. For HTS in the form of

epitaxial $YBa_2Cu_3O_{7-\delta}$ thin films, it has been shown [26] experimentally that the pinning strength U_0 falls off as $(1 - T/T_c)^{3/2}/H$.

For conventional type II superconductors, the Anderson-Kim model [27] of flux creep relates the measured critical current density J_c to the pinning strength and voltage criterion

$$J_c = J_{c0}\left[1-\left(\frac{k_B T}{U_0}\right)\ln\left(\frac{Bd\Omega}{E}\right)\right], \tag{3.4}$$

where J_{c0} is J_c at zero temperature, Ω is the attempt frequency of a flux-hopping event, d is the hopping distance, B is the magnetic induction, and E is the electric field criterion (usually the smallest experimentally discernible electric field) with units volts/meter. Parameters d and Ω depend on temperature and magnetic field, so equation 3.4 must be solved numerically. For any electric field criterion E, there will be a magnetic field or temperature for which J first gives a discernible voltage drop across the length of the superconducting sample.

Hence, a possible discrepancy between J_c values measured in different ways arises. If a high sensitivity is used to define the criterion at which superconductivity disappears, a low J_c value will result. A less sensitive criterion for E will give a correspondingly higher value of J_c. For this reason, it is mandatory that some voltage criterion is set as a standard when measuring J_c in HTS.

It should be noted here that thermally activated flux motion is always present at high temperatures, and thus the effective resistance never goes to zero. This is unlike the situation at low temperatures where flux is so well pinned that current decays only over very large time scales.

3.5. Irreversibility and Flux Creep

It was found experimentally [28],[29] that the irreversibility field $H_{irr} \propto (1 - T/T_c)^{3/2}$. Thermally activated flux motion similarly presents the condition $(1 - T/T_c)^{3/2}/H \propto U_0$ for the pinning strength in HTS. The proportionality constant in this relation is within a factor of 2 of that in the expression for H_{irr}, which led Yeshuran and Malozemoff [29] to assert that H_{irr} is identical with the value of H that makes J_c zero. They coined the term

giant flux creep to describe this identification. Under this interpretation, below H_{irr} flux pinning takes place and a finite critical current flows, whereas above H_{irr} there is no flux pinning and J_c is zero or very small. In the regime above H_{irr} but below H_{c2}, energy is dissipated by the freely moving unpinned flux lines. Therefore, in order to have a persistent transport current it is necessary to stay below H_{irr} not just below H_{c2}.

This analysis brought unity to the understanding of magnetic behaviour in HTS. The giant flux creep model which emphasized weak pinning forces together with high temperatures, explained both the irreversibility line and the sharp fall-off in J_c with magnetic field. The fact that H_{irr} is significantly less than H_{c2} is an important difference between HTS and conventional type II superconductors. The flux pinning and flux creep model is conventional, but the numerical values of the HTS parameters are much greater than those of conventional type II superconductors.

The TAFF model contributed significantly to the early stages of understanding of how HTS carry current. For the first time it introduced a phenomenon (flux creep) that was present in principle all along, but hidden by its extremely small quantitative significance at low temperatures. However, later models, which revised the fundamental picture of flux lines within HTS, were developed that obviated the TAFF model and are discussed in the next section.

3.6. Flux Lattice Melting/Abrikosov Vortex Solid Melting

Since its proposal in 1988 [30], vortex-lattice melting in bulk type II superconductors has become a central topic in the phenomenology of high temperature superconductors. The order, position, and shape of the transition have been investigated theoretically [31],[32] as well as experimentally [33],[34] by a large number of authors. In general, melting of any lattice is phenomenologically defined by the Lindeman criterion, which is described below for a type II superconductor.

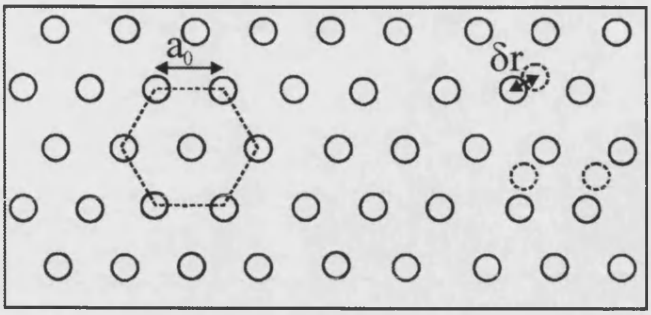

Fig. 3.6 Thermal agitation of the vortex lattice.

As described earlier, when an ideal type II superconductor (no bulk pinning or surface barriers) is in the mixed state, the magnetic vortices penetrate into the sample and generally form a hexagonal lattice. At T=0, if there is no transport current applied, the vortices do not move from their ordered sites. However, at finite temperatures the vortices are thermally agitated about their equilibrium positions by an amount δr (see figure 3.6). Within the phenomenological Lindeman picture of vortex solid melting, if the rms value of this amplitude, defined as $\Delta r = \sqrt{\langle \delta r^2 \rangle}$ exceeds a certain fraction of the mean vortex spacing a_0, the vortex solid will melt and the vortices are free to move around the superconductor at random, in analogy with an atomic liquid. The melting situation described above is known as Lindeman melting, and the critical fraction $c_L = \Delta r/a_0$ (the Lindeman coefficient) is typically in the range 0.1 – 0.3.

Clearly, as the temperature is increased the vibrations will become larger and at some critical field dependent melting temperature $T_m(H)$ the ratio c_L will become greater than the critical melting ratio, at which point the lattice melts. Similarly, if the applied field is increased the vortex separation a_0 will become smaller until again at some field H_m the lattice melts. It is important to note that Lindeman melting is not a microscopic theory of melting, but simply a phenomenological picture of what is going on.

The temperature dependence of the melting field $H_m(T)$ can be found theoretically [35] and has been confirmed experimentally in the case of YBCO by Farrel *et al.*,[36] to be

of the form $H_m(T) \propto (1 - T/T_c)^2$. By contrast, a thermal activation model suggested an exponent of 4/3 or 3/2 instead of 2 – quite inconsistent with the data.

The presence of flux lattice melting in HTS prompted another look at conventional type II superconductors. M. Suenaga *et al* [37] found that in NbTi and Nb_3Sn, a previously unobserved region of reversible flux line motion exists, approximately 1K wide (previously presumed to be so narrow as to be indistinguishable from the upper critical field curve.) The data was again best explained by the flux lattice melting model [35], as contrasted with the thermally activated giant flux creep model. This indicated that when the ratio $\kappa = \lambda/\xi$ is very large (as is the case for Nb_3Sn and the copper oxide superconductors), the standard understanding of flux line motion (TAFF) no longer applies.

The Lindeman picture of vortex solid melting assumes the vortices are three-dimensional lines, Blatter [38] included the effects of electromagnetic and Josephson interactions, in the case of stacks of two-dimensional vortex pancakes. The central result of this was the temperature dependence of the melting field, given by $H_m(T) \propto (1 - T/T_c)^{3/2}$. Although successful for highly anisotropic HTS such as BSCCO, it should be noted here that this model does not apply to YBCO, which is less anisotropic to begin with and contains copper oxide chains that short-circuit the Josephson tunnelling between layers. These and other differences between the HTS BSCCO and YBCO are discussed in the next chapter and the effects of these differences on their magnetic phase diagrams illustrated.

Alternative approaches to Lindeman melting have been suggested, with some predicting a re-entrant melting field at low fields, but this has yet to be observed experimentally. Of more experimental interest is the link between the melting field and the irreversibility line (IL), which defines the field above which magnetic hysteresis disappears. Above the IL, the vortices have enough energy to overcome all the material pinning centres and so move freely and produce a reversible M – H loop. Below the IL, the vortices are pinned by such mechanisms as defects, crystal inhomogeneties or grain boundaries in polycrystalline materials, and so the M(H) loop exhibits strong hysteresis. It is believed

that due to the finite shear modulus of the vortex solid, it is more easily pinned than a vortex liquid, so the IL is often interpreted as the melting line. This has been challenged, however, by Majer [39], who showed that the IL can be the result of surface pinning (Bean-Livingston barriers or Geometrical barriers discussed in the next two sections) and is not related to the microscopic vortex state in the bulk – indeed, they observed hysteresis in the vortex liquid regime, contrary to the simple picture described above. For this reason, the signature of melting should be taken to be ΔM, not the IL, since there is doubt about whether $H_{IL} = H_m$ or not. (Also, the IL is difficult to define since it is dependent upon the sensitivity of the experiment).

3.7. Bean-Livingston Surface Barriers

Bean and Livingston proposed an additional barrier to vortex motion across a normal-superconducting boundary in 1964 [40]. The Bean-Livingston (B-L) energy barrier is a kinetic barrier which results from the interaction between two opposing forces:

- An attractive interaction between a test vortex placed inside the superconductor and its image vortex placed outside the superconductor (to satisfy the electromagnetic boundary conditions), which pulls vortices out.
- A repulsive force due to an interaction with the exponentially decreasing magnetic field inside the superconductor (an interaction with the Meissner screening currents), which pushes the vortices inwards.

The effect of these forces is shown schematically in Figure 3.7. Although the B-L barrier is present at any normal-superconducting boundary, the effects are difficult to observe experimentally since they are frequently dominated by bulk pinning effects, or their significance is reduced through irregular surfaces. Hence B-L barriers have only been observed in very clean bulk crystals. However, superconductors in the form of whiskers have very large surface-volume ratios and can be free of extended defects, making them ideal models for investigating the effects of surface pinning through B-L barriers (see section 7.1).

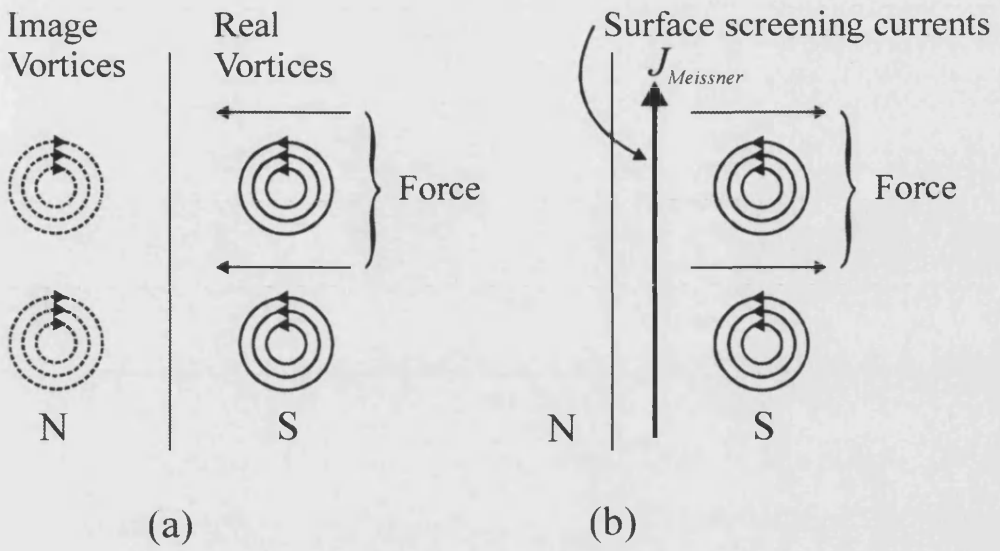

Fig. 3.7 Schematic representation of the attractive interaction (a) and repulsive interaction (b) acting on vortices near a normal (N) – superconducting (S) surface.

Huebener [41] calculated the change in Gibbs free energy per unit length when a single test vortex is placed near a surface due to the B-L barrier. He discovered that the consequence of the barrier was that vortex penetration did not begin until the applied field exceeded a critical entry or penetration field, H_p, greater than the thermodynamic lower critical field, H_{c1}. The variation in Gibbs free energy with distance inside the superconductor is shown schematically in figure 3.8. It is clear from figure 3.8 that for applied fields less than the critical entry field H_p there is a maximum in the vortex line energy somewhere inside the superconductor, which prevents vortex entry – even when the applied field has exceeded H_{c1}. The barrier does not disappear until the maximum in Gibbs free energy is within a ξ of the superconductor surface. The value of the penetration field is found to be

$$H_P = \frac{\Phi_0}{4\pi\mu_0\lambda\xi}, \tag{3.5}$$

which is greater than the thermodynamic critical entry field by a factor of $\kappa/\ln\kappa$. Thus, vortex penetration does not begin until the applied field exceeds H_p, which can be as much as 20 times larger than H_{c1} for the HTS such as BSCCO with $\kappa \approx 100$.

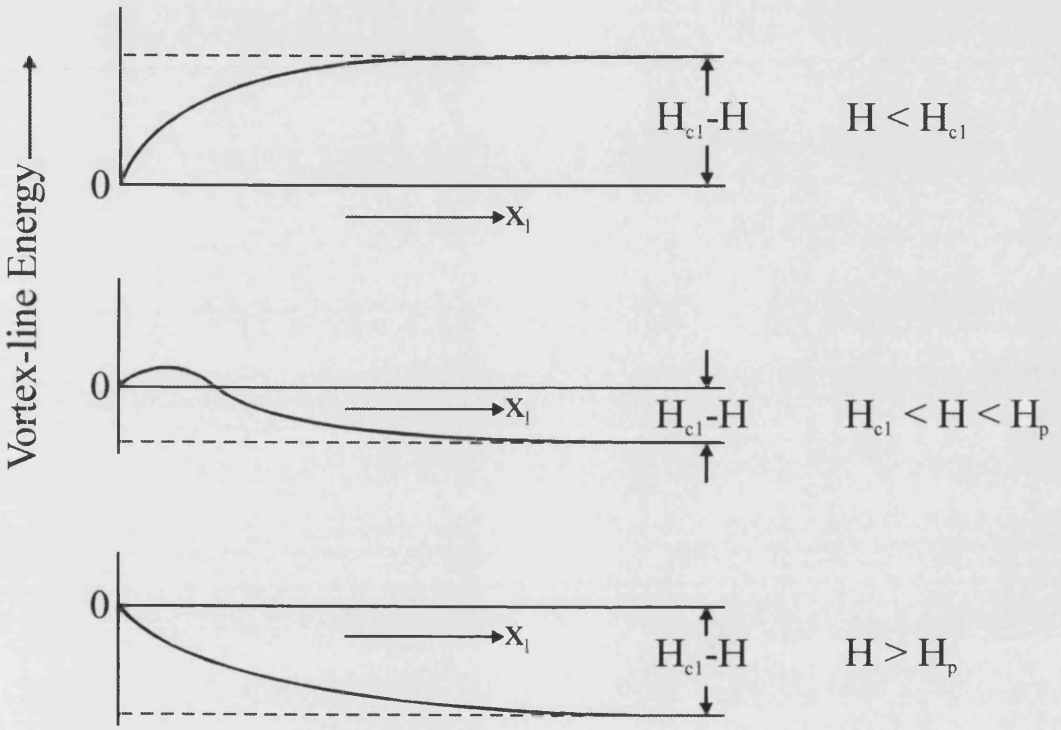

Fig. 3.8 Vortex-line energy as a function of distance, x_l, from the surface of the superconductor for different values of applied magnetic field.

It can also be seen from figure 3.8 that a vortex-free region will exist near the surface, since any entering vortex will "slide" down the energy barrier and either annihilate with its image at the surface if $H < H_p$, or move rapidly to the centre of the superconductor if $H > H_p$ (as the vortices are pushed inwards by the Lorentz force due to the Meissner current). The main limitation of Huebener's expression is that it is based on an isotropic superconductor and assumes there are no vortices already present inside the superconductor when the test vortex is placed there.

An improvement to this model was proposed by Clem [42], which takes account of vortices present inside the superconductor and allows them to relax around the test vortex. In this model, a locally averaged magnetic field is defined, which is a linear sum of the Meissner field, the field due to the image vortices, and the field due to the test vortex, with a vortex free region of width, x_f. The geometry of this model assumes that a field is applied parallel to an infinite plane with a finite thickness, which has a flux density B present inside the bulk of the superconductor. The width of the vortex region, x_f is determined by the boundary condition that the local field must be equal to the applied field, H, at the superconductor boundary. Assuming a constant B inside the interior of the superconductor, the local field variation proposed by Clem is shown in figure 3.9.

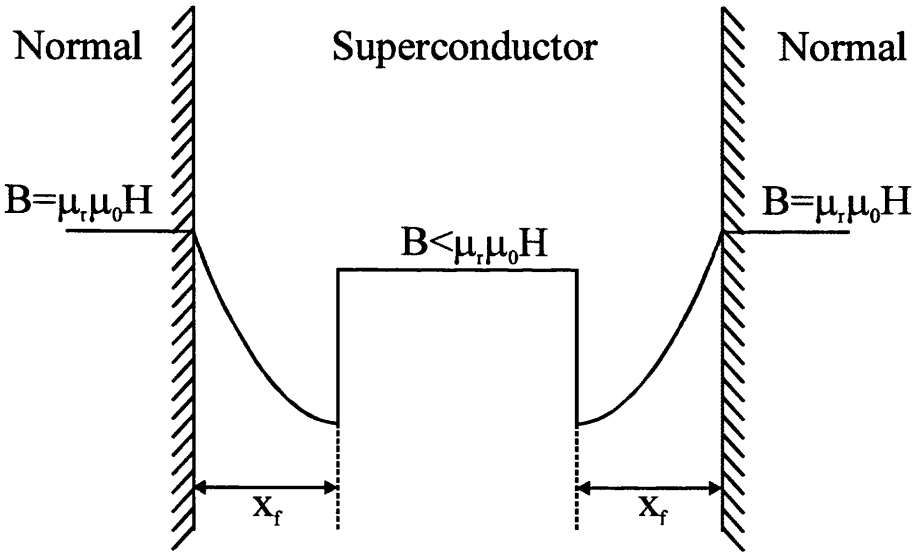

Fig. 3.9 Variation in locally averaged magnetic field across a superconductor as proposed by Clem.

The variation of the Gibbs free energy with distance from the surface is shown schematically in figure 3.10, for different applied fields.

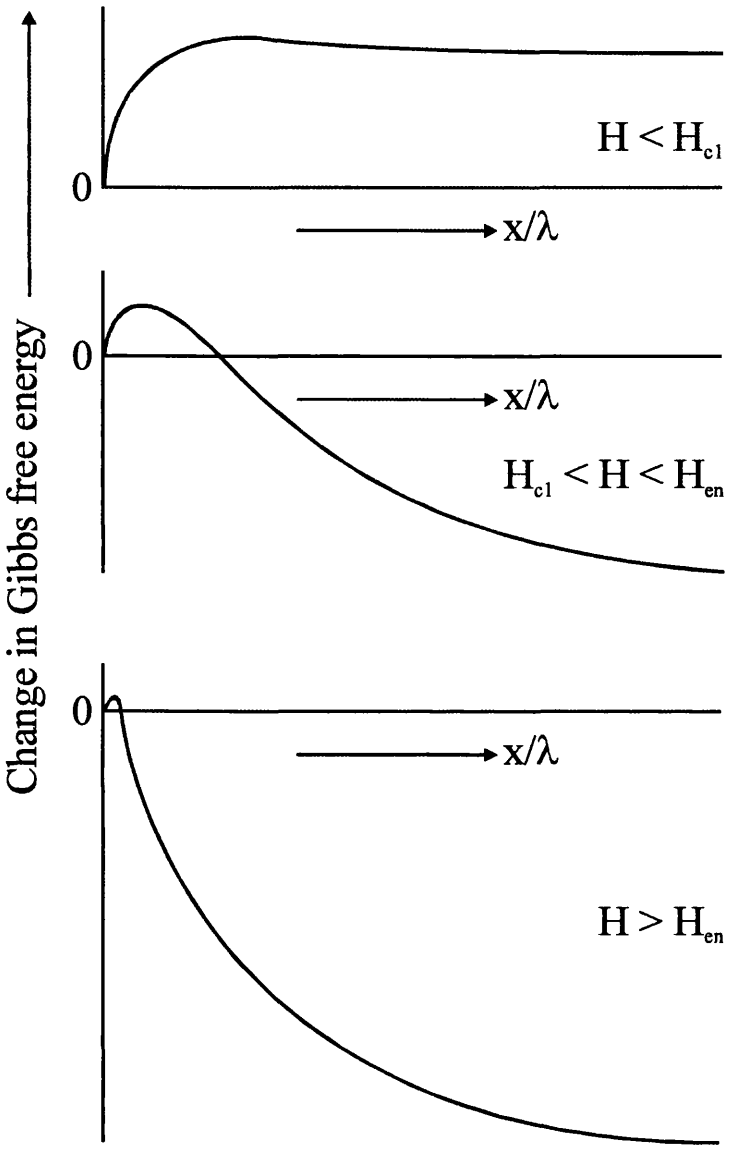

Fig. 3.10 Change in Gibbs free energy for a vortex near the surface of a superconductor for different values of applied field, accounting for interior vortices.

For a given interior flux density B, the maximum in the Gibbs free energy reduces and moves nearer the surface as the external field is increased from zero. When the width of the vortex free region (x_f) is large (compared with ξ), any vortices entering at the surface slide down the energy barrier and are annihilated with their image, as in Huebener's

model. When the maximum in free energy occurs within a vortex core width of the surface, a vortex may enter the vortex-free region and slide down the energy barrier into the bulk of the superconductor, since the Meissner force is now dominating the attractive image term. This first occurs when the applied field is equal to the penetration field H_{en}, which is found to be

$$H_{en}(B) = \left(H_p^2 + B^2\right)^{\frac{1}{2}}, \tag{3.6}$$

where H_p is the penetration field from Huebeners model shown in equation (3.5). However, unlike Huebener's model Clem's model allows for flux density dependence, i.e. $H_{en} = H_{en}(B)$. Equation (3.6) describes the initial leg of the hysteresis cycle, assuming $H_{en}(B)$ is the applied field i.e. the applied field is $\left(H_p^2 + B^2\right)^{\frac{1}{2}}$

$$M = B - H = \sqrt{H^2 - H_p^2} - H \approx \frac{H_p^2}{2H}, \tag{3.7}$$

As the applied field is increased above H_p, vortices enter at the surface, slide down the potential energy hill, doing work on a viscous drag force and dissipating energy. The vortices are then pushed towards the centre of the superconductor by the dominating Meissner force and accumulate at the centre, producing a dome-like flux profile. If the applied field is now reduced, the vortex-free region also reduces since vortices are prevented from leaving by the large potential barrier. However, when the applied field is equal to the critical exit field, the maximum of the Gibbs free energy occurs at the edge of the vortex-free region. The vortices are now pulled towards the surface by the image force, doing energy on the viscous drag force as the slide down the potential hill, eventually annihilating with their image at the surface. The critical exit field is found to be

$$H_{ex}(B) \approx B + \frac{\Phi_0}{16\pi\lambda^2} \approx B, \tag{3.8}$$

leading to $B = \mu_r\mu_0 H$, or $M = 0$ on the return leg of the hysteresis loop.

Thus, Clem's model of pinning by a surface barrier allows a characteristic hysteresis loop to be derived for a system dominated entirely by surface barriers, and this is shown

in figure 3.11. Below the penetration field H_p (defined by (3.5)), there are no vortices inside the superconductor and B = 0. Above H_p, vortices begin to enter and the curve is given by equation (3.6). If the field is now reduced, no vortices may leave the superconductor (hence B remains constant at the value given by the maximum applied field, $B(H_{max})$ in equation (3.6)) until the applied field is equal to the critical exit field. At this point, vortices leave the superconductor and $B = \mu_r \mu_0 H$.

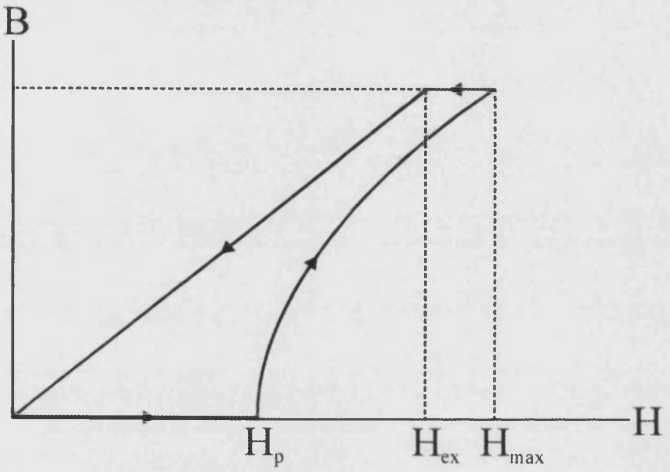

Fig. 3.11 Characteristic hysteresis loop produced using Clem's model of surface pinning.

Burlachkov has used this model of vortex activation over a surface barrier to derive expressions for the temperature dependence of the penetration field in two cases [43]. In one regime the model assumes three dimensional vortex lines are being thermally activated over the surface barrier, whereas in the other regime the vortex lines decouple into stacks of two-dimensional pancake vortices which move quasi-independently of one another. Since the penetration field can be directly determined experimentally from hysteresis loops, Burlachkov's model may be compared directly with experimental data. In the case of two-dimensional pancake vortices the temperature dependence of the penetration field H_p is given by

$$H_p(T) = H_c \exp\left(-\frac{T}{T_0}\right), \tag{3.9}$$

where T_0 is given by

$$T_0 = \frac{\varepsilon_0 d}{\ln\left(\frac{t}{t_0}\right)}, \tag{3.10}$$

Here, d is the separation of the copper-oxide planes, t is the time since application of the field H, t_0 is a fundamental time scale for vortex oscillations, and ε_0 is the vortex energy per unit length. In this model, the weak temperature dependence of H_c and ε_0 is usually neglected, as are bulk pinning effects, and an exponential temperature dependence is seen in the limit of weakly coupled two-dimensional pancake vortices. In the case of strongly coupled pancakes (i.e. three-dimensional vortex lines) a temperature dependence of the form

$$H_p(T) \propto \frac{(T_c - T)^{\frac{3}{2}}}{T}, \tag{3.11}$$

is predicted for vortex creep over a surface barrier. Using this model, a crossover field should be observed in $H_p(T)$, with high fields exhibiting an exponential dependence and low fields showing the dependence in (3.11), as shown in figure 3.12.

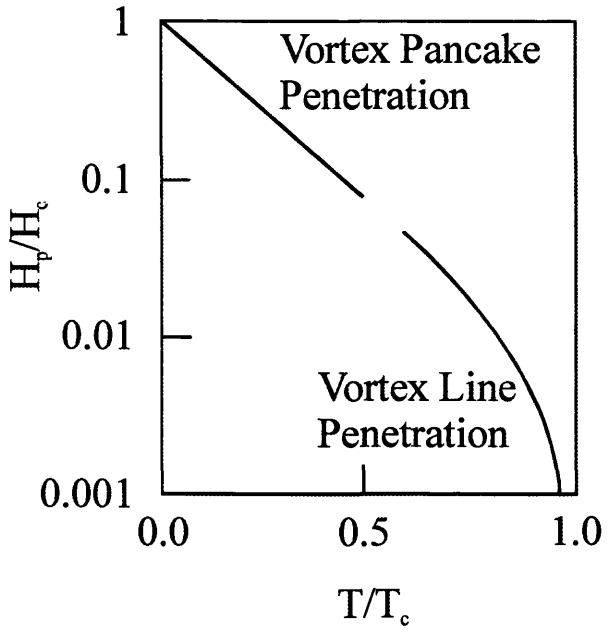

Fig. 3.12 The two regimes of vortex penetration.

Since thermal activation of vortices over a surface barrier is a statistical process, significant relaxation effects are expected, particularly at temperatures near T_c. If the data is captured infinitely slowly this leads to an equilibrium magnetisation curve, which is reversible in the absence of any other pinning mechanisms. In a normal hysteresis loop, when the applied field is swept to a value and then held constant, the superconductor is in a metastable magnetic state, with the magnetisation slowly relaxing towards the equilibrium value.

On the increasing leg of the hysteresis cycle above H_p, relaxation occurs by vortices "hopping" over the vortex free region (via thermal activation) and entering the superconductor, thereby reducing the magnetisation (see figure 3.13). On the decreasing leg, the magnetisation is increased by vortices leaving the superconductor, but vortex exit is opposed by a viscous drag force which acts on the vortex core as it slides down the free energy slope. The equilibrium magnetisation curve is shown in figure 3.13, together with the metastable states obtained on the increasing (M_{en}) and decreasing (M_{ex}) hysteresis legs.

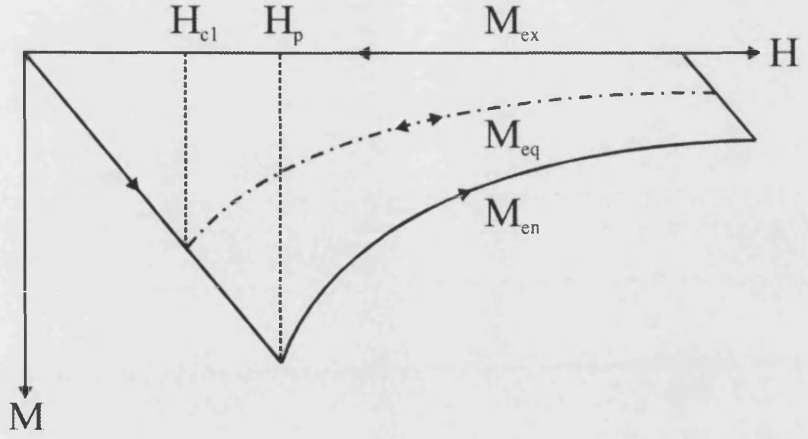

Fig. 3.13 Hysteresis loop showing vortex enter (M_{en}) and exit (M_{ex}), and the equilibrium magnetisation curve (M_{eq}).

A consequence of magnetic relaxation is that both the penetration field H_p and the hysteresis width ΔM (defined by $\Delta M = M_{ex} - M_{en}$) will depend on the rate at which the external field is swept. For very slow sweep rates, the hysteresis width will be small, since the system will relax towards M_{eq}, and the penetration field will approach the thermodynamic lower critical field H_{c1}. However, for fast sweep rates the effects of relaxation can be neglected.

Burlachkov [44] has shown that the relaxation process of vortices exiting and entering a superconductor over a BL is not symmetric, with vortex entry a non-linear function of magnetisation and vortex exit proportional to the internal flux density.

3.8. Geometrical barriers

The Bean-Livingston barriers described earlier were constructed for a field applied parallel to the surface of a semi-infinite sample, which is a rather contrived geometry. Real HTS samples tend to have a platelet geometry with the field usually applied normal to the larger surface, which is a much more complicated geometry. Clearly, there is still an image vortex outside the superconductor (as in the B-L barriers), but now the finite sample thickness must be taken into account.

The geometrical barrier arises because of the Meissner screening currents induced in response to an applied field, which flow around the perimeter of the sample. The direction and magnitude of these currents are such that, if one vortex enters near the edge, the resulting Lorentz force on the vortex tends to drive it towards the centre of the sample. A force due to the line tension of the vortex, which tries to prevent vortex entry, balances this effect. As the applied field is increased from zero, the vortex begins to penetrate at the corners of the sample, where the local field is greater than the penetration field, H_p (the field at which the vortices overcome the geometrical barrier). As the field is further increased, the vortex penetrates further into the sample until the two vortex segments come into contact at the sample equator, at this point the line tension is at a maximum. If the field is increased further the line tension will diminish to the extent that the Lorentz force due to surface screening currents is unopposed and the vortex moves rapidly to the sample centre. Figure 3.14 shows the two extremes of this situation. In figure 3.14(a) the line tension is small and the vortex has only just started to penetrate at the corners of the sample, where geometrical effects enhance the applied field. The situation of figure 3.14(b) is very different; the line tension is at a maximum and the vortex has penetrated as far as possible without complete penetration. In this case applied field is almost equal to the penetration field H_p. When the field is increased further, the vortex will penetrate into the sample and be swept to the centre by the Lorentz force due to the Meissner screening currents.

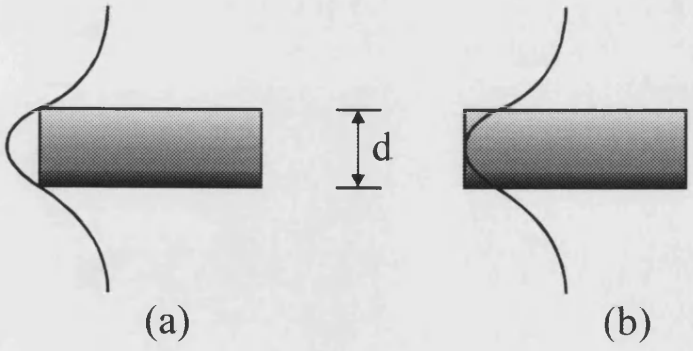

Fig. 3.14 The two extremes of vortex penetration via a geometrical barrier.

An estimate of the height of the geometrical barrier can be obtained by taking the difference between the maximum and minimum line energies. The minimum line energy configuration is when the vortex has penetrated and goes straight through the superconductor with no bends. The vortex line tension per unit length, ε_0, is given by

$$\varepsilon_0 = \left(\frac{\Phi_0}{4\pi\mu_0\lambda}\right)^2, \tag{3.12}$$

where, for the minimum energy, the relevant length is the sample thickness d. For the maximum energy situation the relevant length is an arc of a circle of diameter d, as shown by Kuznetsov [45]. So the total height of the geometrical barrier, E_g, is estimated as

$$E_g = \varepsilon_0 \pi \frac{d}{2} - \varepsilon_0 d = \varepsilon_0 d\left(\frac{\pi}{2} - 1\right), \tag{3.13}$$

Using typical values for BSCCO of $\lambda = 10^{-7}$m and $d = 10^{-4}$m, and substituting in the flux quantum, the barrier has a height of 2×10^8 K, which is extremely large. The height of this barrier precludes any significant thermal activation over the geometrical barrier or any relaxation effects, in stark contrast to the strong relaxation effects predicted for BL surface barriers. Also, in contrast to the BL barrier, which is very sensitive to surface quality, the geometrical barrier is very robust, since it extends over the entire sample width.

Zeldov *et al.* [46] has calculated both the local induction profile and the current distribution in a rectangular strip in the presence of a perpendicular applied field, in both the absence of pinning, i.e. zero bulk critical current, $J_c = 0$, and in the presence of bulk pinning i.e. finite J_c.

Zeldov *et al* [46] considered a thin superconducting strip of rectangular cross section of width 2W ($-$ W < x < W) and thickness d ($-$ d/2 < z < d/2 and d << W) which infinitely extends in the y direction. A perpendicular magnetic field H_a is applied along the positive z direction. In this configuration the resulting Meissner current and field profiles are given by [47],[48]

$$J_y(x) = -\frac{cH_a}{2\pi d}\frac{x}{\sqrt{W^2 - x^2}}, \qquad |x| < W, \tag{3.14}$$

$$B_z(x) = \frac{H_a|x|}{\sqrt{x^2 - W^2}}, \qquad |x| > W, \tag{3.15}$$

Considering only samples with d >> λ and averaging the current density over the thickness $J_y(x)$, the Meissner current exerts a Lorentz force on a vortex, resulting in a position dependent vortex energy per unit length that can be approximated by $\varepsilon(x) = \varepsilon_0 + (\Phi_0/c)\int_x^W J_y(t)dt$, not too close to the edges. ε_0 is the line energy of a non-interacting vortex and Φ_0 is the flux quantum. The vortex potential ε(x), is shown schematically in figure 3.15.

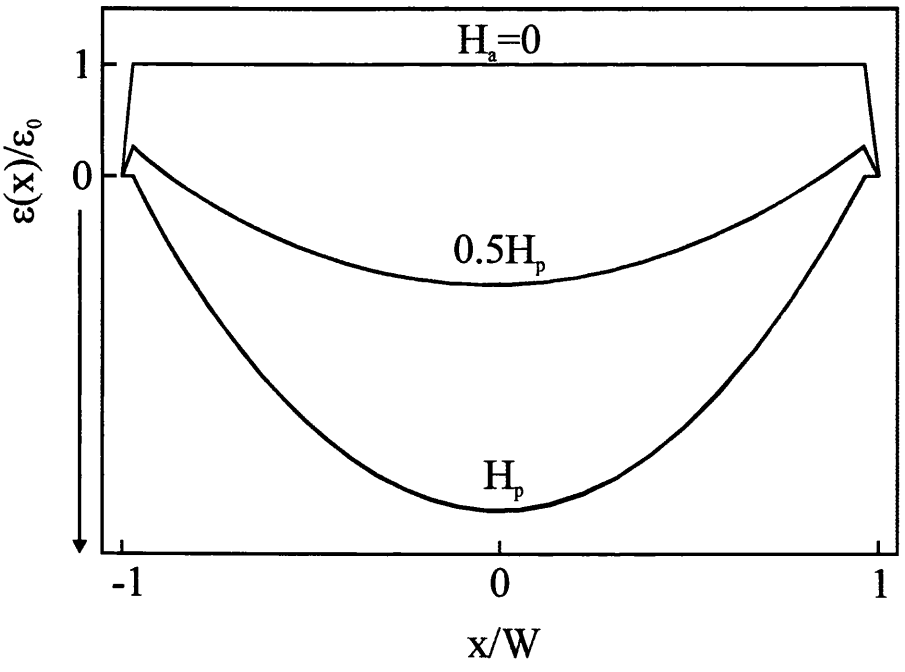

Fig. 3.15 Vortex potential at various applied fields $H_a \leq H_p$. At $H_a = 0$ the potential at the edges of the sample is assumed to drop linearly for simplicity.

In the absence of pinning this leads to an accumulation of flux at the centre of the superconductor, when the applied field exceeds the penetration field, since it becomes energetically favourable for the vortices at the edges to rapidly move inwards (as a result of the Lorentz force due to the Meissner screening currents), resulting in a dome shaped local induction profile calculated by Zeldov *et al* [46], along with the current distribution, given by

$$J_y(x) = 0, \qquad \text{at } |x| < b \text{ or } |x| > W, \tag{3.16}$$

$$B_z(x) = H_a \sqrt{\frac{b^2 - x^2}{W^2 - x^2}}, \qquad \text{at } |x| < b \text{ or } |x| > W, \tag{3.17}$$

and

$$J_y(x) = -\frac{x}{|x|} \frac{cH_a}{2\pi d} \sqrt{\frac{x^2 - b^2}{W^2 - x^2}}, \qquad \text{at } b < |x| < W, \tag{3.18}$$

$$B_z(x) = 0, \qquad \text{at } b < |x| < W, \tag{3.19}$$

where 2b is the width of the vortex filled region in the centre of the strip given by $b \cong W\sqrt{1-(H_p/H_a)^2}$ in the case of d << W. The resulting current and field profiles are shown in figures 3.16(a) and (b). This process, however, is not reversible; if the field is decreased, the vortices remain trapped by the Meissner currents, and the width of the vortex filled region increases, maintaining constant trapped flux in the central region. A reversible situation is obtained at fields of the order of H_{c1} when the vortex filled region fills the entire sample. Hence, in the absence of pinning the geometrical barrier results in hysteretic magnetisation.

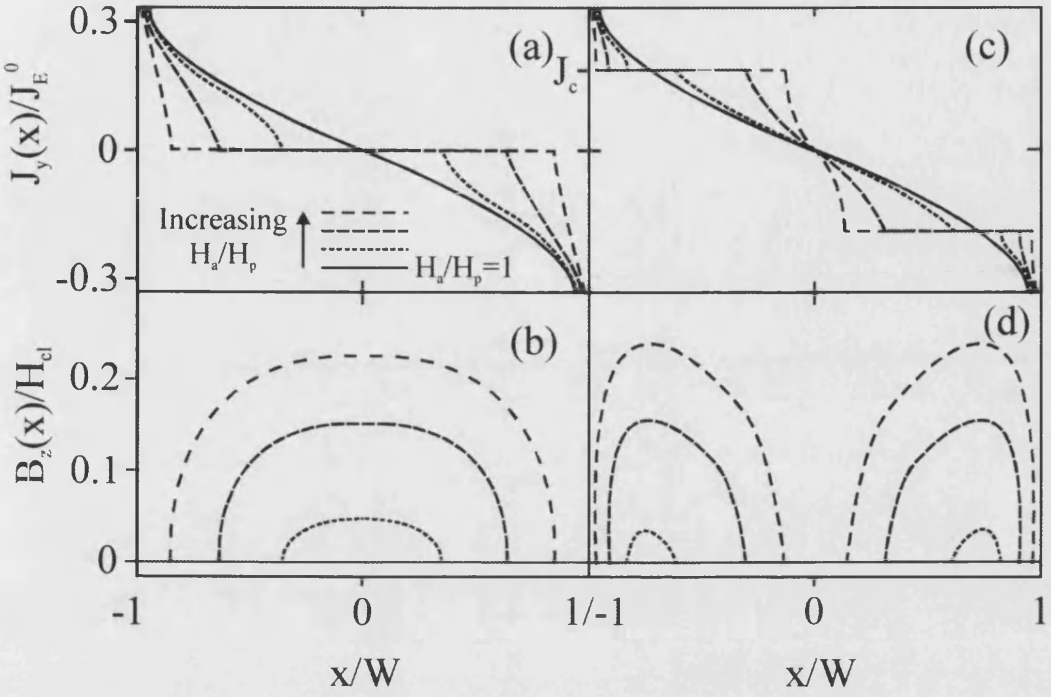

Fig. 3.16 The current and field profiles at increasing values of H_a/H_p for $J_c = 0$ [(a) and (b)] and finite J_c [(c) and (d)] showing vortex accumulation inside the sample.

In the presence of bulk pinning, the initial penetrating vortices do not reach the centre of the sample, and stop at $|x| = b_p$, where the Meissner current density equals the critical current density J_c. As the field increases, vortices form two-isolated vortex filled regions at $a < |x| < b$. The central region, $|x| < a$, remains vortex-free, since $J_y(x) < J_c$ there, and no vortices can penetrate; in the outer $|x| > b$ regions $J_y(x) > J_c$, and no vortices may remain there in a steady state. Note that a significant part of the strip carries supercritical current densities which may exceed J_c significantly. Since these edge currents are comparable to state-of-the-art critical currents in HTS at elevated temperatures, the geometrical barrier is a very significant effect with important practical implications.

To derive the current and field distributions at finite J_c Zeldov *et al* [46] used a similar method as the $J_c = 0$ case, however, the requirement for the current in the vortex filled

regions $a<|x|<b$ is now $|J_y(x)|=J_c$, rather than $J_y(x)=0$, and a rigorous current limitation at the edges, $J_y(x)=J_E$ at $e<|x|<W$ is included. As a result

$$J_y(x)=-J_c f(x)\sqrt{\frac{(a^2-x^2)(b^2-x^2)}{(e^2-x^2)}}, \qquad 0<x<a \text{ or } b<x<e, \tag{3.20}$$

$$-J_c, \qquad a<x<b, \tag{3.21}$$

$$-J_E, \qquad e<x<W, \tag{3.22}$$

and $-J_y(|x|)$ for $x<0$, and

$$B_z(x)=0, \qquad |x|<a \text{ or } b<|x|<e, \tag{3.23}$$

$$\frac{2\pi J_c d}{c}\mathrm{Re}\{f(x)\}\sqrt{\frac{(x^2-a^2)(b^2-x^2)}{(e^2-x^2)}}, \qquad a<|x|<b \text{ or } |x|>e, \tag{3.24}$$

Re{f(x)} is given by the Cauchy integral

$$\mathrm{Re}\{f(x)\}=\frac{2x}{\pi}\left[P\int_b^a \frac{dt/\mathrm{Im}\{F(t)\}}{x^2-t^2}+\frac{1}{\gamma}P\int_e^W \frac{dt/\mathrm{Im}\{F(t)\}}{x^2-t^2}\right], P-\text{principle part} \tag{3.25}$$

where $\gamma = J_c/J_E$ and the boundary conditions on a and b are given by $B_z(\infty)=H_a$, taking $e=W-d/2$ for increasing $H_a > H_p$. P indicates the principle part of the function which is the negative power part of the Laurent series of the function about its pole. The resulting distributions are shown in figures 3.16(c) and (d). As the applied field is increased, a decreases and b increases, so that the vortex filled regions expand in both directions at moderate critical currents.

In chapter 8, the validity of this model is investigated when compared with experimental results of flux penetration into a $Bi_2Sr_2CaCu_2O_{8+\delta}$ single crystal sample placed in a perpendicular magnetic field, taken using the large area SHPM described in chapter 6, which indicate not only different magnitudes of current densities but also current densities of different sign within the same superconducting sample as the applied field is simply increased from zero.

3.9. Suppression of Surface Barriers in Superconductors by Irradiation Induced Defects.

The magnetic properties of the highly anisotropic high temperature superconductors (HTS) continue to attract considerable attention. In particular the physical mechanism controlling the penetration field (H_p) at which flux first enters the bulk of the zero-field-cooled superconductor remains controversial. It is well known that H_p can be much larger than the lower critical field H_{c1} due to the influence of kinetic barriers at the sample edges [49], although this effect is partially compensated by the shape-dependent demagnetisation effect. While a number of distinct types of surface barriers exist, those that are of particular relevance for bulk samples [50], i.e. Bean-Livingston (BL) barriers and Geometrical barriers, have already been discussed in the previous two sections. As mentioned in the previous section, in contrast to the BL barrier, which is strongly suppressed by surface damage, the geometrical barrier is expected to be very robust since the Meissner currents in a flat geometry extend over the entire sample width. It is also sufficiently high that, well below T_c, there should be no appreciable thermal activation over it.

Although a geometrical barrier is often invoked to explain magnetisation data in HTS, compelling evidence exists to the contrary. The pronounced suppression of $H_p(T)$ in $YBa_2Cu_3O_{7-\delta}$ single crystals after low dose electron irradiation was interpreted as evidence for a disorder-sensitive BL barrier [51]. Furthermore it has been recently demonstrated [52] that the penetration field ($T < 50$ K) of single crystal $Bi_2Sr_2CaCu_2O_{8+\delta}$ (BSSCO) whiskers displays an exponential temperature dependence in excellent agreement with recent estimates [53],[43] for the creep of independent 2D pancake vortices over a Bean-Livingston surface barrier. Additional evidence for this conclusion arises from the observed asymmetric relaxation rates for vortex entry and vortex exit [54].

The effects on the surface barrier of the controlled modification of the bulk sample (pinning) properties by irradiation have, until now, not been considered. Burlachkov [43] supposed that the opening of new penetration channels after surface damage by

irradiation changes the prefactor of the temperature dependence of the penetration field H_p (Eq. (3.9)) but not the exponent.

Koshelev *et al.* [55] has recently proposed a model for the influence of columnar defects in layered superconductors on the thermally activated penetration of pancake vortices through the surface barrier. Columnar defects, located near the surface, facilitate penetration of vortices through the surface barrier, by creating "weak spots" where the columnar defects are close enough to the surface to suppress the surface barrier, through which pancakes penetrate into the superconductor. The model of Koshelev *et al* [55] contains two separate cases of columnar defect assisted vortex penetration. In the first case the penetration of a pancake is mediated by an isolated column located near the surface, and in the second, the effective penetration field is suppressed by clusters of columnar defects.

In the model of Koshlev *et al.* [55] vortex penetration consists of two steps (see Figure 3.17): (i) the capturing of the vortex onto a near-surface column and (ii) the detachment of the trapped vortex into the bulk, with each stage controlled by its own activation barrier. The resulting effective barrier for pancake penetration via an isolated column is the maximal value of the two barriers corresponding to the above processes. The capturing process also has a two-channel character and may occur either via the direct motion of a pancake to a column or via nucleation of an anti-vortex at the column and its subsequent advance towards the surface (see figure 3.17). The capturing process is controlled by the channel with the smallest barrier. If the mediating column is located far from the surface, the penetration process is controlled by the transfer of a vortex from the surface to this column. When the column is sufficiently close to the surface, the controlling barrier corresponds to detaching a vortex from the column to the bulk. For any value of external field there exists an optimal location of the column for which the reduction of the barrier is maximal, and penetration of pancakes into the sample occurs mainly via such optimally placed columns. Koshelov's model also allows for increased surface barrier suppression in rare locations where several columns happen to be near the surface. The net contribution to the penetration rate is determined as a balance between their small probability and the strong local suppression of the barrier, the

collective suppression by the column clusters is also estimated and at low temperatures becomes more efficient than the single-column mechanism.

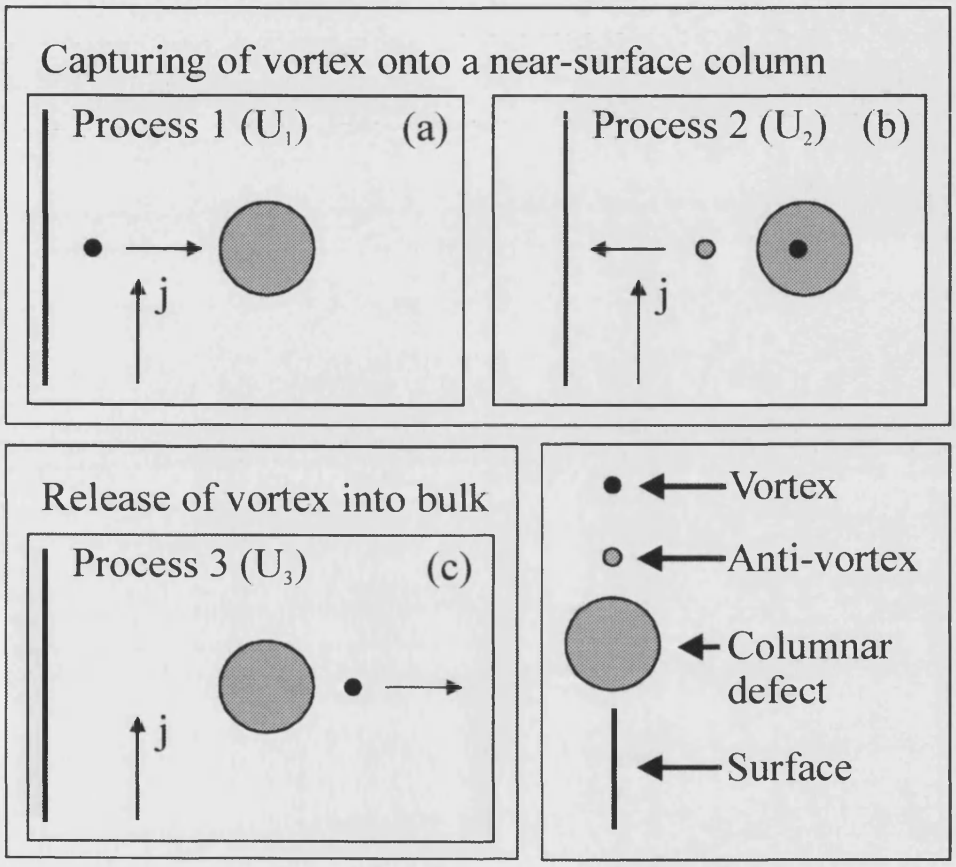

Fig. 3.17 Mechanisms of penetration of the pancake vortex from the surface into the bulk of a superconductor: (a) Nucleation of the vortex at the column via the motion of a vortex from the surface, (b) nucleation of the vortex at the column via motion of an anti-vortex form the column to the surface, and (c) motion of the vortex from the column into the bulk.

Following Koshelev's *et al.* development [55] consider an irradiated superconductor with insulating columnar defects oriented along the c axis in an external field also applied along the c axis. Let an isolated columnar defect have radius R and be located at a distance L from the surface of the superconductor (see figure 3.18). The energy of a pancake vortex located between the surface and column at distance x from the surface consists of two parts: the direct interactions with the column and the surface, $U_{int}(x)$, and the interaction with the Meissner current, $U_j(x)$. Introducing dimensionless variables measuring length in units of R, energy in units of $s\varepsilon_0 \equiv s\Phi_0^2/(4\pi\lambda)^2$, current in units of $c\Phi_0/(4\pi\lambda)^2 R$, and magnetic field in units of $\Phi_0/4\pi\lambda R$. λ is the in-plane London penetration depth and s is the interlayer spacing and the notation $l \equiv L/R$ is used.

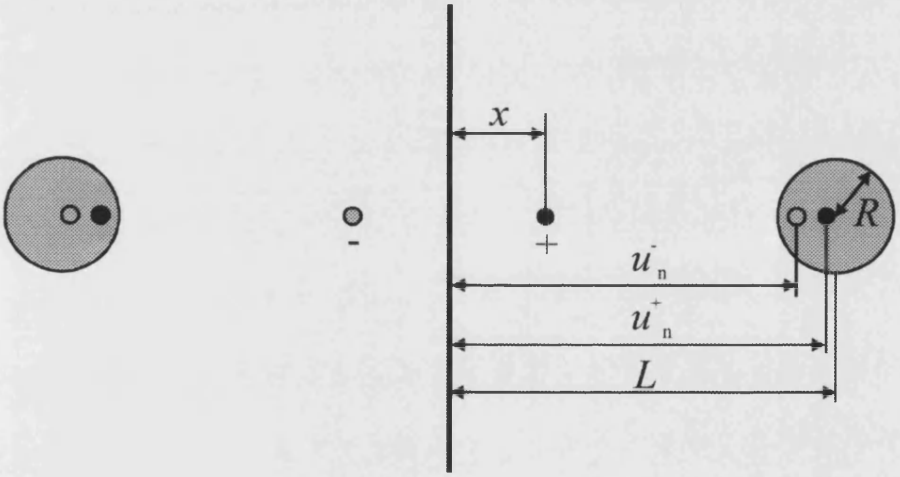

Fig. 3.18 Geometry of Koshelev's *et al.* [55] development: a pancake vortex between the surface and a columnar defect. Interaction with the surface and the column can be described in terms of an infinite set of positive and negative images obtained by multiple subsequent reflections by the surface and the column (only the first two images inside the column are shown).

The interaction of the vortex with either the plain surface or an isolated column is calculated using a similar technique to that used in the case of the Bean-Livingston barrier. The interaction with the surface is obtained by placing a negative vortex at the point $-x$ and the interaction with the isolated column can be obtained by placing a negative vortex at point $l - 1/(l - x)$ inside the column and a positive vortex at the column centre. In the case where the vortex is confined between the column cavity and the surface, adding these images only would not solve the problem because the currents due to the surface image do not satisfy the boundary conditions at the surface of the columnar cavity and vice versa. To compensate the currents of the surface image, its image (reflection) must be added inside the column. This eliminates the vortex in the column centre and adds a vortex at the point $l - 1/(l + x)$. As a result of this the surface image of this vortex must be added at the point $-l + 1/(l + x)$. The reflections are continued until an infinite set of positive and negative images is obtained. The coordinates of the positive (negative) images inside the column after the nth double reflection are labelled as u_n^+ and (u_n^-) [every such image has a corresponding surface image of opposite sign at $-u_n^+$ $(-u_n^-)$]. The $(n + 1)$th image is obtained by reflecting the nth image with respect to the surface and then reflecting it again with respect to the column.

From this Koshelev *et al.* [55] show the interaction energy to be expressed as an infinite series in the coordinates of all images:

$$U_{\text{int}}(x) = \ln\frac{1.47R}{\xi} + \ln 2x + \sum_{n=1}^{\infty} \ln\left|\frac{(u_n^- - x)(u_n^+ - x)}{(u_n^- + x)(u_n^+ - x)}\right|, \tag{3.26}$$

this expression is valid for a vortex located at either side of the column, i.e. for both $0 < x < l - 1$ and $x > l + 1$. The supercurrent distribution around the column containing the trapped vortex coincides with the distribution corresponding to a vortex placed at the point $\sqrt{l^2 - 1}$ and its surface image. The energy of this state is given by

$$U_{tr}(l) = \ln\left(l + \sqrt{l^2 - 1}\right), \tag{3.27}$$

The energy, corresponding to an antivortex at point x, which controls the competing process of antivortex motion from the column to the surface, is given by

$$U_{\rm int}^{av}(x) = U_{\rm int}(x) + 2\ln\frac{\sqrt{l^2-1}-x}{\sqrt{l^2-1}+x} + \ln\left(l+\sqrt{l^2-1}\right), \tag{3.28}$$

Here the second term on the right hand side describes the interaction of the antivortex with the trapped vortex while the third term gives the self-energy of the trapped vortex. To include the interaction with the Meissner currents Koshelev *et al.* [55] use a column (cyclindrical cavity) placed near the surface. When such a column is placed near the surface it disturbs the pattern of the screening supercurrent induced by the external magnetic field and changes accordingly the contribution to the vortex energy arising from surface screening current. The current $\mathbf{j}(\mathbf{r})$ has to satisfy $\nabla.\mathbf{j} = 0$. This means that it can be expressed in terms of a supercurrent potential $\phi_j(\mathbf{r})$ as

$$j_y = -\frac{\partial\phi_j}{\partial x}, \tag{3.29}$$

$$j_x = \frac{\partial\phi_j}{\partial y}, \tag{3.30}$$

Koshelev *et al.* [55] considered the situation where all relevant distances are smaller than the London penetration depth so that the effects of screening can be neglected and $\nabla \times \mathbf{j} = 0$ can be assumed, which implies that the potential satisfies the Laplace equation $\Delta\phi_j = 0$. Koshelev *et al.* [55] noted that the problem of finding the current distribution is equivalent to the polarisation of a metallic cylinder near a metallic surface by an external electric field parallel to the surface. Since the normal components of $\mathbf{j}$ should vanish at the surface and at the column, both the external boundary of the superconductor and the boundary of the column should be equipotential surfaces. Setting $\phi_j(0,y) = 0$, $\phi_j(\mathbf{r})$ is defined as the interaction energy of a vortex at the point $\mathbf{r}$ with the Meissner current. At large distances from the column, the x component of the current must vanish; hence far from the column, $\mathbf{j} = (0,j)$ with $j = cH/(4\pi\lambda)$. The current distribution near an isolated cylinder is given by putting a vortex dipole $(j,0)$ at the centre of the cylinder, which induces the potential

$$\phi_j = -jx\left(1-\frac{1}{(x-L)^2+y^2}\right), \tag{3.31}$$

To satisfy the boundary condition at the surface the surface image of this dipole is added, i.e. a dipole $(-j,0)$ is placed at $x = -L$. However, the currents of this surface image do not satisfy the boundary conditions for the column and it is again necessary to add the column image of the surface image. Continuing this process leads to an infinite set of dipole images inside the column as before. The sequential reflection does not preserve the magnitude of a dipole. Reflecting a pair of opposite vortices located near the point $(x,0)$, Koshelev *et al.* [55] derived that the magnitude of the column reflection of the dipole is smaller by a factor of $1/(l-x)^2$ than the magnitude of the original dipole. The coordinate of the dipole resulting from the n double reflections is denoted as x_n and its magnitude as jp_n. From this Koshelev *et al.* [55] shows the potential can be represented as an infinite series

$$\phi_j(r) = -jx + j\sum_{n=1}^{\infty}\left[\frac{(x-x_n)p_n}{(x-x_n)^2+y^2}+\frac{(x+x_n)p_n}{(x+x_n)^2+y^2}\right], \tag{3.32}$$

and the interaction energy of the vortex (located at the line $y = 0$) with the Meissner current given by

$$\phi_j(x) \equiv \phi_j(x,0) = -jx + 2xj\sum_{n=1}^{\infty}\frac{p_n}{x^2-x_n^2}, \tag{3.33}$$

The vortex – Meissner-current interaction energy becomes $\phi_j(l-1) = -j\sqrt{l^2-1}$ when the vortex is trapped by the column, and the total energy of the trapped vortex is given by

$$U_{tr}(l,j) = \ln\left(l+\sqrt{l^2-1}\right) - j\sqrt{l^2-1}, \tag{3.34}$$

As previously mentioned, in the model of Koshelev *et al.* [55] the penetration of a pancake into an irradiated superconductor happens in two steps: hopping from the surface to a column and detachment from the column into the bulk. The resulting effective barrier is equal to the maximum of the two barriers for the two processes. The nucleation of a vortex at the column (the first step) can occur via two channels: (i) as

motion of a vortex from the surface to a column or (ii) by nucleation at and the subsequent motion of an antivortex from the column to the surface. The effective barrier for this first step is, thus, the smaller one. For every fixed position of the column there exists a certain value $j_{cd}(l)$ of the surface current, above which the state with the one flux quantum trapped in the column becomes energetically favourable:

$$j_{cd}(l) = \frac{\ln\left(l + \sqrt{l^2 - 1}\right)}{\sqrt{l^2 - 1}}, \tag{3.35}$$

The corresponding magnetic field is given by

$$H_{cd}(L) = \frac{\Phi_0}{4\pi\lambda\sqrt{L^2 - R^2}} \ln\left(\frac{L + \sqrt{L^2 - R^2}}{R}\right), \tag{3.36}$$

Using the total energy of the vortex located at the point $(x,0)$,

$$U_v(x) = U_{\text{int}}(x) + \phi_j(x), \tag{3.37}$$

the activation barrier for the vortex to hop from the surface to the column (process 1 in figure 3.17) can be calculated as

$$u_1(l, j, R/\xi) = \max_{0<x<l-1} U_v(x), \tag{3.38}$$

Similarly, using the expression for the energy of the antivortex at the point $(x,0)$ and the vortex inside the column,

$$U_{av}(x) = U_{\text{int}}^{(av)}(x) - \phi_j(x) - j\sqrt{l^2 - 1}, \tag{3.39}$$

and the barrier for the motion of the antivortex from the column to the surface (process 2 in figure 3.17) is given as

$$u_2(l, j, R/\xi) = \max_{0<x<l-1} U_{av}(x), \tag{3.40}$$

The channel that governs vortex penetration depends on the magnitude of the applied current. At small currents the surface-to-column process dominates while at sufficiently large currents the vortex-antivortex mechanism comes into play. The characteristic current $j_{av}(l)$ separating the two regimes depends on the position of the column and is determined by the solution of $u_1(l, j_{av}) = u_2(l, j_{av})$.

The barrier to activate the vortex from the column into the bulk of the superconductor (process 3 in figure 3.17) is given by

$$u_3(l, j, R/\xi) = \max_{x>l+1}[U_v(x)], \qquad j < j_{cd}(l), \tag{3.41}$$

$$\max_{x>l+1}[U_v(x)] - U_{tr}(l, j), \qquad j > j_{cd}(l), \tag{3.42}$$

The total barrier corresponding to the channel surface→column→bulk is given by

$$u(l, j, R/\xi) = \max[\min(u_1, u_2), u_3], \tag{3.43}$$

Koshelev *et al.* [55] calculate the effective reduction of the surface barrier by the column as

$$\delta u(l, j) = u(l, j, R/\xi) - u_0(j, R/\xi), \tag{3.44}$$

which does not depend on the ratio R/ξ, and u_0 is the barrier for pancake penetration through an ideal barrier.

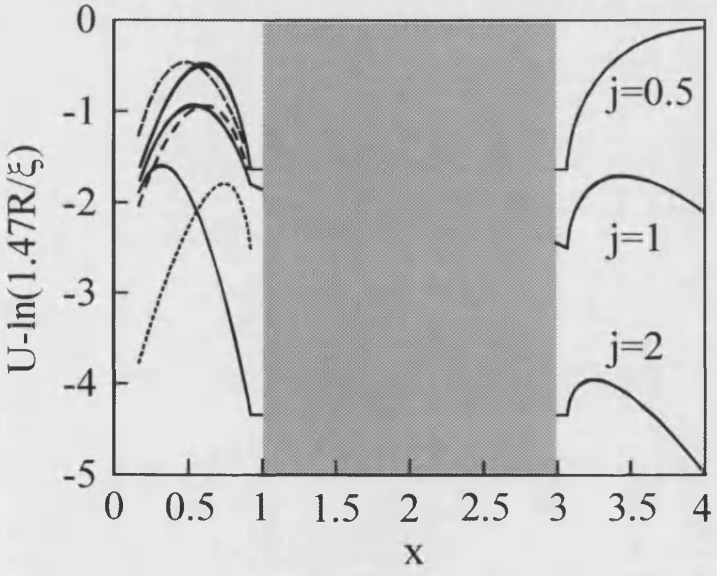

Fig. 3.19 The evolution of the energy profiles with increasing screening surface current j for l = 2. On the left-hand side, solid black lines represent the energy profiles U_v(x) fro the vortex moving from the surface to the column, and dashed lines represent the enrgy profiles for an anti-vortex, U_{av}(x), moving in the opposite direction.

Koshelev *et al.* [55] calculated numerical solutions for each barrier. Figure 3.19 illustrates the evolution of the energy profiles $U_v(x)$ and $U_{av}(x)$ with increasing current for l = 2. At small currents the position of the maximum energy is located on the right hand side of the column while at large currents it is located between the surface and the column. Figure 3.20 shows the l dependence of the total barrier $u(l,j)$ for different l. For every value of the surface current (external field) there is an optimum location of the column l_{opt} for which suppression of the barrier is maximum. It corresponds to the transition between the two mechanisms of penetration, i.e., $u_3(l_{opt},j) = \min(u_1(l_{opt},j),u_2(l_{opt},j))$. Figure 3.21 shows the current dependence of the barrier suppression for an optimally located column $\delta u_{opt}(j) \equiv \delta u(l_{opt}\, j)$. The plot illustrates the main result of the work, the important feature of which is that the dependence saturates at ≈ -0.76 at high currents.

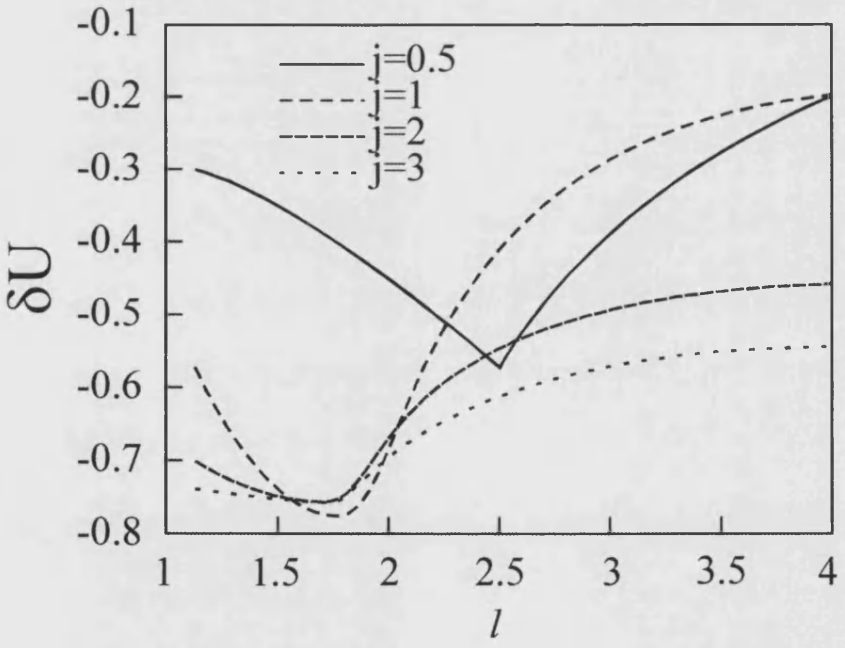

Fig. 3.20 l dependence of the total barrier for penetration from the surface into the bulk for several values of j.

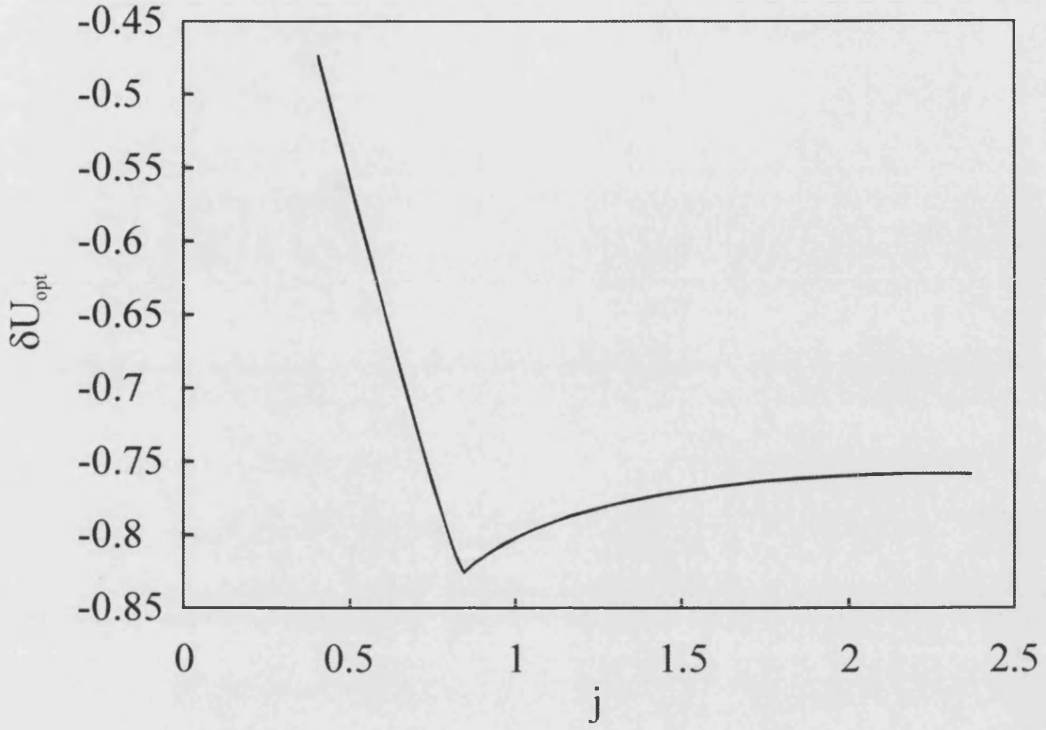

Fig. 3.21 j dependence of the energy barrier reduction for penetration of a vortex from the surface into the bulk for the optimum column location. Plot determines the reduction of the surface barrier in real irradiated samples in the single-column regime.

Perhaps of more importance to the work presented in this thesis is the enhancement of the effective penetration field by the surface barrier. When the penetration field is limited by thermal penetration through the surface barrier, the effective penetration field is determined by the equation $u_0(H_{p0}) = CT$, where the numerical constant $C \approx 20 - 40$ is determined by the experimental time scale and by the attempt frequency. This gives an exponential temperature dependence of the penetration field. In irradiated samples, Koshelev *et al.* [55] expect, the penetration field to be reduced to a lower value determined by $u_0(H_p) + \delta u(H_P) = CT$. In the field range $H_p >> \Phi_0/4\pi\lambda R$ where the barrier reduction approaches the constant value $- 0.76s\varepsilon_0$ Koshelev's *et al.* [55] model predicts $H_p \approx 0.47H_{p0}$.

Koshelev *et al.* [55] also considered the case of a cluster of columns forming close to the surface, which suppress the surface barrier to a greater extent than the isolated column case. The optimal gate for the vortex entry appears as several columns line up next to each other, forming a cut through the sample normal to the surface. The width of the cut is $2R$ and its length is $2NR$, where N is the number of columns in such a cluster (see figure 3.22). In order to find the entry field due to a cluster Koshelev *et al.* [55] used the results of A. I. Buzdin [56] and A. Yu Aladyshkin [57], who calculated the current and field distributions near the edge of a wedgelike surface crack, and applied their findings to a cut normal to the surface made of a chain of N columns. According to A. I. Buzdin [56] and A. Yu Aladyshkin [57] the current near the tip of a thin crack grows as $j\sqrt{2NR/x}$ when the distance x from the tip of the crack (the last column) falls into the interval $R < x << 2NR$ and saturates at $j\sqrt{2N}$ for $x \lesssim R$. Here j is the Meissner current far away from the crack. The suppression of the barrier depends on the relation between the position of the energy maximum x_0 and R.

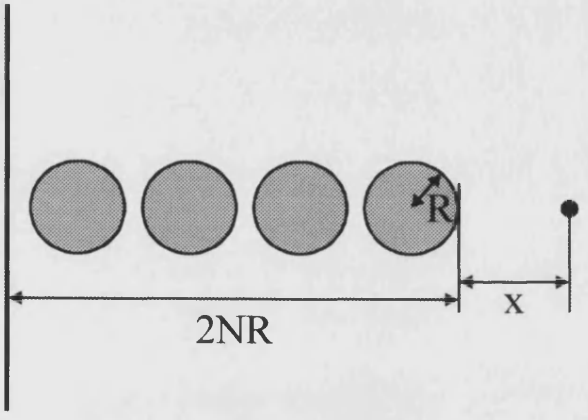

Fig. 3.22 The gate at the surface created by an improbable event when N columns form a chain. Such gates dominate flux penetration at low temperatures.

In order to estimate the effective penetration rate Koshelev *et al.* [55] determined the size of the clusters giving maximal contribution to vortex entry. The probability of finding a chain of N columns in a row scales as $(\pi R n_d)^N$ with n_d being the column concentration. The contribution from such chains to the penetration rate is given by

$$\sum_N \left(\pi R^2 n_d\right)^N \exp\left(\frac{s\varepsilon_0}{T}\ln\frac{\Phi_0 jNR}{c\varepsilon_0}\right) = \sum_N \exp\left(-N\ln\frac{1}{\pi R^2 n_d} + \frac{s\varepsilon_0}{T}\ln\frac{\Phi_0 jNR}{c\varepsilon_0}\right), \tag{3.45}$$

and becomes maximal at the optimal N:

$$N = \frac{s\varepsilon_0}{T\ln\left(1/\pi R^2 n_d\right)} > \max\left[1, \frac{2c\varepsilon_0}{\Phi_0 jR}\right], \tag{3.46}$$

which reduces the condition $x > R$ to

$$T > \frac{s\varepsilon_0}{\ln\left(1/\pi R^2 n_d\right)}\left(\frac{\Phi_0 jR}{2c\varepsilon_0}\right)^2, \tag{3.47}$$

In this "high-temperature" regime the change of the surface barrier is

$$\delta u \approx -s\varepsilon_0 \ln\frac{s\Phi_0 jR}{2cT\ln\left(1/\pi R^2 n_d\right)}, \tag{3.48}$$

$$= -s\varepsilon_0 \ln\frac{sR\Phi_0 H}{8\pi\lambda T\ln\left(1/\pi R^2 n_d\right)}, \tag{3.49}$$

where $j = cH/4\pi\lambda$.

The effective penetration barrier is determined by the relation

$$s\varepsilon_0 \ln\frac{H_c H_T}{H^2} = CT, \tag{3.50}$$

with $H_T = sR\Phi_0/8\pi\lambda T\ln(1/\pi R^2 n_d)$, which gives

$$H_p = \sqrt{H_c H_T}\exp\left(-\frac{CT}{2s\varepsilon_0}\right), \tag{3.51}$$

For the regime $x_0 < R$, corresponding to low temperatures, the energy of the vortex is given by

$$E(x) = -\frac{s\Phi_0}{c} j\sqrt{2nx} + s\varepsilon_0 \ln\frac{x}{\xi}, \tag{3.52}$$

The position of the energy maximum and the barrier are given by

$$x_0 = \frac{c\varepsilon_0}{\Phi_0 j\sqrt{2N}}, \tag{3.53}$$

$$u = s\varepsilon_0 \ln\frac{c\varepsilon_0}{\Phi_0 \xi j\sqrt{2N}} \approx u_0 - \frac{s\varepsilon_0}{2}\ln N, \tag{3.54}$$

Following a similar route as the $x_0 > R$ case Koshelev *et al.* [55] found the optimal cluster length as

$$N = \frac{s\varepsilon_0}{2T\ln\left(1/\pi R^2 n_d\right)} > 1, \tag{3.55}$$

and the change of barrier is

$$\delta u = -\frac{s\varepsilon_0}{2}\ln\frac{s\varepsilon_0}{2T\ln\left(1/\pi R^2 n_d\right)}, \tag{3.56}$$

Contrary to the case of individual columns, the cluster gate exhibits a clear temperature dependence: the depression of the barrier decreases logarithmically with growing temperature. The change of the effective penetration field is determined by

$$s\varepsilon_0 \ln\frac{H_c}{H_p} - \frac{s\varepsilon_0}{2}\ln\frac{s\varepsilon_0}{2T\ln\left(1/\pi R^2 n_d\right)} = CT, \tag{3.57}$$

or

$$H_p = \sqrt{\frac{2T\ln\left(1/\pi R^2 n_d\right)}{s\varepsilon_0}} H_{p0}, \tag{3.58}$$

This formula gives the effective penetration fields at low temperatures. It can be seen that long clusters of columnar defects forming the crack like configurations further suppress the surface barrier (as compared to the effect of an individual column) and serve as a very effective vortex gate into the sample. The collective mechanism is dominant over the single-column mechanism at low temperatures. Comparing equation (3.58) with the single-column result Koshelev *et al.* [55] found that at high magnetic fields the crossover between the single column and collective regimes is expected at the crossover temperature T_{cr}:

$$T_{cr} \approx \frac{s\varepsilon_0}{8\ln\left(1/\pi R^2 n_d\right)}, \tag{3.59}$$

Koshelev's *et al.* [55] calculations suggest that in the regime of thermally activated pancake penetration through the surface barrier, the penetration field is roughly 2 times smaller than the penetration field of unirradiated samples at temperatures above the crossover temperature given by Eq. (3.59) and decreases according to Eq. (3.58) at lower temperatures.

This topic is further discussed in chapter 7, section 7.1, which investigates the suppression of surface barriers for flux penetration in BSCCO whiskers by electron and heavy ion irradiation.

Chapter 4

4. The $Y_1Ba_2Cu_3O_{7-\delta}$ and $Bi_2Sr_2Ca_1Cu_2O_{8+\delta}$ High-T_C Superconductors

This chapter gives a brief description of the important material properties of Yttrium Barium Copper Oxide (YBCO) and Bismuth Strontium Calcium Copper Oxide (BSCCO). A comparison of the two materials structures is given and the differences in their magnetic behavior discussed. The unique properties of the BSCCO whiskers used to investigate the suppression of surface barriers by irradiation induced defects, presented later in chapter 7, are also discussed along with a brief description of the samples growth details.

4.1. Discovery and Structual Analysis

In 1986 J. Georg Bednorz and K. Alex Muller [16] reported that a compound of Lanthanum, Barium, Copper and Oxygen became superconducting at temperatures of the order of 30 K – this was the discovery of the first high temperature superconductor (HTS). Shortly after this, C. W. Chu *et al.*[58] discovered the first HTS material with a transition temperature higher than that of liquid nitrogen, the material was $YBa_2Cu_3O_{7-\delta}$ (abbreviated to YBCO or 1-2-3 from the ratio of its metal atoms), and has a transition temperature of approximately 90 K. A year later, Maeda *et al* [19], reported superconductivity in a compound of Bismuth, Strontium, Calcium and Copper with a transition temperature of approximately 110 K. Further work by Hazen *et al.* [59]

confirmed this result, and also established that there are three superconducting phases in this compound, with very different critical temperatures. For the work contained in this thesis the compound $Bi_2Sr_2CaCu_2O_{8+\delta}$ (or Bi2212) with a T_c of ~ 90 K has been used and hence the properties of this superconducting phase are concentrated on here.

As with all high T_c cuprates, both YBCO and BSCCO have highly anisotropic perovskite crystal structures, with the superconductivity residing almost entirely within the copper-oxide (CuO_2) layers parallel to the a-b planes. Figure 4.1(a) and (b) show the crystal structures of $Bi_2Sr_2CaCu_2O_{8+\delta}$ and $YBa_2Cu_3O_{7-\delta}$ respectively. In the case of BSCCO the copper-oxide planes are separated by sheets of BiO, whereas for YBCO the copper-oxide planes are only separated by a single yttrium atom.

The growth details of the YBCO thin-film and the BSCCO single crystal studied in this thesis are relatively complicated and are not discussed here, but are mentioned briefly in the relevant sections for each investigation (section 7.2 for YBCO and section 8.2 for the BSCCO single crystal), and where necessary references given containing the details of the procedures used. The properties and growth details of the BSCCO whiskers used as alternatives to bulk single crystals in the investigation of the suppression of surface barriers by irradiation (see section 7.1) are given in section 4.4 of this chapter. For both types of superconductor and for each growth method used, subsequent heat treatments and oxygenation procedures are required to obtain the correct oxygen stochiometry. The exact value of the critical temperature depends strongly on the oxygen doping level for both YBCO and BSCCO and, hence, in each case the samples transition temperature, T_c, varies from the maximum value expected from optimum oxygen stoichiometry.

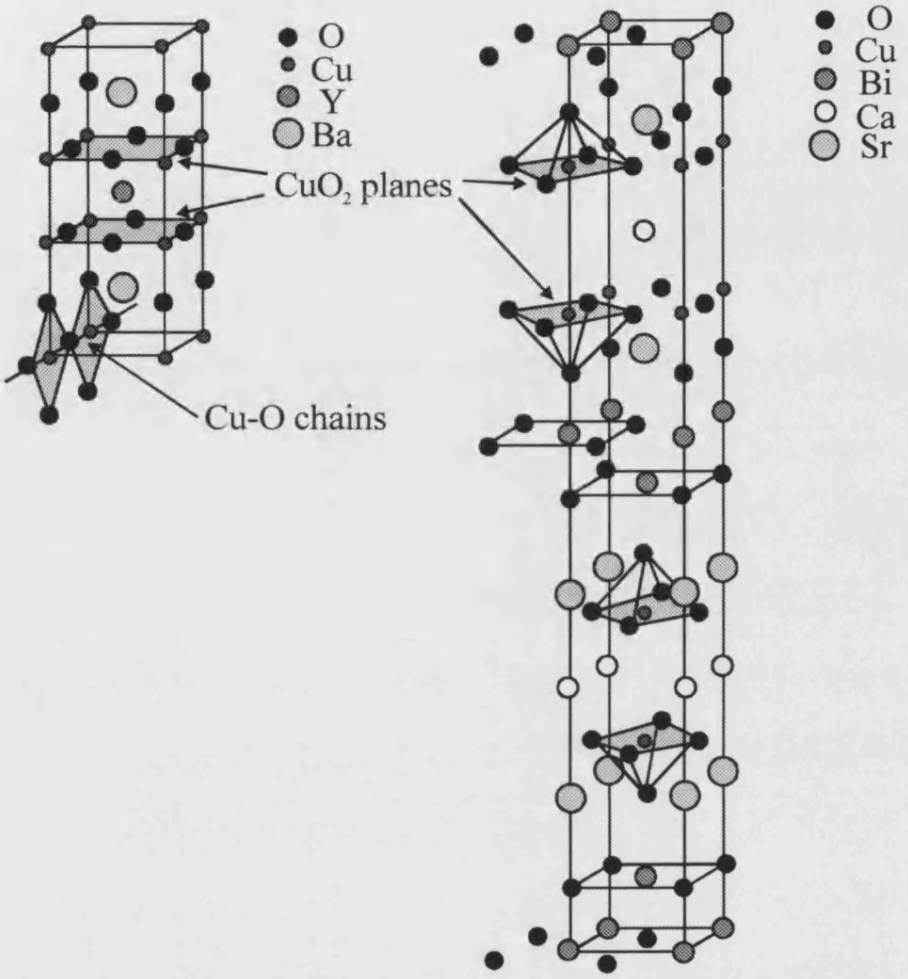

Fig. 4.1 (a) Crystal structure of $YBa_2Cu_3O_{7-\delta}$, and (b) crystal structure of $Bi_2Sr_2CaCu_2O_{8+\delta}$.

4.2. Magnetic Properties

The fundamental parameters of any superconductor are the penetration depth λ and the coherence length ξ, and it is important to have an accurate measurement of these before any theoretical models can be applied to real superconductors. Both λ and ξ can, in principle, be obtained indirectly from magnetisation data through the Ginzburg-Landau expressions for the lower and upper critical fields, given by

$$H_{c1} = \frac{\Phi_0}{4\pi\mu_0\lambda^2}\ln\left(\kappa + \frac{1}{2}\right), \tag{4.1}$$

$$H_{c2} = \frac{\Phi_0}{2\pi\mu_0\xi^2}, \tag{4.2}$$

However, there are several problems with this method of determining λ and ξ. Shape dependent demagnetisation effects can cause large errors in the determination of H_{c1} and hence affect the calculated value of λ. Also when (4.1) and (4.2) are applied to high temperature superconductors, they must be amended to account for the extreme anisotropy of these materials. The modified expressions are given by [60]

$$H_{c1}^{c} = \frac{\Phi_0}{4\pi\mu_0\lambda_{ab}^2}\ln\kappa, \tag{4.3}$$

$$H_{c1}^{ab} = \frac{\Phi_0}{4\pi\mu_0\lambda_{ab}\lambda_c}\ln\left(\frac{\lambda_{ab}}{d} + 1.12\right), \tag{4.4}$$

$$H_{c2}^{c} = \frac{\Phi_0}{2\pi\mu_0\xi_{ab}^2}, \tag{4.5}$$

$$H_{c2}^{ab} = \frac{\Phi_0}{2\pi\mu_0\xi_{ab}\xi_c}, \tag{4.6}$$

In these expressions (4.3 to 4.6) *ab* and *c* denote directions parallel and normal to the copper-oxide planes respectively, and *d* is the distance between CuO_2 planes. The final problem is a result of the large thermal energies involved with the high T_c materials, which effectively smear out the normal-superconducting transition at H_{c2}. This is coupled with the fact that $H_{c2}(0)$ in some HTSs has been found to be larger than experimentally attainable magnetic fields, and hence is not an accurate way of determining ξ. Another problem with this method of determining λ is the fact that the value of H_{c1} can be drastically affected by demagnetisation factors reducing the field of first flux penetration. Also the effects of electromagnetic surface barriers can significantly increase the field of first flux penetration to values larger than the thermodynamic value of H_{c1}.

Techniques for the determination of λ include microwave studies [61], muon spin rotation (μSR) studies [62], direct imaging of vortices using scanning Hall probe microscopy and magnetisation measurements that avoid surface barrier effects by using very slow applied field sweep rates [63]. Recently, Prozorov *et al* [64] have developed an improved microwave method to measure the absolute value of the penetration depth, and have measured $\lambda(T = 0)$ in both $YBa_2Cu_3O_{7-\delta}$ and $Bi_2Sr_2CaCu_2O_{8+\delta}$. The technique involves coating a high-T_c superconductor with a film of low-T_c material of known thickness and penetration depth. The coated sample is then placed in a microwave cavity and the frequency shift measured. The penetration depth of the high-T_c superconductor can be calculated, as it is a function of the frequency shift and the known penetration depth of the low-T_c superconductor. The method has been applied to obtain $\lambda(YBa_2Cu_3O_{7-\delta}) \approx 1460 \pm 150$ Å at $T = 0$ and optimally doped, which compares well with values obtained by other methods such as μSR 1405 ± 92 Å [65]. A value of $\lambda($ $Bi_2Sr_2CaCu_2O_{8+\delta}) \approx 2690 \pm 150$ Å at $T = 0$ and optimally doped, was also obtained using this method which exceeds those obtained by other methods such as μSR, $\lambda \approx$ 1800 Å [66], and reversible magnetisation, $\lambda \sim 2100$ Å [67], but agrees well with the value of $\lambda \approx 2700$ Å [63] obtained from lower critical field measurements. The main advantage of Prozorov's method is that it gives an absolute value of the penetration depth with an accuracy that is only limited by uncertainties in the thickness and penetration depth of the low-T_c superconductor (Al in this case), and gives an estimated accuracy of ± 150 Å.

Determination of ξ present's significant experimental problems in both YBCO and BSCCO because of the rounding of the transition in HTSs leading to poorly defined values of H_{c2}. A critical discussion of the difficulties in determining H_{c2} and ξ for YBCO is given by K. S. Bedell *et al* [68]. A generally accepted value of ξ for YBCO is ~ 10 Å. For BSCCO, less definitive results are available because the effects of anisotropy and the smearing of H_{c2} are even more severe than for YBCO. However, Tinkham [8] suggests that $\xi \approx 20$ Å as a representative value for most of the layered superconductors.

4.3. Magnetic Phase Diagram of YBCO and BSCCO/Anisotropy Effects

The anisotropic nature and other unique material properties of the high temperature superconductors YBCO and BSCCO result in a rich vortex-matter phase diagram divided by numerous transition lines, crossovers and vortex phases such as lattice, glass, and liquid phases. Due to the strong anisotropy, short coherence length, and high critical temperatures of these materials, a melted vortex liquid replaces the conventional Abrikosov lattice in wide regions of the vortex-matter phase diagrams. Also, in addition to the thermodynamic transition lines $H_{c1}(T)$ and $H_{c2}(T)$ in the H-T phase diagram of YBCO and BSCCO, several other phases exist separated by additional transition lines. These include a first order transition line (or solid melting line), an irreversibility line (or de-pinning line), and a transition line that represents the onset of the second magnetisation peak, only recently seen in YBCO. In this section vortex-matter phase diagrams for both clean $YBa_2Cu_3O_y$ and $Bi_2Sr_2CaCu_2O_8$ are presented and similarities between their vortex-matter diagrams discussed.

For BSCCO, the standard experimental picture [69] (see figure 4.2) is that the vortex matter displays at least three distinct phases with three phase boundary lines rather than two main phases (solid and liquid) with only one transition line between them. In figure 4.2 phase B is a reasonably well-ordered solid, phase C is a highly disordered 2D vortex solid, and phase A is either a liquid of vortex lines close to the transition line or a gas of vortex pancakes well above it. The de-pinning boundary line defines the magnetic field above which the magnetisation is reversible. The standard interpretation of this line is that it marks the onset of bulk pinning, with the vortices pinned to pinning sites below the irreversibility line and free to move (and hence produce reversible magnetisation loops) above. The de-pinning line is thus also known as the irreversibility line.

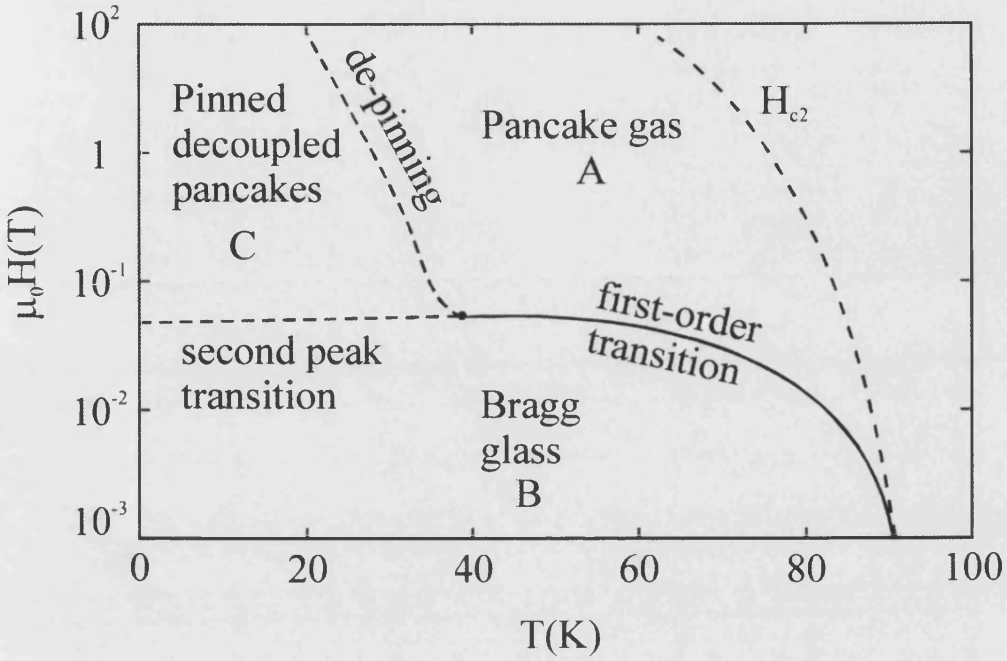

Fig. 4.2 Vortex-matter phase diagram in BSCCO (on a logarithmic scale), showing the different possible vortex phases within the mixed state.

The first order phase transition line represents the melting (or sublimation) of the vortex solid to a vortex liquid (or gas) and is often referred to as the melting line. Vortex lattice melting was first proposed by Gammel *et al* [70] as an interpretation of magnetisation measurements on single crystal YBCO and BSCCO. A sharp, discontinuous step was observed when either the applied field or temperature was swept across the transition line. Vortex lattice melting is analogous to melting in an atomic crystal; with the liquid regime exhibiting no long range order and zero shear modulus, and the solid regime exhibiting a finite shear modulus and a degree of long-range order. Subsequent experiments with other techniques (such as multi-terminal resistance measurements [71]) have confirmed the vortex lattice melting (or sublimation) interpretation.

The second peak transition line is a disorder-driven solid-solid transition interpreted as a decoupling line above which the vortex lines decouple into a stack of weakly correlated 2D pancake vortices. Evidence of the second peak has been obtained with local Hall

probe [72] and bulk magnetisation measurements [73], which exhibit an increase in the magnetisation at the peak field followed by decreasing magnetisation. The peak effect is interpreted as vortex decoupling because the 2D pancakes can accommodate better to the pinning landscape than 3D lines, leading to an enhanced hysteresis width at the crossover field. The peak field is almost independent of temperature and is often called the crossover field H_{cr}. This interpretation has been confirmed by μSR studies [74].

Using different oxygen doping levels, Khaykovich *et al* [72] also demonstrated that the melting line shifts in the H-T plane by the same amount as the crossover field. This indicates that the second peak line may well be a continuation of the melting line below a de-pinning temperature T_{dp}, which is the temperature at which the critical point occurs (sometimes known as the multi-critical point).

As discussed previously in chapter 3, surface barriers create an additional source of hysteresis not connected with bulk pinning, and in very clean (i.e. few pinning centers) crystals can lead to a separation of the melting and irreversibility lines. Also, very strong pinning centers introduced by heavy ion irradiation can alter the phase diagram, producing a 3D disordered solid vortex glass in the low field and temperature region [69],[75].

It should be noted that the phase diagram described here has been the subject of much controversy and is by no means definitive. For example, Blasius *et al* [74] suggest a two-stage melting transition, with the vortex solid first melting, and then decoupling, as the temperature is increased.

The phase diagram of $YBa_2Cu_3O_y$ shares several interesting features already seen in BSCCO and its vortex-matter phase diagram has been extensively studied. T. Nishizaki *et al* [76] have reviewed the progressive results of the vortex-matter phase diagram of YBCO resulting in figure 4.3. T. Nishizaki *et al* [76] introduce the characteristic field $H^*(T)$, interpreted as the field-driven disordering transition line between a relatively ordered vortex-lattice (or Bragg-glass) phase at low fields and a highly disordered vortex-glass phase at high fields. The magnetisation shows a steep increase at the characteristic field $H^*(T)$ defined by a sharp peak in the magnetic-field derivative dM/dH. The field at which the second peak occurs, H_p, is plotted in figure 4.3, and lies

above the characteristic field line H^*. Figure 4.3 also includes the two vortex melting lines $T_m(H)$ and $T_g(H)$.

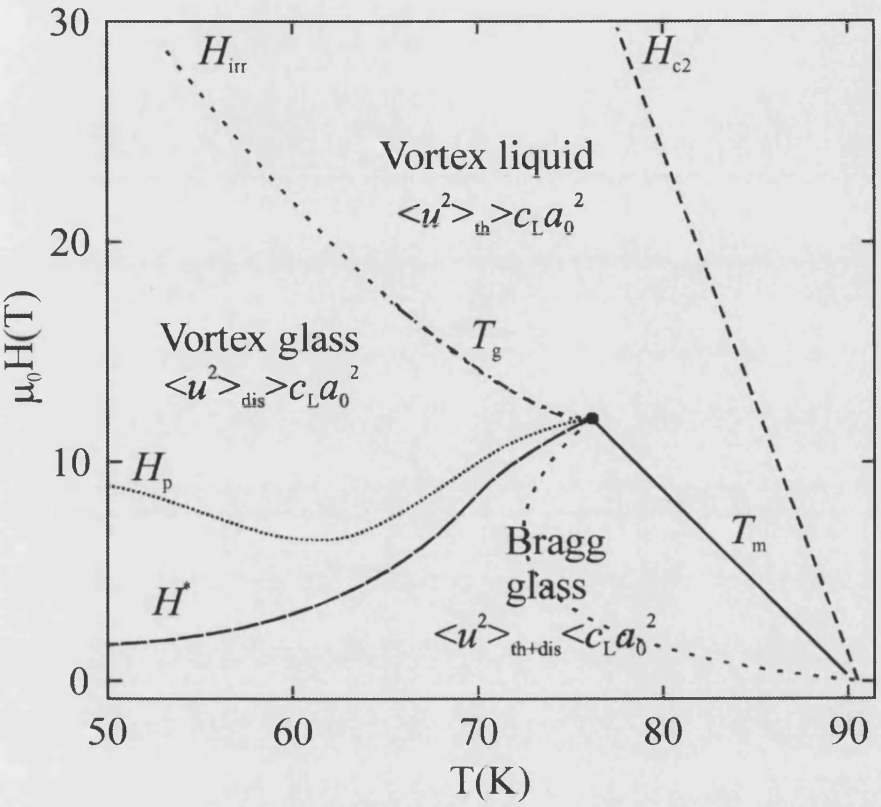

Fig. 4.3 The vortex-matter phase diagram in YBCO, showing the different possible vortex phases within the mixed state.

In figure 4.3 three different vortex-matter phases are seen, the vortex liquid, the vortex glass, and the Bragg glass. The characteristic field $H^*(T)$ divides the vortex-solid phase into two regions, a high-H (low-T) region with strong pinning (vortex glass) and a low-H (high-T) region with weak pining (Bragg glass). Since the Bragg glass is an almost perfect vortex lattice as far as translational order is concerned in spite of a finite pinning force, the Bragg-glass phase melts into the vortex-liquid phase through the first order transition line or melting line $T_m(H)$ similar in origin to the melting line for BSCCO.

Unlike in BSCCO with increasing field, the random pinning induces dislocations and the vortex system undergoes a transition into the disordered vortex-glass phase. The field-driven transition line between the Bragg glass and the vortex glass is connected with both $T_m(H)$ and $T_g(H)$ and the point where they meet in known as the critical point. Above the critical point the melting transition becomes a second-order transition. Since the oxygen vacancies work as randomly distributed point disorder for clean single crystals of YBCCO, vortices in the liquid phase are frozen into the vortex-glass phase with decreasing temperature, T_g.

In the vortex-glass phase above $H^*(T)$, the vortex pinning phenomena are described by the collective pinning theory [77]. In the high-temperature region, however, the vortex-glass phase is reduced and the second peak H_p is pushed up towards higher fields. In BSCCO the dimensional cross over of pancake vortices and the phase transition into a strongly pinned disordered solid have been proposed as possible origins of the second peak. However, the dimensional crossover field is estimated to be ~ 80 T for YBCO which is beyond the characteristic fields H_p and H^* and hence the dimensional crossover mechanism is excluded in this case. Instead the ordered vortex lattice in the Bragg-glass phase becomes unstable due to the generation of dislocations when the mean squared relative displacements $\langle u^2 \rangle$ by thermal and disorder fluctuations become of the order of the lattice spacing a. As in the case of Abrikosov lattice melting, the Lindemann-type criterion $\langle u^2 \rangle \cong c_L^2 a^2$ is applicable to estimate the stability of the different vortex matter phases, where c_L is the Lindemann coefficient. Ertas and Nelson [78] and Kierfeld [79] applied the Lindemann criterion and examined the combined effect of disorder and thermal fluctuations on the vortex lattice, and the Lindemann inequalities for each vortex-matter phase are labelled in figure 4.3.

The irreversibility line $H_{irr}(T)$, as in BSCCO, defines the magnetic field above which the magnetisation is reversible, and above the critical point almost coincides with the vortex-glass transition line. As mentioned above, unlike in BSCCO where the vortex pancakes may decouple, above the irreversibility line YBCO remains a liquid of vortex lines and does not form the pancake gas seen in BSCCO.

4.4. BSCCO Whiskers

Whiskers are long, thin platelet shaped single crystals, which can have very few extended defects, smooth edge-faces and large aspect ratios (typically > 50:1 length:width). In the case of BSCCO whiskers the long side is parallel to the crystallographic *a* axis, the width parallel to the *b* axis and the *c* axis is normal to the thin whisker plane, as shown in figure 4.4.

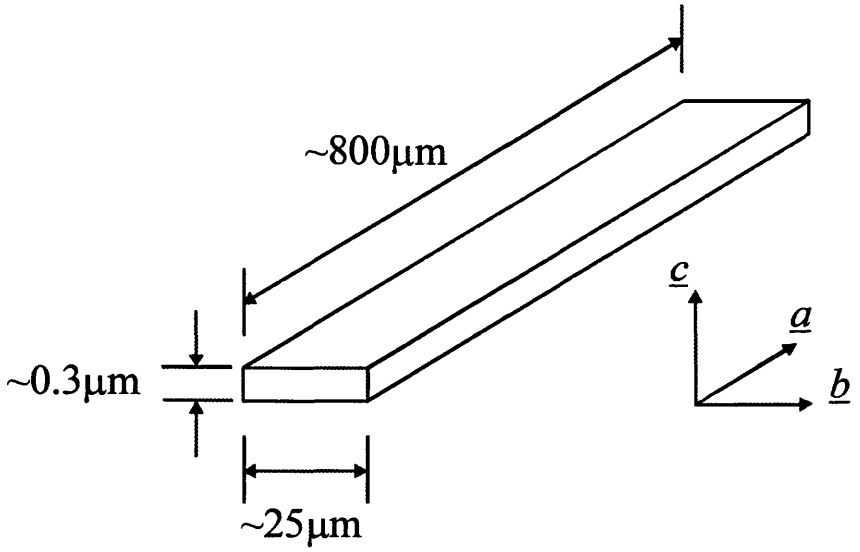

Fig. 4.4 The crystallographic directions of a BSCCO whisker, together with typical dimensions.

The small dimensions and microscopic growth mechanism are what give the whiskers greater crystalline perfection than large, bulk crystals, and make them ideal for investigating the role of surface barriers in their superconducting properties, since they are almost perfect three-dimensional crystals with smooth flat edge faces.

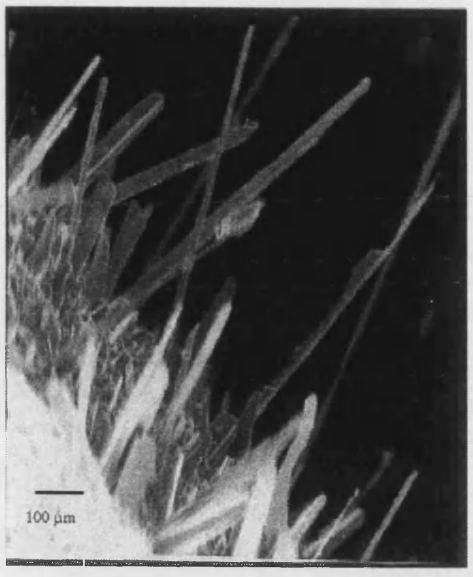

Fig. 4.5 Whiskers growing out from an amorphous growth plate.

A number of individual BSCCO whiskers from the same growth batch have been used to investigate the suppression of surface barriers by irradiation-induced defects, the results of which are presented later in chapter 7 (section 7.1 of this thesis). The samples used in the work presented in this thesis were produced at Bath by annealing a quenched melt of appropriate stoichiometry in flowing oxygen [80]. Figure 4.5 shows many whiskers growing out of a growth plane.

Matsubara *et al* [81] have suggested that the growth of BSCCO whiskers takes place at the base of the whisker, with the growth material provided by a melt at the base of the whisker, and this is known as a self-top-seeding model. Matsubara *et al* [81] used *in-situ* observation of whisker growth to show that whiskers grow from the base. The growth mechanism of BSCCO whiskers is the subject of much debate, however, an investigation of the exact growth mechanism is beyond the scope of this thesis.

The whiskers of BSCCO-2212 phase used in the work contained in this thesis were grown using a melt-quench technique suggested by Matsubara *et al* [81]. The melt-quench technique involves two principle steps: preparation of the glassy growth plates, and growth of the whiskers using appropriate heat treatments.

The growth plates are produced in the following way. First, the powder precursors, which in this case were Bi_2O_3, $SrCO_3$, $CaCO_3$ and CuO, were mixed in the stochiometric ratio (2:1.9:2.2:4). The mixture was then placed in a ball mill and some acetone added to produce a smooth paste, which was then ground for 2 hours. After grinding, the mixture was placed in a fume cupboard to allow the acetone to evaporate, after which the mixture was sieved through a 100μm sieve and placed in an alumina crucible. The mixture was then heated to 1150°C with a temperature ramp of 5°C min^{-1} in a box furnace in an air atmosphere, and held at this temperature for 20 minutes to release the CO_2 and allow the melt to homogenize. Finally, the crucible was removed from the furnace and the liquid poured onto a clean, copper plate and pressed quickly with another plate to form thin amorphous growth plates. It is important to start from an amorphous growth material in order to obtain the correct whisker composition, so the melt-quenched material was checked for crystallinity using X-ray Diffraction (XRD).

Once the growth plates have been made, the second stage is to anneal them in flowing oxygen. For this work, the best results were obtained using a temperature of 860°C and an annealing time of 5 – 7 days. The oxygen flow rate was not found to affect whisker growth. A diagram of the axial furnace used is shown in figure 4.6. Temperature profiles of the furnace showed that near the centre there was a gradient of about 0.6°C cm^{-1}, and the temperature was controlled to within 2°C using a NiCr-NiAl thermocouple and a Eurotherm temperature controller.

At the end of the growth period, the furnace was turned off and the alumina boat quickly removed, to avoid any out-diffusion of oxygen as the furnace cooled, as this would affect the final doping levels (and hence T_c) of the whiskers.

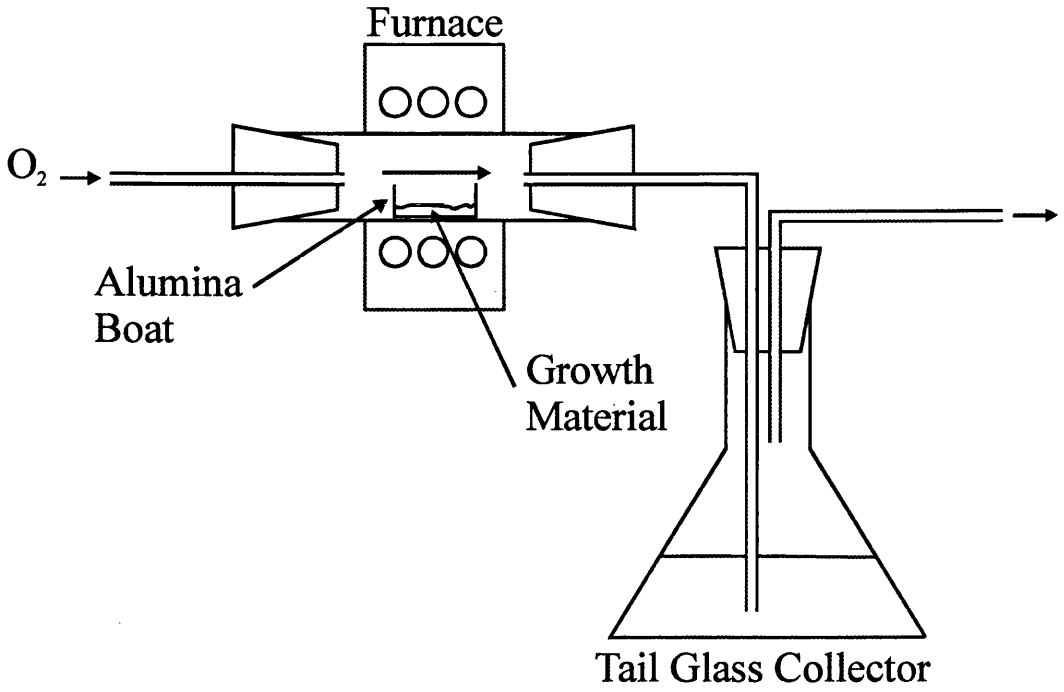

Fig. 4.6 Diagram of the axial furnace used for annealing the growth plates and growing the whiskers.

Chapter 5

5. Hall Probe Design and Fabrication

This chapter gives a brief description of the Hall effect utilized by the sensors described here. Details of the Hall probes used in the work of this thesis are presented and the design and fabrication of the different sensors, and the materials used to fabricate them described. The material properties are explained and the reasons for their use discussed in the context of what makes them good materials for fabricating Hall probes.

5.1. The Hall Effect

In 1879 Edwin Hall discovered that, when a current-carrying conductor is placed in a magnetic field, a voltage is generated in a direction perpendicular to both the current and the magnetic field. This observation, known as the *Hall effect*, arises from the deflection of charge carriers to one side of the conductor as a result of the Lorentz force they experience. It gives information regarding the sign of the charge carriers and their density and also provides a convenient technique for measuring magnetic fields, which we utilize in this thesis.

Consider a conductor in the form of a flat strip carrying a current I in the x direction, as shown in fig 5.1(a), with a uniform magnetic field B applied in the y direction. If the charges are electrons moving in the negative direction with a drift velocity v_d, they experience an upward magnetic force F and are deflected, accumulating at the upper edge leaving an excess positive charge at the lower edge (Fig 5.1(b)). This accumulation of charge at the edges increases until the electrostatic field set up by the charge

separation balances the Lorentz force on the carriers. A sensitive voltmeter or potentiometer connected across the sample as in fig 5.1(b) and (c) can be used to measure the potential difference generated across the conductor, known as the Hall Voltage V_H. If the charge carriers are positive and hence move in the positive x direction as in fig 5.1(c), they experience an upward magnetic force $qv_d \times B$. This force produces a build up of positive charge on the upper edge and leaves an excess of negative charge on the lower edge. Hence, the sign of the Hall voltage generated in the sample is the opposite of the sign of the voltage resulting from the deflection of electrons. The sign of the charge carriers can therefore be determined from a measurement of the polarity of the Hall voltage.

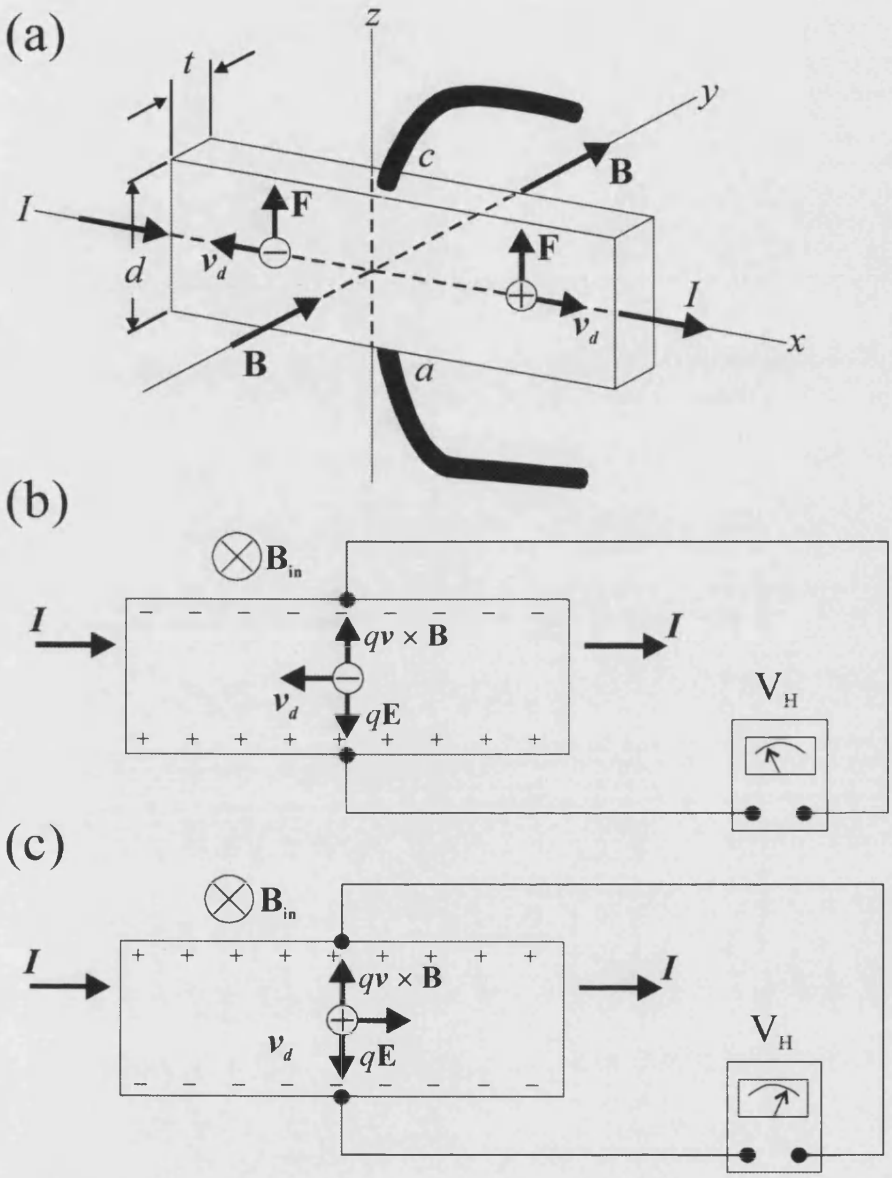

Fig. 5.1 The Hall effect. (a) Hall effect illustrated in a flat strip conductor carrying a current I in the x direction with a uniform magnetic field B applied in the y direction. The Hall voltage is measured between points a and c. (b) Schematic showing that when charge carriers are negative, the upper edge becomes negatively charge, and c is at a lower potential than a. (b) Schematic showing that when charge carriers positive, the upper edge becomes positively charged and c is now at a higher potential than a.

In the equilibrium situation, the electrostatic force qE_H, where E_H is the electric field due to the charge separation (sometimes referred to as the *Hall field*), is directly proportional to the magnetic field, and expressions for the Hall voltage in terms of the material parameters can be derived. In equilibrium, the Lorentz force is equal and opposite to the electrostatic force,

$$-qv_d B = qE_H \tag{5.1}$$

If d is the width of the conductor, the Hall voltage V_H is equal to $E_H d$, or

$$V_H = E_H d = v_d B d \tag{5.2}$$

and the drift velocity can be written in terms of the applied current and the material parameters by

$$v_d = \frac{I}{nqA} \tag{5.3}$$

where A is the cross-sectional area of the conductor and n is the number of charge carriers per unit volume (or charge density). Substituting equation (5.3) into (5.2) we obtain

$$V_H = \frac{IBd}{nqA} \tag{5.4}$$

Since $A=td$, where t is the thickness of the conductor, the Hall voltage can be expressed as

$$V_H = \frac{IB}{nqt} \tag{5.5}$$

The quantity $1/nq$ is referred to as the Hall coefficient R_H. When applied to a 2DEG (two dimensional electron gas, discussed in the next section) the Hall coefficient can simply be written as $R_H = \frac{1}{n_{2d} q}$, where n_{2d} is the two-dimensional carrier density of the 2DEG. This shows that a properly calibrated probe can be used to directly measure the strength of an unknown magnetic field.

5.2. The Two Dimensional Electron Gas

A two-dimensional electron system is formed when electrons are confined to a plane – such as electrons trapped in the potential well formed at the interface of two different types of semiconductors, known as a two dimensional electron gas (2DEG).

Figure 5.2 shows a sketch of the conduction band edge through the 2DEG heterostructure used to fabricate some of the Hall probes used in this thesis. The 2DEG was grown by Molecular Beam Epitaxy (MBE) and is produced at the interface between GaAs and AlGaAs. Since the lattice constants of GaAs and AlGaAs are almost identical, the entire structure can be viewed as a coherent single crystal with modulated conduction- and valence-band edges owing to the much larger bandgap in AlGaAs. The Si-doped AlGaAs is used to provide the carriers, but is separated from the 2DEG by an undoped spacer layer in order to reduce the effect of ionized impurity scattering, which strongly limits the low temperature mobility of bulk doped semiconductors. The electrons from the n AlGaAs diffuse to the GaAs layer where the positive donor impurity charge pulls them towards the AlGaAs/GaAs interface, where they are confined in a very narrow, triangular potential well. Since the width of the well is less than the electron mean free path, the electrons are constrained to move in two dimensions parallel to the plane of the interface.

The 2DEG conductivity is determined principally by the electron mobility, which is reduced by phonon scattering at elevated temperatures (> 100 K) and ionized impurity scattering at low temperatures. To increase the mobility, and hence increase the conductivity, the 2DEG based sensors are used at low temperatures (reducing phonon scattering) with the spacer layer in the heterostructure reducing ionized impurity scattering. Finally the 2DEG electron concentrations (or carrier concentration) in such structures tend to be low, giving rise to a large Hall coefficient and high field sensitivity.

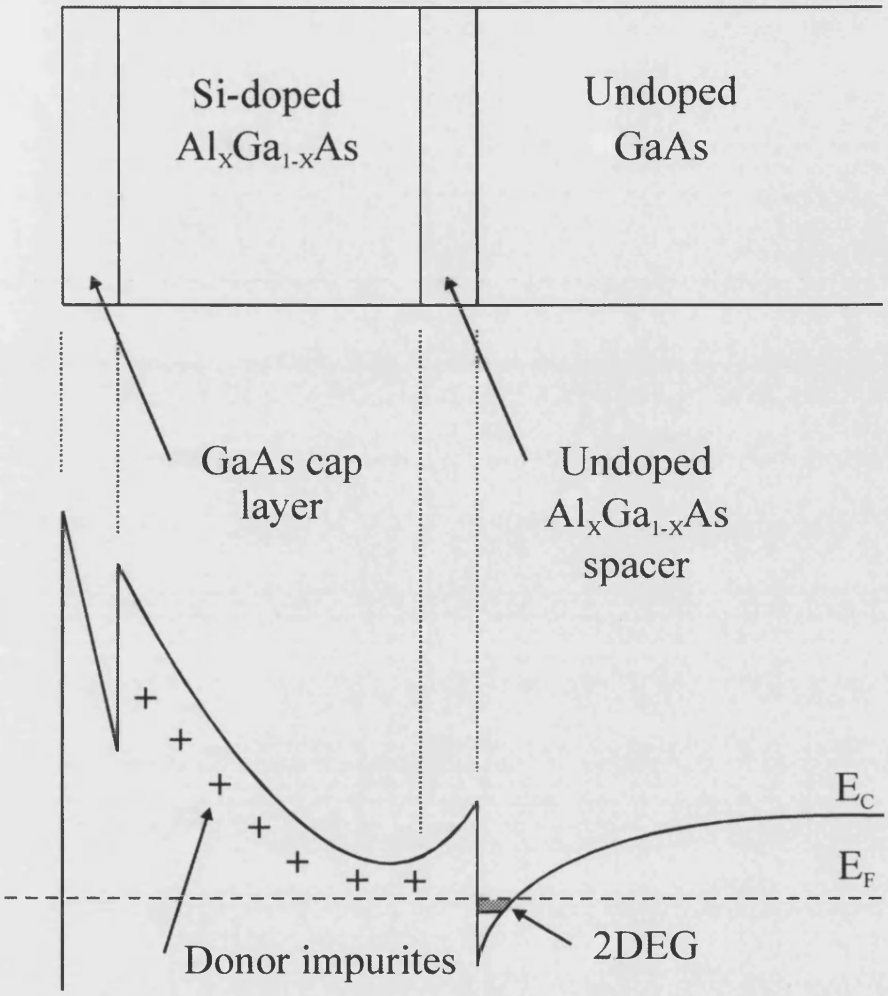

Fig. 5.2 Layer structure of the GaAs/AlGaAs heterostructure (top) used for Hall probe fabrication. Sketch of the corresponding conduction band edge perpendicular to the layers showing the location of the two-dimensional electron gas (bottom).

5.3. Hall Probe Design

Three different Hall probe structures were used in the work described in this thesis. Linear arrays fabricated from a 2DEG heterostructure, scanning Hall probes with integrated tunneling tips, fabricated from the same 2-DEG heterostructure, and scanning Hall probes fabricated from 1-μm-thick *n*-InSb thin films. The 2DEG heterostructure

was chosen to fabricate the linear arrays and scanning Hall probes with integrated tunnelling tips since these were to be used at operating low temperatures. The increased mobility of 2DEGs compared with bulk doped semiconductors at low temperatures results in lower noise figures when used to fabricate Hall sensors for use at low temperature. The linear arrays, based on 2-μm-wide wire widths, were used to investigate the suppression of surface Barriers in BSCCO Whiskers, see section 7.1. The scanning Hall probes, fabricated from the same 2DEG heterostructure as the linear arrays, were used to investigate flux penetration into a superconducting YBCO thin film strip, see section 7.2.

Finally, due to the requirement to optimize minimum detectable fields over a broad range of temperatures up to 300K, combined with the minimum pixel size of 1.25μm, Hall probes were fabricated from 1 μm thick *n*-InSb thin films

(doping level $\cong 2\times10^{16}cm^{-3}$) for use in the system described in chapter 6. Due to the small effective mass of this narrow gap semiconductor, it has an extremely high mobility at high temperatures resulting in much lower noise figures when compared with Hall sensors fabricated from 2DEGs when operated in high temperatures. Hall bars with wire widths of ~1 μm were microfabricated using optical lithography techniques. Figure 5.3 shows the layered nature of the *n*-InSb/GaAs wafer used to manufacture the scanning Hall probes.

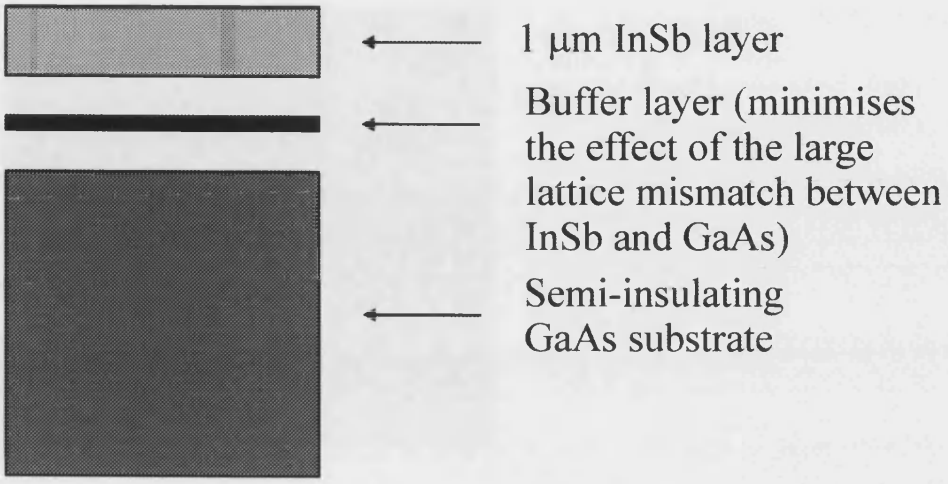

Fig. 5.3 Layer structure of the *n*-InSb/GaAs wafer used to fabricate scanning Hall probes.

5.3.1. Linear Arrays

To allow limited spatial resolution measurements on the BSCCO whiskers, Hall probes were designed as linear arrays, which were lithographically patterned into the heterostructure. Figure 5.4 shows an optical micrograph of a 2μm wire-width array, where the dimension refers to the smallest feature size of the Hall probe. Each fabricated chip contained four serially connected Hall probe elements designed to allow flux profiles across the superconductor to be investigated.

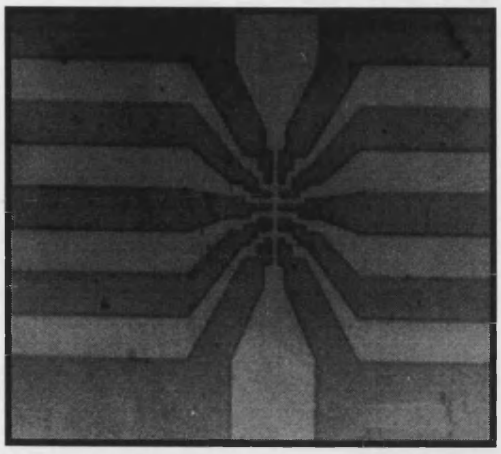

Fig. 5.4 Optical micrograph of a 2μm wire-width linear Hall probe array, where the dimension refers to the smallest feature size of the Hall probe.

5.3.2. Scanning Hall Probes

Both the 2DEG heterostructure and *n*-InSb Hall probes are microfabricated semiconducting devices. The Hall bar is fabricated onto a chip close to one corner and consists of a main current channel and two Hall voltage leads. The details of the scanning Hall probes used to investigate flux penetration into the superconducting YBCO thin film strip are not described here but are readily available [82], and are discussed in section 7.2. An optical micrograph of a ~1μm resolution InSb Hall sensor is shown in Fig. 5.5. Bias dc currents of ~ 4μA-1mA are supplied with a precision current source and the Hall voltage is measured with an AD625 low noise instrumentation amplifier [83]. Fig. 5.6 shows a schematic of the SHPM including the electronics required for the system.

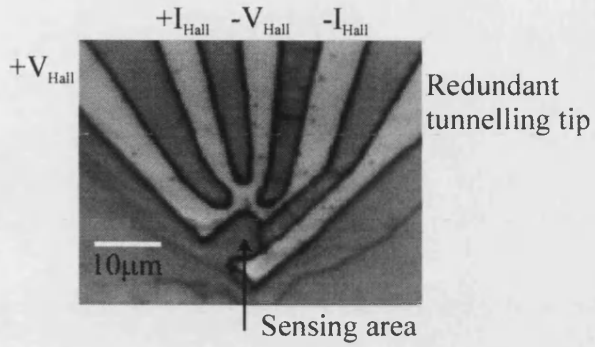

Fig. 5.5 Optical micrograph of a 1 μm resolution InSb Hall sensor.

The InSb Hall probes typically have Hall coefficients of 0.03Ω/G at 300 K. The Hall coefficient is temperature dependent. However, sufficiently high operating currents were used to induce self-heating of the Hall probes to keep their temperature close to 290 K. The dominant noise component up to a certain bias current level I_{max} (>300μA), when 1/f noise abruptly increases, is found to be the Johnson noise, $V_n = \sqrt{4k_B T R_S \Delta f}$, of the Hall bar where R_S and Δf are the resistance of Hall probe voltage leads and measurement bandwidth respectively. Therefore, for $I_{Hall}<I_{max}$, the maximum signal to noise ratio (SNR) of the Hall probe is approximately given by

$$SNR = \frac{I_{Hall} R_H B}{\sqrt{4k_B T R_s \Delta f}} \frac{1}{t}, \tag{5.6}$$

where I_{Hall}, B, R_H are the bias current, magnetic field, and Hall coefficient, respectively. Operating currents up to 300μA can be employed, without significantly increasing the output noise and typical voltage lead resistances are ~3kΩ at 300K. The minimum detectable field of the Hall probes is measured to be ~0.08 μT/√Hz at 300K.

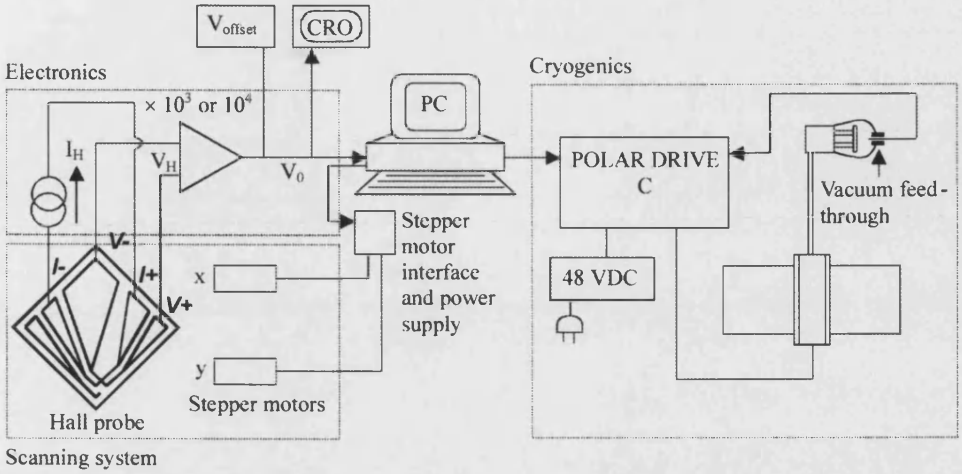

Fig. 5.6 Schematic diagram of the SHPM showing the electronics required to drive the system.

5.4. Hall Probe Fabrication

The Hall sensor arrays were fabricated from epitaxially grown wafers of GaAs/AlGaAs 2DEG heterostructure, using conventional optical lithography and chemical wet etching techniques, described below.

- The wafer was scribed, and then cleaved into chips 5mm × 5mm
- Cleaning

  The chips were placed in beakers of (i) 1-1-1 trichloroethene, (ii) hot acetone and (iii) isopropanol, and cleaned in an ultrasonic bath for 5 minutes in each solvent. They were then dried using a nitrogen jet.
- Each chip was glued to a cover slip with photoresist and then baked at 95°C for 30 minutes, to enable easy handling.
- Photolithography

  Shipley Microposit 1813 positive photoresist was spun onto each chip at a speed of 4000 rpm for 25 seconds, to produce a layer approximately 1.3μm

thick, which was baked for 25 minutes at 95°C. The chips were then exposed to ultraviolet radiation through a chrome mask, to define the Ohmic contacts, and the photoresist developed in Microposit 351 developer for approximately 6 seconds to remove the unwanted areas. Any remaining developer was removed by washing the chips in distilled water.

- Ohmic contacts

  Each chip was dipped in a solution of 1:1 $HCl:H_2O$ and then washed in distilled water, to remove any surface oxide. The chips were then immediately placed into a thermal evaporator and heated to 80°C under high vacuum (~ 4×10^{-6} mbar). Before deposition, the chips were cleaned using an Ar glow discharge for 10 minutes. To make electrical contact to the 2-DEG, 66nm of Ge and then 134nm of Au were deposited, which produce a good Ohmic contact to the 2-DEG when properly annealed (see below). Finally, 20nm of Ti and 200nm of Au were deposited, to produce a contact area suitable for ultrasonic bonding. After removal from the evaporator, the chips were placed in acetone and gently agitated to "lift-off" the unwanted metal regions, leaving just the defined contact pads. This lift-off procedure could be improved if the chips were soaked in chlorobenzene for 12 minutes and then left to dry for 2 hours before developing, which produces an overhang in the photoresist.

- Annealing

  After being cleaned, each chip was placed in a flash annealer and the contacts annealed in a N_2/5% H_2 reducing atmosphere at 430°C for 2 minutes. This produces an n^+ region below the pads which makes a low resistance Ohmic contact to the 2-DEG.

- Etching

  After cleaning and re-mounting the chips, photoresist was spun on at 4000 rpm for 4 second, 6000 rpm for 12 seconds and then baked. The higher spin speed was used to reduce the effects of edge beading (build-up of photoresist

at the edges of the chip) which could cause problems during exposure because of the small dimensions of the Hall bar mask. After the Hall probe array had been exposed and developed, the chips were again baked to reduce damage to the photoresist during etching. To remove any surface oxide the chips were dipped in 1:1 $HCl:H_2O$ and then washed and dried, immediately before etching. They were then etched in a solution of distilled water, 30% H_2O_2 and concentrated H_2SO_4 in the ratio 160:8:1, which produced an etch rate of ~0.2μm min^{-1}. An etch time of 15 seconds was sufficient to deplete the 2-DEG in the unwanted areas. After etching, the chips were washed in distilled water and the remaining resist removed with acetone.

The scanning Hall probes used in the system described in this chapter were fabricated from 1-μm-thick *n*-InSb thin films (doping level $\cong 2\times10^{16}cm^{-3}$), using the same conventional optical lithography and chemical wet etching techniques, described for the Hall sensor arrays. Below is a description of fabrication steps for the scanning Hall probes, with the reader referred back to the Hall sensor array fabrication notes where identical steps are performed.

- The wafer was scribed, and then cleaved into chips 6mm × 6mm
- Cleaning

  (See Hall sensor array notes)
- Each chip was glued to a cover slip with photoresist and then baked at 95°C for 30 minutes, to enable easy handling.
- Photolithography

  As for Hall sensor arrays except; Shipley Microposit 1813 spun at 4000 rpm for 30 seconds, to produce a layer approximately 1.5μm thick. Chips exposed to ultraviolet radiation through a chrome mask (containing Ohmic contacts for four hall sensors) for 10 seconds. Before developing the chips were soaked in chlorobenzene for 12 minutes and then left to dry for 2 hours before developing to produce an overhang in the photoresist. The photoresist

was then developed for approximately 16 seconds to remove the unwanted areas.

- Ohmic contacts

  As for Hall sensor arrays except; To make electrical contact to the InSb, 20nm of Cr and then 209nm of Au were deposited producing a good Ohmic contact to the InSb (no need for annealing), and a contact area suitable for ultrasonic bonding.

- Etching

  As for Hall sensor arrays except; photoresist spun at 5000 rpm for 30 seconds. Any edge beads were removed using q-tips dipped in acetone. The four Hall probes sensing areas were exposed for 5 seconds and developed for 15 seconds. Samples etched in a flowing solution of H_2O:H_2SO_4:H_2O_2 (320:20:20), mixed in the order shown and left to cool for 30 minutes. Etch times of 50-60 seconds, with the sample perpendicular to the direction of flow, were sufficient to remove the 1μm n-InSb layer in the unwanted areas. After etching, flakes of material were found to remain in the channels between the conducting leads. If left, this material allowed current to flow between the channels of the Hall probe without passing through the active region. To remove this material the probes were washed in distilled water and then placed in beakers of acetone in an ultrasonic bath for 15minutes or until all the material was removed. A further ~1μm deep-etch into the GaAs substrate was then carried out between the four Hall probes on each chip to facilitate cleaving.

Once the chips containing the Hall probe arrays had been fabricated they were scribed with a diamond tipped tool and cleaved into individual sensors. It was necessary to mount them onto chip carriers in order to use them to take measurements. The sensors were glued onto custom-made aluminium oxide chip carriers using an Oxford low temperature epoxy, which was cured at 100°C for 20 minutes. An ultrasonic bonder was used to make electrical connections to the sensors, employing 12.5μm diameter gold

wire. This technique uses a pulse of ultrasonic energy to join the wire to the contact pads. To connect the chip carriers to their respective experimental apparatus, enamelled copper connecting wires were soldered to the chip carrier using Indium solder. Indium is preferred over the conventional Pb-Sn solder because of its reliability at low temperatures. Also, it has a superconducting transition temperature of 3.4K, which is below the lowest working temperature of the systems used in this thesis. Figure 5.7(a) and (b) show a fully bonded and mounted Hall sensor array and scanning Hall probe respectively.

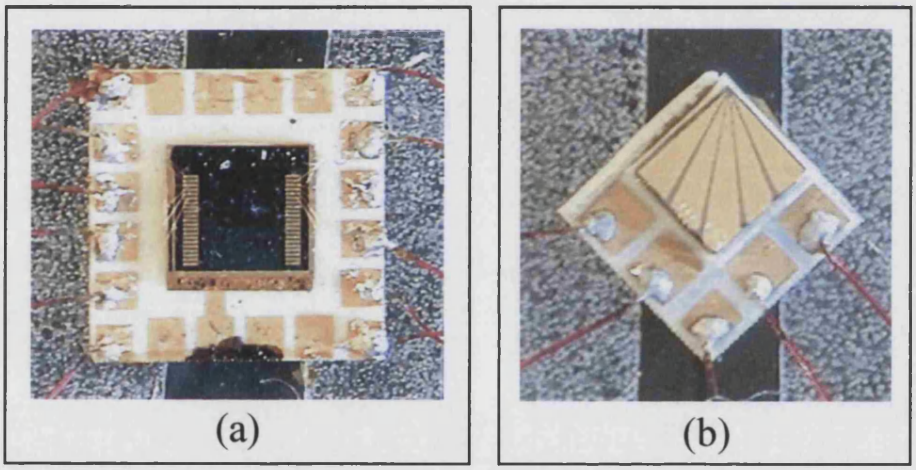

Fig. 5.7 (a) and (b) Optical micrographs of a fully bonded and mounted Hall sensor array and scanning Hall probe respectively.

Chapter 6

6. A Scanning Hall Probe Microscope for Large Area Magnetic Imaging Down to Cryogenic Temperatures

In this chapter the design and construction of the large area SHPM used to collect the majority of the results presented in this thesis is described, along with brief descriptions of any existing techniques and equipment used. The system was custom-built on site in Bath with a large proportion of the work carried out by the author. The main constituent parts of the system are described in detail and a brief evaluation of the systems performance and capabilities at both room and low temperature operation are given at the end of the chapter. Coupled with the current Hall probe magnetic imaging techniques developed in Bath the system enables a unique range spanning the length scales 0.1μm-25mm to be investigated, allowing detailed comparisons between theories and experiments of the local magnetic induction of various magnetic materials, some of which are presented later in this thesis.

6.1. Introduction

Various techniques have been developed to investigate the local magnetic induction of magnetic materials, including scanning Hall probe [82], scanning SQUID [84], and magnetic force (MFM) microscopy [85],[86], Bitter decoration [23], Faraday rotation [87] and magneto-optical Kerr effect imaging [88] and electron holography [89]. Recently, scanning Hall probe microscopy (SHPM) [90],[91],[92],[93],[94], has been

shown to be a very sensitive, non-invasive technique for obtaining quantitative measurements of surface magnetic field profiles with high spatial resolution (<1μm) under variable temperature and magnetic field operation. In one common type of SHPM, a Hall probe with an integrated STM tip mounted on a piezo electric scanner tube is approached towards a sample until a fixed tunnel current is established. The Hall probe is then scanned across the surface to measure the magnetic field and the surface topography simultaneously. This scheme has been very successfully used to study the domain structure of magnetic films and vortices in superconductors with magnetic field sensitivity of ~2.9×10^{-8} T/√Hz at 77K and spatial resolution of ~0.85μm [82]. However such systems are limited to rather small scan areas (≤100μm) on conducting samples. We report here on a novel design for a scanning Hall probe microscope (SHPM) that combines an extremely simple mechanical arrangement with a micron-sized Hall probe coupled to a closed-cycle refrigerator sample stage. This design has several advantages over previous work: First, the mechanical scanning mechanism is extremely simple, allowing high-resolution scans with very large scan areas of conducting and non-conducting samples while still providing good linearity and repeatability. Second, the use of *in-situ* optical alignment techniques for sensor to sample separation combined with closed-cycle refrigeration drastically reduce the time-consuming procedures of loading and switching of samples associated with existing SHPMs. Finally, the cantilever and z-stage design allow constant height scans without a height feedback mechanism, whilst providing *in-situ* adjustment of sensor tilt with respect to the sample plane, and reduce the risk of damage to the sensor and sample in the event of impact. In this chapter we discuss the performance of the system and illustrate its capabilities with images of magnetic materials at 295K and 40K.

6.2. System Concept and Design

6.2.1. Targeted System Capabilities

A SHPM is a near-field magnetic induction imaging system. A Hall probe is raster scanned over the surface of a sample while recording the Hall voltage as a function of the x-y position of the sensor relative to the sample. To achieve maximum spatial

resolution, the Hall probe must be brought as close as possible to the sample. Since most existing SHPMs are piezo tube or piezo bender driven systems their scan areas are limited to ≤ 100μm × 100μm and the successful positioning and alignment of sensor and sample requires great skill. In addition the use of liquid cryogens such as liquid nitrogen and helium to provide cooling often results in significant increases in system size, upkeep costs and sample loading and exchange times. Increased scan areas up to tens of millimetres, closed-cycle refrigeration and ease of alignment while still minimizing sensor-sample separation were the critical design elements of the SHPM presented here. Applications of SHPMs include observations of microscopic magnetic structures in various materials, such as magnetic domains in ferromagnetic materials, quantized flux vortices in type II superconductors and the non-destructive evaluation (NDE) of electronic materials. These applications require variable temperature operation, accurate temperature control (from some tens of Kelvin up to room temperature), high spatial resolution (~1μm), high magnetic field resolution, a controlled sample environment and good optical access to aid sensor-sample alignment. From a user's stand point one also desires a compact, easily assembled system, which requires little or no maintenance and is easy to use. These goals have been achieved by satisfying a number of different design constraints, which are discussed in following sections.

6.2.2. Cryogenic Refrigeration

To achieve a compact, low-maintenance system a closed-cycle refrigerator was chosen to cool the sample instead of liquid cryogens. One of the main potential disadvantages for such refrigerators is the possibility of introducing excess noise into the measurement process via mechanical vibrations or the movement of magnetic components such as pistons. These problems were minimised by using a low-noise Leybold Vakuum GmbH POLAR SC-7 COM Stirling cycle refrigerator. In this refrigerator, all the major moving mechanical components are in the compressor, and the only mechanical link to the cold head is through a 30cm long high-pressure copper gas line. To prevent the transmission of vibrations from the compressor to the cold head the compressor is mounted on an anti-vibration stage isolating it from the main system platform. The physical separation

between the compressor and cold head also significantly reduces the possibility of stray magnetic fields arising at the sensor from the moving parts in the compressor, illustrated in Fig. 6.1. To ensure that the base operation temperature of 35K was achieved, a vacuum of better than 1×10^{-4}mbar was maintained around the cold head minimising thermal conduction between the vacuum walls and the cold head. To limit heating from 300K thermal radiation entering via the optical alignment window, foil radiation shielding was employed to cover the window on completion of sensor alignment.

The main advantages of the POLAR SC-7 COM cooler are its compact size, short cool-down time and low maintenance requirements compared to a liquid cryogen system. This allows samples to be cooled to constant temperatures in the range of 35 to 295K (accurate to ± 0.5K) in times of <10mins. According to the manufacturer, the cooler is engineered for more than three years of maintenance-free, continuous-duty operation.

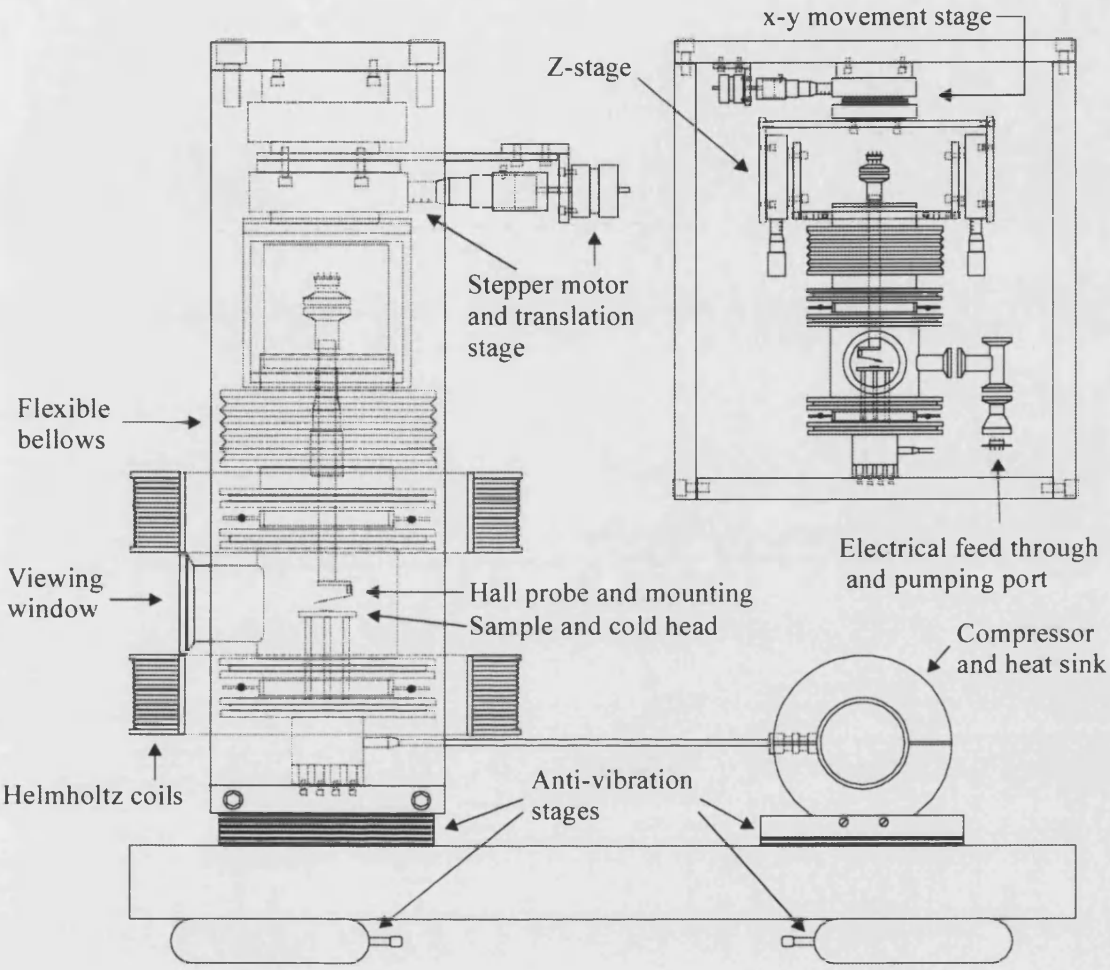

Fig. 6.1 Sketch of the overall microscope system from the side. The inset shows a detailed face on view of the custom x-y-z scanning stage, vacuum link and sample chamber.

To facilitate the use of external stepping motor positioning stages for sensor translation a custom vacuum housing utilising a flexible stainless steal bellows vacuum link was fabricated. The Hall sensor is mounted on a flexible phosphor bronze cantilever at the end of a long, thin walled stainless tube. The cantilever, with its low force constant, is used to reduce the risk of damage to the sensor and sample in the event of impact whilst

having a sufficiently high resonant frequency to reduce the transmission of vibrations to the sensor from the surrounding environment. The tube passes through the bellows and a vacuum seal, where it is brazed to the top of the bellows. The latter are in turn attached to a custom three-axis translation stage (see inset on Fig. 6.1.). The translation stage utilises four micrometer stages positioned orthogonal to one another to provide the three-axes of movement. The longitudinal position of the sensor is adjusted via two mechanically linked micrometer stages, which also provides tilt adjustment of the sensor with respect to the sample plane. Movement in the sample plane is achieved by bolting the longitudinal micrometer stage below the two remaining micrometer stages fixed one on top of the other and rotated through 90 degrees, providing motion in the x and y axes parallel to the sample plane. The inset of Fig. 6.1. also shows the ISO 63 connector with two lateral flanges used as the sample chamber for the SHPM. The addition of a T-piece to the NW16 flange provides the pumping port and electrical feed-through for the system. Optical access to allow accurate alignment of the sensor using a microscope is achieved via a viewing window attached to the NW40 flange. Detaching the bellows from the sample chamber and removing the translation stage and bellows as one unit enables sample turn around times of less than an hour.

6.2.3. The Scanning System

To raster scan the sensor above the sample a pair of stepper motors are connected to the micrometers of two coupled 25mm × 25mm stages. The bulk of the stage is constructed from nonmagnetic aluminium, with some magnetic components, including springs, bearings and the micrometers. Samples are typically scanned at about 1 pixel/s with maximum available scan sizes of 5mm × 5mm at 35K, determined by the retarding force of the vacuum on the bellows, up to 25mm × 25mm at 300K in atmospheric pressure. Scan times are dependent on the number of pixels contained in a scan. With a minimum 1.25μm × 1.25μm pixel size (given by the minimum half step mode of stepper motors), a typical 60μm × 60μm high-resolution scan takes approximately 90 minutes.

The samples are mounted directly on the cold head of the POLAR SC-7 COM Stirling cooler and the two manual z-stages used to optimise the position of the sensor above the

sample to within ~ 1μm, monitored with a binocular microscope via the optical alignment window. The combined cold head and scanning system are mounted on a separate anti-vibration stage from the compressor and fixed to the main system platform. The sensor and cold head are further protected from vibrations in the surrounding environment by mounting the entire system platform on its own anti-vibration stage. A Helmholtz coil pair is placed around the sample chamber allowing the study of samples in magnetic fields of up to 0.06T.

A personal computer is used to control the scanning process and record the measured Hall voltage using a program written in Visual Basic™. This is achieved through the use of a Keithley DAS-801 Data Acquisition card in the PC. The system uses four digital output lines to send control pulses to the stepping motor interface cards (2-bits per motor). Additionally, one of the analogue input lines on the card is used to record the probe output voltage. The card uses a 12-bit analogue-to-digital converter (ADC) with an accuracy of ± 1 least significant bit (LSB). The software operates the card on a bipolar (±5V) range corresponding to an overall data acquisition accuracy of ± 0.5mV, with a maximum conversion frequency of 40kHz. Upon completion of a scan, information is saved as separate forward and reverse data files each containing all relevant scanning parameters. A custom data-analysis program is then used to perform image processing.

6.3. System Operation and Performance

Samples are mounted onto the cold head of the refrigerator using GE varnish to provide good thermal contact. With the translation stage and bellows in place the system is then evacuated using a turbo pumping station to a pressure of $< 1 \times 10^{-4}$ mbar (this requires approximately 1 hour). If sample cooling is required the refrigerator can then be switched on and the desired temperature reached in typically less than 10mins. Once the refrigerator has stabilized at the target temperature the sensor is aligned above the sample and a magnetic field applied to the sample if required. The bias current is then adjusted and an offset voltage is compensated in the Hall voltage amplifier to prevent saturation in the final gain stage before commencing a scan. With the system under

vacuum a maximum x-y scan area of 5mm × 5mm is possible before the stepping-motors can no longer overcome the retarding force imposed on the bellows by the vacuum. For room-temperature operation evacuation of the system is unnecessary increasing the maximum x-y scan area to the full 25mm × 25mm of available movement in the translation stages. It should also be noted here that the work presented in this chapter was recorded solely using probes fabricated from 1-μm-thick *n*-InSb thin films.

6.3.1. Room Temperature Operation

6.3.1.1. (300K) Images of magnetic Media

To illustrate the ability of the system to image ferromagnetic materials at room temperature we examined the magnetic encoding along the stripe of a bankcard and sections taken from formatted 5.25 inch and 3.5 inch floppy disks in zero applied field. Gray-scale images and line scans of individual bits along the magnetic stripe are shown in Fig 6.2(a) and (b). Figure 6.2(a) shows a 1200μm × 20μm gray-scale image of the magnetic field from the stripe, taken with a pixel size of 10μm × 10μm. The graph of Figure 6.2(a) illustrates the stray field along the stripe. Figure 6.2(b) shows an extended 2000μm × 100μm gray-scale image of the magnetic field from the stripe, taken with a pixel size of 10μm × 10μm. The graph of Figure 6.2(b) illustrates the field transitions from positive to negative along the stripe which translate into positive and negative voltage pulses when the stripe is read.

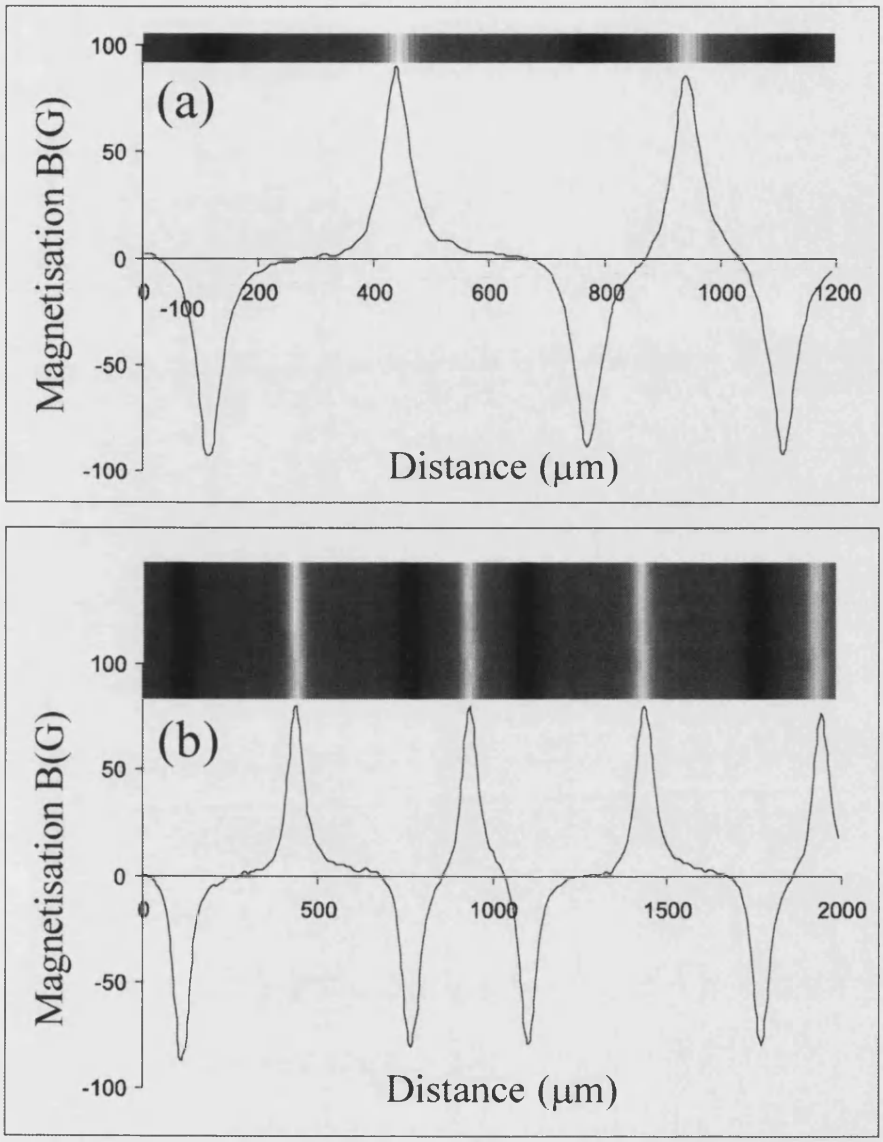

Fig. 6.2 Images of the local magnetic induction along the surface of a bankcard taken at 300 K. (a) Scan area 1200μm × 20μm, pixel size of 10μm × 10μm. The graph of (a) illustrates the stray field along the stripe. (b) Extended 2000μm × 100μm scan area, pixel size of 10μm × 10μm. The graph of (b) illustrates the field transitions from positive to negative along the length of the magnetic stripe.

Fig. 6.3(a). shows a 100 μm × 437.5 μm grey-scale image of the magnetic field from the 5.25 inch sample, taken with a pixel size of 2.5μm × 2.5μm. The scan shows a data track with individual data bits written at a slight angle inside the track. A single data bit was resolved using maximum 1.25μm resolution and is shown in Fig. 6.3(b). The line scan in Fig. 6.3(c). illustrates the stray field along the bit track in the direction of the arrow shown.

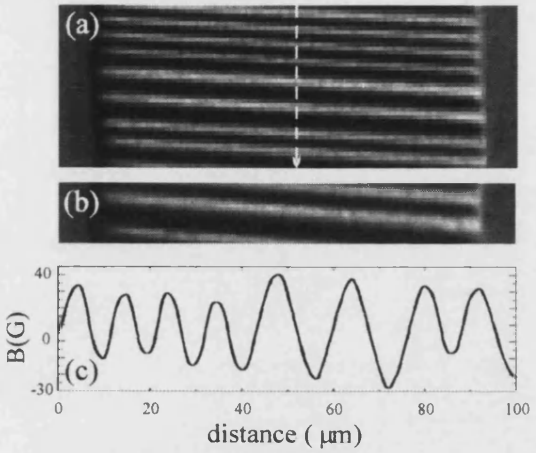

Fig. 6.3 (a) Image of the local magnetic induction of the surface of a 5.25 inch disk sample. Scans taken at 300K with a scan area of 100 μm × 437.5 μm and step size of 2.5 μm, grey scale spans 70G (b) Single data bit resolved using resolution of 1.25 μm and a scan area of 25 μm × 437.5 μm, grey scale spans 60G (c) Line scan along dotted line shown in image (a) illustrating the stray fields along the bit track.

Fig. 6.4(a). shows a similar 37.5 μm × 187.5 μm grey-scale image of the magnetic field from the 3.5 inch disk taken at maximum 1.25μm resolution consistent with images seen in similar studies [93]. The scan shows the difference in bit length on the two disks, with the 3.5 inch disk having a bit length of more than a factor of two smaller than the 5.25 inch disk. Fig. 6.4(b). and (c) also illustrates the difference in the way the data is written. There appears to be little detectable gradient across an image indicating that the sensor height is remaining constant throughout a scan. The linearity, repeatability and reliability

of the scanning system are also confirmed with little difference between separate scans of the same area and no detectable difference between forward and reverse images of individual scans indicating little or no thermal or mechanical drift of the sample during measurements.

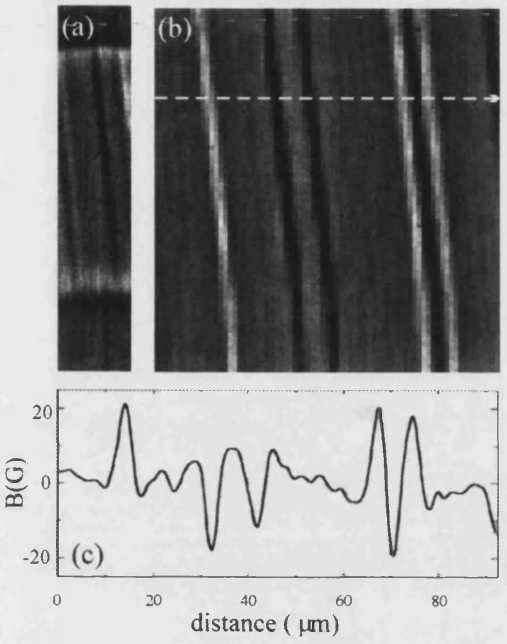

Fig. 6.4 (a) Image of the local magnetic induction at the surface of a 3.5 inch disk sample. Scan taken at 300K with a scan area of 37.5 μm × 187.5 μm and step size of 1.25 μm, grey scale spans 40G (b) 93.75 μm × 100 μm scan of data bits within data track taken with a step size of 1.25 μm, grey scale spans 40G (c) Line scan along dotted line shown in image (b) illustrating the stray field along the bit track.

6.3.1.2. (300K) Non-invasive Current Detection

One promising application for the SHPM is the non-destructive evaluation (NDE) of microelectronic devices, such as flip-chip packages and multichip modules (MCMs). The currents flowing in a microelectronic device produce magnetic fields, which the SHPM could potentially detect. In particular, since magnetic fields at low frequencies pass unimpeded through metal and insulating layers, the SHPM is ideally suited for locating faults buried up to 1 μm below the surface of microelectronic devices.

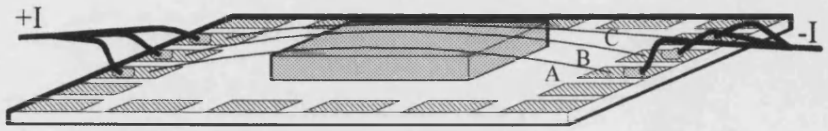

Fig. 6.5 Layout of gold wires used to test the non-destructive evaluation (NDE) capabilities of the large area SHPM.

To test the NDE capabilities of the system, we applied various dc currents through three gold wires stretched over a block of insulating aluminium oxide. Figure 6.5 shows the layout of the wires, with the centre wire B slightly higher than the others. The diameter of the wires was 12.5μm with a spacing of ~250μm. Figure 6.6 shows a 950μm × 37.5μm gray-scale image of the magnetic field from the wires with an applied dc current of ~33mA in each wire, taken with a pixel size of 2.5μm × 2.5μm. The graph of Figure 6.6 illustrates the stray magnetic field along the direction indicated.

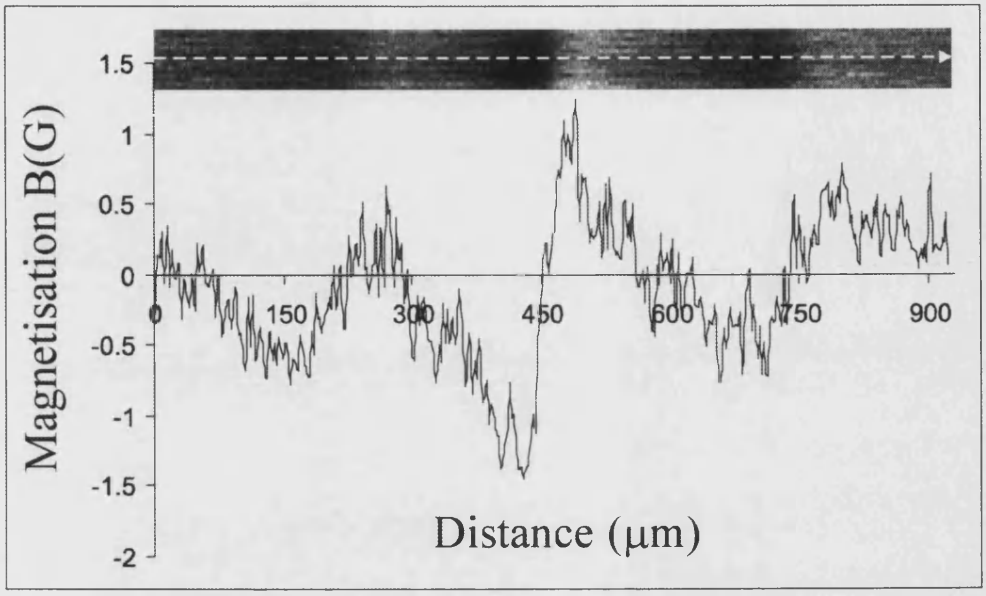

Fig. 6.6 A 950μm × 37.5μm image of the local magnetic field from the three gold wires with an applied dc current of ~33mA in each wire, taken with a pixel size of 2.5μm × 2.5μm. The graph illustrates the stray magnetic field along the direction indicated.

In order to extract the sensor-to-sample separation the stray field from the wires was calculated using Biot-Savart's Law allowing the different heights of each wire to be accounted for, the details of which can be found in Appendix A. Figures 6.7(a) to (d) show 950μm linescans across the wires with applied dc currents in each wire of 50mA, 33mA, 16mA and 10mA respectively, taken with a step size of 1.25μm. In each graph the crosses are the data, and the line is the fit. The fits yield a value of sensor-to-sample separation of ~60μm for wire A, ~15μm for the central wire B, and ~40μm for wire C.

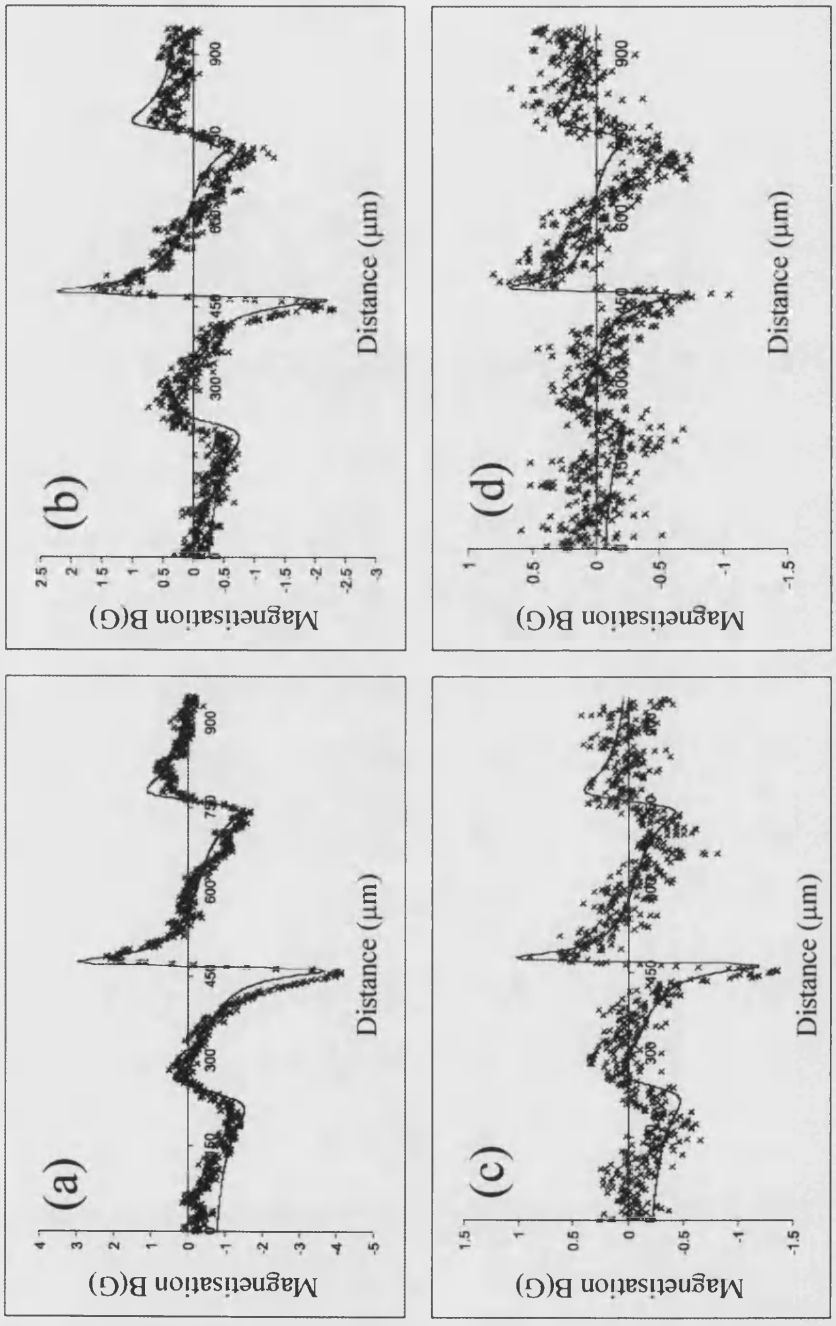

Fig. 6.7(a)-(d) 950μm line scans across the wires with applied dc currents in each wire of (a) 50mA, (b) 33mA, (c) 16mA, and (d) 10mA, taken with a step size of 1.25μm. In each graph the crosses are the experimental data points, and the solid black line is the fit of the stray field from the wires calculated using Biot-Savart's Law.

Figure 6.8 shows a line scan across the wires at the point where they come into contact with the edge of the aluminium block that they are stretched over. At this point all the wires should be at the same height. This is confirmed by the difference of appearance of the scan in comparison with those of figure 6.7, and the quality of the fit to the data with all three wires sensor-to-sample separation set at 25μm.

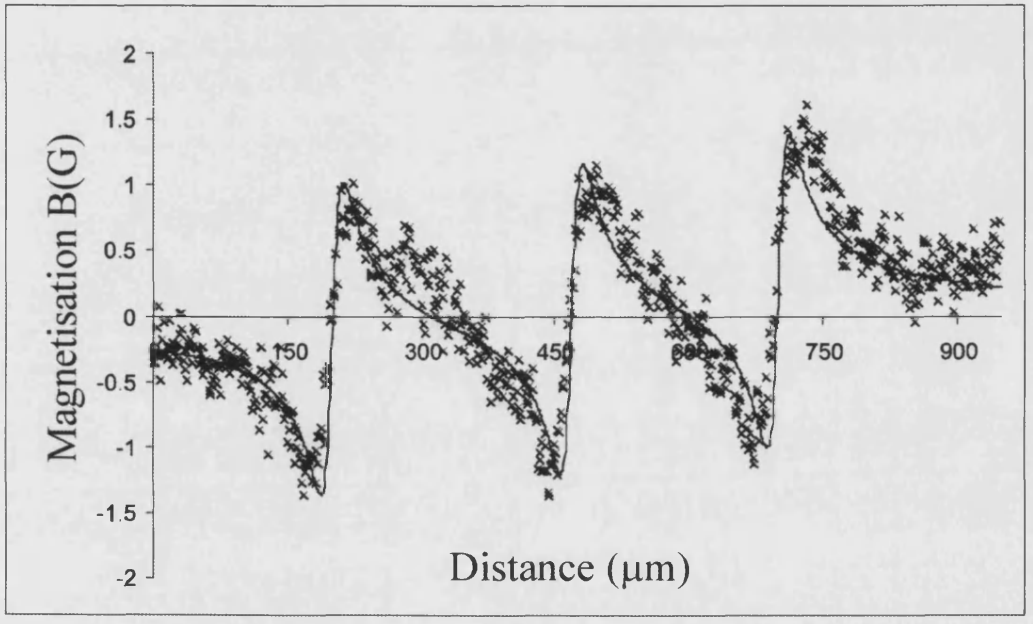

Fig. 6.8 A 950μm line scan across the wires at the point where they come into contact with the edge of the aluminium block that they are stretched over, step size 1.25 μm. The crosses are the experimental data points, and the solid black line is the fit of the stray field from the wires calculated using Biot-Savart's Law with all three wires sensor-to-sample separation set at 25μm.

To further evaluate the NDE capabilities of the system a meander-patterned metal wire was fabricated to produce well defined stray magnetic fields. The 100nm thick gold wire was fabricated by optical lithography and lift off techniques. The meander line is based on repeated 2-mm-long segments of 40μm-wide wires with 20μm spacings. To induce periodic magnetic fields perpendicular to the wire, dc currents of –10 to 10mA were applied through the patterned film. Scans were taken with the longitudinal direction perpendicular to the wire direction in order to detect the field effectively. An optical micrograph of the meander line is shown in figure 6.9, with the direction in which scans where taken indicated.

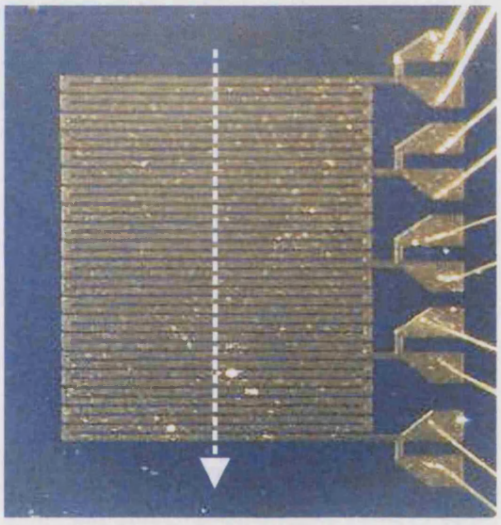

Fig. 6.9 Optical micrograph of the meander line, the dotted white line indicates the direction in which scans where taken of the meander line.

Figure 6.10(a) to (e) show 375μm × 1.25μm gray-scale images and line scans across the meanderline with applied currents of ~10mA, 8mA, 6mA, 4mA and 2mA respectively. Each data set is formed from two scans taken of the same area with the same magnitude of dc current but with different signs. The average of the positive current scan and the inversed negative current scan are then taken to form the final data set. This was found to reduce the effect of noise masking the features of the scans. The stray field of the

meander line was calculated using Biot-Savart's Law, the details of which can be found in appendix A. The calculated stray field using the shape of the wire is shown in figures 6.10(a) to (e) as the solid lines. The fits yield values of sensor-to-sample separation of ~17μm for scans (a)-(c), 10μm for scan (d), and 4μm for scan (e). The performance of the system is drastically reduced at low currents due to the reduction in stray field from the meander line, corresponding to a minimum detectable field of ~ 1 Gauss. However, this is comparable with recently published studies utilizing a magnetoresistive sensor cantilever [95].

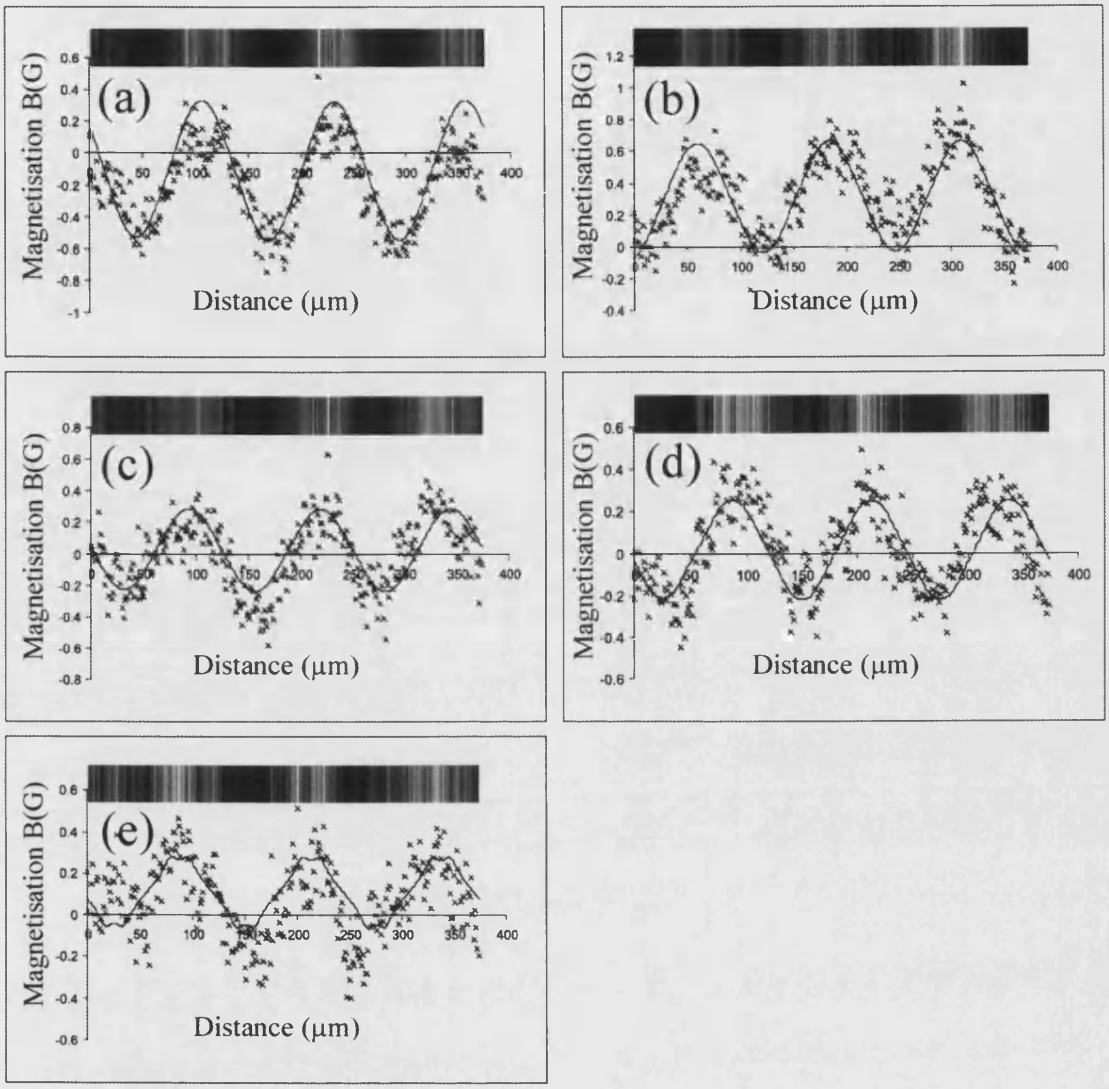

Fig. 6.10(a)-(e) 375μm line scans across the meanderline with applied dc currents of (a) 10mA, (b) 8mA, (c) 6mA, (d) 4mA, and (e) 2mA, taken with a step size of 1.25 μm. The crosses are the experimental data points and the calculated stray field is shown as the solid black lines.

6.3.2. Low Temperature Operation

6.3.2.1. (40K) Images of a Superconducting Quantum Interference Device

Figure 6.11(a). shows an optical micrograph of the pick up coil of a thin film YBCO superconducting quantum interference device (SQUID). All scans were taken at 40K after zero-field cooling of the sample. The gray-scale images and line scans from the scan areas (i) and (ii) are shown in figure 6.11(b). For each scan a field of approximately 30G was applied normal to the surface of the SQUID and a scan taken, the field was then removed and the same area scanned again to investigate the irreversibility of vortex penetration. In each case the left hand image and line scan are those taken in the applied field and those on the right taken after field removal. Figure 6.11(c) shows a gray-scale image and line scan of a small section of the solid outer loop of the SQUID.

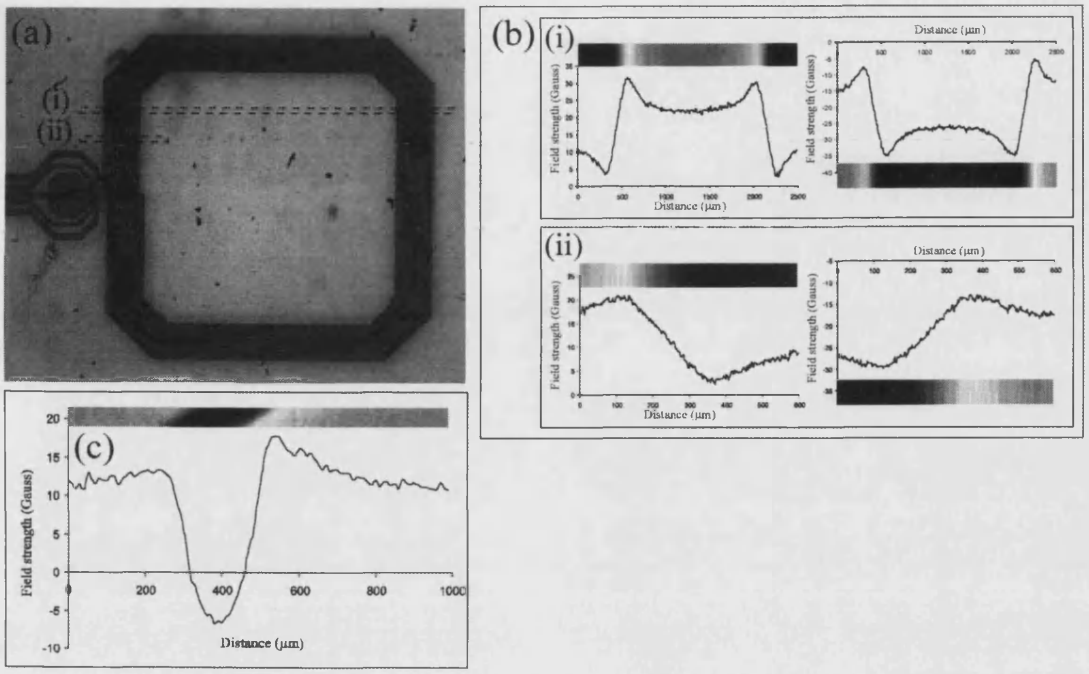

Fig. 6.11(a) Optical micrograph of the pick up coil of a thin film YBCO superconducting quantum interference device (SQUID), illustrating the scan areas (i) and (ii). (b)(i) and (ii) Images and line scans of the YBCO SQUID after zero field cooling to 40 K and the application of a 30 G magnetic field and subsequent field removal. (i) Left, 2500μm × 20μm (10 μm step size) image and line scan in a 30 G magnetic field. (i) Right, 2500μm × 20μm (10 μm step size) image and line scan after field removal. (ii) Left, 600 μm × 5 μm (2.5 μm step size) image and line scan in a 30 G magnetic field. (ii) Right, 600 μm × 5 μm (2.5 μm step size) image and line scan after field removal. (c) 1000 μm × 80 μm image and line scan of the local magnetic induction of a small section of the solid outer loop of the SQUID in a 30 G magnetic field.

6.3.2.2. (40K) YBCO Squares

The array of superconducting $YBa_2Cu_3O_{7-\delta}$ (YBCO) squares used in this study was grown by electron-beam co-evaporation of the metals on an MgO substrate. It was patterned using conventional optical lithography and Ar-ion milling, and subsequently annealed to an over-doped state in atomic oxygen. The array is made up of 20μm × 20μm YBCO squares separated by 5μm ion milled channels and has a critical temperature of 88±0.1 K. The lattice vector of the array was placed at 45° to the x and y axes to improve image definition and aid later image processing. Fig. 6.12(a). shows a zero-field cooled scan at 40K taken in an applied field of approximately 40G normal to the surface of the array. The scan area is 80μm × 80μm with a step size of 1.25μm. The superimposed grid of squares in Fig. 6.12(b) indicates the locations of the YBCO squares. As expected the applied field is screened from the regions above the centres of the YBCO squares due to the establishment of a Bean-like thin film critical state [11]. To further understand the behaviour of flux penetration in the square array the sample was field-cooled to 40K in 30G and scans taken of the same area with the field on and then removed. Fig. 6.12(c) with the field applied shows almost uniform induction indicating that very little magnetisation is induced. After the applied field is removed some of the flux remains trapped in the squares, indicated by the areas of high field, shown as bright spots in Fig. 6.12(d) and another Bean-like critical state is established for decreasing fields. Fig. 6.12(e) shows linescans in the directions indicated which show the flux profiles more clearly.

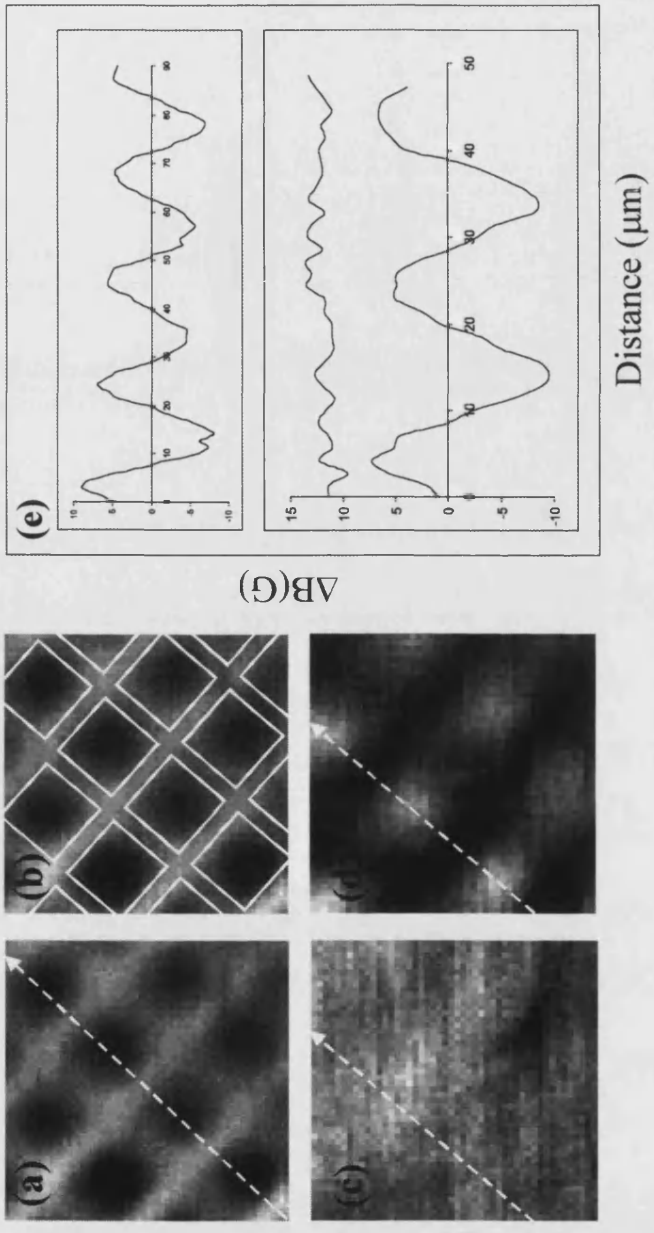

Fig. 6.12 (a) Image of array of 20μm YBCO squares after zero field cooling to 40K followed by the application of 40G. Scan area 80 μm × 80μm, step size 1.25μm, gray scale spans 18G (b) same image with superimposed grid indicating location of YBCO squares. Images after field-cooling to 40K in 30G (c) and (d) after removal of applied field. Scan area 60 μm × 60μm, step size 1.25μm, gray scale spans 16G (e) line scans indicated in (a), (c), (d).

6.3.2.3 (50-80K) YBCO thin-film square

The superconducting $YBa_2Cu_3O_{7-\delta}$ (YBCO) thin film used in this study was grown by Pulsed Laser Deposition (PLD) on a $LaAlO_3$ 10 mm × 10 mm × 1 mm single crystal substrate at Julich KFZ GmbH. The 200 nm thick film was patterned into five 1 mm × 1 mm squares using conventional optical lithography and chemical wet etching in a solution of HCl. The five squares are arranged in a dice display format, i.e. one at each corner of the substrate and one in the centre, and the film has a critical temperature of 90±1 K. The central square was chosen for investigation in this study and the system aligned to this square. Fig. 6.13(a). shows a zero-field cooled scan at 50K taken in an applied field of approximately 260G normal to the surface of the thin film square. The scan area is 1600μm × 1600μm with a step size of 20μm.

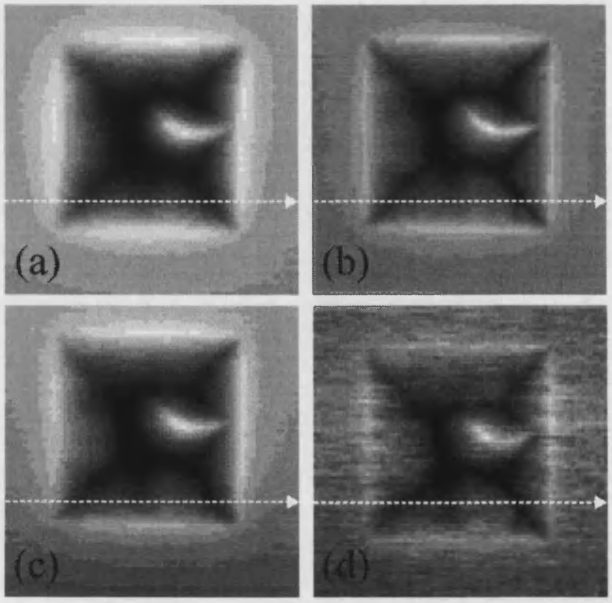

Fig. 6.13 Zero-field cooled images of a 1 mm × 1 mm YBCO thin film square taken at temperatures of (a) 50 K, (b) 60 K, (c) 70 K, and (d) 80 K, in an applied field of approximately 260 G normal to the surface of the square. Scan area 1600 μm × 1600 μm, step size 20 μm.

As expected the applied field is screened from the regions above the centre of the YBCO square due to the establishment of a Bean-like thin film critical state [11]. The irregular shaped high-field region in Fig. 6.13(a), starting near the centre of the sample and extending to the right hand edge, is believed to be the result of damage to the thin film, in the form of a scratch or defect, allowing flux to penetrate into the sample more easily in this region. To further understand the temperature dependent behaviour of flux penetration into the thin film square zero-field cooled scans at 60, 70, and 80 K were taken in an applied field of approximately 260G. Figs. 6.13(b) to (d) show the 1600μm × 1600μm scans taken, with a step size of 20μm, at each temperature 60, 70, and 80 K respectively.

Graphs in Figs. 6.14(a)-(d) show the local magnetic induction along the direction of the line scans indicated by the dotted lines in Figs. 6.13(a) to (d). The reason for the increase in noise seen in the image of Fig. 6.13(d), and the line scan of Fig. 6.14(d) is two-fold. Firstly, at elevated temperatures near T_c the degree to which magnetic flux is screened from within the supeconducting sample is reduced, therefore there is less contrast between the field inside the superconductor and the field outside, resulting in a smaller Hall probe voltage signal. Secondly, due to an oversight the Hall current was not adjusted to give the largest possible Hall voltage, without saturation of the signal, for the measured magnetic field. This resulted in a decrease in the signal-to-noise ratio.

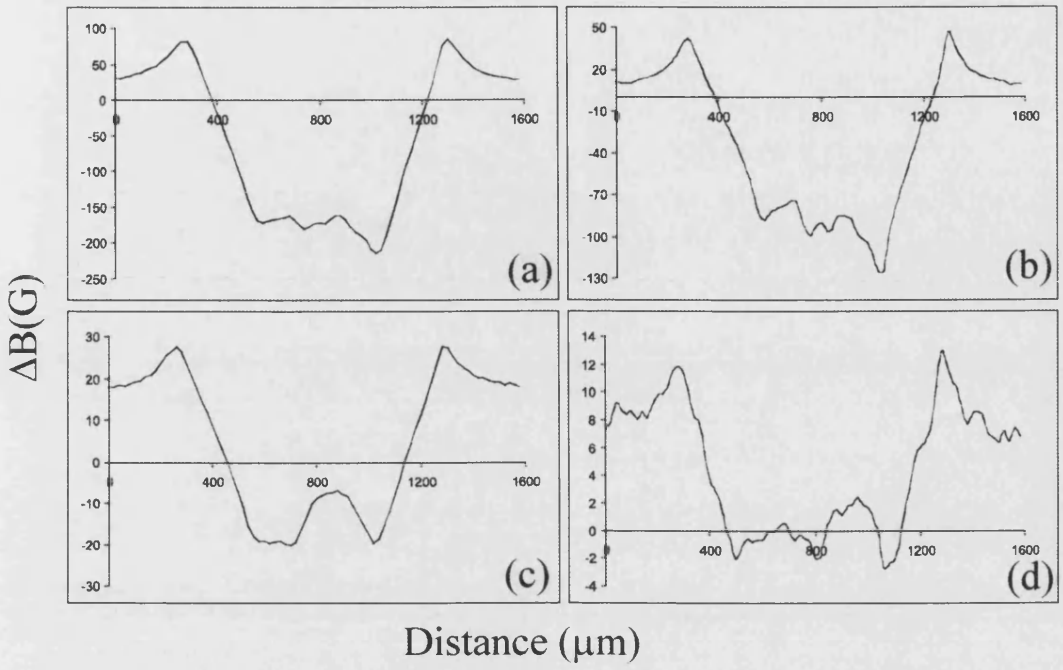

Fig. 6.14(a)-(d) Line scans indicated by the dotted white lines in Fig. 6.13(a) to (d).

Chapter 7

7. Experimental Results

In this chapter the results of two separate investigations are presented. The first investigation looks at the suppression of surface barriers for flux penetration in BSCCO whiskers by electron and heavy ion irradiation, and the second investigation looks at flux penetration in a superconducting YBCO thin film strip using scanning Hall probe microscopy. Both studies were carried out whilst development of the large area SHPM of chapter 6 was taking place. The author was not the principle worker concerned with the second investigation but was involved as a co-worker in most aspects of the investigation.

7.1. Suppression of Surface Barriers for Flux Penetration in BSCCO Whiskers by Electron and Heavy Ion Irradiation

7.1.1. Introduction

In this section systematic investigations of the effect of electron and heavy-ion irradiation on the surface barrier in $Bi_2Sr_2CaCu_2O_{8+\delta}$ whiskers are presented. Whiskers have the advantage that they are almost perfect three-dimensional crystals with flat edge faces and show very weak bulk pinning; moreover, their small cross-section of 0.4 × 12 μm^2 means that the field perturbation (or the magnetic moment) due to the presence of a surface barrier overwhelms that produced by the Bean critical state due to bulk pinning.

7.1.2. Irradiation of Whiskers

Irradiation by swift heavy ions introduces strongly pinning amorphous columnar defects into the superconducting matrix. The effect of this on the surface barrier should be threefold [55], as discussed in section 3.9. Firstly, the attraction between the vortex and the surface is altered by the presence of the columnar defects. This is taken into account by summing over an infinite number of image vortices inside the columnar defects as well as outside the sample. More importantly the fact that the Meissner current is restricted to flow between the specimen surface and the columnar defects, means that the current density will be larger than in the sample before irradiation; for the investigated defect density of 5×10^{10} cm^{-2} it has been calculated as larger by a factor of nearly two [55]. The Meissner current is expected to be largest near the circumference of the columns, closest to the surface, leading to the nucleation of vortices on the first "row" of defects in the sample. Thus, the introduction of non-superconducting holes near to the surface is effectively equivalent to the creation of preferential "channels" for penetration. This effect leads to a decrease of the prefactor of Eq. 3.9, by an amount proportional to the increase of the Meissner current.

The final consequence of heavy ion irradiation is that, since the first vortices are nucleated on a column (of radius c_0), one should account for the fact that the vortex free energy per unit length ε_0 is decreased by the pinning energy $U_P=\varepsilon_0(c_0/2\xi)^{1/2}$ [96]. Naively this is expected to lower both T_0 and the prefactor in Eq. (3.9) yielding:

$$H_P \approx \sqrt{2}\kappa \frac{\varepsilon_0 - U_P}{\Phi_0 s} \exp\left[\frac{T \ln(t/t_0)}{(\varepsilon_0 - U_P)s}\right] \qquad (7.1)$$

The effects of electron irradiation are more subtle. The introduction of point defects by this method increases the pinning energy as well as the vortex entropy due to pancake wandering [69] so that T_0 is again reduced, be it to a much lesser extent than after heavy ion irradiation. However, there is no substantial modification of the image force or of the Meissner currents, so that the main effect is expected to arise from surface damage.

A number of individual BSCCO whiskers from the same growth batch have been investigated. The samples were produced at Bath by annealing a quenched melt of

appropriate stoichiometry in flowing oxygen; a more detailed description of the whisker growth and characterisation is given in Ref. 80 [80]. The whiskers are of high crystallographic perfection and have no extended defects, although there may be some point defects, which give rise to bulk pinning at very low temperatures (T < 20 K). They do not have optimum oxygen stoichiometry as indicated by their critical temperatures, which are estimated to be 77 K and 79 K for whiskers I and II respectively. These estimates were obtained by fitting a cubic polynomial to the high temperature H_p(T) data and extrapolating to zero field. Due to their very regular surfaces and narrow widths (whisker I had dimensions 108 × 12 × 0.4 μm^3, whisker II had dimensions 44 × 12 × 0.4 μm^3), the magnetic properties of these whiskers are dominated by surface effects, and they represent model systems for flux penetration studies.

Samples I(AG) and I(EI) represent the same whisker before (as-grown, AG) and after electron irradiation (EI). The latter was performed at 20 K using 2.5 MeV electrons from a Van de Graff accelerator, which produces randomly-distributed isolated Frenkel pairs. The damage produced by the known dose of 160 mC is estimated to be 1.7×10^{-4} d.p.a (displacements per atom) [97]. Agglomeration of small defect clusters is expected when the sample is warmed to room temperature for transfer to the measuring cryostat. The residual damage, after room temperature annealing, is in the range of $(0.6\text{-}1.2)\times10^{-4}$ d.p.a. Whisker II(HII) has been irradiated along the c-axis with heavy ions (9 GeV Pb ions) at 20 K and a total fluence of 5×10^{10} ions/cm^2 ($B_\phi \cong$ 1 T). Each ion is known to produce a continuous amorphous track through the whisker with a diameter of 5-7 nm [98]; the induced columnar defect serves as an orientated pinning site for vortices. In this case there is no unirradiated reference data set but, since all the whiskers from this growth batch behaved in a very similar fashion, the virgin H_p(T) is expected to coincide with that of whisker I(AG) to within ±25%.

7.1.3. Experimental Apparatus

Measurements have been carried out using miniature GaAs/AlGaAs heterostructure Hall probe arrays based on a 2 μm wide wire width with 4 μm centre-to-centre spacing between Hall voltage contacts, as discussed in section 5.3.1. The probes were operated

with a 2 μA rms 32 Hz ac current and the Hall voltage detected with a lock-in amplifier. The whiskers were positioned in the desired location on the Hall probe with a micromanipulator where they were held by their mutual electrostatic attraction see inset of Fig. 7.3. Characterization of the same whisker was attempted both before and after irradiation, but this was not always possible due to damage that sometimes occurred during manipulation. The samples were then mounted on a temperature-controlled probe and inserted into a ^{4}He cryostat containing a small superconducting solenoid, with the magnetic field applied along the whisker c-axis, perpendicular to the (largest) a-b face, as shown in figure 7.1.

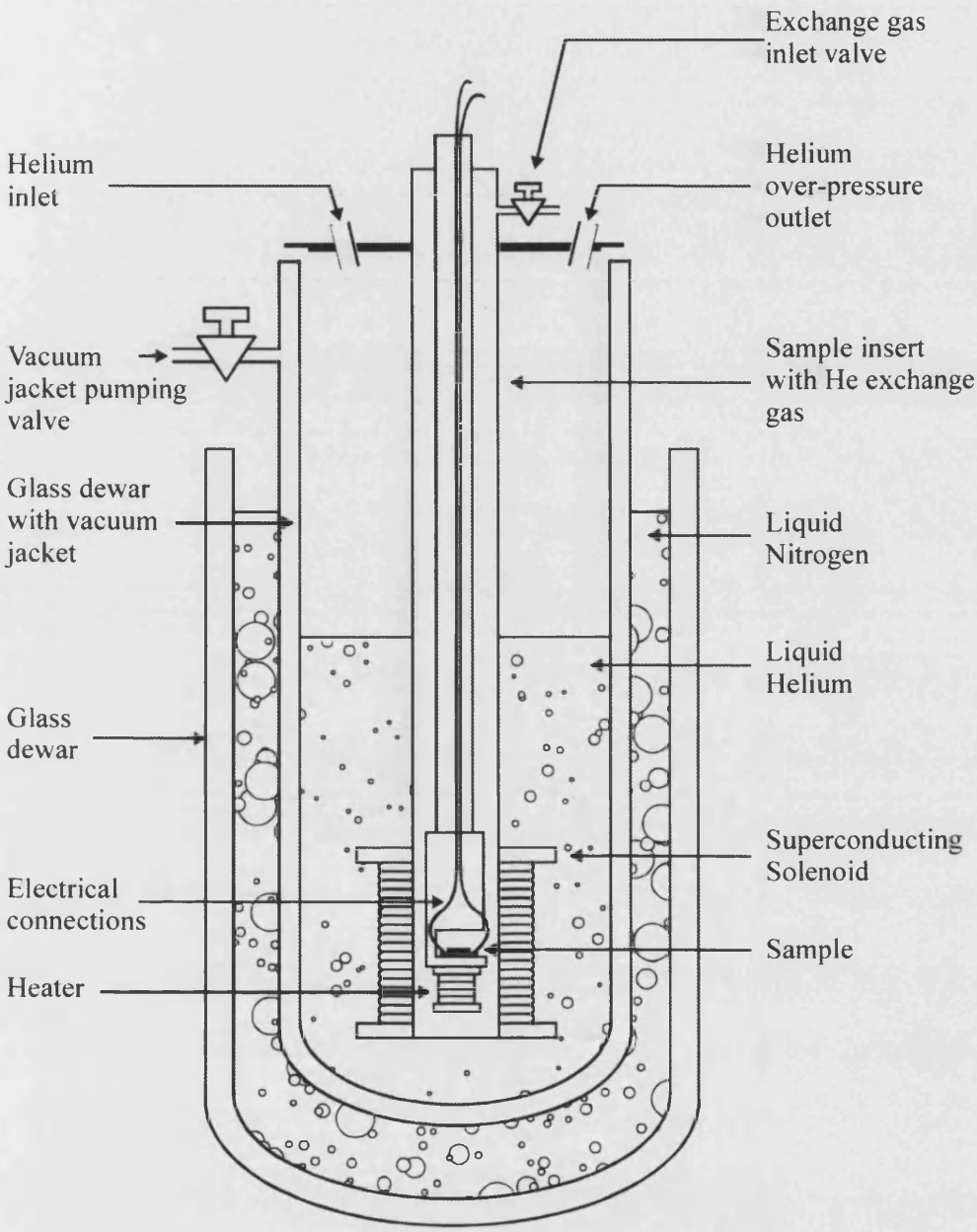

Fig. 7.1 Diagram of the ^{4}He cryostat, including the superconducting solenoid and glass dewar.

7.1.4. Results and Discussion

Figure 7.2. shows six ''local'' magnetisation loops (defined by $\mu_o M_l = B_m - \mu_o H_a$, where B_m is the measured induction and H_a is the applied field) measured at the centre of the whiskers at temperatures of 10, 20, 40, 50, 65, and 70 K. The symbol M_l is used to differentiate between our "local" magnetisation and the conventional bulk magnetisation. The field is applied parallel to the crystallographic *c*-axis (the thin dimension of the whisker). In each panel, H_p can be identified as the field at which M_l deviates sharply from a linear diamagnetic behaviour near the origin. The magnitude of the ''local'' magnetisation and the Meissner slope depends to some extent on the separation between whisker and Hall probe, which may vary not only when the whisker is repositioned on the array, but also as function of temperature. However, H_p is independent of such considerations. Clearly the penetration fields and the width of the hysteresis loops reduce very rapidly as the temperature is increased in all cases. At 40 K, and above, the asymmetry between the increasing and decreasing branches of the local magnetisation loops of all the whiskers are entirely characteristic of a system dominated by a surface barrier [49]. This arises because the surface barrier hinders vortex entry much more than vortex exit [51]. At low temperatures, *e.g.* at 10 K, the $M_l(H)$ loops become more symmetric and it appears that bulk pinning is beginning to play a role. Figure 7.2. allows a direct comparison of the effect of irradiation on the ''local'' magnetisation loops of the whiskers. Electron irradiation (I(EI)) results in a sharp reduction in the penetration field at a given temperature as compared to the virgin state (I(AG)), with even stronger suppression evident in the heavy-ion irradiated whisker (II(HII)) consistent with theory [55], described in section 3.9.

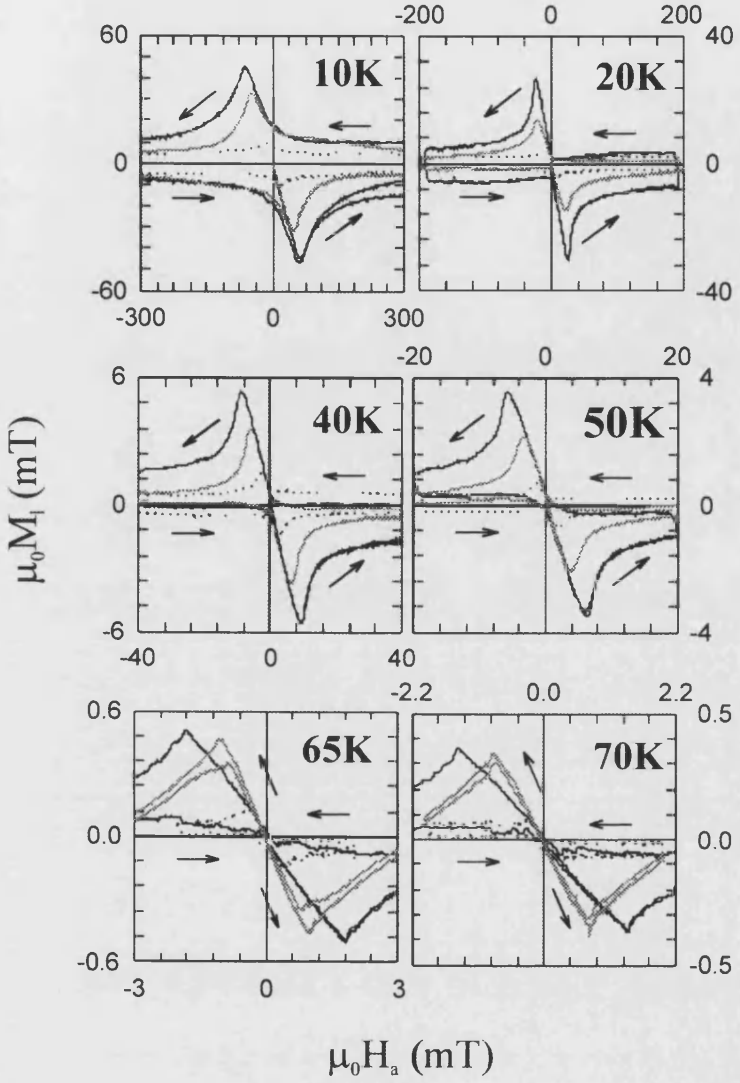

Fig. 7.2 Local magnetisation loops at various temperatures for whisker I(AG) (solid black lines), I(EI) (dark grey lines) and II(HII) (black dashed lines) measured near the sample centre with the applied field parallel to the c-axis.

Figure 7.3 shows the temperature dependence of the penetration field for each sample on a semi-logarithmic plot. At low temperatures ($T \leq 50$ K) an exponential temperature dependence of the form predicted in equation (3.9) is displayed over nearly two orders of magnitude in H_p in all cases. Irradiation seems to reduce the prefactor of Eq. (3.9)

with almost no change in the exponent. This is illustrated in Fig. 7.3 by the near parallel fit lines for whiskers I(AG), I(EI) and I(HII) at T<50K, which yield values for T_0 of 18.5 K, 17 K and 19.4 K respectively. These agree well with values of 18 K and 14 K measured previously in different unirradiated whiskers [52], and compare reasonably well with estimates of 10±1 K [53] and 27.3 K [98] in large BSCCO single crystals. The prefactor is reduced by a factor 1.2 for the electron-irradiated whisker, and by a factor 3.6 in the ion-irradiated whisker, in good agreement with recent calculations [55]. Also shown on this figure (dashed line) is a fit to Eqn. (3.9) for the unirradiated whisker where the temperature dependence of $\varepsilon_0(T)$ has been explicitly included assuming $\varepsilon_0(T)s=1000K\times(1-T/T_c)$, $\kappa=120$ and $\ln(t/t_0)=30$. Note that the data has had to be scaled by 1/12 to get asymptotic agreement at low temperature, and even then the fit is relatively poor above T=20K. This is attributed to the fact that equation 3.9 has been calculated in the London approximation and neither treats the vortex core nor the nucleation of the instability of the order parameter at the point of vortex entry and is therefore not a full description of penetration. Demagnetisation effects may also contribute to the need for the scaling factor of the data. It should be noted here that the approximately constant slope observed in figure 7.3, even after heavy ion irradiation, is in contradiction to the predictions of equation 7.1. The inapplicably of (7.1) is perhaps to be anticipated since, in the presence of columnar defects, the maximum of the penetration barrier will lie at an intermediate position between the surface and defect, which will not have been lowered by the full pinning energy.

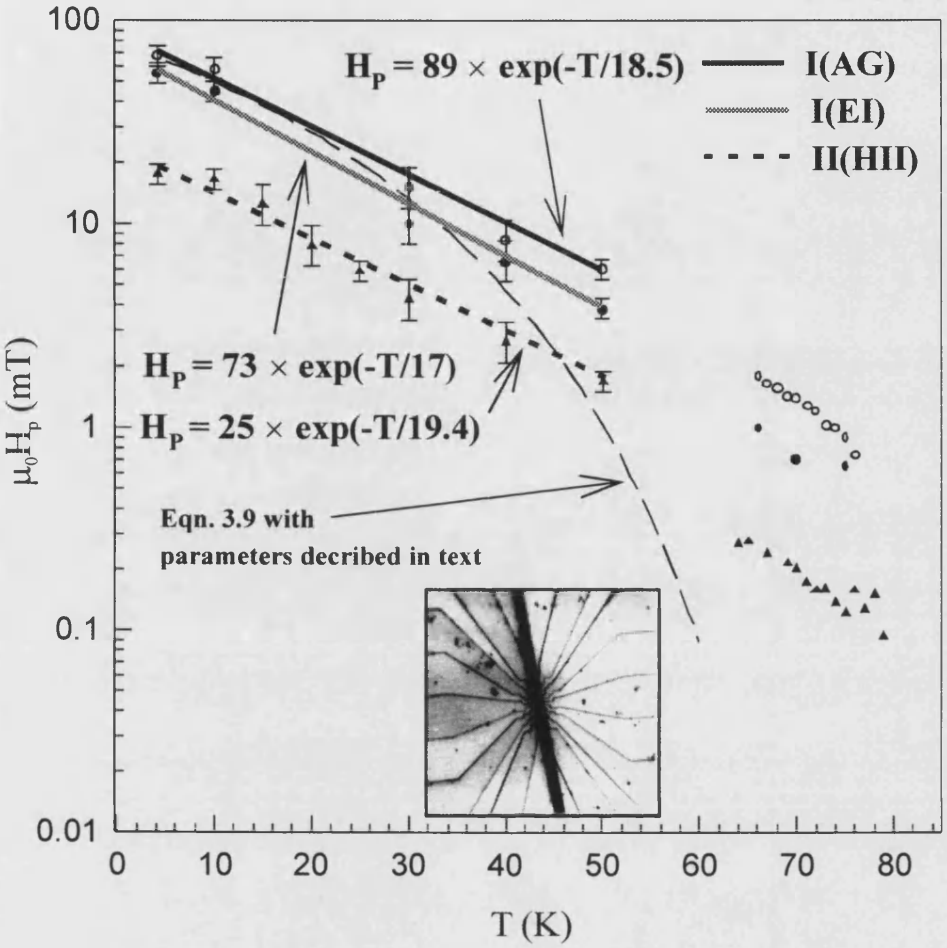

Fig. 7.3 Temperature dependence of the field of first flux penetration, $H_p(T)$, for whisker I(AG) (open circles), I(EI) (filled circles) and II(HII) (filled triangles). The dashed line is a fit to Eqn. 3.9 for the parameters indicated in the text. The inset shows an optical micrograph indicating the relative orientation of whisker I(AG) and the Hall bar.

At higher temperatures (T > 50 K) a good fit to Eq. (3.9) cannot be obtained using the same set of parameters that was used to generate the dashed line in Fig. 7.3. In Refs, 52 [52] the behaviour in this regime was tentatively attributed to the penetration of well-correlated flux lines over a BL barrier. To gain a deeper insight into this regime the irreversibility at a given temperature is estimated via the quantity $\Delta M_l(T)=M_l\downarrow(2H_p,T)-M_l\uparrow(2H_p,T)$, where $M_l\downarrow(2H_p,T)$ and $M_l\uparrow(2H_p,T)$ are the measured values of the local

magnetisation , M_L, at applied field values of twice the penetration field, H_p, on the decreasing and increasing leg of the magnetisation loops respectively for each temperature. This is plotted in Fig. 7.4. for the different samples as a function of temperature. Since the width of the whiskers studied here are only ~ 5-10 times the separation between the whisker and Hall probe, which changes a little each time a sample is mounted, ΔM_l can vary by as much as 25% between manipulations and only effects of greater magnitude can be considered significant. The irreversibility of whisker I(AG) is found to be reduced many fold by electron irradiation (I(EI)), suggesting that, even at these high temperatures, its origin is predominantly due to a BL-type surface barrier. This is consistent with results on large BSCCO single crystals [99], where the transport critical current was shown to fall by a factor of up to twenty when surface barriers were eliminated in a Corbino measurement geometry. The situation is not so clear-cut in the heavy-ion irradiated whisker (II(HII)), which displays quite a wide plateau in ΔM_l, with magnitude slightly larger than whisker I(EI). It is proposed that in this case heavy ion irradiation both decreases the surface barrier and increases the bulk pinning for flux lines via the introduction of amorphous columnar defects. It is noted that the sharp drop in $\Delta M_l(T)$ near 75 K may be due to the same entropic reduction of pinning that causes the barrier to decrease in this temperature regime.

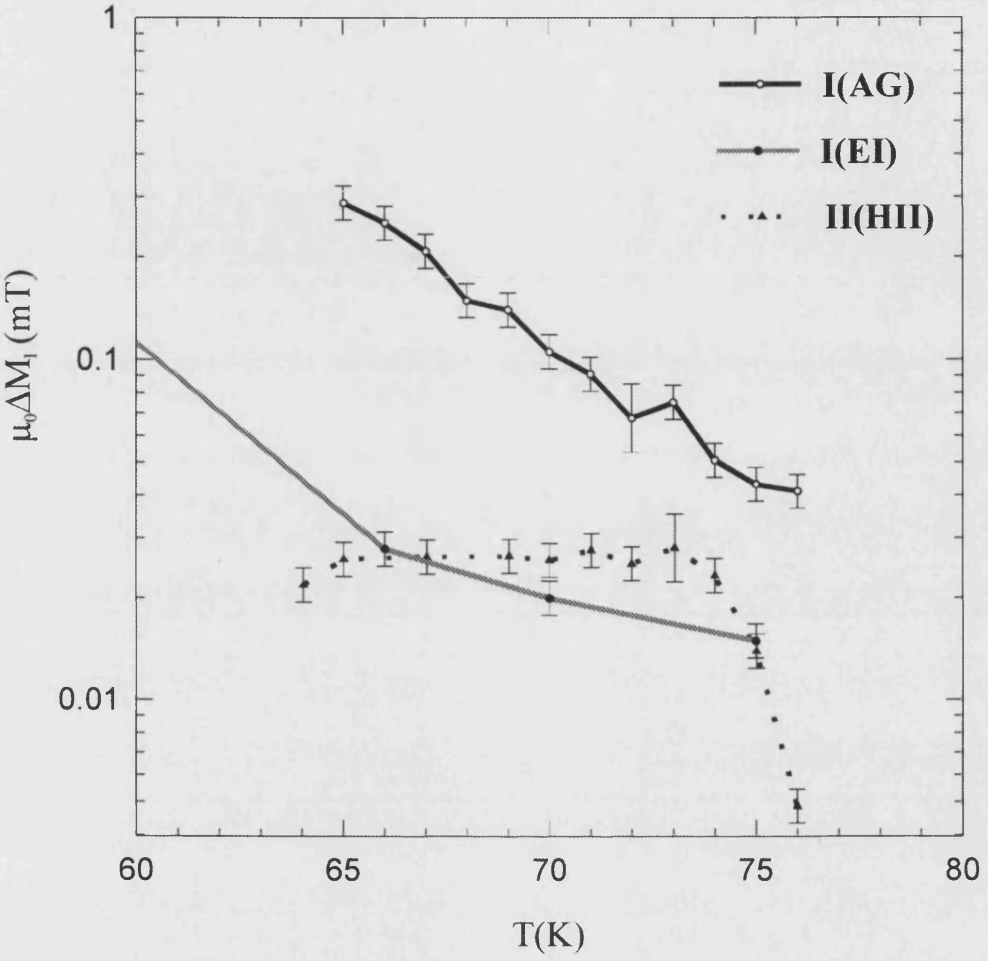

Fig. 7.4 Measured irreversibility $\mu_o\Delta M_I$ (see definition in text) calculated at $2.H_p$ for whisker I(AG) (solid black line), I(EI) (dark grey line) and II(HII) (dotted line) with the field applied parallel to the *c*-axis.

7.2. Scanning Hall Probe Microscopy of Flux Penetration into a Superconducting YBCO Thin Film Strip

7.2.1. Introduction

In this section scanning Hall probe microscopy (SHPM) has been used to directly observe the microscopic mechanism of flux penetration into a thin-film superconducting meander line as the applied field and/or transport current is varied. The 0.35-μm-thick $YBa_2Cu_3O_{7-\delta}$ (YBCO) (001) film used in the study was grown on a MgO substrate at 690°C by electron-beam coevaporation of metals by Prof. Richard Humphrey's group at QinetiQ in Malvern, UK.

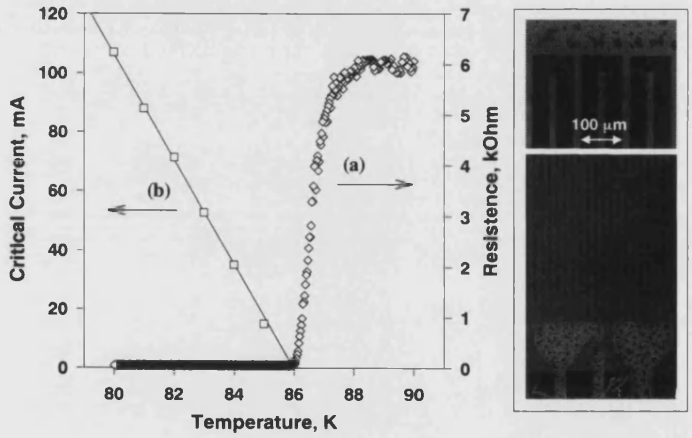

Fig. 7.5 (a) The resistive transition of the YBCO meander line and (b) measurements of the critical current as a function of temperature. Optical micrographs of the meander line are shown on the right.

The meander line has a total length of approximately 8 cm and is based on repeated 2-mm-long segments of 40-μm-wide wires with 20 μm spacings, as shown in figure 7.5. The meander line was patterned using conventional optical lithography and Ar-ion milling, and subsequently annealed to an overdoped state in atomic oxygen. The original film had a critical temperature of 88.0 ± 0.1 K as measured by magnetisation. Figure 7.5

depicts the resistive transition of the meander line as well as measurements of the critical current, which yield the transition temperature 86.0 ± 0.1 K after annealing and a critical current of 2.2×10^6 A/cm^2 at 77 K. The critical current is inferred from an abrupt drop in $d(\log V)/(\log I)$, where I is the transport current and V is the voltage along the meander line, which corresponds to a crossover from creep to flux flow.

7.2.2. Experimental Apparatus

Magnetic-field maps of the meander line were generated using the same custom-built SHPM based on a low-temperature scanning tunnelling microscope (STM), developed at Bath [82], previously mentioned in earlier chapters. Two different types of Hall probes were used to collect the results presented here. A high spatial resolution 0.3 μm probe with field resolution of ~ 3 μT/√Hz at 77 K patterned in a GaSb/InAs/GaSb heterostructure by electron-beam lithography, and a high-sensitivity 0.85 μm probe with field resolution of ~ 30 nT/√Hz at 77 K patterned in a GaAs/AlGaAs heterostructure by optical lithography. To facilitate STM tracking without shorting the meander line, the sample (excluding contact pads) was covered with 200 nm of dielectric Si_3N_4 and 100 nm of conducting Au. The Hall probe is kept to within ~ 0.3 μm of the surface of the meander line whilst scans are recorded.

7.2.3. Results and Discussion

Several different locations on the meander line have been studied and in all cases it was found that flux penetration (due to an applied current or magnetic field) occurs in the form of flux bundles at specific "weak" spots near the edge of the superconducting strip. Figure 7.6 shows SHPM images across the edge of a superconducting strip, which occupies the bottom-left-hand corner of the image. The sample has been field-cooled (FC) to 65 K in –0.5Oe, trapping about eight vortices in the scanned part of the strip (see figure 7.6(a)). A magnetic field perpendicular to the meander line (or a transport current along it) has then been applied at this temperature. Figure 7.6(b) depicts the local induction over the sample surface after a magnetic field of 16 Oe was applied. The subsequent image after field removal was found to be identical to figure 7.6(a). However, if the applied field (current) exceeds a critical value, flux was found to

penetrate into the sample and remain there after field removal. This critical value is used to define the penetration field H_p (current I_p). This definition is microscopic in nature and differs from the penetration field (current) derived from macroscopic measurements.

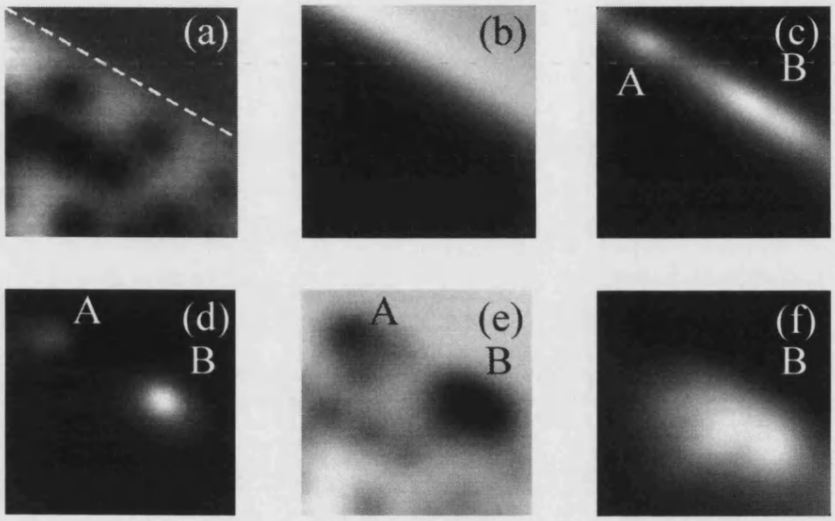

Fig. 7.6 SHPM scans of the edge of the YBCO strip (lower left) after (a) FC in -0.5Oe to 65K [gray scale (GS) spans 0.5G], (b) after application of 16Oe to the -0.5Oe FC state at 65K (GS 32G), after application (to the -0.5Oe FC state) and removal of (c) 32Oe at 65K (GS 7.2G), (d) 100mA at 70K (GS 1.8G), (e) -20Oe (GS 1.4G), (f) -70mA at 77K (GS 3.6G). Scan size is 25×25 μm^2. White dashed line indicates sample boundary.

Figure 7.6 shows the flux distribution after the application and removal from the earth FC state of (c) 32 Oe at 65 K, (d) 100 mA at 70 K, (e) – 20 Oe at 70 K, and (f) 70 mA at 77 K. Figures 7.6(c)-(f) show that flux penetrates into the sample in the form of flux bundles with large numbers of flux quanta (~25 in the largest bundle and ~7 in the smallest calculated from the measured local magnetic induction) which enter the sample at the same locations at the edge of the strip under application of $I > I_p$ or $H > H_p$ (regions A and B in figures 7.6(c)-(f)). This was found to be true at all locations of the sample regardless of temperature, field, current, or magnetisation history. At lower temperatures it can be seen that flux enters along a narrow strip at the edge of the

sample, as shown in figure 7.6(c). At higher temperatures, when the effective penetration depth is larger and pinning is weaker, flux penetration is dominated by the weakest spot at the edge of the sample (figure 7.6(f)). Also, the vortices trapped inside the strip after field-cooling do not move.

The thin-film strip geometry is characterised by large demagnetisation factors, and the Meissner shielding currents are strongly enhanced at the edges of the strip. At the meander line edge the surface magnetic field can be approximated by [13] $B \approx H_a \sqrt{W/d}$, where H_a is the applied field, W is the half width of the strip and d is the thickness, and in this case should be almost 8 × bigger than the applied field. As a consequence, surface roughness and edge imperfections, as well as damage to the superconductor during lithographic processing, may become important to the onset of flux penetration in such samples.

To establish whether a correlation between the distribution of penetrated flux and the surface topography exists the gating mode of the SHPM was utilised, which maps a modulation of the Hall voltage signal due to electric fields arising near the sample when it is subjected to a large sample voltage. The local electric fields depend upon the local sample-probe separation and, therefore, yield a map of the topography with a resolution of ~ 0.3 μm. The sample was initially cooled in the Earth's field and the meander line topography acquired (see figure 7.7(a)). The image was captured at a scan height of ~ 0.3 μm above the sample surface. A field (or current) has then been applied to the strip (figure 7.7(b)) and the penetration field established by comparison of the magnetic images before the application and after the removal of the magnetic field (current). The onset of flux penetration after application of 22 Oe at 65 K is shown in figure 7.7(c). A field higher than the penetration field was next applied to the earth FC sample and the profile of the penetrated flux after the removal of the field was captured (figure 7.7(d)). This procedure was repeated at different temperatures as shown in figures 7.7(d)-(f) for 65, 70, and 77 K. Again flux enters the strip at weak spots at the edge of the sample, e.g. A in figs 7.7(c)-(f). Line scans of the penetrated flux at different temperatures and the gating image along the edge of the superconducting strip, Figure 7.7(g), demonstrate that

there is a good correlation between sample topography and the penetration spots – the maxima of the magnetic induction occur at the minima of the gating voltage, which correspond to thinner regions of the sample (marked by the vertical arrows in figure 7.7(g)). The same correlation was seen in almost all locations studied on the meander line. The measured thickness variations are estimated as ~ 20 nm on a ~ 5-μm-length scale over the meander line surface.

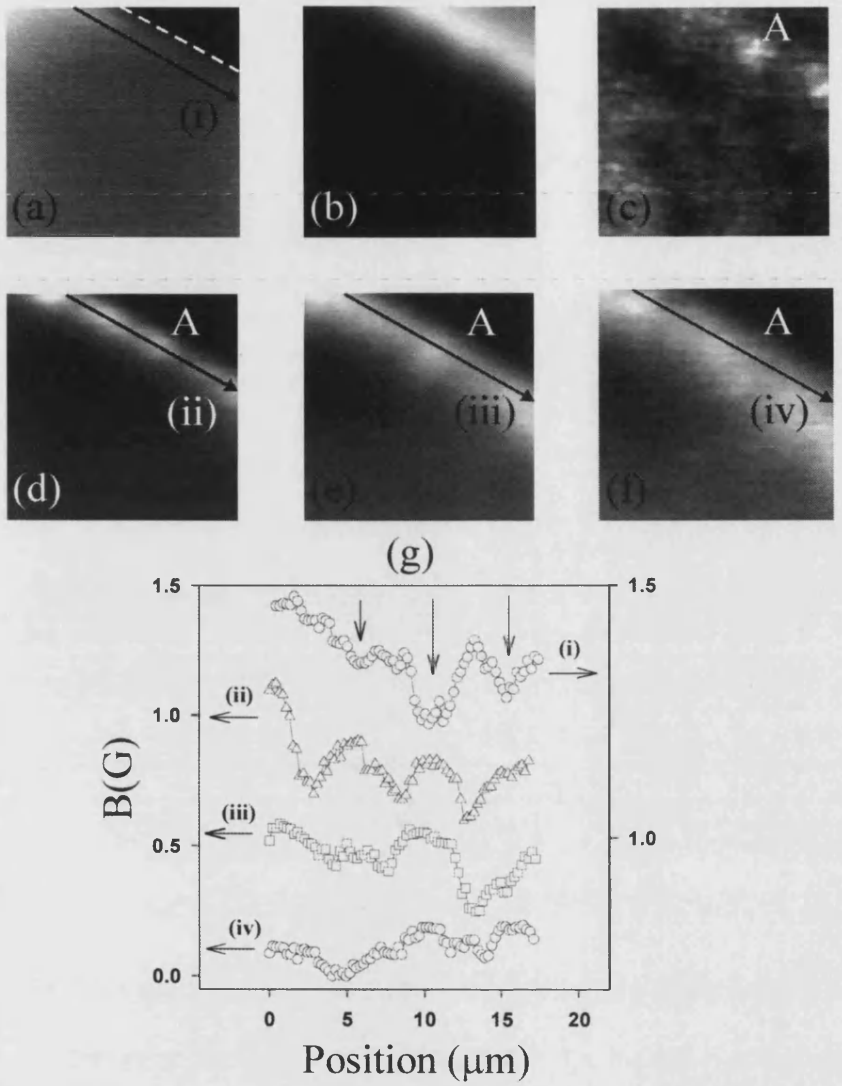

Fig. 7.7 (a) Gating image of the surface of the sample (lower left, white dashed line indicates sample boundary). (b) SHPM image after application of 32Oe to the -0.5Oe FC state at 65K [gray scale (GS) spans 73G]. SHPM scans after application (to the -0.5Oe FC state) and removal of (c) 22 Oe at 65K (GS 1.9G), (d) 32 Oe at 65K (GS 12.6G), (e) 32 Oe at 70K (GS 14.7G), (f) 16 Oe at 77K (GS 6.3G). (g) Gating response and magnetic induction close to the edge of the superconducting strip along the solid black lines shown in (a), (d)-(f) offset for clarity. The vertical arrows indicate the maxima of penetrated flux and minima of the strip height. Scan size is 25×25 μm^2.

Another important feature of the flux penetration, resolved using the submicron Hall probe, is the quasiperiodic modulation of the transport current along the strip edges after the onset of the penetration process. Figure 7.8 shows surface plots of the local induction above the edge of the YBCO strip (FC in – 0.5 Oe to 65 K) after (a) application of 32 Oe at 65 K and (b) removal of the field. The modulation in figure 7.8(a) shows seven peaks along the edge of the sample with an average peak-to-peak distance of ~ 3.5 μm and a peak-to-valley amplitude of ~ 12 G. The modulation is quite pronounced at temperatures well below T_c resulting in modulation of the penetrated flux after field (current) removal, see figure 7.8(b), where approximately seven white peaks of local induction along the edge of the strip are present with peak-to-valley amplitude ~ 8 G. The wavelength of the modulation was found to decrease as the temperature was reduced, suggesting a connection with the penetration depth. It is speculated that the modulation may be the precursor of the dentritic penetration structures observed in Nb films [100]. The measured penetration field and penetration current are linear functions of temperature in the range 65 – 80 K, which suggests that the penetration field is inversely proportional to the square of the penetration depth.

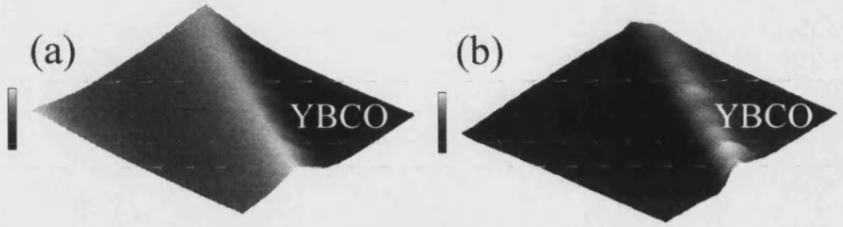

Fig. 7.8 Surface plots of the local induction above the edge of the YBCO strip after (a) application of 32Oe to the -0.5Oe FC state at 65K [gray (GS) scale spans 82G], and (b) removal of the applied field (GS 21G). The meander line is in the upper-right-hand corner. Scan size is 25×25 μm^2.

The dynamic instability of the order parameter [101],[102],[103] predicts that flux penetrates the superconductor in the form of a modulated strip along the edge of the sample, which is in qualitative agreement with the results shown in Figure 7.8. However, the penetration field evaluated from references [102],[103] is higher (H_p ~ 100 Oe for YBCO) and the modulation wavelength is shorter (~ 12 nm) than the measured values presented here. This is not surprising since Refs [102],[103] neglect the magnetic fields created by superconducting currents, leaving the coherence length as the only important length scale in the problem. Accounting for the estimated demagnetisation factor of 8 for our system reduces the predicted penetration field H_p from 100 to 12 Oe, which is much closer to the measured values. Attempts have been made to incorporate order parameter fluctuations into a theory of the thin-film Bean-Livingston barrier in the presence of strong pinning and edge roughness [104]. However, this yields estimates of H_p that are more than an order of magnitude smaller than the measured values presented here. It is believed that this discrepancy will be resolved if the work can be extended to realistically account for the presence of thickness variations and edge roughness.

Chapter 8

8. Scanning Hall Probe Microscopy of Flux Penetration into a Superconducting $Bi_2Sr_2CaCu_2O_{8+\delta}$ Platelet-like Single Crystal Sample

This chapter presents flux penetration studies in a high quality superconducting $Bi_2Sr_2CaCu_2O_{8+\delta}$ platelet-like single crystal using the large area SHPM described previously in chapter 6. All the work was carried out on the same $Bi_2Sr_2CaCu_2O_{8+\delta}$ single crystal sample placed in a perpendicular magnetic field, and the local magnetic induction was investigated at various field and temperature values. The low field results compare favourably with existing theories and experimental results for vortex dynamics in thin flat samples [46]. However, a new regime is revealed near the second magnetisation peak (see section 3.8) which was not seen before, and appears to indicate that the sample not only has areas with different current density magnitudes but also current densities of different sign within the same region of the superconducting sample as the applied field is simply increased from zero.

8.1. Introduction

In this section the large area SHPM has been used to directly observe the penetration of flux into a superconducting $Bi_2Sr_2CaCu_2O_{8+\delta}$ platelet-like single crystal sample. In particular, the role of geometrical barriers for flux penetration has been studied and the

validity of the model suggested by Zeldov *et al* [46], detailed in Chapter 3 section 3.8, investigated.

8.2. $Bi_2Sr_2CaCu_2O_{8+\delta}$ Single Crystal Sample

The $Bi_2Sr_2CaCu_2O_{8+\delta}$ single crystal sample used in the work presented here was grown using a floating zone technique [105] by Prof. Tsuyoshi Tamegai's group at the University of Tokyo, Japan. The sample is a square platelet-like single crystal with dimensions of 1010μm × 1010μm × 51μm, and a transition temperature of 91.0 ± 1.1 K. Figure 8.1 shows the single crystal sample mounted on its copper cooling plate.

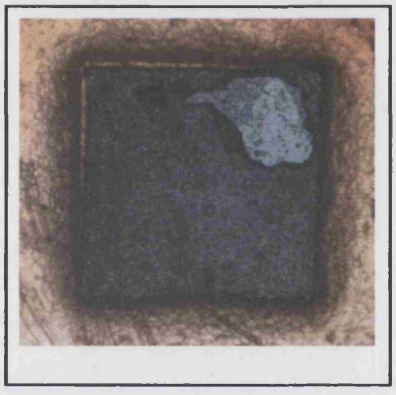

Fig. 8.1 Optical micrograph of the $Bi_2Sr_2CaCu_2O_{8+\delta}$ single crystal sample, mounted on its copper cooling plate.

8.3. Experimental Setup

Due to the relatively large size of the BSCCO single crystal sample used in the study the majority of the scans taken in the investigation were single line scans, rather than two-dimensional scans, recorded across the centre of the sample. This was done to reduce the time needed to complete a scan, thus increasing the number of scans that could be taken in a set period of time, and as a result reducing the minimum step size that could be used for each scan.

Unlike previous samples, which were mounted directly onto the cold head of the refrigerator using GE varnish to provide good thermal contact, the BSCCO single crystal

was mounted on a polished copper plate using melted paraffin wax. The plate was then bolted onto the cold head with a thin layer of heat sink compound between the copper plate and the cold head to provide good thermal contact. This arrangement was found to hold the sample in place for long periods of time without damaging the fragile single crystal and allowed unlimited numbers of cooling cycles without remounting the sample.

8.4. Results and Discussion

8.4.1 Low fields, high temperatures

The two-dimensional image shown in Figure 8.2 was taken at T = 82 K in an applied magnetic field of 10 G. The scan area is 1600 μm × 1600 μm with a step size of 25 μm. The line scan along the direction indicated is consistent with those of Figure 8.3 and illustrates the dome-like profile of the flux inside the superconductor, derived analytically by Zeldov *et al* [46]. In this model Zeldov *et al* [46] assumes no pinning and only a single region of current density, J_E, at the edge of the sample corresponding to the Meissner screening currents. The model is only valid at high temperatures and low fields where the effects of pinning are not important.

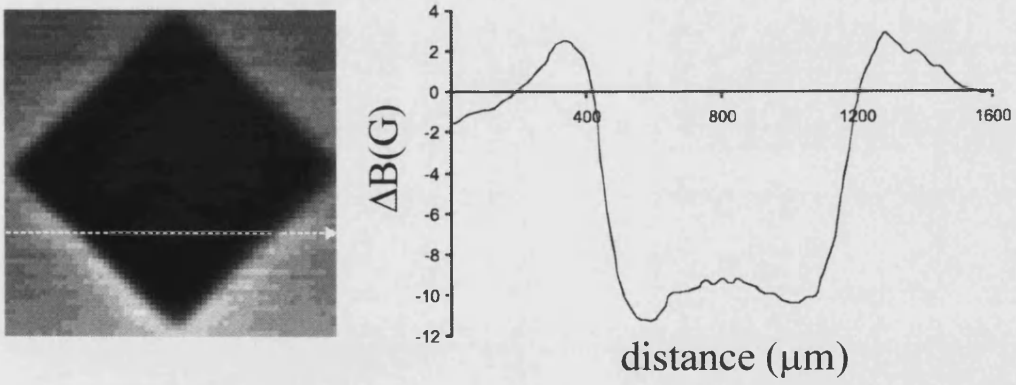

Fig. 8.2 Image of the BSCCO single crystal after zero field cooling to 82 K followed by the application of 10G, the image shows the orientation of the sample with respect to the scan axes of the SHPM. Line scan in the direction indicated illustrates the dome-like profile of the flux inside the superconductor.

Figure 8.3 shows the initial line scans taken across the BSCCO single crystal sample, illustrating the evolution of the flux profile inside the superconductor with increasing temperature. The sample was orientated as shown in Fig. 8.2 and the line scans taken of the BSCCO single crystal at its widest point. In each case the sample was zero-field cooled to the appropriate measurement temperature and a 10 G magnetic field applied perpendicular to the sample surface. The line scans are 1600 μm in length, and were recorded using a step size of 5 μm.

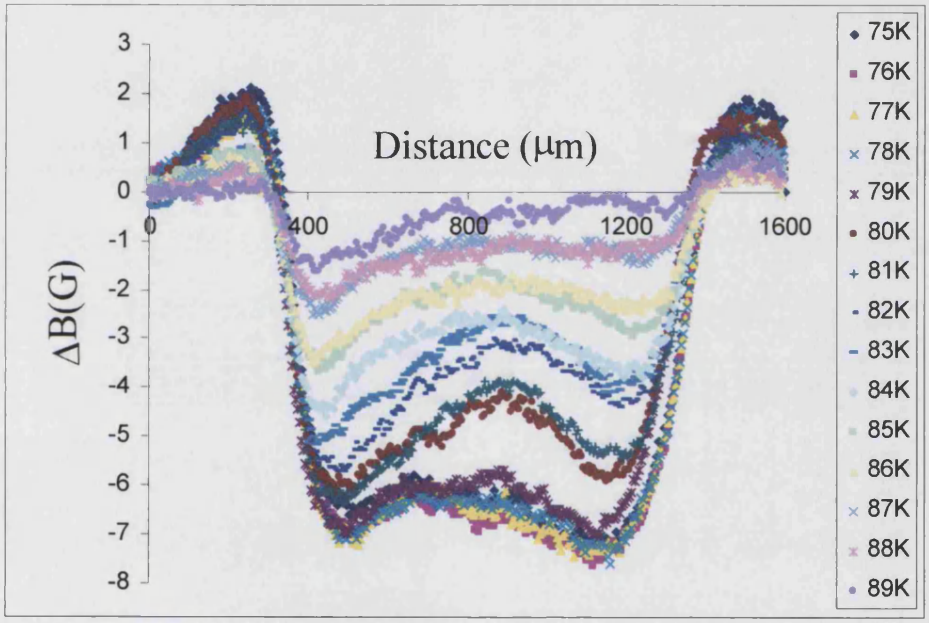

Fig. 8.3 Initial zero-field cooled field profiles in the $Bi_2Sr_2CaCu_2O_{8+\delta}$ single crystal at various temperatures recorded in an applied magnetic field of 10G. As the temperature increases, additional vortices penetrate and expand the vortex-filled region in the centre of the sample.

Separate plots of the line scans at each of the measurement temperatures, along with fits to the data based on the dome shaped local magnetic induction profile as calculated by Zeldov *et al* [46] are shown in figures 8.4(a)-(o) (see section 3.8, equation 3.17). (The Mathcad programs used to calculate the fits to all the experimental data shown in this chapter can be found in Appendix A). As T_c = 91 K is approached more vortices penetrate at the constant value of applied magnetic field. The results compare well with theory and similar experimental results presented by Zeldov *et al* [46], who argues that this behaviour is a direct consequence of the geometrical barrier in thin flat samples. Note that, while the screening behaviour at the edge of the crystal is rather well described by the fits, the dome profile is not. This is presumably due to residual pinning and defects in the crystal. Figure 8.5 shows a plot of the temperature dependence of the width of the edge current density, δ_E, derived from the fits to the experimental data, indicating an approximately linear relationship between δ_E and T in this measurement regime.

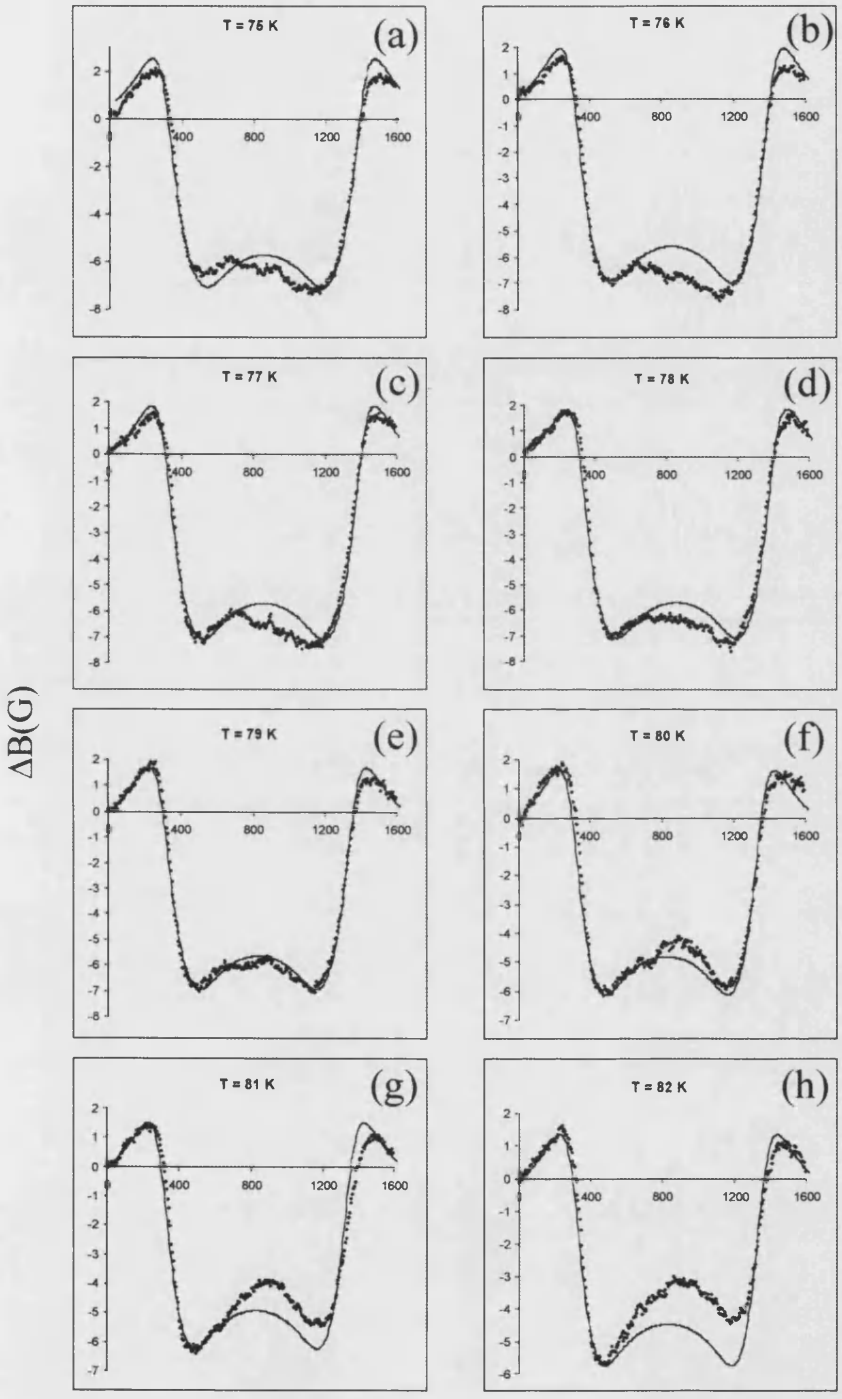

Fig. 8.4(a)-(h) Separate plots and fits to the data (shown in figure 8.3) based on the dome profile of the local magnetic induction as calculated by Zeldov *et al* [46].

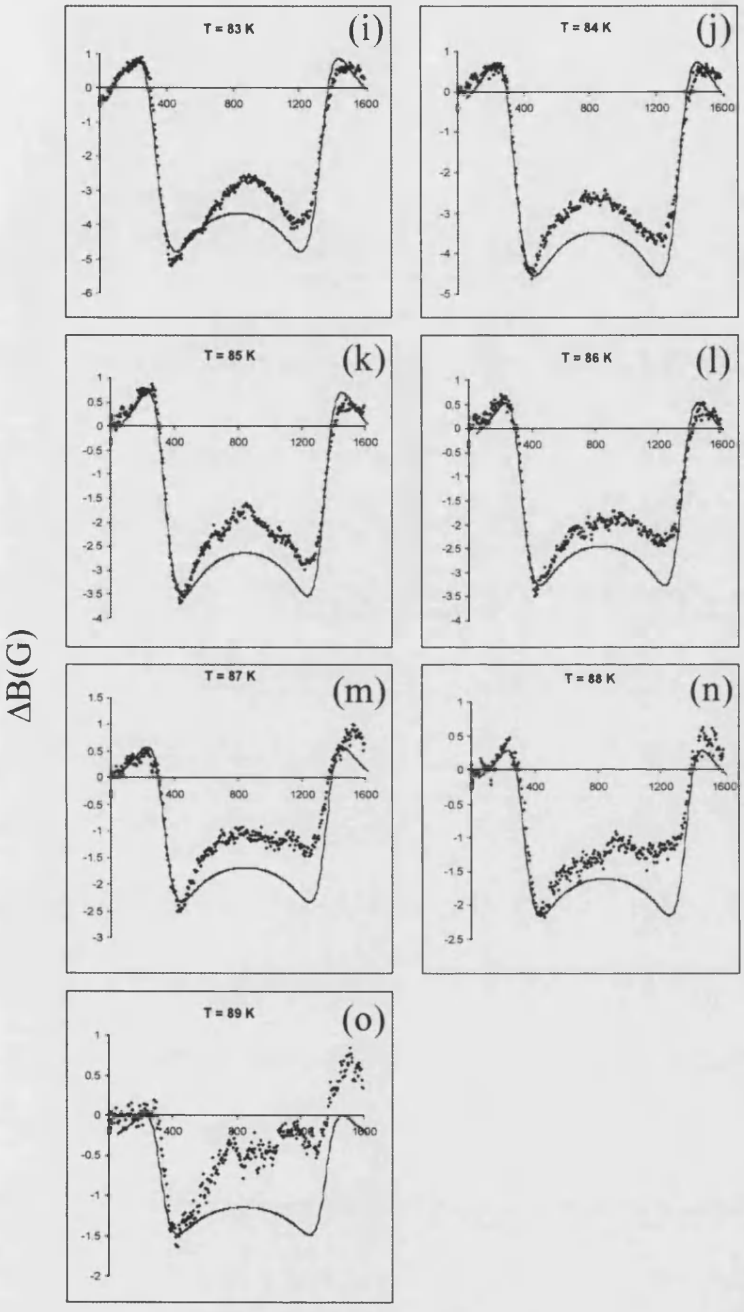

Fig. 8.4(i)-(o) continued plots and fits to the data (shown in figure 8.3) based on the dome profile of the local magnetic induction as calculated by Zeldov *et al* [46].

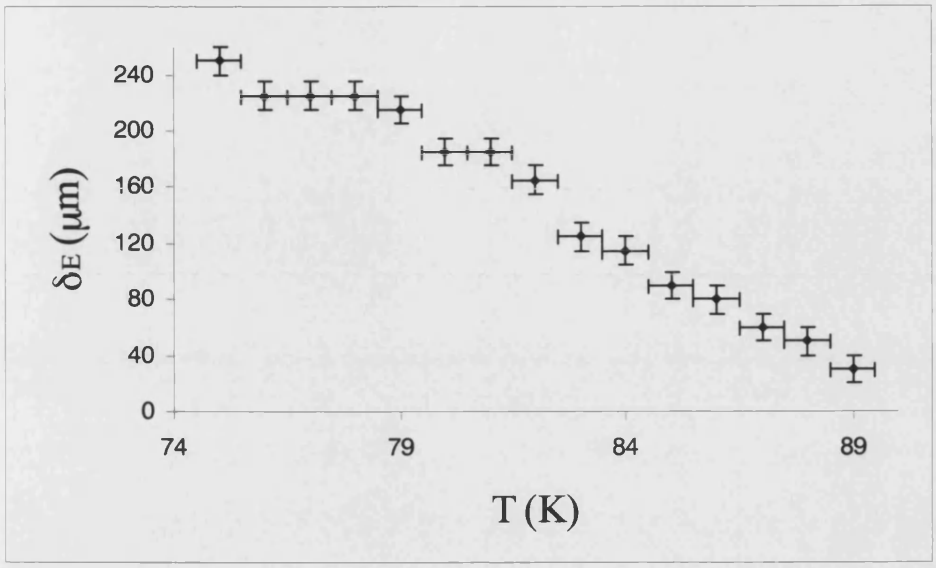

Fig. 8.5 Temperature dependence of the width of the edge current density, δ_E.

To gain a better understanding of the applied magnetic fields and temperature 'phase space' for our BSCCO single crystal sample 'local' magnetisation loops were measured at temperatures of 35, 40, 45, 50, 55, 60, 65, and 70 K shown in Figs.8.6(a)-(h), respectively. The magnetisation loops were recorded by positioning the sensor in the centre of the sample, and lowering it as close to the sample surface as possible. The applied magnetic field was then swept with the sensor stationary and the resulting local magnetisation $\mu_0 M_l = B_l - \mu_0 H$ recorded.

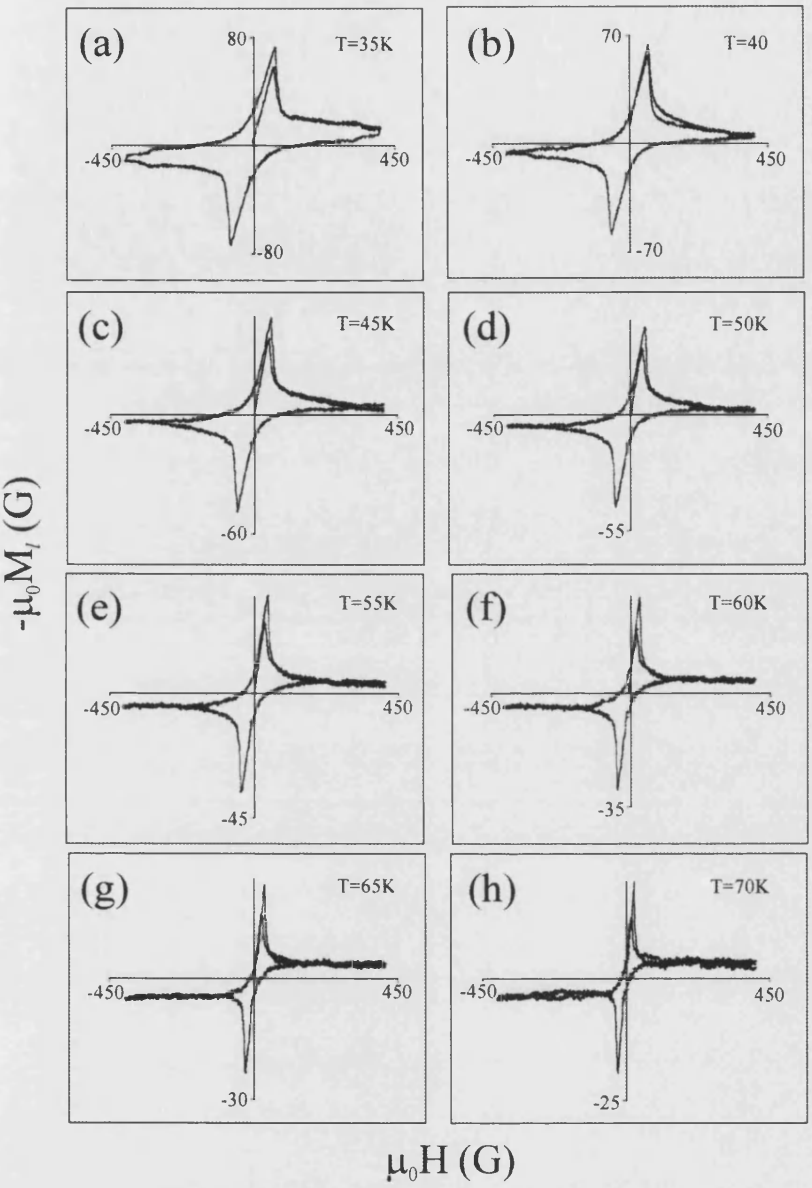

Fig. 8.6(a)-(h) Local magnetisation loops at various temperatures of the BSCCO single crystal sample, measured at the sample centre, with the applied magnetic field perpendicular to the sample surface.

As mentioned in chapter 4, section 4.3, at low temperatures and high fields a second peak in the magnetisation of BSCCO is observed. The second peak effect is interpreted as a vortex decoupling transition into almost independent two-dimensional pancakes which can better accommodate the pinning landscape than three-dimensional lines, leading to an enhanced value of critical current density, J_c, above the second peak than below it. At low temperatures the second peak is seen as a sharp increase in the magnetisation to a peak value, followed by decreasing magnetisation with increasing field, the so called 'fishtail' structure. Figure 8.7 shows the typical form of the second peak observed in the magnetisation loop of BSCCO seen at low temperatures [72].

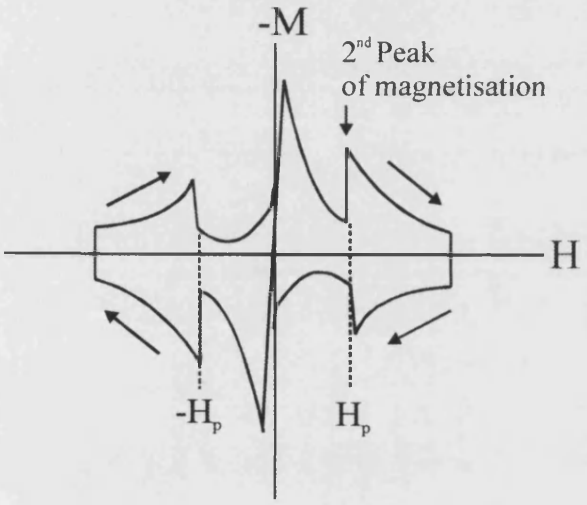

Fig. 8.7 Schematic representation of the second magnetisation peak seen in BSCCO at low temperatures.

Because of the relatively high minimum temperature available for investigation here (T = 35 K and the second peak is only observed for T < 40 K and only clearly observed for T ≤ 30 K), the signature of the second peak effect in the BSCCO single crystal sample is seen simply as a region of strong but relatively flat magnetisation which drops off quite fast above H_p, as shown in figures 8.6(a) and (b), rather than a pronounced second

magnetisation peak followed by a decrease at higher fields. Figure 8.8 shows a larger plot of the data of figure 8.6(a) illustrating these features in more detail.

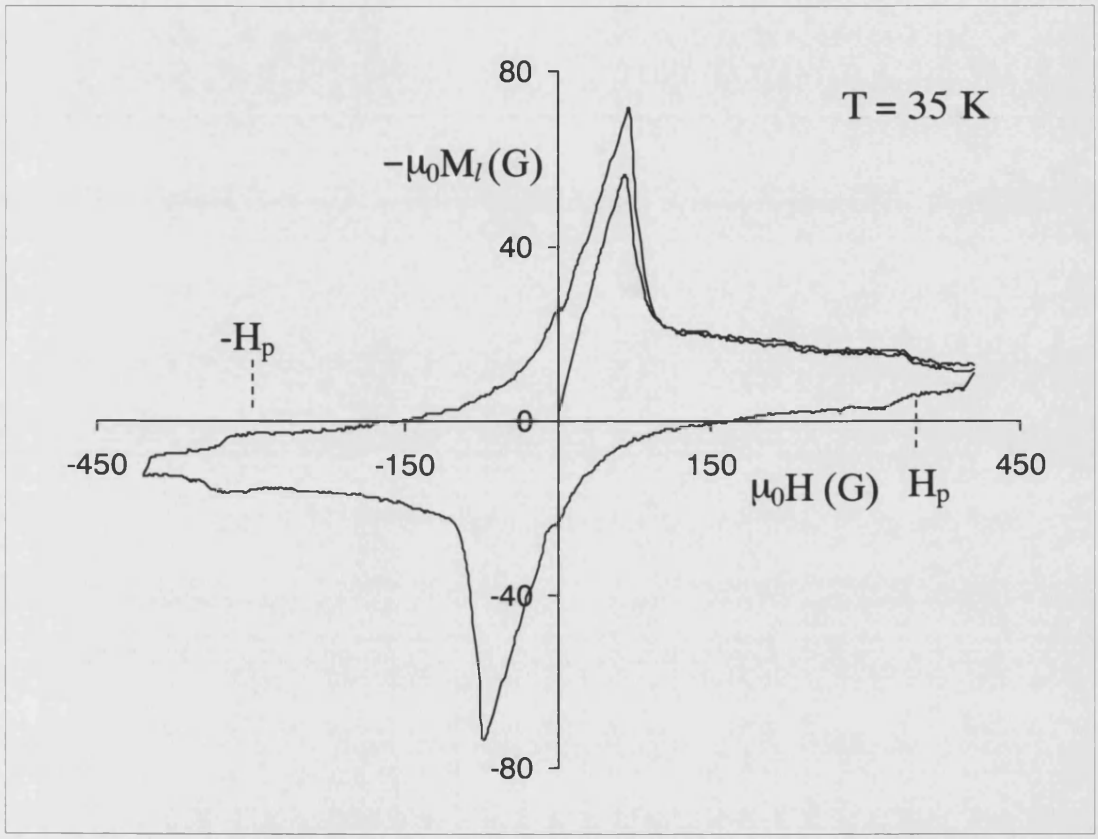

Fig. 8.8 Large plot of the magnetisation loop of the BSCCO single crystal taken at T = 35 K, illustrating the second peak magnetisation effect seen at this temperature.

Using the results of the magnetisation loops, the values of the applied magnetic field corresponding to the point where the magnetisation has fallen to ~ 70% of its first peak value were calculated for each temperature. Figure 8.9 shows the half width line scans taken at temperatures of 35, 40, 45, 50, 55, 60, 65, and 70 K, in the corresponding calculated applied magnetic fields, respectively. The scans were recorded to give an initial feel for the flux profile within the sample at various applied magnetic field and

temperature combinations. In each case the sample was zero-field cooled to the appropriate measurement temperature and the corresponding value of magnetic field applied perpendicular to the sample surface. The line scans are 800 μm in length, and were recorded using a step size of 5 μm. Again, the scans illustrate a dome-like flux profile within the sample in good agreement with the model of Zeldov *et al* [46] of flux profiles in thin flat samples.

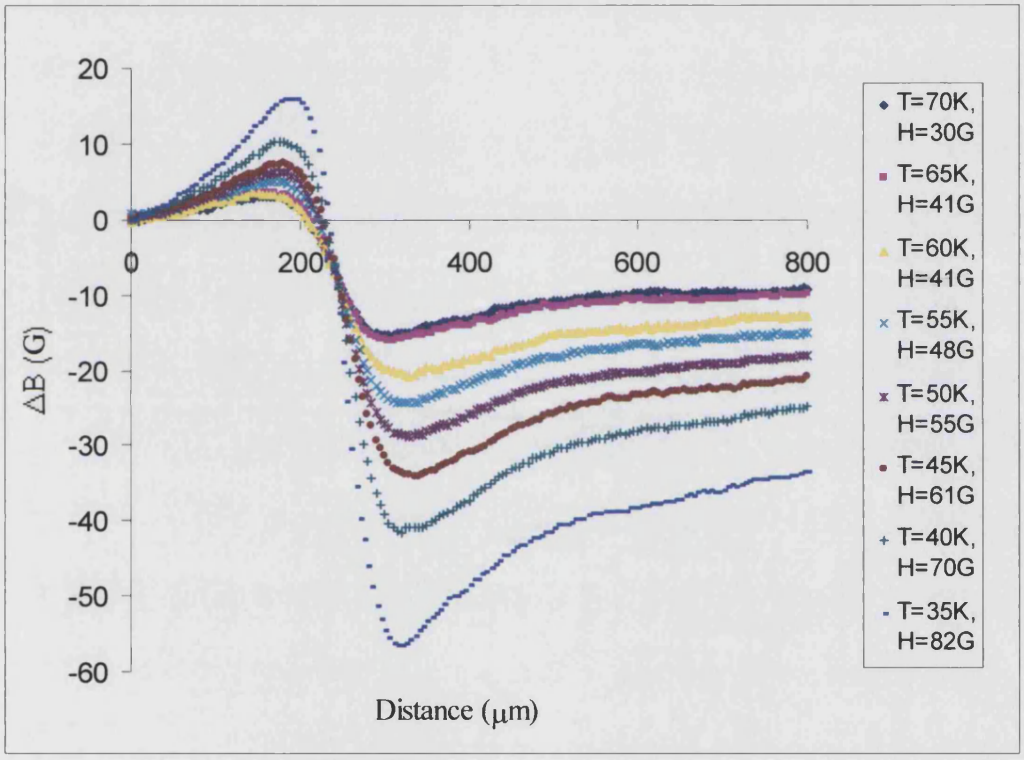

Fig. 8.9 Half-width zero-field cooled line scans of the BSCCO single crystal sample taken at various temperature and field combinations. Line scans 800μm with a step size of 5μm.

8.4.2 High fields, low temperatures

The two-dimensional scan of figure 8.10 shows the new orientation of the sample used to collect the line scans of figure 8.9 and the subsequent line scans presented here. The scan was taken at T = 40 K with an applied magnetic field of 70 G. The scan area is 1600 μm × 1600 μm with a step size of 25 μm. The line scan along the direction indicated is consistent with those of Figure 8.9 and illustrates the profile of the flux inside the superconductor over its entire width.

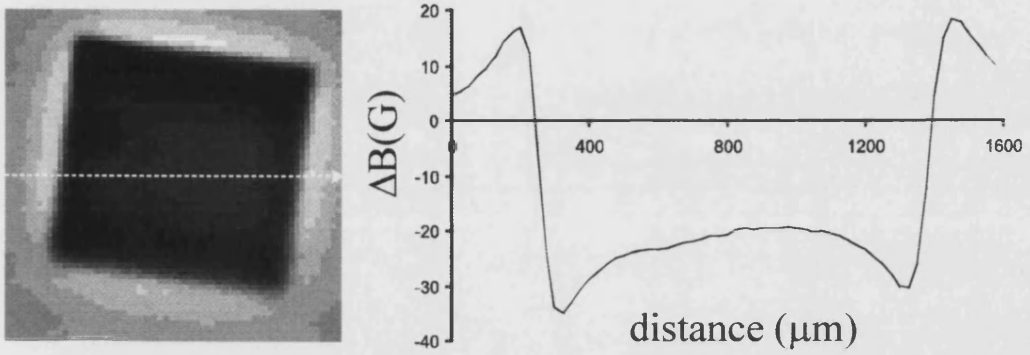

Fig. 8.10 Image of the BSCCO single crystal after zero-field cooling to 40 K followed by the application of 70G, the image shows the orientation of the sample with respect to the scan axes of the SHPM. The Line scan along the direction indicated illustrates the profile of the flux inside the superconductor over its entire width.

To systematically investigate the low temperature flux profile within the BSCCO single crystal sample with increasing applied magnetic field line scans were taken at T = 50 K in fields of 390, 360, 350, 340, 330, 165, 40, and 20G. In each case the sample was zero-field cooled to 50 K and the corresponding value of magnetic field applied perpendicular to the sample surface. The line scans are 1600 μm in length, and were recorded using a step size of 2.5 μm. Figures 8.11(a)-(h) show the evolution of the flux profile within the BSCCO sample with increasing magnetic fields, fits to the line scans taken in applied magnetic fields of 360, 350, 340, 330, and 165 are also shown based on the dome-shaped local magnetic induction profile without pinning as calculated by Zeldov *et al*

[46]. A fit to the data is not shown at 390G as at this elevated field value the model of Zeldov *et al* [46] is no longer valid due to enhanced pinning at these high field values above the second peak. Considering that pinning is not included in the model the fits to the jumps due to Meissner screening at the edges and the dome profiles are surprisingly good except at the very lowest fields where weak residual pinning is presumably sufficient to screen flux almost entirely from the sample. Indeed, in keeping with the results of the magnetisation loop recorded at 50 K (see figure 8.12), flux screening is more pronounced at low applied fields (H < 40G) increasing to a maximum value around the applied field corresponding to the Meissner peak at ~50G and then decreasing with increasing field. Figure 8.12 illustrates the positions of the line scans of figure 8.11(a)-(h) on the magnetisation loop. At applied magnetic fields of 165G and above, the profile takes on that of the one predicted by Zeldov *et al* [46] shown by the good agreement of the fits with the experimental data. From the fits to the data the width of the edge current density region, δ_E, was calculated at each field and its dependence on applied magnetic field is plotted in Figure 8.13. As with the dependence of δ_E on temperature, the relationship with applied magnetic field also appears to be approximately linear in this measurement regime.

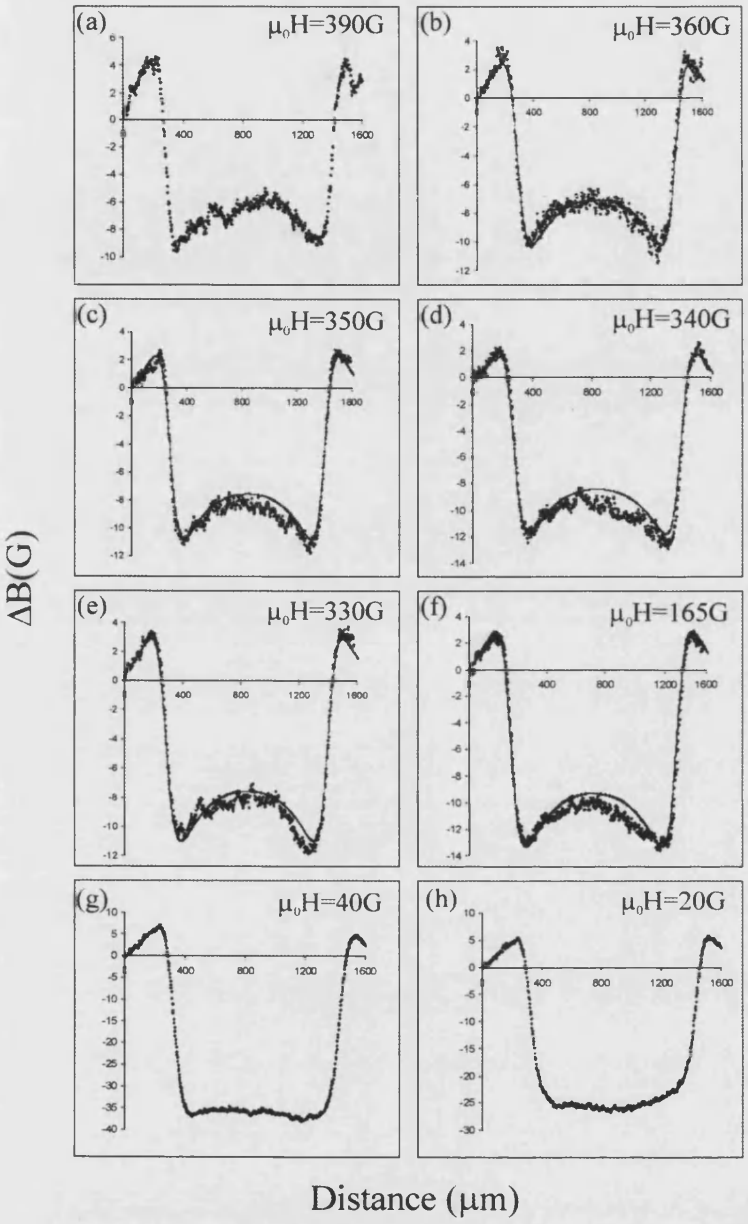

Fig. 8.11(a)-(h) Zero-field cooled line scans across the BSCCO single crystal sample at 50 K in various applied magnetic fields. Figs. 8.11(b) to (f) include fits to the data based on the dome profile model of Zeldov *et al* [46] shown as the solid black lines.

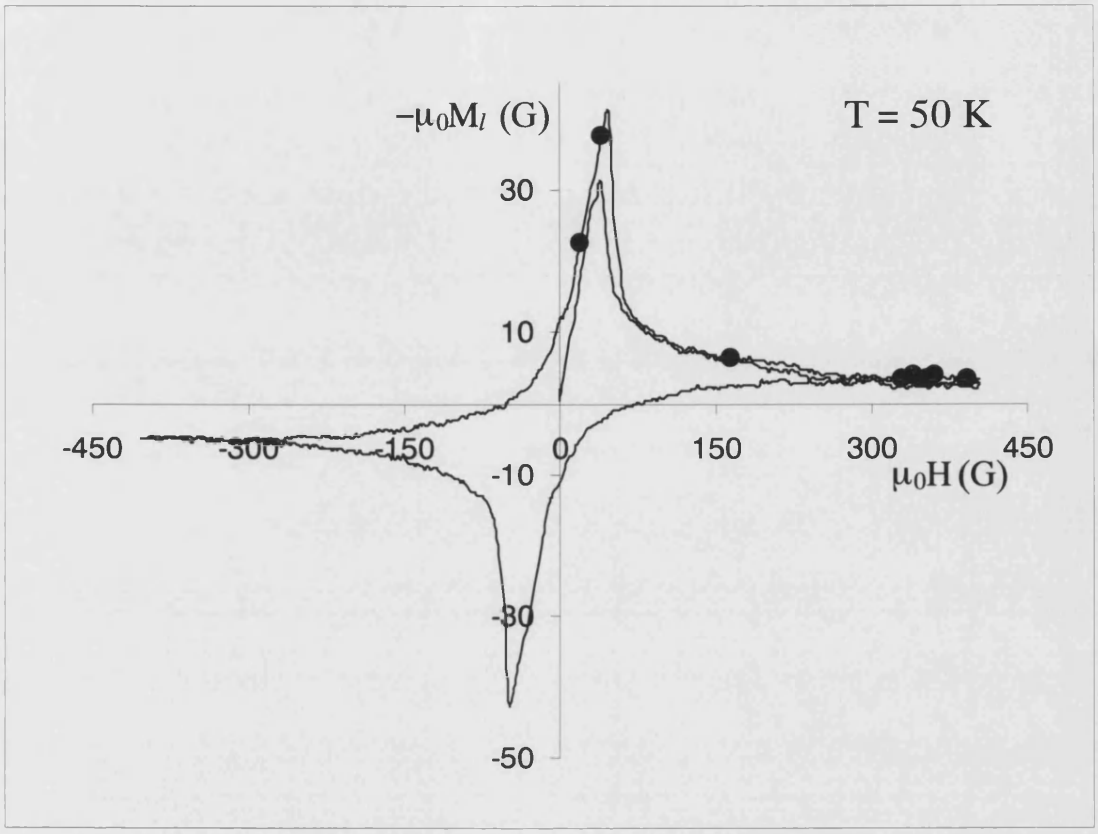

Fig. 8.12 Large plot of the magnetisation loop of the BSCCO single crystal taken at T = 50 K, illustrating the positions of the line scans of figure 8.11(a)-(h) on the magnetisation loop.

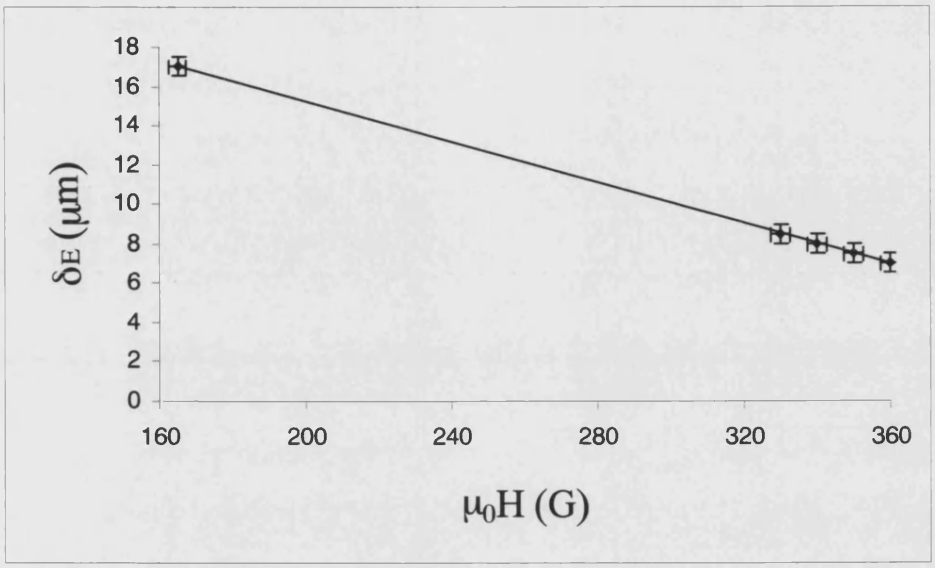

Fig. 8.13 Plot of the edge current density width, δ_E, dependence on applied magnetic field, calculated from the results of the fits to the experimental data taken at T = 50 K. The relationship appears to be linear in this measurement regime indicated by the good fit of the linear trend line to the data.

Since we were particularly interested in flux profiles near the second peak more line scans were taken at the system base temperature of 35 K, across the same point of the sample, in fields of 390, 350, 308, 100, 40, and 20G. In each case the sample was zero-field cooled to 35 K and the corresponding value of magnetic field applied perpendicular to the sample surface. The line scans are 1600 μm in length, and were recorded using a step size of 2.5 μm. Figures 8.14(a)-(f) show the evolution of the flux profile inside the sample with increasing field at this temperature. As at 50 K, screening is more pronounced at low applied fields (H ≤ 40G). At this lower temperature pinning effects are expected to dominate and the dome-like profile is no longer expected. Unlike at 50 K, where the flux profile within the superconductor shows no significant features apart from that of a dome-like profile, the scan of Figure 8.14(a) taken at T = 35 K in an

applied field of 390G shows complex features very different from the simple dome-like profile predicted by Zeldov *et al* [46] for high temperatures and low fields.

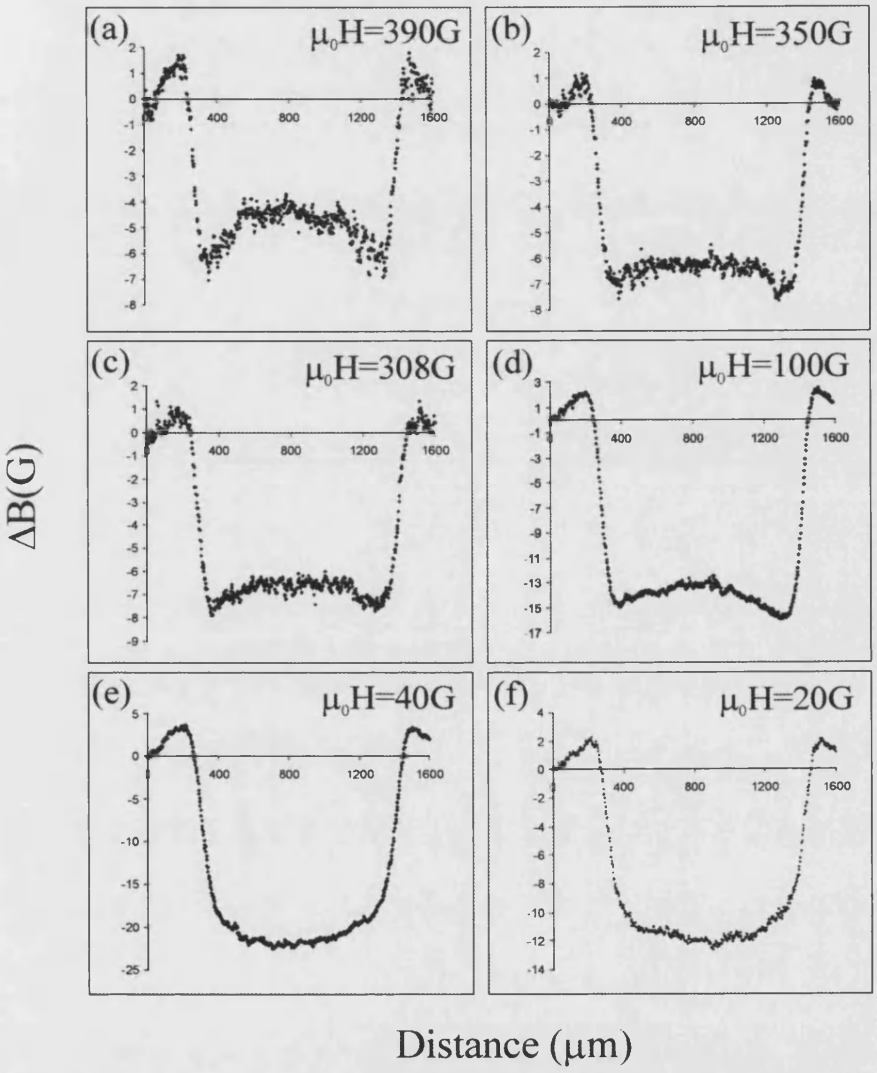

Fig. 8.14(a)-(f) Zero-field cooled line scans across the BSCCO single crystal sample at 35 K in various applied magnetic fields. Line scans 1600 μm, recorded with a step size of 2.5 μm.

Figure 8.15 shows a larger plot of the flux profile recorded at T = 35 K in an applied field of 390 G, illustrating the cusp-like features seen in the flux profile near the centre of the scan, and at ~1/4 and 3/4 of the way across it (indicated with vertical arrows).

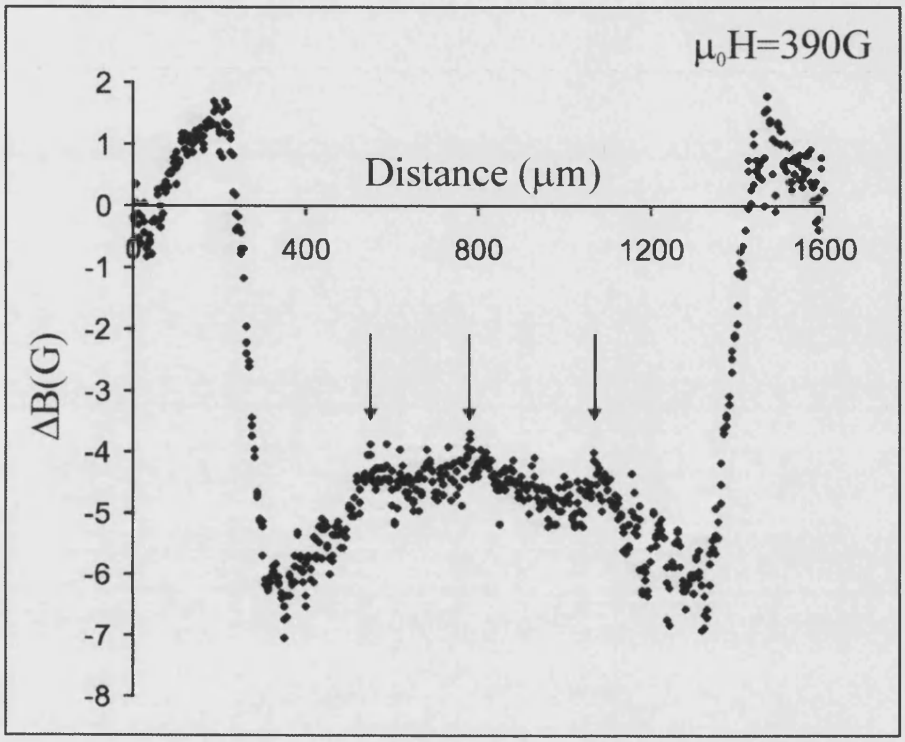

Fig. 8.15 Flux profile inside the BSCCO single crystal sample recorded at T = 35 K, after zero-field cooling, in an applied magnetic field of 390G. The plot shows the complex features seen in the flux profile within the sample indicated by the vertical arrows.

These features in the flux profile shown in figure 8.15 seem likely to be related to the second magnetisation peak. From figure 8.8 it can be seen that at an applied magnetic field of 390G the sample has passed beyond the second peak into the strong pinning regime. Since the second peak transition is driven by the local magnetic induction (i.e. $T_p = T_p(B)$), the dome profile causes the high pinning region to nucleate at the centre of the sample and grow out towards the edges as the applied field is increased (see Figure

8.16). Hence, it is possible that for H ~ H_p there exist two separate regions of critical current density within the superconducting sample, corresponding to the two different pinning regimes, as well as the edge current density corresponding to the Meissner screening currents. This is unlike the dome profile model for low fields and high temperatures where only the edge current density is assumed to exist.

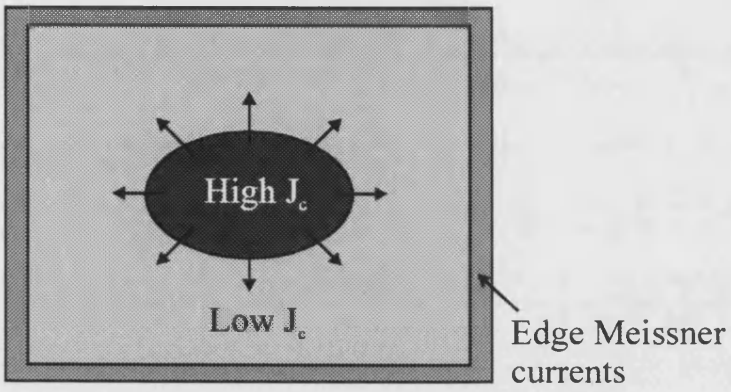

Fig. 8.16 Second peak magnetisation effect results in two separate current density regions in applied fields of H~ H_p. The region of high J_c nucleates at the centre and grows outwards as the applied field is increased.

To further investigate this scans were taken at T = 35 K in fields of 380, 390, 395, 400, 405, and 410G, shown in figures 8.17 to 8.22, respectively. In each case the sample was zero-field cooled to the 35 K and the corresponding value of magnetic field applied perpendicular to the sample surface. The line scans are 1600 μm in length, and were recorded using a step size of 2.5 μm. Data were fitted to a model where various regions of the sample are assigned a uniform critical current density which is fully saturated at these high fields (J = J_c). The current density changes discontinuously at the interfaces between these regions. While this is unphysical it is a rather good approximation to the true situation in the high field limit.

Figure 8.17 shows the plot of the data recorded at T= 35 K in an applied magnetic field of 380G, along with a fit to the data. In this case the model assumes a single region of

current density starting at the centre of the sample and extending across its entire width meeting with the edge current density at an interface near the edge of the sample (indicated by the vertical lines in fig. 8.17). The fit parameter Zd refers to the height of the Hall sensor above the sample surface, assumed to be 60μm in each case.

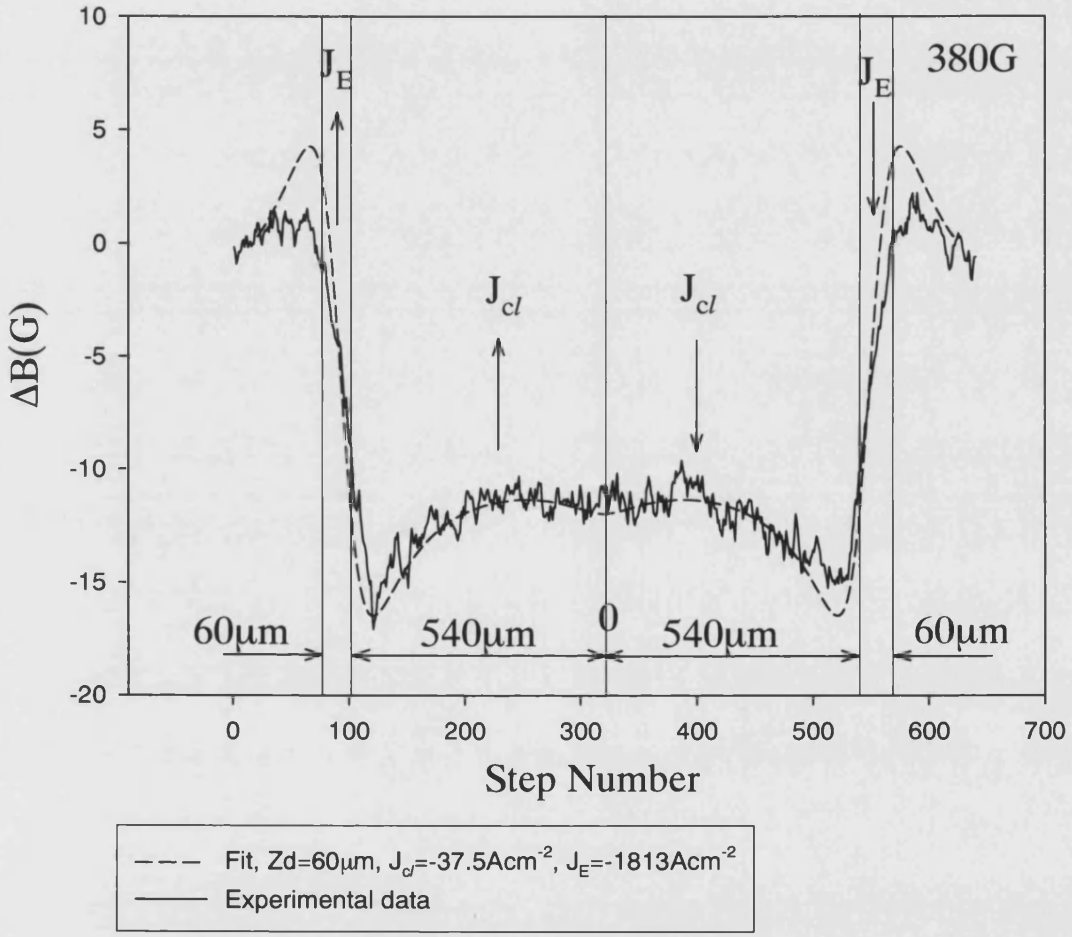

Fig. 8.17 Plot of the line scan recorded at T = 35 K in an applied magnetic field of 380G, and the fit to the data (dotted line) assuming a single region of current density, J_c, within the sample, along with the edge current density, J_E, corresponding to the Meissner screening currents at the edge of the sample. The directions and locations of the current density regions are indicated by the vertical arrows and lines.

Figure 8.18 shows the plot of the line scan recorded at T = 35 K in an applied magnetic field of 390G along with a fit of the data based on the model with two current densities, J_{cl}, and, J_{ch}, as well as the edge current density region due to the Meissner screening currents. As mentioned previously, the two current density regions are a result of the second peak effect at high fields and low temperatures forming two separate regions of critical current density, one reversed high critical current density region, J_{ch}, in the centre, and the other of lower current density, J_{cl}, extending to the edge of the sample. Because the second peak effect is driven by the local magnetic induction within the sample, the interface between the inner high critical current density region and the outer lower critical current density region will move from the centre outwards as the applied magnetic field increases. The directions and approximate locations of the different current density regions are indicated by the vertical lines and arrows in figure 8.18. The effect of these separate regions of current density on the flux profile within the BSCCO single crystal sample are very pronounced, with a peak in the collected flux at the centre of the sample clearly visible.

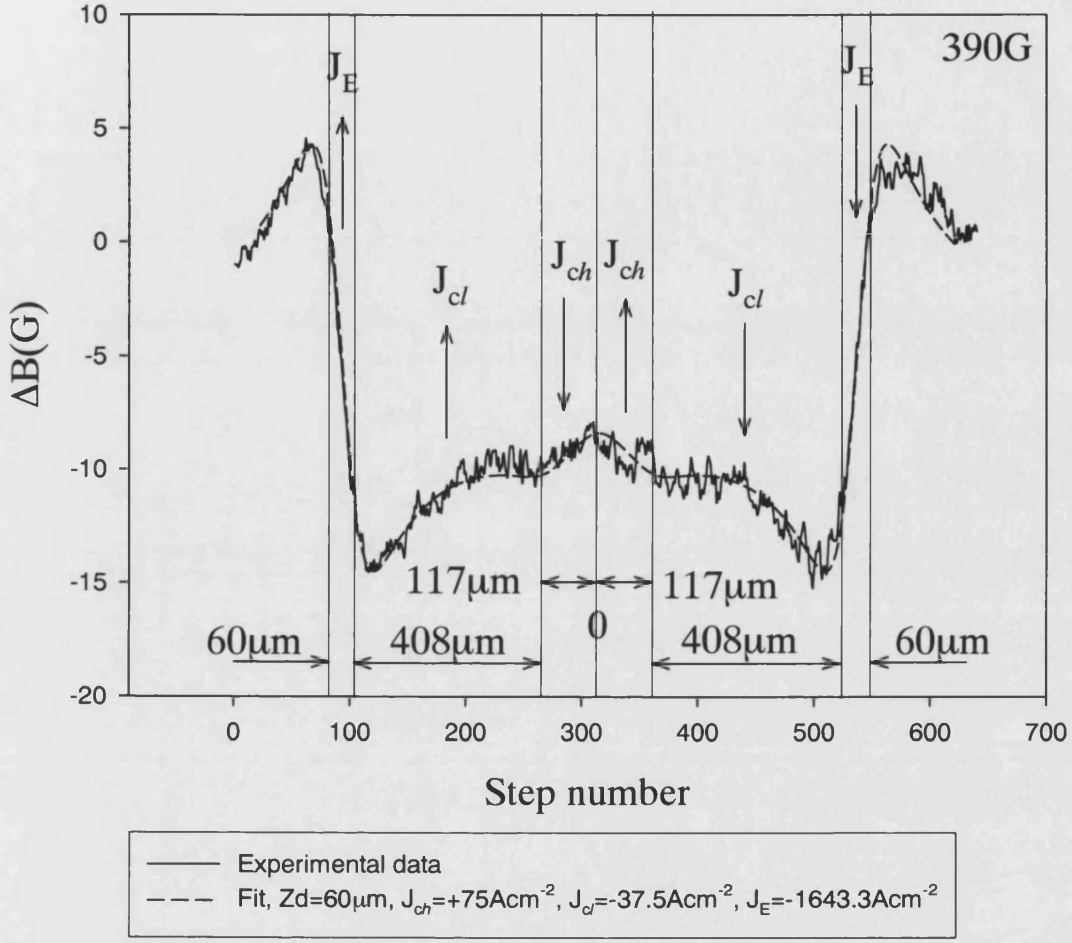

Fig. 8.18 Plot of the line scan recorded at T = 35 K in an applied magnetic field of 390G, and calculated fit to the data (dotted line) assuming two separate regions of current density. A high current density region, J_{ch}, at the centre of the sample and a lower current density region, J_{cl}, near the edge of the sample, as well as the current density at the edge of the sample, J_E.

Figure 8.19 shows the plot of the line scan recorded at T = 35 K in an applied magnetic field of 395G along with a fit of the data based on the same form of the model as for figure 8.18, again assuming two regions of current density within the sample as well as the edge current density corresponding to the Meissner screening currents. As expected a slight movement of the interface between the inner high current density region, J_{ch}, and the outer low current density region, J_{cl}, away from the centre of the sample towards the edge is seen.

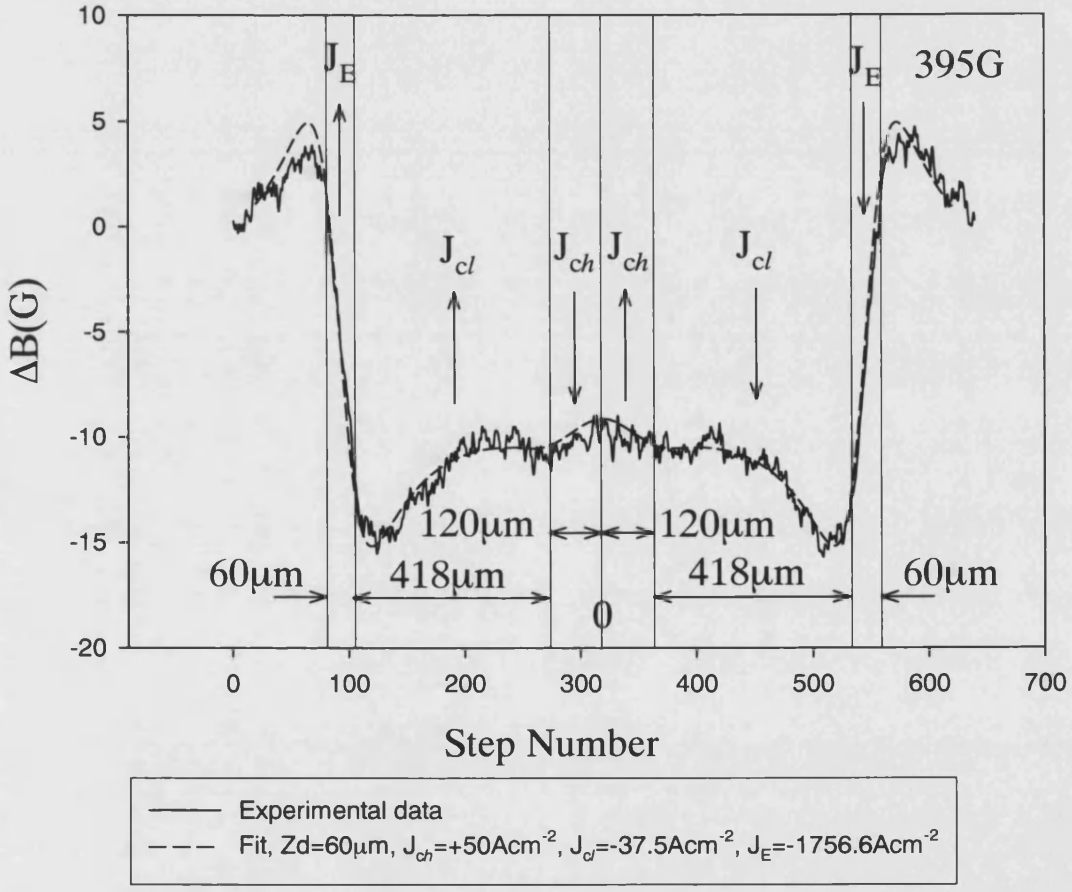

Fig. 8.19 Plot of the line scan recorded at T = 35 K in an applied magnetic field of 395G, and calculated fit to the data, again, assuming two separate regions of current density.

Figure 8.20 shows the plot of the line scan recorded at T = 35 K in an applied magnetic field of 400G along with a fit of the data, in this case, assuming three separate regions of current density of different magnitudes and directions as well as the edge current density due to the Meissner screening currents. The fit to the data is achieved by having three regions of current density one of which is a very thin, high magnitude region, J_{cI}, at the interface between the regions with current densities J_{cl} and J_{ch}, with opposite sign. This situation is again seen at T = 35 K in applied magnetic fields of 405, and 410G shown in figures 8.21 and 8.22, respectively. In each case the fit is achieved by assuming three current density regions with the interface between the two regions of current density J_{cl} and J_{ch}, and the corresponding interface current density J_{cI}, moving towards the outer edge of the sample, as expected from the interpretation in terms of a local magnetic induction transition at the second peak.

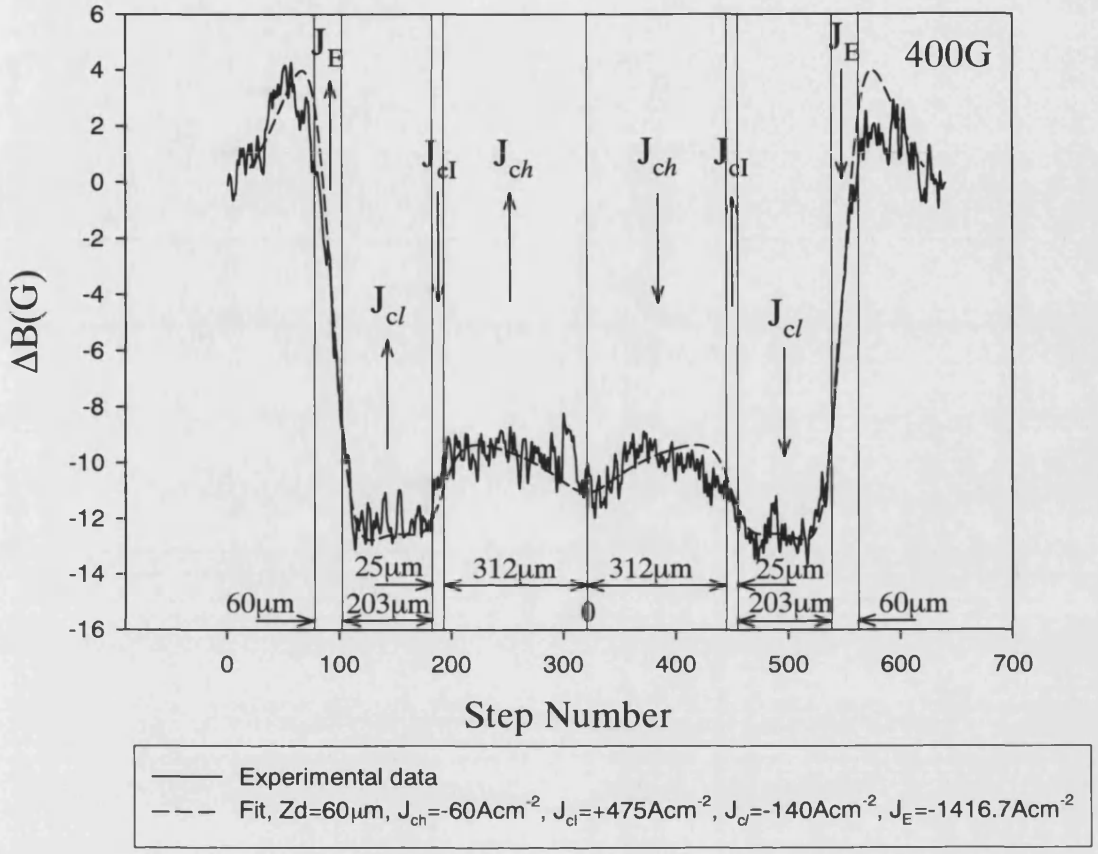

Fig. 8.20 Plot of the line scan recorded at T = 35 K in an applied magnetic field of 400 G, and calculated fit to the data, in this case, assuming three separate regions of current density as well as the current density at the edge of the sample corresponding to the Meissner screening currents. A very thin, high-magnitude current density, J_{cI}, with opposite sign to the other current density regions is thought to exist at the interface between J_{ch} and J_{cl} at increased applied fields.

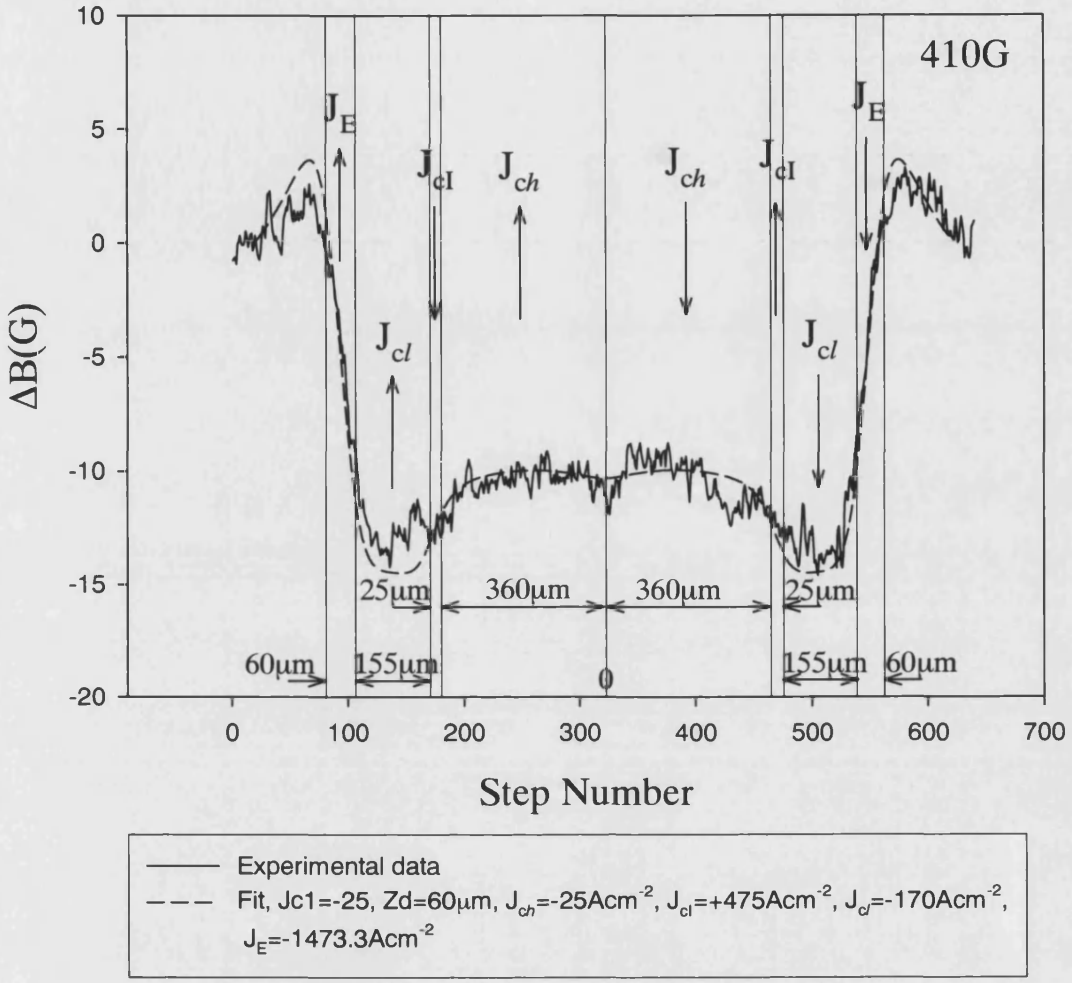

Fig. 8.21 Plot of the line scan recorded at T = 35 K in an applied magnetic field of 405 G, and calculated fit to the data, again, assuming three separate regions of current density.

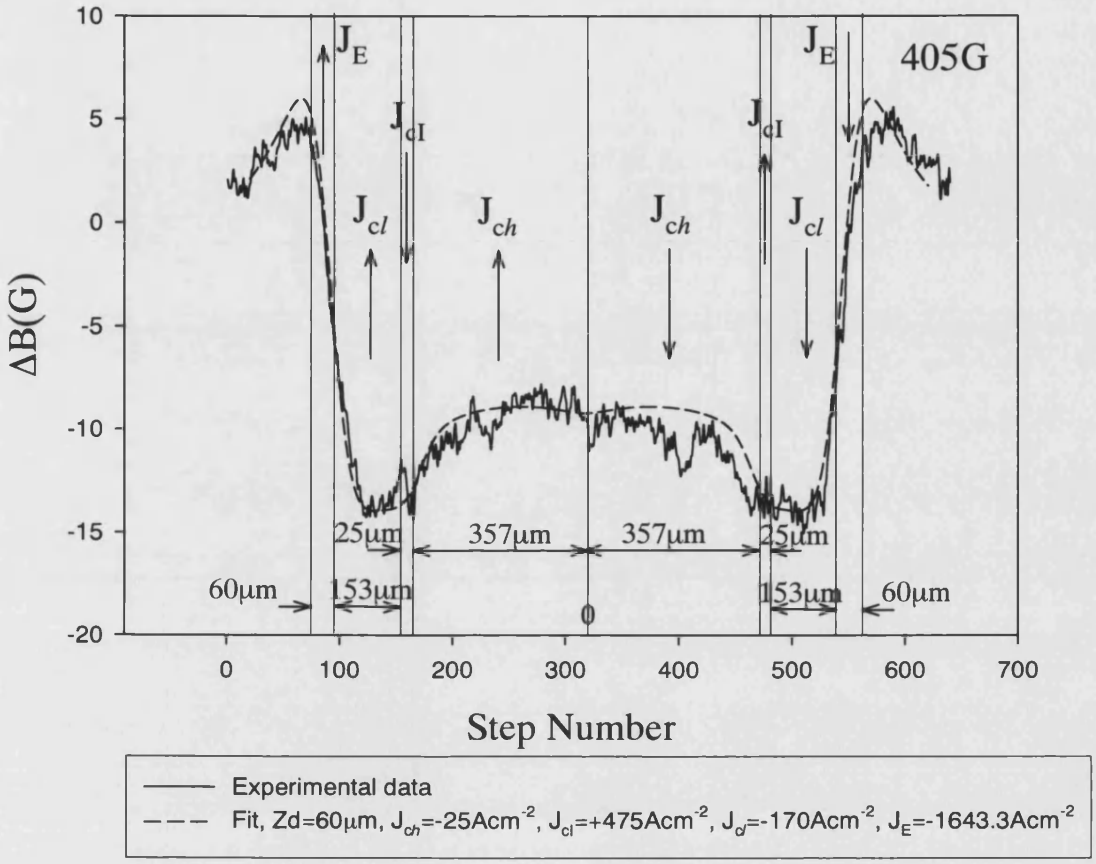

Fig. 8.22 Plot of the line scan recorded at T = 35 K in an applied magnetic field of 410 G, and calculated fit to the data assuming three separate regions of current density. The very thin, high-magnitude current density, J_{cI}, was found to persist even at this large value of applied field.

The appearance of the very thin, high magnitude current density region, J_{cI}, with opposite sign to the two current density regions which flank it was not anticipated and is a new effect not previously seen by other workers. It is believed that the interface between the two regions of current density J_{ch} and J_{cl} is unstable, and the interface current density, J_{cI}, seen at high fields, is the result of the formation of a topological barrier for flux to exit the high current density region, J_{ch}, at the centre of the sample.

When the centre of the sample first reached the transition at $T = T_p(B_l)$ a region of much higher critical current suddenly nucleates there, as this region grows it attempts to screen additional flux from this region of the sample. Since the region is topologically bounded on all sides there is no way for this pinned flux to exit the sample. As a consequence the growing interface of J_{ch} region becomes unstable, and a strip of reversed current density appears spontaneously to compensate the flux that would otherwise have been screened out.

The investigation at fields above 410G was not possible due to higher field values being beyond the capabilities of the electromagnets used to produce the applied magnetic fields in this study, but would be a worthy extension of the investigation presented here.

Chapter 9

9. Preliminary GaMnAs Results

Preliminary local magnetic induction scans at the surface of two different GaMnAs films with in-plane magnetisation are presented here, revealing information about the domain structures with in these materials. The results were recorded using the large area SHPM described in chapter 6 and another custom built high resolution SHPM previously developed at the University of Bath. The results agree relatively well with existing work in the field, but are presented here as a short preliminary investigation into whether the domain structures could be studied using the facilities available at Bath rather than a full investigation of the actual domain structures themselves.

9.1. GaMnAs Samples

Realising ferromagnetism in III – V based diluted magnetic semiconductors (DMS) has opened up the possibility of novel semiconducting devices which combine the functionality of semiconductors with that of ferromagnetic materials [106],[107],[108]. In magnetic materials, both the size and the shape of the magnetic domains are among the most fundamental quantities, because they reflect the magnitude and anisotropy of the microscopic exchange interaction. In addition, the domain structure is associated with the carrier conduction and the possible minimum size of magnetic bits in magnetic recording media, which are of technological importance for both electronic and magnetic devices.

Several scanning probe microscopic techniques for studying local magnetic properties, which detect the magnetic field from the sample surface, have been developed, such as the magnetic-force microscope [85], the scanning superconducting quantum interference device microscope [109], and the scanning Hall probe microscope (SHPM) [90]. SHPM has advantages of less magnetic invasiveness for the specimen and a wider operating temperature range.

SHPM measurements of the magnetic domain structures in ferromagnetic semiconducting GaMnAs films are presented here, recorded using the large area scanning hall probe microscope described in chapter 6 and an existing custom built high resolution SHPM developed at Bath [82].

Two different samples have been investigated. A 50 nm thick $Ga_{0.96}Mn_{0.04}As$ film with a T_c of ~ 72K, referred to as Mn014, and a 50 nm thick $Ga_{0.92}Mn_{0.08}As$ film with a T_c of ~ 112K, referred to as Mn031. Both samples were grown expitaxially on semi-insulating GaAs substrates by the use of molecular-beam epitaxy at the University of Nottimgham by Dr Kevin Edmonds. Due to the lattice mis-match the GaMnAs layers are under compressive strain and the magnetic anisotropy favours in-plane magnetisation of the layers.

The large area scanning Hall probe microscope of chapter 6 was used for the measurements of sample Mn014 and the high resolution SHPM used for the measurements of sample Mn031, with no external field applied to the samples in either case.

9.2. 2-D Scans

Figure 9.1 shows the SHPM image of Mn014 at 50 K. The scanned area is 160 μm × 160 μm with a step size of 2.5 μm. The grayscale of the image denotes the magnetic field perpendicular to the sample surface B_z, with an image contrast of ~ 1 G. The observed magnetic structure corresponds to the stray field from the boundary between the magnetic domains.

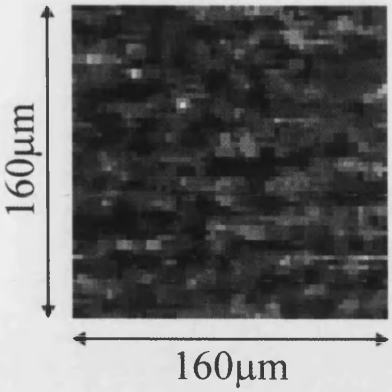

Fig. 9.1 Image of the GaMnAs film Mn014 in zero field at T = 50 K, recorded using the large area SHPM. Scan area 160 μm × 160 μm, step size 2.5 μm, gray scale spans ~ 1 G.

The appearance of the domain structure shown in figure 9.1 has a slight resemblance to the maze pattern seen as a result of wandering of stripe domains, often observed in the conventional ferromagnetic materials [110]. However, the maze pattern has only previously been seen in perpendicularly magnetised GaMnAs films [111],[112] and it is thought that the slight resemblance is merely a result of the relatively low spatial resolution of the image. This is further confirmed by the SHPM image shown in figure 9.2 of Mn031 taken at 77K. Figure 9.2 shows a 10 μm × 10 μm scan with a step size of 0.078 μm, with an image contrast of ~ 1 G. The image of Figure 9.2 is much more reminiscent of the domain structures previously seen in GaMnAs films with in-plane magnetisation [112], the distributions of the domains size and B_z vary and the arrangement of the domains appears random with several regions in the image showing no domain wall structure. Therefore it is thought that the image of figure 9.1 is an averaging of features similar to those seen in figure 9.2 and has no relation to the physical mechanisms involved with the maze pattern.

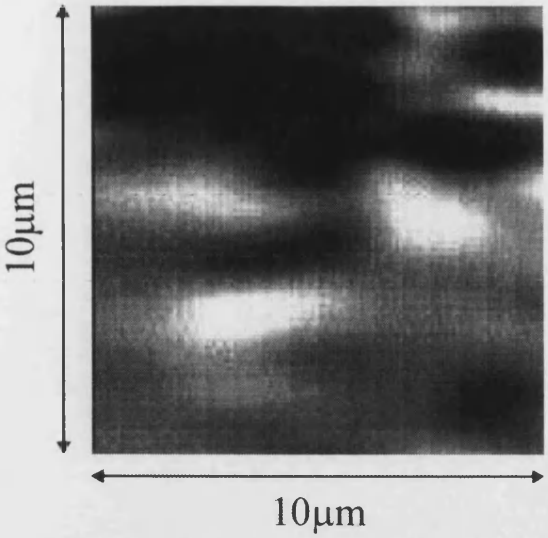

Fig. 9.2 Image of the GaMnAs film Mn031 in zero field at T = 77 K, recorded using the high resolution SHPM. Scan area 10 μm × 10 μm, step size 0.078 μm, grayscale spans ~ 1 G.

Figure 9.3(a)-(i) shows the temperature evolution of the domain structure seen in sample Mn031, at temperatures from 77 K up to 120 K. Each image is a 10 μm × 5 μm scan of the same area of the sample at increasing temperatures. At 120 K there appears to be no domain wall structure present in the image with the remaining grayscale at this temperature simply due to noise. Figure 9.4 shows a plot of the image grayscale, ΔB, for each image, (a) to (i) of figure 9.3, against temperature. From figure 9.4 it can be seen that the Curie temperature occurs at approximately 115 K, as above this temperature ΔB is no longer due to domain wall structure.

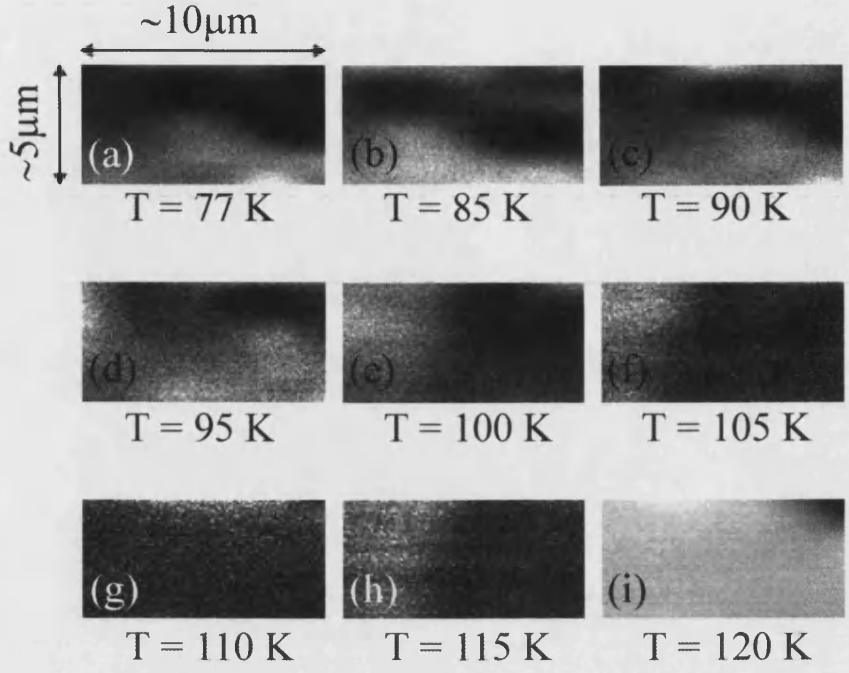

Fig. 9.3(a)-(i) Images of the same area of the GaMnAs film Mn031 in zero field and increasing temperatures of 77, 85, 90, 95, 100, 105, 110, 115 and 120 K, respectively. Scan area 10 μm × 5 μm, step size 0.078 μm.

Unfortunately a direct comparison of each measurement technique and sample is not possible as sample Mn014 was only viewed using the large area SHPM and conversely Mn031 was only measured using the high resolution SHPM. Repeated measurements of each film using both SHPMs are required in order to clarify the effects of the measurement procedure on the domain structures appearance, and to further investigate the nature of domain structures in GaMnAs films.

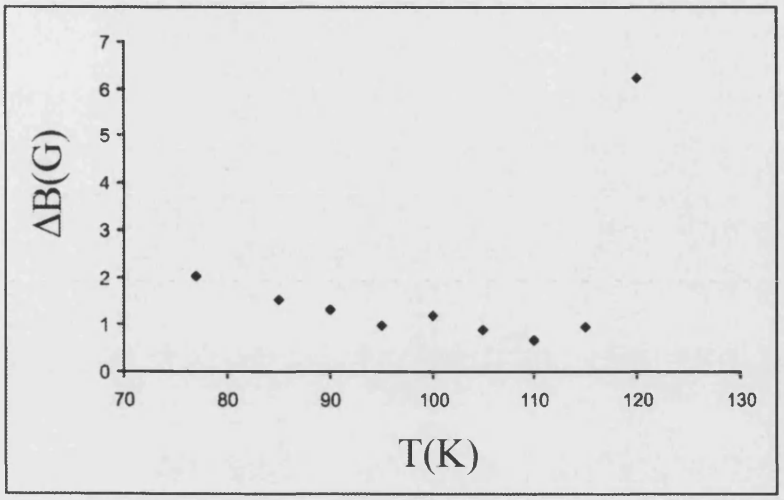

Fig. 9.4 Plot of the image grayscale, ΔB, for each image, (a) to (i) of figure 9.3, against temperature.

Chapter 10

10. Conclusions and Future Work

10.1. Conclusions

Many separate conclusions can be drawn from the work contained in this thesis, primarily in the four main research areas presented here; the evaluation of the large area SHPM, the suppression of surface barriers for flux penetration in $Bi_2Sr_2CaCu_2O_{8+\delta}$ whiskers by electron and heavy ion irradiation, the scanning Hall probe microscopy results of flux penetration into a superconducting $YBa_2Cu_3O_{7-\delta}$ thin-film strip, and the scanning Hall probe microscopy results of flux penetration into a superconducting $Bi_2Sr_2CaCu_2O_{8+\delta}$ platelet-like single crystal and $YBa_2Cu_3O_{7-\delta}$ thin film sample, recorded using the large area SHPM.

10.1.1 Evaluation of the large area SHPM

An extremely simple mechanical scanning stage has been combined with a micron-sized InSb Hall probe coupled to a closed-cycle refrigerator to build a novel scanning Hall probe microscope with high spatial resolution and large scan area. The capabilities of the instrument have been illustrated with images of data storage disks at 300K, superconducting squares at 40K, and superconducting thin-films at temperatures between 35 K and 80 K. Individual data bits from 5.25inch and 3.5inch floppy disks have been resolved using the SHPM, yielding quantitative information concerning bit size and magnetisation. The SHPM has also been successfully used to illustrate the temperature dependence of flux penetration into $YBa_2Cu_3O_{7-\delta}$ thin-film squares. Flux

penetration into an array of $YBa_2Cu_3O_{7-\delta}$ squares has also been successfully imaged after various field histories.

10.1.2 Suppression of Surface Barriers for Flux Penetration in BSCCO Whiskers by Electron and Heavy Ion Irradiation

Compelling evidence has been presented indicating that flux penetration in $Bi_2Sr_2CaCu_2O_{8+\delta}$ whiskers is governed by creep over Bean-Livingston-type surface barriers, which can be considerably weakened by high-energy electron or swift heavy ion irradiation. The greater reduction in penetration field, H_p, after heavy ion irradiation compared with that of electron irradiation is consistent with recent theory for the influence of columnar defects in layered superconductors [55]. At low temperatures ($T <$ 50 K) the exponential form of $H_p(T)$ is in reasonable agreement with existing theories [53],[43] for creep of 2D pancakes over a BL-barrier, and the magnitude of the reduction in the prefactor of the exponential form of $H_p(T)$ after electron and heavy ion irradiation is in fair agreement with recent calculations [55]. At higher temperatures ($T >$ 50 K) irradiation also suppresses the penetration field and the irreversibility, suggesting that their origin is again due to BL-type surface barriers. It is tentatively proposed that the creep of flux lines over BL surface barriers is important in this regime.

10.1.3 Scanning Hall Probe Microscopy of Flux Penetration into a Superconducting $YBa_2Cu_3O_{7-\delta}$ Thin Film Strip

It has been found that flux penetrates into a $YBa_2Cu_3O_{7-\delta}$ superconducting strip in the form of flux bundles at "weak" spots near the edge and established that these tend to correspond to slightly thinner regions of the film. The penetrated flux is spatially modulated along the edge of the strip with a temperature dependent period. The origin of the thickness variations is not fully understood but it is speculated that they may arise due to the inhomogeneous distribution of crystallographic defects. The results suggest that the production of smoother films and probably also better control of the lithographic process so as to avoid edge damage should increase the working field/current range of HTS devices.

10.1.4 Scanning Hall Probe Microscopy of Flux Penetration into a Superconducting $Bi_2Sr_2CaCu_2O_{8+\delta}$ Platelet-like Single Crystal Sample

At low fields (≤ 360G) and high temperatures (T ≥ 50 K) it has been shown that flux penetration into a superconducting $Bi_2Sr_2CaCu_2O_{8+\delta}$ platelet-like single crystal sample is in good agreement with theory and similar results presented by Zeldov *et al* [46], indicating that the flux penetration into the superconducting $Bi_2Sr_2CaCu_2O_{8+\delta}$ platelet-like single crystal sample is governed by a geometrical barrier as seen in thin flat samples. However, a new regime is indicated at high fields (≥ 390G) and low temperatures (T ≤ 35 K), near the second magnetisation peak. In this regime the sample not only has areas with different current density magnitudes but also current densities of different sign within the same region of the superconducting sample as the applied field is simply increased from zero. This is partly explained in terms of the nucleation of the second peak with a dome profile allowing two separate regions of critical current density to exist within the superconducting sample in fields of $H \sim H_p$, one high critical current region, J_{ch}, at the centre of the sample growing outwards with increasing applied magnetic field and a lower critical current region, J_{cl}, outside of this. However, at very high fields (≥ 400G), the region of reversed current density becomes compressed in a very narrow interface region, and a region of current density with normal sign forms at the sample centre. The origin of these complex phenomena is unclear but it is believed to be the result of the formation of a topological barrier for flux to exit the high current density region, J_{ch}, at the centre of the sample. This is in keeping with the movement of the interface current density region, J_{cI}, towards the outside of the sample with increasing applied magnetic field, corresponding to the expansion of the high current density region, J_{ch}. Much more work needs to be done before this fascinating behaviour will be understood in detail.

10.2. Future Work

With respect to the performance and operation of the large area SHPM. Development of faster scanning speeds, via better computer control of the stepper motor translation stages and improved data acquisition would represent a marked improvement to the

system. Also, a decrease in the minimum step size of the stepper motor stages, achieved by using stepper motors with an increased number of steps per revolution or the introduction of gearing to the existing motors, would effectively increase the spatial resolution of the SHPM if used with scanning Hall probe sensors with wire widths comparable or less than the minimum step size. However, the introduction of gearing may lead to "mechanical lag" in the movement translation stages resulting in inaccurate movement of the sensor.

An obvious immediate use of the SHPM would be to collect more results to extend the investigation of flux penetration into the superconducting $Bi_2Sr_2CaCu_2O_{8+\delta}$ platelet-like single crystal sample. Further study would hopefully reveal the underlying mechanism causing the, as yet, unexplained behaviour of the current density with increasing applied magnetic field. An extension to the preliminary investigation of the local magnetic induction of GaMnAs films to reveal information about the domain structures in these materials would also be an important extension to the work presented in this thesis. However, because of the small fields and high resolution requirements associated with these samples it is unlikely that the work could be carried out using the large area SHPM but would be possible using the existing high resolution SHPM previously developed at the University of Bath.

One possible large-scale future application for the large area SHPM could be in the non-destructive evaluation of microelectronic devices, such as flip-chip packages and multichip modules (MCMs). The currents flowing in a microelectronic device produce magnetic fields, which the SHPM could potentially detect. In particular, since magnetic fields at low frequencies pass unimpeded through metal and insulating layers, the SHPM is ideally suited for locating faults buried up to 1 μm below the surface of microelectronic devices. However, the spatial resolution of the large area SHPM would need to be increased, and Hall probes of greater sensitivity than those available at present would be required for this to be a viable possibility.

Appendix A

Calculations using the "Mathcad" software package

A.1 Calculation of the magnetic field from three gold wires each at different heights

Current in wires $I := 10 \cdot 10^{-3}$

Height above wire1 $g := 60 \cdot 10^{-6}$

Height above wire2 $h := 15 \cdot 10^{-6}$

Height above wire3 $i := 40 \cdot 10^{-6}$

$\mu := 4 \cdot \pi \cdot 10^{-7}$

Step size $x := 2.5 \cdot 10^{-6}$

Distance along x-axis $W := (0, 1 .. 760)$

Magnetic filed along x-axis at hight g,h,i

$$B_W := \frac{(\mu \cdot I \cdot (W - 195)) \cdot x}{2 \cdot \pi \cdot \left[g^2 + (((W - 195) \cdot x))^2\right]} + \frac{(\mu \cdot I \cdot (W - 375)) \cdot x}{2 \cdot \pi \cdot \left[h^2 + (((W - 375) \cdot x))^2\right]} + \frac{(\mu \cdot I \cdot (W - 610)) \cdot x}{2 \cdot \pi \cdot \left[i^2 + (((W - 610) \cdot x))^2\right]}$$

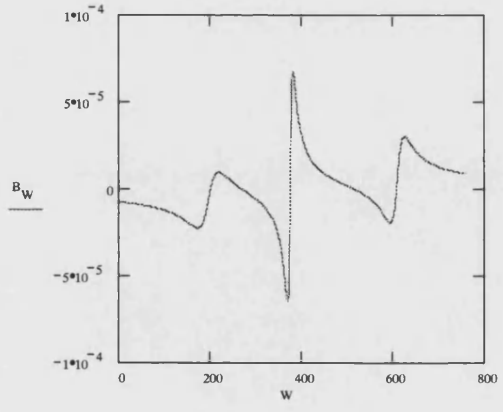

B =

	0
0	-7.485·10 -6
1	-7.513·10 -6
2	-7.541·10 -6
3	-7.57·10 -6
4	-7.598·10 -6
5	-7.627·10 -6
6	-7.657·10 -6
7	-7.686·10 -6
8	-7.716·10 -6
9	-7.746·10 -6
10	-7.776·10 -6
11	-7.807·10 -6
12	-7.838·10 -6
13	-7.869·10 -6
14	-7.9·10 -6
15	-7.932·10 -6

A.2 Calculation of the magnetic field from three gold wires each at the same height

Current in wires $I := 30 \cdot 10^{-3}$

Height above wire1 $g := 25 \cdot 10^{-6}$

Height above wire2 $h := 25 \cdot 10^{-6}$

Height above wire3 $i := 25 \cdot 10^{-6}$

$\mu := 4 \cdot \pi \cdot 10^{-7}$

Step size $x := 2.5 \cdot 10^{-6}$

Distance along x-axis $W := (0, 1 .. 760)$

Magnetic filed along x-axis at hight g,h,i

$$B_W := \frac{(\mu \cdot I \cdot (W - 160)) \cdot x}{2 \cdot \pi \cdot \left[g^2 + (((W - 160) \cdot x))^2\right]} + \frac{(\mu \cdot I \cdot (W - 375)) \cdot x}{2 \cdot \pi \cdot \left[h^2 + (((W - 375) \cdot x))^2\right]} + \frac{(\mu \cdot I \cdot (W - 560)) \cdot x}{2 \cdot \pi \cdot \left[i^2 + (((W - 560) \cdot x))^2\right]}$$

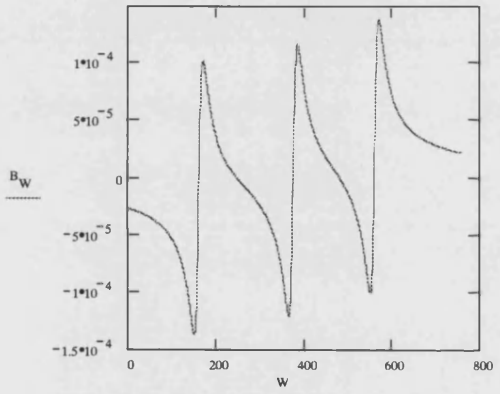

$B =$

	0
0	$-2.562 \cdot 10^{-5}$
1	$-2.574 \cdot 10^{-5}$
2	$-2.586 \cdot 10^{-5}$
3	$-2.598 \cdot 10^{-5}$
4	$-2.61 \cdot 10^{-5}$
5	$-2.622 \cdot 10^{-5}$
6	$-2.635 \cdot 10^{-5}$
7	$-2.648 \cdot 10^{-5}$
8	$-2.66 \cdot 10^{-5}$
9	$-2.673 \cdot 10^{-5}$
10	$-2.686 \cdot 10^{-5}$
11	$-2.699 \cdot 10^{-5}$
12	$-2.713 \cdot 10^{-5}$
13	$-2.726 \cdot 10^{-5}$
14	$-2.74 \cdot 10^{-5}$
15	$-2.754 \cdot 10^{-5}$

A.3 Calculation of the magnetic field from the meander-patterned gold wire

Current in meander line $I := 8 \cdot 10^{-3}$

Wire width of meanderline $W := 45 \cdot 10^{-6}$

Height of sensor above meanderline $h := 17 \cdot 10^{-6}$

$\mu := 4 \cdot \pi \cdot 10^{-7}$

$i := \frac{I}{W}$

Step size $x := 1.25 \cdot 10^{-6}$

Number of steps along x-axis $X := (0, 1 .. 300)$

$$B_X := \sum_{j=1}^{10} \left[\mu \frac{(-1)^j \cdot i}{20} \right] \cdot \ln \left[\frac{\left[h^2 + \left[((X + 90 - 50 \cdot j) \cdot x) + \frac{W}{2} \right]^2 \right]}{\left[h^2 + \left[(X + 90 - 50 \cdot j) \cdot x - \frac{W}{2} \right]^2 \right]} \right]$$

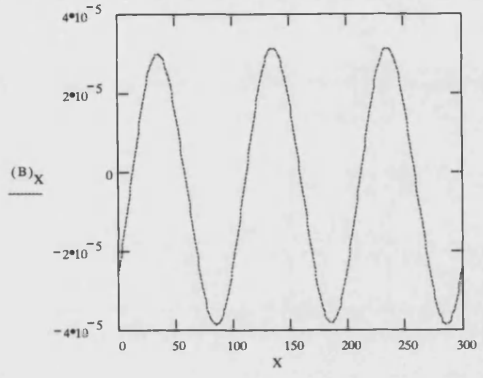

$(B)_X =$

$-2.607 \cdot 10^{-5}$
$-2.416 \cdot 10^{-5}$
$-2.22 \cdot 10^{-5}$
$-2.021 \cdot 10^{-5}$
$-1.819 \cdot 10^{-5}$
$-1.615 \cdot 10^{-5}$
$-1.41 \cdot 10^{-5}$
$-1.204 \cdot 10^{-5}$
$-9.971 \cdot 10^{-6}$
$-7.899 \cdot 10^{-6}$
$-5.825 \cdot 10^{-6}$
$-3.752 \cdot 10^{-6}$
$-1.683 \cdot 10^{-6}$
$3.796 \cdot 10^{-7}$
$2.433 \cdot 10^{-6}$
$4.475 \cdot 10^{-6}$

A.4 Dome profile simulation of the magnetic flux inside the BSCCO single crystal sample based on equation 3.17, section 3.8.

$ZW := 0.0565 + 0 \cdot i$ $\quad Hc1 := 78.7$

$Zd := 0.0051 \quad h := 0.0010$

$c := 3 \cdot 10^{10}$ $\quad Zb := ZW - .0009$ $\quad Hp := Hc1 \cdot \sqrt{\frac{Zd}{ZW}} \cdot 0.6$

$j := 0 .. 700 \quad h := .01$

$Ha := 1.6 \cdot Hp$

$Zx0_j := -(1.5 \cdot ZW) + 2.5 \cdot 10^{-4} \cdot j$

$Ha = 22.699$

$Ha := 360$

$Hp = 14.187$

$$ZI1_j := \int_{-ZW}^{-Zb} \frac{-Zx}{|Zx|} \frac{c \cdot Ha}{2 \cdot \pi \cdot Zd} \cdot \sqrt{\frac{Zx^2 - Zb^2}{ZW^2 - Zx^2}} \cdot \frac{(Zx0_j - Zx)}{2 \cdot \left[(Zx0_j - Zx)^2 + h^2\right]} dZx$$

$$ZI2_j := \int_{Zb}^{ZW} \frac{-Zx}{|Zx|} \frac{c \cdot Ha}{2 \cdot \pi \cdot Zd} \cdot \sqrt{\frac{Zx^2 - Zb^2}{ZW^2 - Zx^2}} \cdot \frac{(Zx0_j - Zx)}{2 \cdot \left[(Zx0_j - Zx)^2 + h^2\right]} dZx$$

$ZB := \frac{\pi \cdot Zd}{c} \frac{4 \cdot \pi}{10} \cdot (ZI1 + ZI2)$

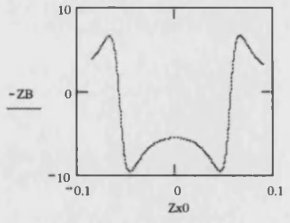

$-ZB =$

	0
0	3.855
1	3.887
2	3.92
3	3.953
4	3.987
5	4.021
6	4.055
7	4.09
8	4.125
9	4.16
10	4.196
11	4.232
12	4.269
13	4.306
14	4.344
15	4.382

$\frac{Ha - ZB_{100}}{Hc1} = 4.62$

A.5 Simulation of the magnetic field from the BSCCO single crystal sample in an applied field of 380G

$Fact := 1$

$g0 := 0.15$

$ZW := 0.06 + 0i$

$Hc1 := 300$

$Zd := \frac{ZW}{10}$

$Za := 0.4 \cdot ZW$

$h := Zd$

$Jc1 := -37.5$

$Zb := ZW - .006$

$Hp := Hc1 \cdot \sqrt{\frac{Zd}{ZW}} \cdot 0.6$

$JE := 320 \left(1 - \frac{1}{g0}\right)$

$j := 0 .. 600$

$Jc2 := -37.5$

$Zx0_j := -1.25\,ZW + j \cdot 0.00025$

$$ZI1_j := \int_{-Za}^{0} \frac{Jc1}{2} \cdot \frac{(Zx0_j - Zx)}{(Zx0_j - Zx)^2 + h^2} dZx \qquad ZI2_j := \int_{-Zb}^{-Za} \frac{Jc2}{2} \cdot \frac{(Zx0_j - Zx)}{(Zx0_j - Zx)^2 + h^2} dZx$$

$$ZI3_j := \int_{-ZW}^{-Zb} \frac{JE}{2} \cdot \frac{(Zx0_j - Zx)}{(Zx0_j - Zx)^2 + h^2} dZx$$

$$ZI4_j := \int_{0}^{Za} \frac{-Jc1}{2} \cdot \frac{(Zx0_j - Zx)}{(Zx0_j - Zx)^2 + h^2} dZx \qquad ZI5_j := \int_{Za}^{Zb} \frac{-Jc2}{2} \cdot \frac{(Zx0_j - Zx)}{(Zx0_j - Zx)^2 + h^2} dZx$$

$$ZI6_j := \int_{Zb}^{ZW} \frac{-JE}{2} \cdot \frac{(Zx0_j - Zx)}{(Zx0_j - Zx)^2 + h^2} dZx$$

$$ZBZ := \left(\frac{\pi \cdot Zd \cdot 4 \cdot \pi}{10}\right) \cdot (ZI1 + ZI2 + ZI3 + ZI4 + ZI5 + ZI6)$$

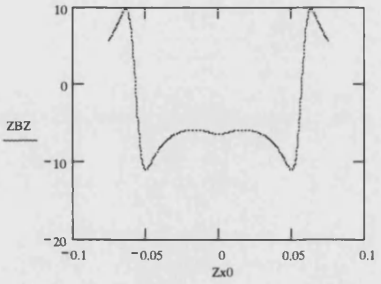

$$M_{j,0} := \frac{Zx0_j}{.00025} + 321 \qquad M_{j,1} := ZBZ_j - 5.5$$

A.6 Simulation of the magnetic field from the BSCCO single crystal sample in an applied field of 390G

$Fact := 1$

$g0 := 0.15$

$ZW := 0.0585 + 0 \cdot i$

$Hc1 := 300$

$Zd := \frac{ZW}{10}$

$Za := 0.2 \cdot ZW$

$h := Zd$

$Jc1 := 75$

$Zb := ZW - .006$

$Hp := Hc1 \cdot \sqrt{\frac{Zd}{ZW}} \cdot 0.6$

$JE := 290 \cdot \left(1 - \frac{1}{g0}\right)$

$j := 0 .. 600$

$Jc2 := -37.5$

$Zx0_j := -1.25\,ZW + j \cdot 0.00025$

$$ZI1_j := \int_{-Za}^{0} \frac{Jc1}{2} \cdot \frac{(Zx0_j - Zx)}{(Zx0_j - Zx)^2 + h^2}\, dZx \qquad ZI2_j := \int_{-Zb}^{-Za} \frac{Jc2}{2} \cdot \frac{(Zx0_j - Zx)}{(Zx0_j - Zx)^2 + h^2}\, dZx$$

$$ZI3_j := \int_{-ZW}^{-Zb} \frac{JE}{2} \cdot \frac{(Zx0_j - Zx)}{(Zx0_j - Zx)^2 + h^2}\, dZx$$

$$ZI4_j := \int_{0}^{Za} \frac{-Jc1}{2} \cdot \frac{(Zx0_j - Zx)}{(Zx0_j - Zx)^2 + h^2}\, dZx \qquad ZI5_j := \int_{Za}^{Zb} \frac{-Jc2}{2} \cdot \frac{(Zx0_j - Zx)}{(Zx0_j - Zx)^2 + h^2}\, dZx$$

$$ZI6_j := \int_{Zb}^{ZW} \frac{-JE}{2} \cdot \frac{(Zx0_j - Zx)}{(Zx0_j - Zx)^2 + h^2}\, dZx$$

$$ZBZ := \left(\frac{\pi \cdot Zd \cdot 4 \cdot \pi}{10}\right) \cdot (ZI1 + ZI2 + ZI3 + ZI4 + ZI5 + ZI6)$$

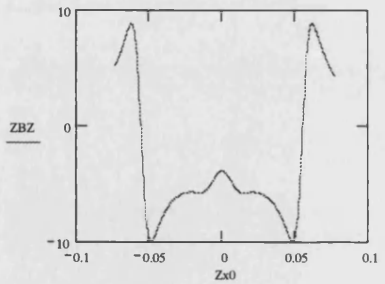

$$M_{j,0} := \frac{Zx0_j}{.00025} + 315 \qquad M_{j,1} := ZBZ_j - 4.5$$

A.7 Simulation of the magnetic field from the BSCCO single crystal sample in an applied field of 395G

$Fact := 1$

$g0 := 0.15$

$ZW := 0.05975 + 0 \cdot i$

$Hc1 := 300$

$Zd := \frac{ZW}{10}$

$Za := 0.2 \cdot ZW$

$h := Zd$

$Jc1 := 50$

$Zb := ZW - .006$

$JE := 310 \cdot \left(1 - \frac{1}{g0}\right)$

$Hp := Hc1 \cdot \sqrt{\frac{Zd}{ZW}} \cdot 0.6$

$j := 0 .. 600$

$Jc2 := -37.5$

$Zx0_j := -1.25\,ZW + j \cdot 0.00025$

$$ZI1_j := \int_{-Za}^{0} \frac{Jc1}{2} \cdot \frac{(Zx0_j - Zx)}{(Zx0_j - Zx)^2 + h^2}\, dZx \qquad ZI2_j := \int_{-Zb}^{-Za} \frac{Jc2}{2} \cdot \frac{(Zx0_j - Zx)}{(Zx0_j - Zx)^2 + h^2}\, dZx$$

$$ZI3_j := \int_{-ZW}^{-Zb} \frac{JE}{2} \cdot \frac{(Zx0_j - Zx)}{(Zx0_j - Zx)^2 + h^2}\, dZx$$

$$ZI4_j := \int_{0}^{Za} \frac{-Jc1}{2} \cdot \frac{(Zx0_j - Zx)}{(Zx0_j - Zx)^2 + h^2}\, dZx \qquad ZI5_j := \int_{Za}^{Zb} \frac{-Jc2}{2} \cdot \frac{(Zx0_j - Zx)}{(Zx0_j - Zx)^2 + h^2}\, dZx$$

$$ZI6_j := \int_{Zb}^{ZW} \frac{-JE}{2} \cdot \frac{(Zx0_j - Zx)}{(Zx0_j - Zx)^2 + h^2}\, dZx$$

$$ZBZ := \left(\frac{\pi \cdot Zd \cdot 4 \cdot \pi}{10}\right) \cdot (ZI1 + ZI2 + ZI3 + ZI4 + ZI5 + ZI6)$$

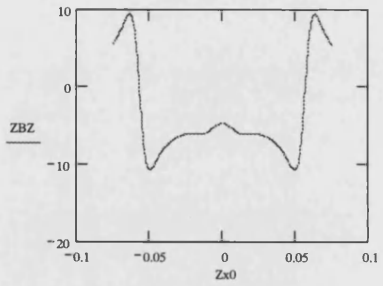

$$M_{j,0} := \frac{Zx0_j}{.00025} + 319 \qquad M_{j,1} := ZBZ_j - 4.5$$

A.8 Simulation of the magnetic field from the BSCCO single crystal sample in an applied field of 400G

$Fact := 1$

$g0 := 0.15$

$ZW := 0.06 + 0 \cdot i$

$Hc1 := 300$

$Zd := \frac{ZW}{10}$

$Za := 0.6 \cdot ZW$

$h := Zd$

$Jc1 := -60$

$Zb := ZW - .006$

$Hp := Hc1 \cdot \sqrt{\frac{Zd}{ZW}} \cdot 0.6$

$JE := 250 \cdot \left(1 - \frac{1}{g0}\right)$

$j := 0 .. 600$

$Jc2 := -175$

$Zx0_j := -1.25\,ZW + j \cdot 0.00025$

$$ZI1_j := \int_{-Za}^{0} \frac{Jc1}{2} \cdot \frac{(Zx0_j - Zx)}{(Zx0_j - Zx)^2 + h^2}\, dZx \qquad ZI2_j := \int_{-Zb}^{-Za} \frac{Jc2}{2} \cdot \frac{(Zx0_j - Zx)}{(Zx0_j - Zx)^2 + h^2}\, dZx$$

$$ZI3_j := \int_{-ZW}^{-Zb} \frac{JE}{2} \cdot \frac{(Zx0_j - Zx)}{(Zx0_j - Zx)^2 + h^2}\, dZx$$

$$ZI4_j := \int_{0}^{Za} \frac{-Jc1}{2} \cdot \frac{(Zx0_j - Zx)}{(Zx0_j - Zx)^2 + h^2}\, dZx \qquad ZI5_j := \int_{Za}^{Zb} \frac{-Jc2}{2} \cdot \frac{(Zx0_j - Zx)}{(Zx0_j - Zx)^2 + h^2}\, dZx$$

$$ZI6_j := \int_{Zb}^{ZW} \frac{-JE}{2} \cdot \frac{(Zx0_j - Zx)}{(Zx0_j - Zx)^2 + h^2}\, dZx$$

$$ZBZ := \left(\frac{\pi \cdot Zd \cdot 4 \cdot \pi}{10}\right) \cdot (ZI1 + ZI2 + ZI3 + ZI4 + ZI5 + ZI6)$$

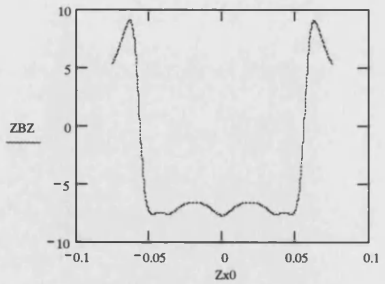

$$M_{j,0} := \frac{Zx0_j}{.00025} + 321 \qquad M_{j,1} := ZBZ_j - 5.0$$

A.9 Simulation of the magnetic field from the BSCCO single crystal sample in an applied field of 405G

$Fact := 1$

$g0 := 0.15$

$ZW := 0.0595 + 0 \cdot i$

$Hc1 := 300$

$Zd := \frac{ZW}{10}$

$Za := 0.35 \cdot ZW$

$h := Zd$

$Jc1 := -20$

$Zb := ZW - .006$

$Hp := Hc1 \cdot \sqrt{\frac{Zd}{ZW}} \cdot 0.6$

$JE := 330 \cdot \left(1 - \frac{1}{g0}\right)$

$j := 0 .. 600$

$Jc2 := -20$

$Zx0_j := -1.25\,ZW + j \cdot 0.00025$

$$ZI1_j := \int_{-Za}^{0} \frac{Jc1}{2} \cdot \frac{(Zx0_j - Zx)}{(Zx0_j - Zx)^2 + h^2}\, dZx \qquad ZI2_j := \int_{-Zb}^{-Za} \frac{Jc2}{2} \cdot \frac{(Zx0_j - Zx)}{(Zx0_j - Zx)^2 + h^2}\, dZx$$

$$ZI3_j := \int_{-ZW}^{-Zb} \frac{JE}{2} \cdot \frac{(Zx0_j - Zx)}{(Zx0_j - Zx)^2 + h^2}\, dZx$$

$$ZI4_j := \int_{0}^{Za} \frac{-Jc1}{2} \cdot \frac{(Zx0_j - Zx)}{(Zx0_j - Zx)^2 + h^2}\, dZx \qquad ZI5_j := \int_{Za}^{Zb} \frac{-Jc2}{2} \cdot \frac{(Zx0_j - Zx)}{(Zx0_j - Zx)^2 + h^2}\, dZx$$

$$ZI6_j := \int_{Zb}^{ZW} \frac{-JE}{2} \cdot \frac{(Zx0_j - Zx)}{(Zx0_j - Zx)^2 + h^2}\, dZx$$

$$ZBZ := \left(\frac{\pi \cdot Zd \cdot 4 \cdot \pi}{10}\right) \cdot (ZI1 + ZI2 + ZI3 + ZI4 + ZI5 + ZI6)$$

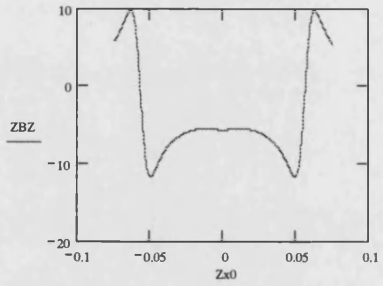

$$M_{j,0} := \frac{Zx0_j}{.00025} + 318 \qquad M_{j,1} := ZBZ_j - 4.0$$

A.10 Simulation of the magnetic field from the BSCCO single crystal sample in an applied field of 410G

$Fact := 1$

$g0 := 0.15$

$ZW := 0.06 + 0 \cdot i$

$Hc1 := 300$

$Zd := \frac{ZW}{10}$

$Za := 0.6 \cdot ZW$

$h := Zd$

$Jc1 := -18.75$

$Zb := ZW - .006$

$Hp := Hc1 \cdot \sqrt{\frac{Zd}{ZW}} \cdot 0.6$

$JE := 260 \cdot \left(1 - \frac{1}{g0}\right)$

$j := 0 .. 600$

$Jc2 := -112.5$

$Zx0_j := -1.25\,ZW + j \cdot 0.00025$

$$ZI1_j := \int_{-Za}^{0} \frac{Jc1}{2} \cdot \frac{(Zx0_j - Zx)}{(Zx0_j - Zx)^2 + h^2}\, dZx \qquad ZI2_j := \int_{-Zb}^{-Za} \frac{Jc2}{2} \cdot \frac{(Zx0_j - Zx)}{(Zx0_j - Zx)^2 + h^2}\, dZx$$

$$ZI3_j := \int_{-ZW}^{-Zb} \frac{JE}{2} \cdot \frac{(Zx0_j - Zx)}{(Zx0_j - Zx)^2 + h^2}\, dZx$$

$$ZI4_j := \int_{0}^{Za} \frac{-Jc1}{2} \cdot \frac{(Zx0_j - Zx)}{(Zx0_j - Zx)^2 + h^2}\, dZx \qquad ZI5_j := \int_{Za}^{Zb} \frac{-Jc2}{2} \cdot \frac{(Zx0_j - Zx)}{(Zx0_j - Zx)^2 + h^2}\, dZx$$

$$ZI6_j := \int_{Zb}^{ZW} \frac{-JE}{2} \cdot \frac{(Zx0_j - Zx)}{(Zx0_j - Zx)^2 + h^2}\, dZx$$

$$ZBZ := \left(\frac{\pi \cdot Zd \cdot 4 \cdot \pi}{10}\right) \cdot (ZI1 + ZI2 + ZI3 + ZI4 + ZI5 + ZI6)$$

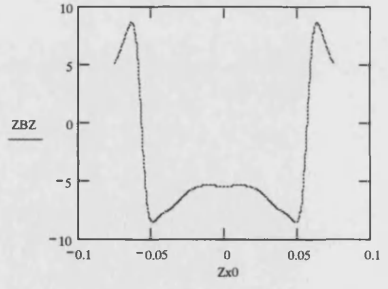

$$M_{j,0} := \frac{Zx0_j}{.00025} + 321 \qquad M_{j,1} := ZBZ_j - 5.0$$

Appendix B

Published Work

The work presented in this thesis has led to the following publications

Scanning Hall probe microscopy of flux penetration into a superconducting $YBa_2Cu_3O_{7-\delta}$ *thin film strip*, A. N. Grigorenko, S. J. Bending, J. K. Gregory, and R. G. Humphreys, Appl. Phys. Letts. **78**, 1586 (2001).

Suppression of surface barriers for flux penetration in $Bi_2Sr_2CaCu_2O_{8+\delta}$ *whiskers by electron and heavy ion irradiation*, J. K. Gregory, M. S. James, S. J. Bending, C. J. van der Beek, and M. Konczykowski, Phys. Rev. B **64**, 134517 (2001).

A scanning Hall probe microscope for large area magnetic imaging down to cryogenic temperatures, J. K. Gregory, S. J. Bending, and A. Sandhu, Rev. Sci. Instrum. **73**, 3515 (2002).

References

[1] J.D.Jackson, Classical Electrodynamics, Wiley, New York (1962)

[2] C.Kittel, Introduction to solid state physics, 6th edition, Wiley, New York (1986)

[3] V.L.Ginsburg and L.D.Landau, Zh. Eksp. Teor. Fiz. **20**, 1064 (1950)

[4] J.Bardeen, L.N.Cooper, and J.R.Schrieffer, Phys. Rev. **108**, 1175 (1957)

[5] L.N.Cooper, Phys. Rev. **104**, 1189 (1956)

[6] A.A.Abrikosov, Fundamentals of the Theory of Metals, North-Holland, Amsterdam (1988)

[7] A.A.Abrikosov, Zh. Eksp. Teor. Fiz. **32**, 1442 (1957)

[8] M.Tinkham, Introduction to superconductivity, Second edition, McGraw-Hill (1996)

[9] S.J.Bending, A.Oral, J.R.Clem, I.I.Kaya, S.Ooi, T.Tamegai, M.Henini, IEEE Transactions on applied superconductivity **9**(2), 1820-1823 Part 2, June (1999)

[10] C.P.Bean, Phys. Rev. Lett. **8**, 250 (1962)

[11] E.H.Brandt, M.V.Indenbom and A.Forkl, Europhys. Lett. **22**, 735 (1993)

[12] E.H.Brandt and M.V.Indenbom, Rev. Rev. B **48**, 12893 (1993)

[13] E.Zeldov, J.R.Clem, M.McElfresh and M.Darwin, Phys. Rev B. **49**, 9802 (1994)

[14] P.W.Anderson, Phy. Rev. Lett. **9**, 309 (1962)

[15] Y.B.Kim, C.F.Hempstead, and A.R.Strnad, Phys. Rev. **131**, 2486 (1963)

[16] J.G.Bednorz and K. A.Muller, Z. Phys. B **64,** 189 (1986)

[17] J.R.Gavalar, App. Phys. Lett. **23,** 480 (1973)

[18] M.K.Wu, J.R.Ashburn, C.J.Torng, P.H.Hor, R.L.Meng, L.Gao, Z.J.Huang, Y.Q.Wang, and C.W.Chu, Phys. Rev. Lett. **58,** 908 (1987)

[19] H.Maeda, Y.Tanaka, M.Fukutomi, and T.Asanno, Japanese Journal of Applied Physics, **27**, L209 (1988)

[20] Z.Z.Sheng and A.M.Hermann, Nature, **332,** 55 (1989)

[21] S.T.Ruggiero and D.A.Rudman, Superconducting Devices, Academic Press Inc (1990)

[22] A.A.Abrikosov, Fundamentals of the theory of metals, Noth-Holland, Amsterdam (1988)

[23] G.J.Dolan, F.Holtzberg, C.Feild, and T.R.Dinger, Phys. Rev. Lett. **62**, 2184 (1989)

[24] C.W.Hagen and R.Griessen, Phys. Rev. Lett. **62**, 2857 (1989)

[25] J.Lohle K.Mattenberger, O.Vogt, and P.Wachter, J. Applied. Phys. **72,** 1030 (1992)

[26] Z.H.Wang, Sup. Sci. Tech, **12**, 421-425 (1999)

[27] P.W.Anderson and Y.B.Kim, Rev. Mod. Phys. **36**, 39 (1964)

[28] K.A.Muller, M.Takashige, and J.G.Bednorz, Phys. Rev. Lett. **58**, 1143 (1987)

[29] Y.Yeshuran, A.P.Malozemoff, Phys. Rev. Lett. **60**, 2202 (1988)

[30] D.R.Nelson, Phys. Rev. Lett. **60**, 1973 (1988)

[31] E.H.Brandt, Phys. Rev. Lett. **63**, 1106 (1989)

[32] G.Blatter and B.Ivlev, Phys. Rev. B **50**, 10272 (1994)

[33] A.Schilling H.R.Ott, and Th.Wolf, Phys. Rev. B **46**, 14 253 (1992)

[34] H.Safar, P.L.Gammel, D.A.Huse, D.J.Bishop, J.P.Rice, and D.M.Ginsberg, Phys. Rev. Lett. **69**, 824 (1992)

[35] A.Hougton, R.A.Pelcovits and A.Sudbo, Phys. Rev. B, **40**, 6763 (1989)

[36] D.Farrell, J.P.Rice, and D.M.Ginsberg, Phys. Rev. Lett. **67,** 1165 (1991)

[37] M.Suenaga, A.K.Ghosh, Youwen Xu, and D.O.Welch, Phys. Rev. Lett. **66,** 1777 (1991)

[38] G.Blatter, V.Geshkenbein, A.Larkin, and H.Nordborg, Phys. Rev. B **54**, 72 (1996)

[39] D.Majer, E.Zeldov, and M.Konczykowski, Phys. Rev. Lett. **75**, 1166 (1995)

[40] C.P.Bean and J.D.Livingston, Phys. Rev. Lett, **12**, 14 (1964)

[41] R.P.Huebener, Magnetic flux structures in superconductors, Berlin, Springer-verlag, (1979)

[42] J.R.Clem, Poceedings of the 13th International conference on low temperature physics, **3**, 102 (1974)

[43] L.Burlachkov, V.B.Geshkenbein, A.E.Koshelev, A.I.Larkin, and V.M.Vinokur, Phys. Rev. B, **50**, 16770 (1994)

[44] L.Burlachkov, Phys. Rev. B **47**, 8056 (1993)

[45] A.V.Kuznetsov, D.V.Eremenko, and V.N.Trofimov, Phys. Rev. B, **56**, 9064 (1997)

[46] E.Zeldov, A.I.Larkin, V.B.Geshkenbein, M.Konczykowski, D.Majer, B.Khaykovich, V.M.Vinokur, and H.Shtrikman, Phys. Rev. Lett. **73**, 1428 (1994)

[47] A.I.Larkin and Yu.N.Ovchinnikov, Zh. Eksp. Teor. Fiz. 61, 1221 (1971)

[48] R.P.Huebener, R.T.Kampwirth, and J.R.Clem, J. Low Temp. Phys. **6**, 275 (1972)

[49] A.M.Cambell and J.E.Evetts, Critical currents in superconductors, Taylor and Francis, London, p142 (1972)

[50] E.H.Brandt, Rep. Prog. Phys. **58**, 1465 (1995)

[51] M.Konczykowski, L.I.Burlachkov, Y.Yeshurun, and F.Holtzberg, Phys. Rev. B. **43**, 13707 (1991)

[52] M.James, S.T.Stoddart, S.J.Bending, S.Aukkaravittayapun, P.J.King, and M.Henini, Phys. Rev. B 56, R5771, (1997)

[53] V.N.Kopylov, A.E.Koshelev, and I.F.Schegolev, Physica C **170**, 291 (1990)

[54] M.S.James, Ph.D. thesis, University of Bath (2000)

[55] A.E.Koselev and V.M.Vinokur, Phys. Rev. B. 64, 134518 (2001)

[56] A.I.Buzdin and M.Daumens, Physica C **294**, 257 (1998)

[57] A.Yu.Aladyshkin, A.S.Mel'nikov, I.A.Shereshevsky, I.D.Tokman, Physica C **361,** 67 (2001)

[58] C.W.Chu et al., Phys. Rev. Lett. **58** (9), 908 (1987)

[59] R.M.Hazen, C.T.Prewitt, R.J.Angel, N.L.Ross, L.W.Finger, C.G.Hadidiacos, D.R.Veblen, P.J.Heaney, P.H.Hor, R.L.Meng, Y.Y.Sun, Y.Q.Wang, Y.Y.Xue, Z.J.Huang, L.Gao, J.Bechtold, and C.W.Chu, Phys. Rev. Lett. **60**, 1174 (1988)

[60] J.R.Waldram, Superconductivity of metals and cuprates, Institute of Physics, Bristol (1996)

[61] T.Jacobs, S.Sridhar, Qiang Li, G.D.Gu and N.Koshizuka, Phys. Rev. Lett. **75**, 4516 (1995)

[62] C.M.Aergeter, S.L.Lee, H.Keller, E.M.Forgan and S.H.Lloyd, Phys. Rev. B **54** R15661 (1996)

[63] M.Niderost, R.Frassanito, M.Saalfrank, A.C.Mota, G.Blatter, V.N.Zavaritsky, T.W.Li, and P.H.Kes, Phys. Rev. Lett. **81**, 3231 (1998)

[64] R.Prozorov, R.W.Giannetta, A.Carrington, P.Fournier, R.L.Greene, P.Guptasarma, D.G.Hinks, and A.R.Banks, Appl. Phys. Lett. **77**, 4202 (2000)

[65] D.A.Bonn, Ruixing Liang, T.M.Riseman, D.J.Baar, D.C.Morgan, Kuan Zhang, P.Dosanjh, T.L.Duty, A.MacFarlane, G.D.Morris, J.H.Brewer, W.N.Hardy, C.Kallin, and A.J.Berlinsky, Phys. Rev. B **47**, 11314 (1993)

[66] S.L.Lee, P.Zimmermann, H.Keller, M.Warden, I.M.Savic, R.Schauwecker, D.Zech, R.Cubitt, E.M.Forgan, P.H.Kes, T.W.Li, A.A.Menovsky, and Z.Tarnawski, Phys. Rev. Lett. **71**, 3862 (1993)

[67] V.G.Kogan, M.Ledvij, A.Yu.Simonov, J.H.Cho, and D.C.Johnston, Phys. Rev. Lett. **70**, 1870 (1993)

[68] K.S.Bedell, I.Minui, D.Meltzer, J.R.Schrieffer, and S.Doniach, "Phenomenology and Applications of High Temperature Superconductors", Addison Wesley, Reading, MA, p.164 (1992)

[69] B.Khaykovich, M.Konczykowski, E.Zeldov, R.A.Doyle, D.Majer, P.H.Kes and T.W.Li, Phys. Rev. B **56**, R517 (1997)

[70] P.L.Gammel, L.F.Schneemeyer, J.V.Wasczak, and D.J.Bishop, Phys. Rev. Lett. **61**, 1666 (1988)

[71] D.T.Fuchs, R.A.Doyle, E.Zeldov, D.Majer, W.S.Seow, R.J.Drost, T.Tamegai, S.Ooi, M.Konczykowski, P.H.Kes, Phys. Rev. B **55**, R6156 (1997)

[72] B.Khaykovich, E.Zeldov, D.Majer, T.W.Li, P.H.Kes, and M.Konczykowski, Phys. Rev. Lett. **76**, 2555 (1996)

[73] G.Yang, P.Shang, S.D.Sutton, I.P.Jones, J.S.Abell and C.E.Gough, Phys. Rev. B **48**, 4054 (1993)

[74] T.Blasius, Ch.Niedermayer, J.L.Tallon, D.M.Pooke, A.Golnik, and C.Bernhard, Phys. Rev. Lett, **82**, 4926 (1999)

[75] S.Ryu, A.Kapitulnik, and S.Doniach, Phys. Rev. Lett. **77**, 2300 (1996)

[76] T.Nishizaki, N.Kobayashi, Supercond. Sci. Technol. **13**, 1-11 (2000)

[77] G.Blatter, M.V.Feigel'man, V.B.Geshkenbein, A.I.Larkin, V.M.Vinokur, Rev. Mod. Phys. **66**, 1125 (1994)

[78] D.Eratas and D.R.Nelson, Physics C **272**, 79 (1996)

[79] J.Kierfeld, Physica C **300**, 171 (1998)

[80] S.Aukkaravittayapun, P.J.King, K.A.Benedict, Y.I.Latyshev, I.G.Gorlova, S.Zybtsev, A.Campbell, R.A.Doyle, J.Johnson, W.S.Seow, Physica C **270**, 231 (1996)

[81] I.Matsubara, R.Funahashi, K.Ueno, H.Ishikawa, Jn. Cryst. Growth 167, 570 (1996)

[82] A.Oral, S.J.Bending, and M.Henini, Appl. Phys. Lett. **69**, 1324 (1996)

[83] Analog Devices, Programmable gain instrumentation amplifier AD625 data sheet, http://www.analog.com, 2000

[84] C.C.Tsuei, J.R.Kirtley, C.C.Chi, L.S.Yu-Jahnes, A.Gupta, T.Shaw, J.Z.Sun and M.B.Ketchen, Phys. Rev. Lett. **73**, 593 (1994)

[85] Y.Martin, D.Rugar, and H.K.Wickramasinghe, Appl. Phys. Lett. **52**, 244 (1988)

[86] A.Moser, H.J.Hug, I.Parashikov, B.Stiefel, O.Fritz, H.Thomas, A.Varatoff, H.J.Guntherodt, and P.Chaudhari, Phys. Rev. Lett. **74**, 1847 (1995)

[87] P.B.Alers, Phys. Rev. **105**, 104 (1957)

[88] A.A.Polyanskii, A.Gurevic, A.E.Pashitski, N.F.Heinig, R.D.Redwing, J.E.Nordman, and D.C.Larbalestier, Phys. Rev. B **53**, 8687 (1996)

[89] T.Matsuda, A.Fukuhara, T.Yoshioka, S.Hasegawa, A.Tonomura, and Q.Ru, Phys. Rev. Lett. **66**, 457 (1991)

[90] A.M.Chang, H.D.Hallen, L.Harriot, H.F.Hess, H.L.Loa, J.Kao, R.E.Miller, and T.Y.Chang, Appl. Phys. Lett. 61, 1974 (1992)

[91] D.Davidovic, S.Kumar, K.H.Reich, J.Siegel, S.B.Field, R.D.Tiberio, R.Hey, and K.Ploog, Phys. Rev. Lett. **76**, 815 (1996)

[92] A.Oral, S.J.Bending and M.Henini, J. Vac. Sci. Technol. B **14**, 1202 (1996)

[93] A.Sandhu, H.Masuda, A.Oral, and S.J.Bending, Jpn. J. Appl. Phys., Part 1 40, 4321 (2001)

[94] A.Sandhu, H.Masuda, K.Kurosawa, A.Oral, and S.J.Bending, Electron. Lett. 37, 1335 (2001)

[95] M.Nakamura, M.Kimura, K.Sueoka, and K.Mukasa, Appl. Phys. Lett, **80**, 2713 (2002)

[96] C.J van deer Beek, M.Konczykowski, R.J.Drost, P.H.Kes, N.Chikumoto, and S.Bouffard, Phys. Rev. B **61**, 4259 (2000)

[97] H.Vichery, F.Rullieralbenque, H.Pascard, M.Konczykowski, R.Kormann, D.Favrot, G.Collin, Physica C **159**, 689 (1989)

[98] V.Hardy, D.Groult, J.Provost, M.HerVieu, B.Raveau, S.Bouffard, Physica C **178**, 255 (1991)

[99] S.F.W.R.Rycroft, R.A.Doyle, D.T. Fuchs, E.Zeldov, R.J.Drost, P.H.Kes, T.Tamegai, S.Ooi, and D.T.Foord, Phys. Rev. B **60**, 757 (1999)

[100] C.A.Duran, P.L.Gammel, R.E.Miller, and D.J.Bishop, Phys. Rev. B **52**, 75 (1995)

[101] H.Fraham, S.Ullah, and A.T.Dorsey, Phys. Rev. Lett. **66**, 3067 (1991)

[102] I.Aranson, M.Gitterman, and B.Ya.Shapiro, Phys. Rev. B **51**, 3092 (1995)

[103] I.Aranson, B.Ya.Shapiro, and V.Vinokur, Phys. Rev. Lett. **76**, 142 (1996)

[104] A.V.Kuznetsov, D.V.Eremenko, and V.N.Trofimov, Phys. Rev. B **59**, 1507, (1999)

[105] N.Motohira, K.Kuwahara, T.Hasegawa, K.Kishio and K.Kitazawa, J. Ceram. Soc. Jpn. **97**, 1009 (1989)

[106] H.Ohno, H.Munekata, T.Penney, S.von Molnár, and L.L.Chang, Phys. Rev. Lett. **68**, 2664 (1992)

[107] H.Ohno, A.Shen, F.Matsukura, A.Oiwa, A.Endo, S.Katsumoto, and Y.Iye, Appl. Phys. Lett. **69**, 363 (1996)

[108] H.Munekata, A.Zaslavsky, P.Fumagalli, and R.J.Gambino, Appl. Phys. Lett. **63**, 2929 (1993)

[109] L.N.Vu, M.S.Wistrom, and D.J.Van Harlingen, Appl. Phys. Lett, **63**, 1693 (1993)

[110] A.Hubert, R.Schafer, Magnetic Domians, Springer, New York (1998)

[111] T.Shono, T.Hasegawa, T.Fukumura, F.Matsukura, and H.Ohno, Appl. Phys. Lett. **77**, 1363 (2000)

[112] T.Fukumura, T.Shono, K.Inaba, T.Hasegawa, H.Koinuma, F.Matsukura, and H.Ohno, Physica E **10**, 135 (2001)